

Charles Mockett  
Werner Haase  
Dieter Schwamborn *Editors*

# Go4Hybrid: Grey Area Mitigation for Hybrid RANS-LES Methods

Results of the 7th Framework Research  
Project Go4Hybrid, Funded by the  
European Union, 2013–2015



*European Commission  
Research Directorate General*

 Springer

The Springer logo, which consists of a stylized chess knight piece.

# Notes on Numerical Fluid Mechanics and Multidisciplinary Design

Volume 134

## Series editors

Wolfgang Schröder, Lehrstuhl für Strömungslehre und Aerodynamisches Institut,  
Aachen, Germany  
e-mail: office@aia.rwth-aachen.de

Bendiks Jan Boersma, Delft University of Technology, CA Delft, The Netherlands  
e-mail: b.j.boersma@tudelft.nl

Kozo Fujii, The Institute of Space and Astronautical Science, Kanagawa, Japan  
e-mail: fujii@flab.eng.isas.jaxa.jp

Werner Haase, Neubiberg, Germany  
e-mail: whac@haa.se

Ernst Heinrich Hirschel, Zorneding, Germany  
e-mail: e.h.hirschel@t-online.de

Michael A. Leschziner, Imperial College of Science Technology and Medicine,  
London, UK  
e-mail: mike.leschziner@imperial.ac.uk

Jacques Periaux, Paris, France  
e-mail: jperiaux@free.fr

Sergio Pirozzoli, Università di Roma "La Sapienza", Roma, Italy  
e-mail: sergio.pirozzoli@uniroma1.it

Arthur Rizzi, KTH Royal Institute of Technology, Stockholm, Sweden  
e-mail: rizzi@aero.kth.se

Bernard Roux, Technopole de Chateau-Gombert, Marseille Cedex, France  
e-mail: broux@13m.univ-mrs.fr

Yurii I. Shokin, Siberian Branch of the Russian Academy of Sciences,  
Novosibirsk, Russia  
e-mail: shokin@ict.nsc.ru

*About this Series*

*Notes on Numerical Fluid Mechanics and Multidisciplinary Design* publishes state-of-art methods (including high performance methods) for numerical fluid mechanics, numerical simulation and multidisciplinary design optimization. The series includes proceedings of specialized conferences and workshops, as well as relevant project reports and monographs.

More information about this series at <http://www.springer.com/series/4629>

Charles Mockett · Werner Haase  
Dieter Schwamborn  
Editors

# Go4Hybrid: Grey Area Mitigation for Hybrid RANS-LES Methods

Results of the 7th Framework Research  
Project Go4Hybrid, Funded by the European  
Union, 2013–2015

 Springer

*Editors*

Charles Mockett  
CFD Software E+F GmbH  
Berlin  
Germany

Werner Haase  
Aeronautics Consultants  
Neubiberg  
Germany

Dieter Schwaborn  
Deutsches Zentrum für Luft- und Raumfahrt  
e.V. (DLR)  
Institut für Aerodynamik und  
Strömungstechnik  
Göttingen, Niedersachsen  
Germany

ISSN 1612-2909

ISSN 1860-0824 (electronic)

Notes on Numerical Fluid Mechanics and Multidisciplinary Design

ISBN 978-3-319-52994-3

ISBN 978-3-319-52995-0 (eBook)

DOI 10.1007/978-3-319-52995-0

Library of Congress Control Number: 2017935819

© Springer International Publishing AG 2018

This work is subject to copyright. All rights are reserved by the Publisher, whether the whole or part of the material is concerned, specifically the rights of translation, reprinting, reuse of illustrations, recitation, broadcasting, reproduction on microfilms or in any other physical way, and transmission or information storage and retrieval, electronic adaptation, computer software, or by similar or dissimilar methodology now known or hereafter developed.

The use of general descriptive names, registered names, trademarks, service marks, etc. in this publication does not imply, even in the absence of a specific statement, that such names are exempt from the relevant protective laws and regulations and therefore free for general use.

The publisher, the authors and the editors are safe to assume that the advice and information in this book are believed to be true and accurate at the date of publication. Neither the publisher nor the authors or the editors give a warranty, express or implied, with respect to the material contained herein or for any errors or omissions that may have been made. The publisher remains neutral with regard to jurisdictional claims in published maps and institutional affiliations.

Printed on acid-free paper

This Springer imprint is published by Springer Nature

The registered company is Springer International Publishing AG

The registered company address is: Gewerbestrasse 11, 6330 Cham, Switzerland

# Foreword

It is observed in many technical applications that RANS models show inherent technology limitations for certain types of flows (for example, flows with large/massive separation, flows with strong mixing zones, flows with strong interactions of different flows features). For this reason, there is a continuous drive within the turbulence community to augment RANS models with Scale-Resolving Simulation (SRS) capabilities. Motivated by the high cost of conventional Large Eddy Simulation (LES) and Wall Modeled LES (WMLES) for wall boundary layer simulations, hybrid RANS-LES models have been developed over the past two decades. From the numerous different hybrid approaches, the Go4Hybrid project was mainly centered around models of the DES family (Spalart 2009), which are the most prominently used hybrid RANS-LES models in industrial simulations today.

The original goal in the development of hybrid models was the formulation of methods where all(!) attached and mildly separated boundary layers are covered in RANS-mode and where only detached regions are treated by LES. A good example is an aircraft with the landing gear extracted, where only the highly unstable mixing zone behind the landing gear would be covered by LES whereas all boundary layers around the aircraft are covered by RANS. Even this seemingly simple goal poses significant challenges. The first one is the ‘shielding’ of the RANS boundary layer against any unwanted influences from the LES formulation. In the original DES formulation, this aspect was only partly achieved. This resulted in highly problematic effects on the solution, especially Grid Induced Separation (GIS) (Menter and Kuntz 2003). GIS appeared as a result of the reduction of the eddy-viscosity inside the RANS boundary layers due to the impact of the grid-dependent LES model formulation. Especially in general industrial flow simulations, safe shielding is a major requirement for a reliable model. Improved shielding has subsequently been achieved through adding shielding functions as proposed by Menter and Kuntz (2003), finally resulting in Delayed Detached Eddy Simulation (DDES) (Spalart et al. 2006; Grikskevich et al. 2012). But even with DDES, the shielding is not perfect and can be broken under practical conditions and care has to be exercised by the user. While many studies focus on the LES side of hybrid RANS-LES models,

the importance of maintaining the integrity of attached RANS boundary layers cannot be over-stressed. Experience over the last decades has shown that most industrial users cannot reliably adhere to complex grid generation requirements related to this issue, partly due to a lack of understanding of the details of the methods, partly due to a lack of support from the meshing tools, but mostly due to the sheer complexity of the geometry of their application. When dealing with hybrid RANS-LES methods, one is therefore well advised to consider their ability of shielding the boundary layers from unwanted LES influences. Several model formulations within this book address this issue as a central point of their design.

The second critical aspect with respect to global hybrid models (meaning the user selects one model formulation for the entire domain and the model itself determines where to act in RANS and where in LES mode) is the fidelity with which they switch from RANS to LES mode. ‘Switching’ does not only mean that the model formulation changes, but that there is a sufficiently rapid appearance of unsteady resolved turbulence structures in the ‘transitional’ zone between RANS and LES. In global hybrid models, this ‘transition’ is triggered by an instability. The speed with which resolved turbulence structures appear depends both on the type of flow and on the model formulation. For highly unstable flows, e.g. flows past bluff bodies, all models tend to switch swiftly from RANS to LES mode. However, many more technical flows are dominated by Separating Shear Layers (SSL). The most prominent example is a backward facing step flow, where the attached boundary layer upstream of the step transitions into a free mixing layer past the step. The SSL does not push the flow very hard into LES mode and the fidelity with which this transfer happens depends strongly on the details of the model formulation (as well as on meshing and numerics details). The original DES/DDES model family shows a fairly slow RANS-LES transition, due to the relatively high LES eddy-viscosity levels under such conditions. It is interesting to note that this deficiency is linked closely with the desire of achieving reliable shielding of the attached RANS boundary layers. So, to a certain degree, there is a balance between shielding and rapid RANS-LES transition.

When using global hybrid models, one should also never forget that the ‘RANS-LES’ transition is an inherently unphysical process. In the real world, the upstream turbulent boundary layer already injects ‘resolved’ turbulence into SSL thereby suppressing the 2D-transitional process observed in global hybrid models. The optimization of global hybrid models reduces the extent of this unphysical ‘transition’ zone. However, there are scenarios where the flow instability is not strong enough to push the simulation from RANS to LES even with optimal model formulations. In such cases, zonal methods need to be developed, where the user selects the RANS and LES zones during pre-processing. More importantly, algorithms are employed at the RANS-LES interfaces to convert modeled turbulence into resolved turbulence. This is typically achieved through synthetically generated turbulence based on the upstream RANS solution. This is a much more complex technology, both from the formulation of the methods themselves as well as with regards to the user interaction required.

The Go4Hybrid project has addressed all of the above issues by different degrees. The main focus was devoted to global hybrid RANS-LES methods and this is also the area, where the most substantial progress has been achieved. However, numerous interesting aspects of zonal methods have been investigated and those findings will contribute in the longer term to improved model formulations for industrial CFD simulations.

As an observer and reviewer to the project, I enjoyed being part of this very active and cooperative group. Many useful discussions took place during the project and much useful work has been conducted in the relatively short project timeframe. The project was managed in a very goal-oriented manner and a good balance between model advancement and solidification of findings through proof-of-concept experiments was achieved. Finally, complex test cases demonstrated that some of the more mature methods are ready for industrial use.

To me, as an active turbulence modeler, the findings of the Go4Hybrid project go beyond just a number of ready-to-use new model formulations, but offer a substantial wealth of inspiring ideas and new modeling elements on the subject. I am convinced that every reader interested in this topic will similarly benefit from the book at hand.

Florian Menter  
Senior Fellow, ANSYS Germany GmbH



# Preface

Computational fluid dynamics (CFD) is nowadays applied extensively in all aerodynamics-based topics of aircraft design, development and optimization. Since standard CFD approaches still lack accuracy in areas of highly nonlinear, unsteady flows close to the borders of the flight envelope, the aeronautical industry is increasingly willing to apply more costly scale-resolving methods, if such are able to provide a real predictive alternative for critical situations. While Large Eddy Simulation (LES) may be a viable option in certain areas, it is still far too costly—if not impossible—to apply it to high Reynolds number flows about even moderately complex configurations. Thus, the family of Hybrid RANS-LES Methods (HRLM) currently appears to be the best candidate for the next generation of CFD methods to increase solution fidelity at an industrially feasible expense.

HRLM have been proven to perform considerably better than conventional Reynolds-Averaged Navier-Stokes (RANS or URANS) approaches in situations with strong flow separation, but they are less effective once they have to deal with weakly unstable<sup>1</sup> flows, e.g. thin separation regions or shear layers in general. In such cases, resolved structures develop only very slowly, resulting in areas where the total amount of turbulence (both in modeled and resolved terms) is unphysically low. These so-called “Grey Areas” often lead to results that are worse than those of RANS simulations.

Unfortunately, such grey area situations appear in many of the flows important close to the borders of the flight envelope, e.g. near maximum lift. Accordingly, there is a strong necessity to mitigate the grey area in order to provide the industry with Hybrid RANS-LES approaches that are trustworthy for relevant flow situations. Precisely this was the primary objective of the Go4Hybrid project, which focused on two main aspects: to provide viable extensions to HRLM mitigating the grey area problem in non-zonal approaches and to improve embedded methods, such that they are applicable to arbitrarily complex geometries.

---

<sup>1</sup>Note, that unstable refers here to an easy switching from an unresolved to a resolved modeling of turbulence.

The improvements derived in the course of the project have been assessed against both fundamental and more complex test cases and thus the editors sincerely hope that this book provides a helpful compendium for the reader interested in this kind of method and grey area mitigation in particular. In this respect also the Common Assessment Platform—to our knowledge a new idea in the framework of European projects—may provide interesting insight into the behavior of the different approaches.

The whole outcome of the Go4Hybrid project described in this book and the goals achieved showcase the excellent cooperation between the partners involved. Their collaboration—fostered by the financial support of the European Union – has not only benefitted the organizations involved, but will also lead to a wide dissemination of the knowledge acquired both through education of students and the close links to the industry. The latter are particularly reflected in the long list of ten Industrial Observers and two Associate Partners of Go4Hybrid.

This volume compiles all technical work and achievements obtained in the Go4Hybrid project, starting with an overview of the project in Part I “The Go4Hybrid Project”, followed by the presentation of the approaches used in Part II “Presentation of Approaches”. In Part III “Results for Fundamental Test Cases” and Part IV “Results for Complex Test Cases” all relevant results are presented and discussed. An activity was set up within Go4Hybrid referred to as the “Common Assessment Platform” (CAP) with the goal to implement and assess the most promising partner methods developed in the project using a common CFD code. The major findings of this endeavor can be found in Part V “The Common Assessment Platform”. Last but not least, Part VI contains the “Conclusions” drawn. All references (used in the different parts and chapters) can be found at the end of the book.

Thanks and congratulations are due to the Go4Hybrid partners, whose expertise and open collaboration made the project both clearly successful as well as highly enjoyable. Special thanks are also due to the Associate Partners and Industrial Observers, some of whom contributed actively to lively discussions in the meetings as well as to the final workshop.

Additional thanks are due to D. Knörzner, the European Commission’s Scientific Officer to the project, who was always very supportive of the project and provided every help necessary.

Last but not least, the editors of this book would like to express their gratitude to W. Schröder, the General Editor of the Springer series ‘Notes on Numerical Fluid Mechanics and Multidisciplinary Design’, as well as to A. Feldhusen-Hoffmann for their help and editorial advice, and of course to the Springer team around L. di Cecco.

Berlin, Germany  
München, Germany  
Göttingen, Germany  
November 2016

Charles Mockett  
Werner Haase  
Dieter Schwamborn

# Contents

## Part I The Go4Hybrid Project

<b>The Go4Hybrid Project—Motivation and Objectives, Project Structure, Test Cases and Project Partners</b> . . . . .	3
C. Mockett and W. Haase	

## Part II Presentation of Approaches

<b>Non-zonal Approaches for Grey Area Mitigation</b> . . . . .	17
C. Mockett, M. Fuchs, F. Thiele, S. Wallin, S.H. Peng, S. Deck, J.C. Kok, H. van der Ven, A. Garbaruk, M. Shur, M. Strelets and A. Travin	
<b>Improved Embedded Approaches</b> . . . . .	51
M. Shur, M. Strelets, A. Travin, A. Probst, S. Probst, D. Schwamborn, S. Deck, A. Skillen, J. Holgate and A. Revell	

## Part III Results for Fundamental Test Cases

<b>Free Shear Layer</b> . . . . .	91
Shia-Hui Peng	
<b>The Spatially Developing Flat Plate Turbulent Boundary Layer</b> . . . . .	109
Sébastien Deck	

## Part IV Results for Complex Test Cases

<b>Single-Stream Round Jet at <math>M = 0.9</math></b> . . . . .	125
M. Fuchs, C. Mockett, M. Shur, M. Strelets and J.C. Kok	
<b>Delta Wing at High Angle of Attack</b> . . . . .	139
J. Kok, M. Fuchs and C. Mockett	
<b>3-Element Airfoil</b> . . . . .	155
A. Probst, S. Probst and D. Schwamborn	

**2D Wall-Mounted Hump** . . . . . 173  
A. Garbaruk, E. Guseva, M. Shur, M. Strelets and A. Travin

**EC135 Helicopter Fuselage.** . . . . . 189  
N. Ashton, M. Fuchs, C. Mockett and B. Duda

**Part V The Common Assessment Platform**

**Rationale of Comparison in a Single CFD code** . . . . . 205  
M. Fuchs, C. Mockett, A. Skillen and A. Revell

**Direct Comparison of Non-zonal Methods** . . . . . 209  
M. Fuchs and C. Mockett

**Direct Comparison of Embedded Approaches** . . . . . 235  
A. Skillen, J. Holgate and A. Revell

**Part VI Conclusions**

**The Go4Hybrid Project Achievements** . . . . . 255  
C. Mockett and S. Wallin

**References** . . . . . 275

**Part I**  
**The Go4Hybrid Project**

# The Go4Hybrid Project—Motivation and Objectives, Project Structure, Test Cases and Project Partners

C. Mockett and W. Haase

## 1 Motivation and Objectives

Computational Fluid Dynamics (CFD) has become a key technology in the rapid and cost-effective design of green aircraft with reduced fuel consumption and aero-acoustic noise emissions. In general, this has led to increasing emphasis on numerical simulations compared to wind tunnel investigations.

The accurate and efficient prediction of turbulent flow, however, represents one of the central limitations of CFD, with precise methods requiring unfeasible computational resources and more efficient methods introducing approximations and inaccuracy. A new family of hybrid Reynolds Average Navier-Stokes—Large Eddy Simulation (RANS-LES) methods have recently emerged, which offer a significant increase in accuracy whilst limiting expense to levels that are affordable with current and near-future computational capacity.

Figure 1 exhibits the status quo at the beginning of the Go4Hybrid project and demonstrates the applicability of hybrid RANS-LES methods including DES approaches as well as wall-modelled LES (WMLES) for the flow areas given. The acronym SAS refers to the hybrid method known as “scale-adaptive simulation”.

Despite excellent results by hybrid RANS-LES methods, a fundamental issue remained to be addressed, known as the grey area problem. This aspect concerns the transition region between the RANS and LES modes of such hybrid methods. As the grey area problem has a particularly detrimental impact on flows featuring shallow regions of boundary layer separation and re-attachment, the accuracy of hybrid RANS-LES predictions was downgraded, and applications with respect to

---

C. Mockett (✉)

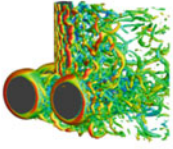
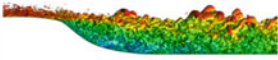
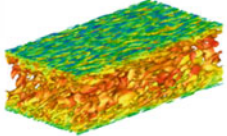
CFD Software E+F GmbH, Bismarckstr. 10-12, 10625 Berlin, Germany  
e-mail: charles.mockett@cf-d-berlin.com

W. Haase

Aeronautics Consultants, Max-Löw-Str. 14a, 85579 Neubiberg, Germany  
e-mail: whac@haa.se

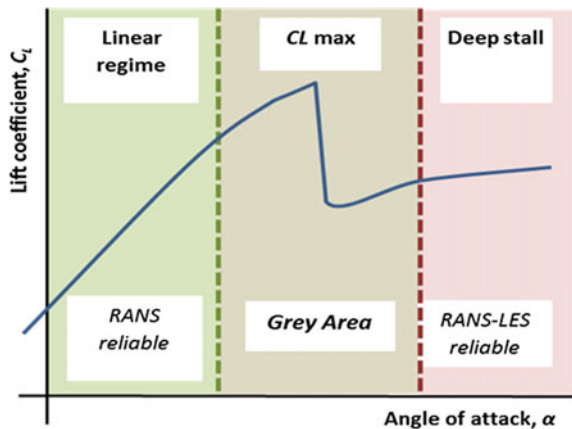
© Springer International Publishing AG 2018

C. Mockett et al. (eds.), *Go4Hybrid: Grey Area Mitigation for Hybrid RANS-LES Methods*, Notes on Numerical Fluid Mechanics and Multidisciplinary Design 134, DOI 10.1007/978-3-319-52995-0\_1

"Globally unstable" flows	"Locally unstable" flows	"Stable" flows
		
Applicability of DES-like methods		
Applicability of SAS	(SAS requires forcing to enter scale-resolving mode)	
Embedded approaches necessary		
Applicability/suitability of WMLES		
	Embedded approaches recommended if separation location can be readily defined and/or if definition of RANS/LES zones is practicable. Otherwise careful use of shielded DES-like approaches (e.g. DDES) recommended.	

**Fig. 1** Summary of method applicability prior to Go4Hybrid; Adapted from Best Practice Guide of the ATAAC project

**Fig. 2** Schematic of *grey area* impact on aerodynamic wing simulations—the *grey area* problem compromises predictive accuracy for the most important flow regimes



aerodynamic and aero-acoustic flows, such as wings near the borders of the flight envelope and jet noise, tended to suffer from grey area issues.

This problem is well characterised by Fig. 2. It underpins the reliability of RANS approaches for aerodynamic wing/profile approaches in the area of low angle-of-attack, the reliability of RANS-LES methods for deep stall, but the problem around stall—caused by drawbacks encountered in the hybrid RANS-LES methods.

Because of the importance of  $C_L$ -max for aircraft design, work focused on eliminating or at least reducing grey area issues will have a high impact for industrial CFD.

The Go4Hybrid project was initiated to pursue the development and demonstration of improvements to hybrid RANS-LES methods in order to reduce the severity of the grey area issue (or eliminate it entirely). As will be seen throughout the contributions in this book, these goals have been successfully met.

A range of approaches to reducing the grey area severity have been developed and evaluated. The evaluation took into account not only the predictive accuracy of the improved methods but also practical issues, such as computational expense and user-friendliness. A balance was struck between simple academic test cases (for reduced computational expense and more pure evaluation) and complex application test cases (for demonstrating applicability).

Technically, a two-pronged strategy was adopted. On the one hand, grey area mitigation strategies for non-zonal hybrid approaches have been pursued. These methods are inherently more flexible and applicable to complex industrial geometries, however they suffer most strongly from grey area effects. On the other hand, zonal or embedded strategies have the potential to eliminate the grey area problem entirely. However, these zonal methods are inherently more complicated to set up and are most readily applied only to simple configurations or a limited class of industrial problems, and are hence far from being a generalised tool in a complex industrial environment. Improvements to the flexibility and applicability of embedded hybrid strategies therefore constituted the second aim of the Go4Hybrid efforts.

All the development work focused on just two academic test cases. The direct comparability and ranking of the methods was facilitated by the use of common grids and a common numerical assessment platform, CAP.

The latter was used as a possibility to circumvent the use of different codes normally in use by the Go4Hybrid partners, codes that are different with respect to numerical issues. Hence, the CAP served as a basic software tool where the different methods have been employed and tested to ensure a direct comparison. Considerable effort was undertaken to achieve comparable results, and the CAP exercise yielded valuable conclusions.

To complement the fundamental test cases, the demonstration of industrial applicability was enabled by a range of complex application cases, including delta wing flow, jet noise investigations, flow around a three-element airfoil, a shallow recirculating flow, and the flow around a complex helicopter fuselage.

The direct outcome of the project was a significant improvement in the predictive accuracy of hybrid RANS-LES methods for practical flows affected in the past by the grey area issue. Since this issue is typically strongly pronounced in flows representative of engineering performance limits, the practical impact is seen to be very significant. Moreover, a wide range of industrial applications will benefit from these new findings, including for example external aerodynamics of aircraft, automobiles and rail vehicles, as well as gas turbines for propulsion and power generation and aircraft noise sources such as jet and airframe noise.

As said in the beginning, by increasing the predictive accuracy and reducing user burden for the mentioned key applications, the Go4Hybrid project was able to



contribute to the increased adoption of simulation in contrast to expensive experiments, e.g. wind tunnel tests. The project therefore contributed to an increased competitiveness and technical leadership of European industry.

The transfer of the developed methods to industrial application is facilitated by the high-profile observer and associate partner group with ten industrial observers and two (industrial) associate partners. High levels of participation in these groups indicates both the strong interest as well as the importance of the work on grey area mitigation for hybrid RANS-LES methods in the Go4Hybrid project.

## 2 Project Structure

The Go4Hybrid project was structured in 4 main work packages, all of them split into specific tasks. Figure 3 sketches the project structure and shows in addition the relation to the test case structure.

The “main objective layer” demonstrates that the grey area mitigation (GAM) methods are the driving elements generating the work packages and tasks. The dual strategy described above is reflected in the two main technical work packages 2 and 3, dedicated to GAM for non-zonal methods and improved embedded approaches, respectively. The work packages are summarised as follows.

### 2.1 Work Package 1

The first work package dealt with all issues of the general management, and includes all tasks referring to project management, **Task 1.1**, web site set-up and maintenance, and knowledge dissemination and exploitation. **Task 1.2** is directly coupled

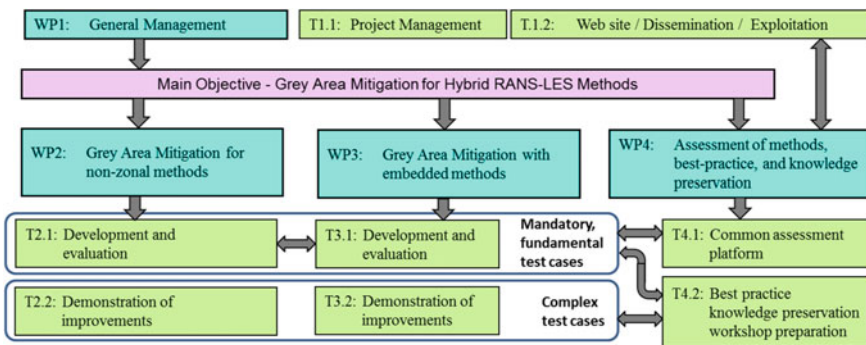


Fig. 3 Work packages and tasks for the Go4Hybrid project

with **WP4**, to a smaller extent with **Task 4.1**, but to a larger extent with **Task 4.2**, concerned with knowledge preservation and the preparation of the final workshop.

## 2.2 *Work Package 2*

Work package 2 dealt with the grey area mitigation (GAM) methods applied to non-zonal methods. Here, a range of different approaches have been studied, which reduce the severity of the grey area problem. The methods developed are applicable as a “retro-fit” to existing hybrid RANS-LES methods in general. WP2 was split into two tasks, first of all **Task 2.1** concerning development and validation of new and/or advanced GAM methods. This work was solely based on the fundamental shear layer test case, see the “Test Case Repository” section below. Moreover, to receive results from different CFD methods used by the partners, this case was mandatory for all partners working on non-zonal methods and mandatory meshes were specified. The new GAM methods were then applied to complex test cases to demonstrate the achieved improvements, **Task 2.2**.

## 2.3 *Work Package 3*

Work package 3 was dedicated to improvements to embedded methods, i.e. approaches where a local LES region is inserted into a more global RANS simulation. This approach makes it necessary to introduce realistic turbulent content at the inlet to the scale-resolving domain, equivalent to the modelled turbulence in the upstream RANS region. Synthetic turbulence approaches such as those of Jarrin et al. (2006) or Adamian and Travin (2010) were studied and further developed. The challenge here was to “transform” modelled turbulence into resolved content on the usually finer embedded grid such that the grey area behind the interface is minimised. A key objective was to increase the flexibility and suitability of embedded strategies to more complex and generalised applications. **WP3** was split into two tasks, similar to **WP2**, with **Task 3.1** dealing with the development and validation of the new methods on the fundamental (mandatory) test case of a flat plate boundary layer. As for the shear layer in **WP2**, this case was mandatory for all partners working on embedded methods. Finally, **Task 3.2** was dedicated to the demonstration of the new methods for cases with clear industrial relevance.

## 2.4 *Work Package 4*

Work package 4 was dedicated to an assessment of the GAM methods combined with best-practice recommendations and the preservation of the obtained

knowledge. A close link was established with *Task 1.2* and here in particular with dissemination and exploitation of knowledge in relation to the common-code assessment work and the final workshop that took place at the end of the project in September 2015, with about 50 participants from 7 countries.

*Task 4.1* dealt with the assessment of methods. A selection of methods was ported into one common CFD platform, OpenFOAM. The motivation for this initiative was to eliminate code-dependency in the direct comparison of different GAM approaches. The common-code work was based on the two mandatory (fundamental) test cases, see the test case matrix below.

The second task in *WP 4, Task 4.2*, is concerned with best practice, knowledge preservation and the organization of the final workshop. The link to *Tasks 2.1* and *3.1*, dealing with fundamental test cases, is essential results were presented completely based on work carried out in these two tasks. The link to *Tasks 2.2* and *3.2* is related to best-practice, knowledge preservation and again the final workshop, all items that are directly connected to the final results presented in the current book, the final reporting and of course the knowledge gained in the Go4Hybrid project.

### 3 Test Case Repository and Partners Involved

The test case repository, presented below in Table 1, is divided into two main areas, namely fundamental and complex demonstration cases. Fundamental test cases were used to receive fast results and answers with respect to the new/advanced methods within “reasonable” computing times. As said, the fundamental cases were mandatory and employed mandatory meshes.

Furthermore, the applicability of the innovative GAM approaches was demonstrated on complex, industrially relevant, hence challenging problems, including an aero-acoustic application.

It should be noted as well that two of the industrially relevant test cases were defined by the associated partners, Airbus Defence and Space and Airbus Helicopters, while the third on noise propagation has been proposed by the observer Rolls-Royce. Concerning the observer and associate partners in the Go4Hybrid project, please see Sect. 4.

To provide the reader with the appropriate points-of-contacts related to the test cases run in the Go4Hybrid project, Table 2 can be used. The test case coordinators are highlighted (“COORD”), while participating partners are listed as “Partners”. It can be seen that at least two partners were working on each industrial (I.x) case in order to enable cross-partner comparisons.

**Table 1** Test case repository

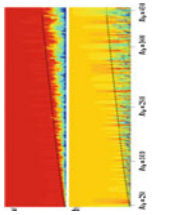
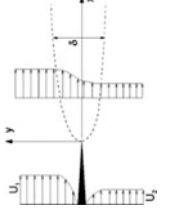





 <p><b>F.1—Flat plate boundary layer</b>  <math>Re_0</math> up to 4300          (Exp. and DNS data)  <b>Mandatory TC for all WP3 partners</b></p>	 <p><b>F.2—Spatial shear layer</b>  <math>Ma = 0.12</math>  <math>Re_0 = 2900</math>  <b>Mandatory TC for all WP2 partners</b></p>	 <p><b>L.1—Helicopter</b>          Proposed by: Airbus helicopters  <math>Ma = 0.21</math>  <math>Re = 4.8 \times 10^6/m</math></p>	 <p><b>L.2—Vortex flow experiment (VFE-2)</b>          Proposed by: Airbus defence and space  <math>M = 0.07</math>,  <math>Re = 1 \times 10^6</math>,  <math>\alpha = 23^\circ</math></p>
<p><b>Justification for TC:</b> Wide scope of practical applications in various domains of aeronautics, highly challenging for embedded methods, active field of research for high-Re wall turbulence</p>	<p><b>Justification for TC:</b> Shear layers are present in almost any flow of practical interest. TC exhibits grey area problem causing incorrect prediction of the spreading rate</p>	<p><b>Justification for TC:</b> Industrial—Initially shallow separation from smooth rear fuselage region, high geometric complexity, comprehensive measurements</p>	<p><b>Justification for TC:</b> Industrial—Comprehensive measurements; strong vortices with pronounced grey area, and therefore strong need for GA mitigation</p>

Table 1 continued

 <p><b>I.3—3-element airfoil—DLR-F15</b>  <math>Ma = 0.15</math>  <math>\alpha = 7.05^\circ</math>  <math>Re = 2.094 \times 10^6</math></p>	 <p><b>I.4—2d hump</b>  <math>Ma = 0.1</math>  <math>Re = 9.36 \times 10^5</math></p>	 <p><b>I.5—Round jet aeroacoustics</b>  Proposed by:  <b>Rolls-Royce</b>  <math>Ma = 0.9</math>  <math>Re = 10^6</math></p>
<p><b>Justification for TC:</b> Complex—confluent shear/boundary layers; shallow separation from smooth surface; complex “elliptic” interaction of different flow regions</p>	<p><b>Justification for TC:</b> Complex—shallow separation, reattachment, recovery of attached boundary layer; mitigation of GA in separated shear layer necessary to predict the main flow features</p>	<p><b>Justification for TC:</b> Industrial—initial jet shear layer strongly affected by grey area (delayed formation of resolved vortices); very important source of aircraft noise</p>

**Table 2** Partner-per-test-case matrix

Test Case	Partner	CFDB	NTS	DLR	FOI	NLR	ONERA	UMAN
F.1 - Flat Plate Boundary Layer			Partner	Partner			COORD	Partner
F.2 - Spatial Shear Layer	Partner		Partner		COORD	Partner	Partner	
I.1 - Helicopter	Partner							COORD
I.2 - Vortex Flow Exp. VFE2	Partner					COORD		
I.3 - 3-Element Airfoil			Partner	COORD	Partner	Partner	Partner	Partner
I.4 - 2d Hump			COORD	Partner	Partner			
I.5 - Round Jet		COORD	Partner			Partner		Partner

#### 4 Partners, Observers, Associate Partners

The following table presents partners, observers and associate partners involved in the Go4Hybrid project. In the first column, P stands for project partners, O, for observers, and A for associate partners.

	Organisation (abbreviation)	Point(s) of contact	Address
P	CFDB	Charles Mockett Marian Fuchs Frank Thiele charles.mockett@cfdb-berlin.com	CFD Software E + F GmbH Bismarckstr. 10–12 10625 Berlin Germany
P	NTS	Michael Strelets Michael Shur strelets@mail.rcm.ru	28 Grazhdanski Avenue 195220 Saint-Petersburg Russia
P	DLR	Dieter Schwamborn Axel Probst dieter.schwamborn@dlr.de	Bunsenstrasse 10 37073 Göttingen Germany
P	FOI	Shia-Hui Peng Stefan Wallin shia-hui.peng@foi.se	Gullfösgatan 6 16490 Stockholm Sweden
P	NLR	Johan Kok johan.kok@nlr.nl	P.O. Box 90502 1006 BM Amsterdam The Netherlands
P	ONERA	Sebastien. Deck sebastien.deck@onera.fr	8 rue des Vertugadins 92190 Meudon

(continued)

(continued)

	Organisation (abbreviation)	Point(s) of contact	Address
			France
P	UniMAN	Alistair Revell Alex Skillen alistair.revell@manchester.ac.uk	C40 George Begg School of MACE The University of Manchester Manchester, M13 9PL United Kingdom
		Neil Ashton neil.ashton@oerc.ox.ac.uk	Oxford e-research centre University of Oxford 7 Keble road Oxford, Ox13qg England United Kingdom
O	Bombardier Transportation	Peter Gözl, Fabian Brännström peter.goelz@de.transport. bombardier.com	Am Rathenaupark 16761 Hennigsdorf Germany
O	GE Global Research	Vittorio Michelassi Dominic von Terzi vonterzi@ge.com	Freisinger Landstrasse 50 D-85748 Garching b. München Germany
O	NUMECA	Charles Hirsch charles.hirsch@numeca.be	Chaussée de la Hulpe, 189 1170 Brussels Belgium
O	EDF	Sofiane Behamadouche sofiane.benhamadouche@edf.fr	06 quai Watier 78401 Chatou France
O	PSA Peugeot-Citroen	Gaëlle Servera gaelle.servera@mpsa.com	PSA Peugeot Citroën Centre Technique de Vélizy A Case courrier VVA1405 2 Route de Gisy 78943 Vélizy-Villacoublay Cedex France
O	Rolls-Royce Deutschland	Mathias.Steger mathias.steger@rolls-royce.com	15827 Blankenfelde-Mahlow Germany
O	Saab Aeronautics	Sebastian Arvidson sebastian. arvidson@saabgroup.com	Bröderna Ugglas gata 58188 Linköping Sweden
O	ANSYS	Florian Menter florian.menter@ansys.com	Staudenfeldweg 20 83624 Otterfing Germany
O	Volkswagen AG	Octavian Frederich octavian. frederich@volkswagen.de	Letterbox 011/1697 38440 Wolfsburg Germany

(continued)

(continued)

	Organisation (abbreviation)	Point(s) of contact	Address
O	EXA	Ehab Fares ehab@exa.com	EXA GmbH Curiestr. 4 70563 Stuttgart Germany
		Benjamin Duda bduda@exa.com	Exa GmbH Landshuter Allee 8 80637 München Germany
A	Airbus Defence and Space	Mauro Molino mauro.molino@airbus.com	Rechliner Straße 85077 Manching Germany
A	Airbus Helicopters Deutschland	Łukasz Paluzsek lukasz.paluzsek@airbus.com	Industriestrasse 4 86607 Donauwoerth Germany



**Part II**  
**Presentation of Approaches**

# Non-zonal Approaches for Grey Area Mitigation

**C. Mockett, M. Fuchs, F. Thiele, S. Wallin, S.H. Peng, S. Deck, J.C. Kok, H. van der Ven, A. Garbaruk, M. Shur, M. Strelets and A. Travin**

## 1 Introduction

The term non-zonal approach is applied in Go4Hybrid to refer to hybrid RANS-LES methods in which the model, not the user, defines the regions in which RANS and LES modes are active. Such methods are inherently more applicable to complex geometries than embedded approaches, however they are more susceptible to the grey area problem.

---

C. Mockett (✉) · M. Fuchs · F. Thiele  
CFD Software Entwicklungs- und Forschungsgesellschaft mbH (CFDB),  
Bismarckstr. 10-12, 10625 Berlin, Germany  
e-mail: charles.mockett@cfdb-berlin.com

S. Wallin · S.H. Peng  
Unit of Aeronautical and Autonomous Systems, Swedish Defence  
Research Agency, FOI, 16490 Stockholm, Sweden

S. Deck  
ONERA, The French Aerospace Lab, 92190 Meudon, France  
e-mail: sebastien.deck@onera.fr

J.C. Kok · H. van der Ven  
Netherlands Aerospace Centre NLR, Anthony Fokkerweg 2,  
1059 Amsterdam, CM, Netherlands

A. Garbaruk · M. Shur · M. Strelets · A. Travin  
New Technologies and Services (NTS), 5A, Krasnogo Kursanta Street,  
197198 St.-Petersburg, Russia

A. Garbaruk · M. Shur · M. Strelets · A. Travin  
St.-Petersburg Polytechnic University, 29, Polytechnicheskaya Street,  
195258 St.-Petersburg, Russia

This chapter describes the various approaches for grey area mitigation proposed by the relevant partners for non-zonal hybrid approaches. As far as possible, detailed descriptions are provided to encourage the implementation of the approaches in different codes.

All methods have in common the aim to destabilise the early separated shear layer. Some methods apply stochastic forcing to this end, whereas others seek to reduce the damping influence of eddy viscosity here. An important secondary goal has been to develop approaches that are as far as possible generally applicable and suitable for the simulation of complex geometries.

The grey area mitigation (GAM) strategies are as far as possible decoupled from the underlying hybrid RANS-LES method. Ideally, this would mean that the GAM enhancements can be applied as a retro-fit to any existing non-zonal hybrid RANS-LES approach, however various complications may limit the extent to which this is achievable in practice.

Each of the following subsections describes the methods proposed by each Go4Hybrid partner active in the relevant Task 2.1. Where applicable, references to existing publications of the methods are also listed.

## 2 Application of Alternative SGS Forms for Grey Area Mitigation

### 2.1 *Rationale*

A novel approach (Mockett et al. 2015) is formulated to improve the behaviour of DES in the region where an attached boundary layer (handled with RANS) flows into a separated shear layer (to be resolved using LES). The approach aims to be generally-applicable and retain the non-zonal nature of DES. Furthermore, the formulation is local and can be readily implemented in general-purpose solvers. The approach incorporates alternative SGS model formulations that discern between quasi 2D and developed 3D flow states. The modification leads to a strong reduction of eddy viscosity in the early shear layer and consequently a significant acceleration of RANS to LES transition (RLT).

Additionally, this approach can be combined with the  $\tilde{\Delta}_\omega$  vorticity-adaptive grid scale proposal of NTS, see Sect. 6 (Alternative, Shear Layer Adapted, Subgrid Length-Scale for Non-Zonal Hybrid RANS-LES Methods), and comprehensive testing (Fuchs et al. 2014, 2015) of both formulations in isolation and in combination has been carried out by CFDB, as is reported in later chapters.

## 2.2 Formulation

For convenience we adopt a generalised notation for the LES models considered. For DES models in LES mode, the following form can be derived under the assumption of local equilibrium (i.e. equality of the dissipation and generation terms of the underlying transport equations):

$$v_{sgs} = (C_{sgs}\Delta)^2 \mathcal{D}_{sgs}(u) \quad (1)$$

where different choices of  $C_{sgs}$  (the calibrated model parameter),  $\Delta$  (the grid scale measure) and  $\mathcal{D}_{sgs}(u)$  (a differential operator acting on the resolved velocity field) give different SGS model formulations (see e.g. Table 1).

DES is a modification to an existing RANS model whereby the model's length scale,  $L_{RANS}$  is substituted by a DES length scale. The ‘‘delayed DES’’ (DDES) formulation (Spalart et al. 2006) used here includes a shield function that detects attached turbulent boundary layers and aims to ensure RANS mode there, irrespective of the grid resolution. The DDES length scale is

$$L_{DDES} = L_{RANS} - f_d \max(0, L_{RANS} - L_{LES}), \text{ with } L_{LES} = \Psi C_{DES} \Delta. \quad (2)$$

$C_{DES}$  is a model parameter analogous to the Smagorinsky constant and  $\Psi$  is a term designed to compensate for unwanted activity of low-Re terms in LES mode (Spalart et al. 2006). Both these terms as well as the RANS length scale depend on the underlying RANS model. For the Spalart–Allmaras (SA) model (Spalart and Allmaras 1994),  $L_{RANS}$  is given by the wall-normal distance  $d_w$ ,  $C_{DES} \approx 0.65$  has been calibrated for decaying isotropic turbulence and the low-Re correction term is given by

$$\Psi^2 = \min \left\{ 10^2, \frac{1 - \frac{C_{b1}}{C_w \kappa^2 f_w^*} [f_{t2} + (1 - f_{t2}) f_{v2}]}{f_{v1} \max(10^{-10}, 1 - f_{t2})} \right\},$$

with  $\kappa = 0.41$ ,  $f_w^* = 0.4241$  and other parameters as defined by the SA model.

**Table 1** Summary of model formulations in LES mode

Model	$C_{sgs}$	$\mathcal{D}_{sgs}(u)$
Smagorinsky	$C_S$	$\sqrt{2S_{ij}S_{ij}}$
WALE	$C_W$	$S_W^*$
$\sigma$	$C_\sigma$	$S_\sigma^*$
DES	$\sqrt{A} C_{DES} \Psi$	$S_{RANS}^*$
WALE-DES	$\sqrt{A} C_{DES} \Psi$	$B_W S_W^*$
$\sigma$ -DES	$\sqrt{A} C_{DES} \Psi$	$B_\sigma S_\sigma^*$

For definitions of  $S_W^*$  and  $S_\sigma^*$  see Eqs. (4) and (6), respectively. Coefficient  $A$  depends on the underlying RANS model and may or may not be constant

The DDES shield function  $f_d$  is formulated as

$$f_d = 1 - \tanh \left[ (C_{d1} r_d)^{C_{d2}} \right],$$

$$r_d = \frac{v_t + \nu}{\kappa^2 d_w^2 \max \left( \sqrt{\frac{\partial U_i}{\partial x_j} \frac{\partial U_i}{\partial x_j}}, 10^{-10} \right)}, \quad (3)$$

which is close to 0 inside the boundary layer and blends rapidly to 1 near the boundary layer edge. Furthermore, in free shear flows  $f_d = 1$  leading to  $L_{DDES} = L_{LES}$ . For standard SA-DDES, the values  $C_{d1} = 8$  and  $C_{d2} = 3$  were proposed Nicoud et al. (2011).

As mentioned, DES can be mapped to a Smagorinsky model form in LES mode, for which several well-established shortcomings are known. Of greatest relevance here is the Smagorinsky model's inability to correctly handle laminar-to-turbulent transition, where its sensitivity to mean flow shear gives rise to high levels of eddy viscosity that attenuate the (resolved) transition process. Turning to DES, the same mechanism contributes to the RLT problem, hampering the development of resolved turbulence arising from the natural shear layer instability.

Several models without this shortcoming have been formulated by the LES research community, however many of these (e.g. dynamic and high-pass filtered models) involve non-local terms that are impractical for industrial CFD solvers.

The WALE (Nicoud et al. 1999) and  $\sigma$  (Nicoud et al. 2011) models—proposed by Nicoud and co-workers—however seem particularly promising for further consideration. In these approaches local velocity gradient information is processed to distinguish between essentially two-dimensional situations such as plane shear, for which very low eddy viscosity is generated, and three-dimensional turbulence, where regular SGS model activity is recovered. This should offer a highly effective measure for accelerating RANS to LES transition whilst maintaining a practical and robust local formulation. Note that our goal in adopting the WALE and  $\sigma$  approaches in the LES mode of DES is exclusively targeted at such RLT improvement—the use of these models in a DES framework renders issues regarding their near-wall behaviour irrelevant, since the RANS branch of DES is active there.

The key changes relative to the Smagorinsky model involve the differential operator acting on the velocity field ( $\mathcal{D}_{sgs}(u)$  in Eq. (1)). For the WALE model, this term is defined as

$$\mathcal{D}_{sgs}(u) = S_w^* = \frac{\left( \mathcal{S}_{ij}^d \mathcal{S}_{ij}^d \right)^{3/2}}{\left( S_{ij} S_{ij} \right)^{5/2} + \left( \mathcal{S}_{ij}^d \mathcal{S}_{ij}^d \right)^{5/4}}, \quad (4)$$

where  $S_{ij} = 1/2(\partial U_i/\partial x_j + \partial U_j/\partial x_i)$  and  $\mathcal{S}_{ij}^d$  is the traceless symmetric part of the square of the velocity gradient tensor

$$\begin{aligned}
S_{ij}^d &= \frac{1}{2} \left( g_{ij}^2 + g_{ji}^2 \right) - \frac{1}{3} g_{kk}^2 \delta_{ij}, \\
g_{ij}^2 &= g_{ik} g_{kj}, \\
g_{ij} &= \frac{\partial U_i}{\partial x_j}.
\end{aligned} \tag{5}$$

For the  $\sigma$  model, the corresponding definition is

$$\mathcal{D}_{sgs}(u) = S_{\sigma}^* = \frac{\sigma_3(\sigma_1 - \sigma_2)(\sigma_2 - \sigma_3)}{\sigma_1^2}, \tag{6}$$

where  $\sigma_1 \geq \sigma_2 \geq \sigma_3 \geq 0$  are the three singular values of the velocity gradient tensor  $\mathbf{g} = g_{ij}$ . We chose the second method proposed by Nicoud et al. (2011) to compute these, since it is self-contained and involves negligible computational overhead.

Although derived with very different considerations, both the WALE and  $\sigma$  models return very low values of SGS viscosity in plane shear flows and involve negligible computational overhead. The analysis in Nicoud et al. (2011) however indicates that the  $\sigma$  model possesses greater generality. Both approaches were tested for a range of complex flows, from which a preference for the  $\sigma$  emerged; although returning similar results for flows approximating planar shear, the  $\sigma$  formulation performed far superior to WALE for the more complex delta wing flow topology (Fuchs et al. 2015), see in see in Part IV: Chapter “Delta Wing at High Angle of Attack”.

To modify DES to behave like the WALE and  $\sigma$  models in LES mode, we leave the length scale substitution unmodified (Eq. 2) and introduce an additional function to substitute the corresponding term for  $\mathcal{D}_{sgs}(u)$  in the LES mode region only. The velocity gradient invariant in the underlying RANS model,  $S_{RANS}^*$ <sup>1</sup> is substituted by

$$S_{(W,\sigma)-DDES}^* = S_{RANS}^* - f_d \text{pos}(L_{RANS} - L_{LES}) \left( S_{RANS}^* - B_{W,\sigma} S_{W,\sigma}^* \right), \tag{7}$$

where the operator used to detect DES97 RANS and LES mode acts as

$$\text{pos}(a) = \begin{cases} 0 & \text{if } a \leq 0 \\ 1 & \text{if } a > 0 \end{cases}.$$

Where the DDES shield function  $f_d$  is active, the values are blended smoothly according to the value of  $f_d$ . As such, the blending occurs at the same location as the length scale blending of DDES. Note that if the grid is sufficiently coarse that the interface between RANS and LES would occur outside the boundary layer (according to DES97), Eq. (7) gives a discontinuous switch between  $S_{RANS}^*$  on the RANS side and  $B_{W,\sigma} S_{W,\sigma}^*$  on the LES side of the interface. On the other hand, if we

---

<sup>1</sup>For the SA model,  $S_{RANS}^* = \sqrt{2\Omega_{ij}\Omega_{ij}}$  is substituted (not  $\tilde{S}$ ).

would not apply the discontinuous pos-function in Eq. (7), the LES mode of the  $S_{(W,\sigma)-DDES}^*$  term would be activated as soon as  $f_d$  deviates from zero, which would not be desirable considering the coarseness of the grid.

It was found that the  $f_d$  function needed recalibrating for the WALE and  $\sigma$  DDES variants, since the rapid drop in  $S_{(W,\sigma)-DDES}^*$  near the boundary layer edge caused thinning of the shielded region. For SA-based WALE-DDES and  $\sigma$ -DDES, setting the value of  $C_{d1} = 10$  in Eq. (3) was found to restore equivalent blending to standard SA-DDES. Corresponding results are shown in the following section.

For the SA model, the coefficient  $A$  is defined as

$$A_{SA} = \frac{C_{b1} f_{v1} \tilde{S}}{C_{w1} f_w S^*}. \quad (8)$$

The resulting form of the model in LES mode is given in Table 1 with reference to Eq. (1). The factor  $B_{W,\sigma}$  is included in  $\mathcal{D}_{sgs}(u)$  such that  $C_{sgs}$  is equivalent between DES variants, since  $C_{DES}$  contributes to the RANS-LES interface determination and the pure LES models have widely different values of  $C_{sgs}$ . In principle the value of this parameter can be derived as  $B_{W,\sigma} = C_{W,\sigma}^2 / C_S^2$ , which is checked for isotropic turbulence as shown in the next section. For a given underlying RANS model and numerical method, a single value of  $C_{DES}$  is hence maintained for all variants. The expression for  $\Psi$  is unaltered by the WALE/ $\sigma$  modification.

### 2.3 Calibration for Isotropic Turbulence

Whilst improving RLT behaviour, the proposed modifications give unchanged functionality in “fully-developed” LES turbulence. This is demonstrated using decaying isotropic turbulence, for which model and code-specific values of  $C_{sgs}$  and the coefficients  $B_W$  and  $B_\sigma$  have been calibrated. The arising calibrated values are listed in Table 2 and strong similarity for the turbulent spectra is seen in Fig. 1. The calibrated values are quoted only as a guideline, since recalibration for a different numerical implementation is considered essential.

### 2.4 Shield Function Recalibration

As mentioned previously, the boundary layer shielding function  $f_d$  needed to be recalibrated for use in conjunction with the WALE-DDES and  $\sigma$ -DDES variants. A flat plate boundary layer on an “ambiguous” grid (Spalart et al. 2006), i.e. one where  $\Delta < \delta$  is used for this purpose. Note that this exercise has so far only been

**Table 2** Values of model parameters calibrated for isotropic turbulence

Parameter	Calibrated value
$C_S$	0.20
$C_W$	0.58
$C_\sigma$	1.68
$C_{DES}$ (for SA-DES)	0.65
$B_W$	8.08
$B_\sigma$	67.8

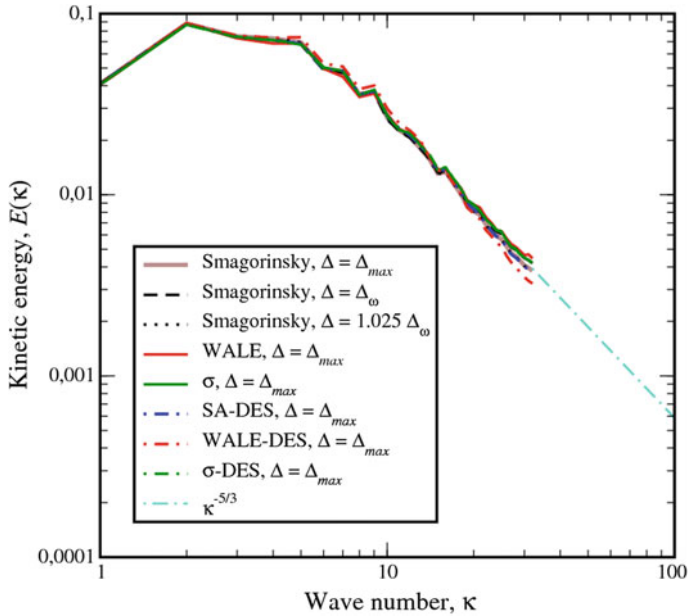


**Fig. 1** Comparison of spectra for decaying isotropic turbulence obtained on a  $64^3$  grid from all model variants using the constant values listed in Table 1. Also shown are spectra obtained using the  $\tilde{\Delta}_\omega$  grid scale definition proposed by NTS (see Sect. 5)

carried out for SA-based DDES variants and that different values could be expected to be suitable for different underlying RANS models (Gritskevich et al. 2011).

Recalibrating the shield function (Eq. 3) coefficient to  $C_{d1} = 10$  whilst leaving the exponent unchanged at  $C_{d2} = 3$  restores functionality equivalent to standard SA-DDES. Example plots for SA-WALE-DDES are shown in Fig. 2 (identical behaviour was seen for SA- $\sigma$ -DDES).



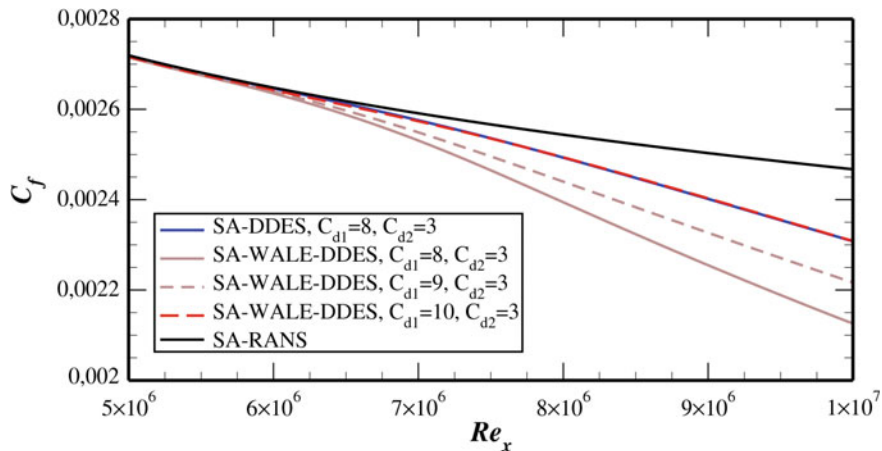


Fig. 2 Recalibration of boundary layer shielding function of SA-WALE-DDES for a flat plate on an “ambiguous” grid

### 3 Towards Grey-Area Mitigation Based on Different Energy Transfer Methods

#### 3.1 Scale Energy Transfer in PANS Methods

In a computational model of turbulent flow with partly resolved turbulence the primary task for the turbulence model is to dissipate the cascaded energy at the smallest resolved scales. For an energy-consistent method where we are solving for the unresolved turbulence kinetic energy,  $K_u$  (or  $K_{SGS}$ ), the dissipated energy at the resolved scales is added as a production term to the unresolved energy. The magnitude of the energy dissipation is closely related to the physical equilibrium spectral energy cascade.

In a computational model of turbulent flow with varying resolution in time and space, the additional energy transfer associated with the changing resolution must be considered, which will add new dynamics into the equations for momentum and unresolved turbulence. The additional energy transfer between resolved and unresolved scales is decoupled from the physical energy cascade and is an artefact of the computational setup.

Girimaji and Wallin (2011, 2013) derived these additional energy transfer terms in the case of varying computational resolution in the stream-wise direction. The same approach can be taken also for resolution variation in the cross-stream direction (Wallin and Girimaji 2014), which is of relevance in e.g. partly resolved boundary layer flows.

The PANS equations for the unresolved turbulence  $K_u = f_k K$  when  $f_k$  is varying can be written

$$\frac{DK_u}{Dt} = P_u - \varepsilon_u + \frac{\partial}{\partial x_k} \left( v' \frac{\partial K_u}{\partial x_k} \right) + P_{Tr} + D_{Tr} \quad (9)$$

where

$$P_{Tr} = \frac{K_u Df_k}{f_k Dt} \quad (10)$$

$$D_{Tr} = -\frac{K_u}{f_k} \frac{\partial}{\partial x_k} \left( \left( v + \frac{v_u}{\sigma_k} \right) \frac{\partial f_k}{\partial x_k} \right) \quad (11)$$

are the energy scale transfer terms mainly in the stream-wise and cross-stream directions, respectively. These are directly quantified in these relations without any ad hoc modelling.

The first term,  $P_{Tr}$ , represents the transfer of turbulence energy from resolved to unresolved scales when the resolution is decreased when following the flow. That is when  $Df_k/Dt$  is positive. The opposite, increasing resolution, results in a negative  $P_{Tr}$  and a transfer of energy from unresolved to resolved scales.

The second term,  $D_{Tr}$ , represents the redistribution of turbulence energy mainly in the cross stream direction. This term will result in a flux of unresolved turbulence from regions with low  $f_k$  to regions with high  $f_k$ . Computations of partly resolved boundary layers would require that  $f_k$  decreases from 1 near the wall to some low value in the outer part of the boundary layer. The additional  $D_{Tr}$  term will then result in a sharpening of the interface region forcing unresolved turbulence in the inner part of the transition region. And, more importantly, forcing the resolved turbulence in the outer part of the transition region.

Corresponding terms in the momentum equation need to be introduced. The basic requirements on such a model are (i) the model should conserve the additional energy scale transfer and (ii) the model should interact with the mean flow at the smallest resolved scales. Different approaches can be taken including stochastic forcing and test filtering. In Wallin and Girimaji (2011) and Girimaji and Wallin (2013) the simplest possible approach was taken by introducing an energy transfer viscosity  $\nu_{Tr}$ . Energy conservation will dictate

$$\nu_{Tr} = \frac{P_{Tr} + D_{Tr}}{2S_{ij}S_{ij}}, \quad S_{ij} = \frac{1}{2} \left( \frac{\partial U_i}{\partial x_j} + \frac{\partial U_j}{\partial x_i} \right) \quad (12)$$

Also energy transfer to the resolved scales can be realized through a negative  $\nu_{Tr}$ . Usually negative viscosity is associated with unbounded exponential growth of resolved energy, but with the aid of energy conservation the growth is limited by the unresolved turbulence  $K_u$ . This was demonstrated in Girimaji and Wallin (2013).

### 3.2 Some Results

Decaying isotropic turbulence was computed (Girimaji and Wallin 2013) with changing resolution in time, see Fig. 3. The resolution is controlled by the PANS parameter  $f_k$  on a fixed fine grid. The energy scale transfer described above is used. The case with decreasing resolution where  $f_k$  is going from 0.3 to 0.7 is well predicted and the energy is consistently transferred from resolved to unresolved scales. Also the more difficult case with increasing resolution is at least qualitatively captured.

Channel flow at  $Re_\tau = 4000$  was computed. Here, the cross-stream transfer term  $D_{Tr}$  is active. The mean velocity is not well predicted and not shown here. Figure 4 shows the shear stress split into resolved, unresolved and scale transfer. The transfer term strongly transfers energy to the unresolved scales in the outer part of the interface region. Interesting to note that the iso-surface of zero total viscosity ( $= \nu + \nu_u + \nu_{Tr}$ ) clearly shows turbulence-like streaks with relatively small length scales without any explicit structural forcing.

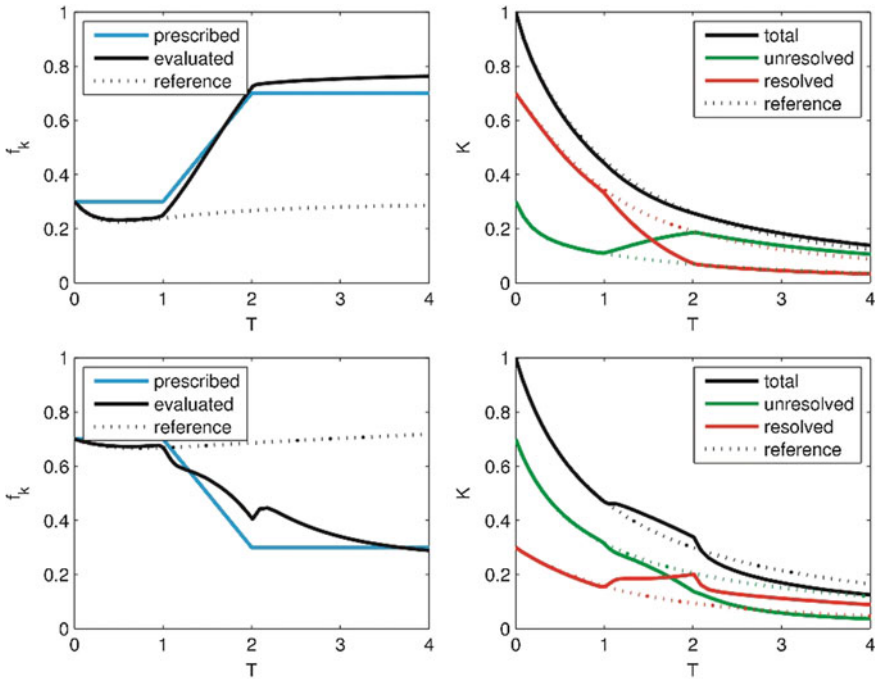


**Fig. 3** Decaying isotropic turbulence with decreasing (*top*) and increasing (*bottom*) resolution with energy scale transfer active

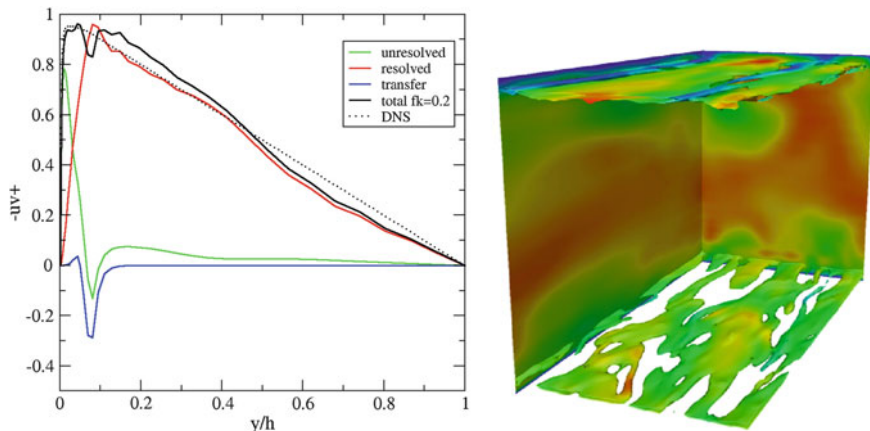


**Fig. 4** Channel flow,  $Re = 4000$ , with energy scale transfer active. Shear stress (*left*) and iso-surface of zero total viscosity (*right*)

### Scale Energy Transfer in Terms of $\nu_t$

Consider the energy spectrum in Fig. 5. In the inertial range the spectrum is given by

$$E(\kappa) = C^* \varepsilon^{2/3} \kappa^{-5/3} \quad (13)$$

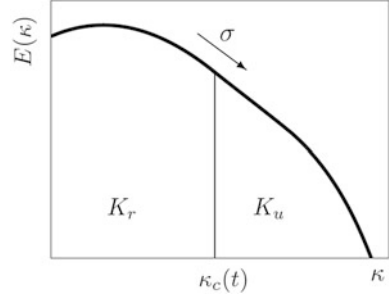
with the Kolmogorov constant  $C^* \approx 1.5$ . The physical energy transfer rate,  $\sigma$ , from resolved to unresolved energy, or the energy cascade, is constant within the inertial range and equals the dissipation rate  $\varepsilon$  for equilibrium turbulence. In a turbulence resolved simulation the cut-off between resolved and unresolved (sub grid) scales is given by the cut-off wave number  $\kappa_c$ . The energy transfer, from resolved to unresolved scales is given by  $\sigma$  and is represented by the SGS dissipation through the SGS viscosity,  $\nu_{SGS}$ .

For simulations with variable resolution,  $\kappa_c(t)$ , additional energy must be transferred between resolved and unresolved scales. Let us denote this additional transfer as  $\sigma_{Tr}$ . In equilibrium flows (constant spectrum) this is identical to  $\mathcal{P}_{Tr}$  in the PANS formulation. Now, the additional transfer can be related to the model spectrum

$$\sigma_{Tr} = -E(\kappa_c) \frac{d\kappa_c}{dt} = -C^* \left( \frac{\varepsilon}{\kappa_c} \right)^{2/3} \frac{1}{\kappa_c} \frac{d\kappa_c}{dt}. \quad (14)$$

With the filter  $\Delta = \pi/\kappa_c$  one gets

**Fig. 5** Energy spectrum divided into resolved and unresolved parts ( $K_r$  and  $K_u$ ) by the cut-off wave number  $\kappa_c$



$$\sigma_{Tr} = \frac{C^*}{\pi^{2/3}} (\varepsilon \Delta)^{2/3} \frac{1}{\Delta} \frac{d\Delta}{dt} \quad (15)$$

Here,  $\varepsilon$  can be estimated from the SGS dissipation,  $\varepsilon \approx (v_{SGS})S^2$ ,  $S^2 = 2S_{ij}S_{ji}$ ,  $S_{ij} = (U_{i,j} + U_{j,i})/2$ .

The total energy transfer rate from resolved to unresolved scales for variable resolution (VR) simulations is then given by the sum  $\sigma_{VR} = \sigma + \sigma_{Tr}$ . Or  $\sigma_{VR} = f_{VR}\sigma$ , where (with  $\sigma = \varepsilon$ )

$$f_{VR} = 1 + \frac{\sigma_{Tr}}{\sigma} = 1 + \frac{C^*}{\pi^{2/3}} \frac{\Delta^{2/3}}{\varepsilon^{1/3}} \frac{1}{\Delta} \frac{d\Delta}{dt} \quad (16)$$

Decreasing filter width ( $d\Delta/dt < 0$ ) implies reduced SGS dissipation and with  $f_{VR} < 0$  there is a net negative dissipation. Here, one must be clear that this is only a computational consequence that is not related to physical back scatter.

With an eddy-viscosity model for the SGS stresses the SGS dissipation is given by  $\varepsilon \approx v_{SGS}S^2$ . The variable resolution is considered simply by replacing SGS viscosity by  $v_{VR} = f_{VR}v_{SGS}$ .

In the expression for  $f_{VR}$ , the derivative is evaluated as the advection by the resolved flow

$$\frac{1}{\Delta} \frac{d\Delta}{dt} = \frac{d\ln(\Delta)}{dt} = \left( \frac{\partial \ln(\Delta)}{\partial t} + U_k \frac{\partial \ln(\Delta)}{\partial x_k} \right). \quad (17)$$

The estimate of the SGS dissipation, or  $\varepsilon$ , might be cumbersome with insufficient resolution and numerical dissipation. At least the molecular viscosity should be added to  $v_{SGS}$  so that  $\varepsilon \approx (v + v_{SGS})S^2$  but better approximations might be needed. The term  $\Delta^{2/3}/\varepsilon^{1/3}$  is the time scale of the unresolved turbulence and can be expanded to (using  $v_{SGS} = (C_s \Delta)^2 S$ , with  $C_s = 0.12$ )

$$\frac{\Delta^{2/3}}{\varepsilon^{1/3}} \approx \left( \frac{\Delta^2}{(v + v_{SGS})S^2} \right)^{\frac{1}{3}} = \left( \frac{\Delta^2}{(v + C_s^2 \Delta^2 S)S^2} \right)^{\frac{1}{3}} \approx \frac{1}{C_s^{2/3} S} \quad (18)$$

For avoiding division by zero when  $S \rightarrow 0$  we will limit  $S$  by some fraction of a viscous time scale,  $\max(S, c_1 \nu / \Delta)$ .

The final expression for the variable-resolution correction then becomes

$$f_{VR}(\Delta) = 1 + \frac{C_{VR}}{\max(S, c_1 \nu / \Delta)} \left( \frac{\partial \ln(\Delta)}{\partial t} + U_k \frac{\partial \ln(\Delta)}{\partial x_k} \right) \quad (19)$$

where

$$C_{VR} = \frac{C^*}{\pi^{2/3} C_s^{2/3}} \approx 2.9 \quad (20)$$

Negative  $f_{VR}$  would lead to negative  $\nu_{SGS}$ . With  $\nu_{VR} < -\nu$  the total viscosity becomes negative and the computation might become numerically unstable. Such situation can only be permitted when the computational back scatter is connected with a transport equation for the SGS energy. If not,  $f_{VR}$  should be limited to 0, or possible slightly negative values. Also a similar upper limit should apply, maybe  $f_{VR} < 2$ .

Limiting  $f_{VR}$  will effectively pile up the rate of change of the filter width. Hence, the limiting of  $f_{VR}$  must be accomplished with diminishing rate of change of the filter width. Since the flow is transported by the velocity field, the filter width must be governed by a transport equation. The equation is derived from the following assumptions.

First, let  $g_0 = \ln(\Delta_0)$ , where  $\Delta_0$  is the filter width from the present hybrid method. Then, let  $g = \ln(\Delta)$  be the modified filter with the implicit requirement that  $|f_{VR}(\Delta) - 1| < 1$ . Following a stream line

$$f_{VR}(t) = 1 + C \frac{dg(t)}{dt} \quad (21)$$

where  $C = C_{VR} / \max(S, c_1 \nu / \Delta^2)$ . Moreover, an equation for  $g(t)$  could be

$$\frac{dg(t)}{dt} = c' (g_0(t) - g(t)) \quad (22)$$

Hence,  $g(t)$  is driven towards  $g_0(t)$ . The limitation of  $f_{VR}(\Delta)$  (or  $|f_{VR} - 1| < C_{FLim}$ ), where  $C_{FLim}$  might be slightly different than unity, can be implied as

$$\left| C \frac{dg}{dt} \right| = |C c' (g_0 - g)| < C_{FL} \quad (23)$$

or

$$c' = \frac{1}{C} \min\left(c'_0, \frac{C_{FL}}{|g_0 - g|}\right) \quad (24)$$

which gives

$$\begin{aligned} \frac{dg}{dt} &= \frac{1}{C} \min\left(c'_0, \frac{C_{FLim}}{|g_0 - g|}\right) (g_0 - g) \\ f_{VR} &= 1 + \min\left(c'_0, \frac{C_{FLim}}{|g_0 - g|}\right) (g_0 - g) \\ v_{VR} &= f_{VR} v_{SGS} \end{aligned} \quad (25)$$

where the energy-transfer corrected viscosity  $v_{VR}$  replaces the ordinary SGS viscosity  $v_{SGS}$ .

The behaviour of  $g = \ln(\Delta)$  following the transport equation is illustrated in Fig. 6 for a situation that mimics the mixing layer. The green curve ( $g_0$ ) corresponds to a typical hybrid length scale that falls from a RANS level for  $x < 0$  to a LES level with slightly increasing grid size in the downstream direction until  $x \approx 1$  where the grid is coarsened. The red curve is the corresponding solution of the transport equation for  $g$  that is relaxed towards the  $g_0$  value. The rate of change is clearly visible and is illustrated by  $f$  (or actually  $f - 1$  in this plot) where the magnitude of the rate of change is limited to 1. Hence, the SGS viscosity with the energy transfer correction,  $v_{Tr}$ , will be effectively close to zero for  $x \lesssim 0.3$ .

Extending to a PDE (compressible flow) gives

$$\frac{\partial \rho g}{\partial t} + U_k \frac{\partial \rho g}{\partial x_k} = \frac{\rho}{C} \min\left(c'_0, \frac{C_{FLim}}{|g_0 - g|}\right) (g_0 - g) + \frac{\partial}{\partial x_k} \left( \left( \mu + \frac{\mu_t}{\sigma_g} \right) \frac{\partial g}{\partial x_k} \right) \quad (26)$$

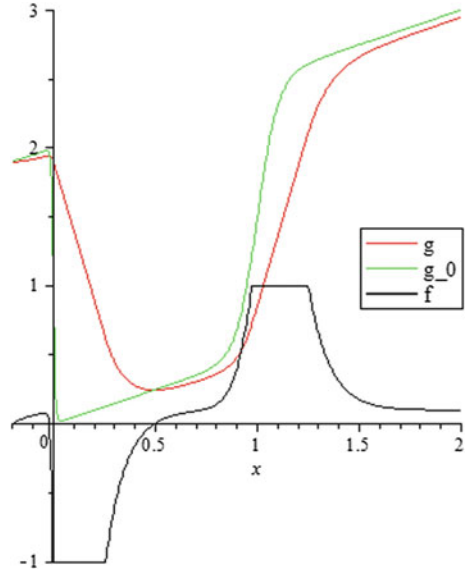
where  $C = C_{VR}/\max(S, c_1 v/\Delta_0^2)$  and the coupling to the baseline model is concluded here.

- $g_0 = \ln(\Delta_0)$  is given by the length scale of the baseline model ( $\Delta$  in the LES region and  $\Delta_{RANS} = l_{RANS}/C_s$  in the RANS region).
- The RANS viscosity is unchanged and the corrected viscosity in the LES region is given by

$$v_{VR} = f_{VR} v_{SGS}, f_{VR} = 1 + \min\left(c'_0, \frac{C_{FLim}}{|g_0 - g|}\right) (g_0 - g) \quad (27)$$

- where  $C_{VR} = 2.9$ ,  $c_1 = 10$ ,  $c'_0 = 2.0$ ,  $\sigma_g = 0.1$ ,  $C_{FLim} = 1.0$ .

**Fig. 6** Solution of  $g(x)$  for a case similar to the mixing layer with fixed  $U_C = 0.2$ ,  $c'_0 = 2$  and  $c_1 = 10$



### 3.3 Peng HYB0 with Energy Transfer Correction

The next step is to implement the  $f_{VR}$  corrected SGS viscosity for a hybrid model and we choose Peng HYB0 model to start with. Peng HYB0 model is given here in a slightly different form. The RANS length scale is  $\tilde{l}_\mu = f_\mu \kappa d$ , where  $\kappa = 0.418$  and  $d$  is the wall distance. The wall damping function is  $f_\mu = \tanh(R_t^{1/3}/2.5)$  where  $R_t = \tilde{\mu}/\mu$ ,  $\tilde{\mu} = \rho \tilde{l}_\mu^2 S$ ,  $S^2 = 2S_{ij}S_{ji}$  and  $S_{ij} = (U_{i,j} + U_{j,i})/2$ .  $f_\mu = 1$  away from walls.

The LES length scale is  $l_{SGS} = C_s \Delta$  where  $C_s = 0.12$  and  $\Delta = \sqrt{(\Delta_{\max}^2 + \Delta_{\text{vol}}^2)}/2$ ,  $\Delta_{\max} = \max(\Delta_x, \Delta_y, \Delta_z)$  and  $\Delta_{\text{vol}} = \delta V^{1/3}$ .

The modified RANS length scale considering interface matching is  $l_\mu = f_s \tilde{l}_\mu$  where

$$f_s = \frac{1}{2} \left( e^{-\frac{R_s^{0.75}}{4.75}} + e^{-\frac{R_s^{0.3}}{2.5}} \right), R_s = (\tilde{l}_\mu / l_{SGS})^2 \quad (28)$$

The hybrid length scale now becomes

$$l_h = \begin{cases} l_\mu, \tilde{l}_\mu < \Delta \\ l_{SGS}, \tilde{l}_\mu \geq \Delta \end{cases} \quad (29)$$

and the hybrid viscosity  $\mu_h = \rho l_h^2 S$ .



The energy transfer extension is implemented as following:

1. The equation for  $g$  follows Eq. (26).
2. The driving filter width  $\Delta_0 \rightarrow g_0$  is given by  $\Delta_0 = \tilde{l}_\mu/C_s$  in RANS or  $\Delta_0 = \Delta$  in LES.
3. Inflow B.C. for  $g$  is  $g_\infty = \ln(v_{T,\infty}/\sqrt{K_\infty})$ . Wall B.C. is  $g_{wall} = -20$  (corresponds to  $\Delta \rightarrow 0$ ).
4. The SGS viscosity is modified according to Eq. (27). The RANS viscosity is kept unchanged.
5. The tentative values for the model coefficients are:
  - $\sigma_g = 0.1$  for high smoothing of  $g$
  - $C^* = 1.5$
  - $c'_0 = 2.0$
  - $C_{FLim} = 1.0$

For the first test computations  $C^* = 5.0$  was used to exaggerate the effect and  $C_{FLim} = 0.8$  for avoiding effective viscosities too close to zero.

### 3.4 DDES with Energy Transfer Correction

The idea is to apply the energy transfer correction in the same way as for the HYB0 model above. In addition to the  $v_T$  equation (or the  $K-\omega$  equations), the equation for  $g$  is applied.

The energy transfer extension is implemented as following:

1. The equation for  $g$  follows Eq. (26).
2. The driving filter width  $\Delta_0 \rightarrow g_0$  is given by  $\Delta_0 = l_{RANS}/C_s$  in RANS or  $\Delta_0 = \Delta$  in LES.
3. Inflow B.C. for  $g$  is  $g_\infty = \ln(v_{T,\infty}/\sqrt{K_\infty})$ . Wall B.C. is  $g_{wall} = -20$  (corresponds to  $\Delta \rightarrow 0$ ).
4. The SGS viscosity is modified according to Eq. (27). The RANS viscosity is kept unchanged.
5. The model coefficients are:
  - $\sigma_g = 0.1$  for high smoothing of  $g$
  - $C^* = 1.5$
  - $c'_0 = 2.0$
  - $C_{FLim} = 1.0$  or slightly lower

### 3.5 *Energy-Backscatter Function Incorporated in the LES Mode*

The so-called “grey-area” problem in hybrid RANS-LES modelling is closely associated to the RANS-LES interface, being usually reflected by a delayed re-establishment of resolved turbulence in the LES region neighboring immediately to the RANS region. To improve the prediction, one may either improve the fed-in turbulence contents from RANS to LES via the interface or enhance the turbulence-resolving capabilities of the LES mode. Apart from the PANS-based method described previously, another method to examine is further introduced, which invokes the energy-backscatter function in the SGS model formulation to enhance turbulence-resolving capability in the LES region. This means that the SGS model is of mixed type that is able to induce instantaneous reverse energy transfer from the SGS to the resolved large-scale turbulence, in conjunction with the conventional energy dissipation based on the SGS eddy-viscosity formulation. The theoretical analysis and derivation of the SGS modelling formulation was reported previously by Peng and Davidson (2001) applying the Leonard expansion (Peng and Davidson 2009) to the SGS residual stress tensor. The SGS stress tensor has been modelled in a two-term formulation (Peng 2012), namely,

$$\tau_{ij} \approx \underbrace{(C_L f_L \Delta)^2 \frac{\partial \bar{u}_i}{\partial x_k} \frac{\partial \bar{u}_j}{\partial x_k}}_{\text{Leonard Term, } L_{ij}} - \underbrace{2f_D v_{sgs} \bar{S}_{ij}}_{\text{Second Term}} \quad (30)$$

The first term is the Leonard term, which is similar to a similarity SGS model and plays a role in backscattering turbulent energy from SGS to large-scale turbulence, and the second term is the conventional part for energy dissipation based on SGS eddy viscosity. The SGS viscosity in the second term is determined in the form of the Smagorinsky model or cast in a formulation of one-equation SGS model based on the SGS turbulent kinetic energy  $k_{sgs}$ . In previous work for modelling calibration,  $v_{sgs}$  has been modelled with the Smagorinsky model.

The capability of LES with the two-term SGS model has been well demonstrated for turbulent channel flow (Peng 2012), as shown in Fig. 7 as an example in computation for turbulent channel flow at  $Re_\tau = 550$ .

Note that the Leonard term can be viewed as the leading term in the reconstruction series of the conventional similarity model with double-filtered residuals according to Peng and Davidson (2001). In Fig. 8a the modelled turbulent shear stress by the Leonard term is illustrated in comparison with that by the Smagorinsky term. In Fig. 8b, the energy-backscatter function due to the Leonard term is further analyzed. The energy transfer has been approximated with  $\varepsilon = -\tau_{ij} S_{ij}$ . It is shown that the Leonard term has induced about (15–20)% reverse energy transfer of the total. In general, the two-term SGS model (of mixed type) has shown an overall reasonable performance. The LES mode is then incorporated into hybrid RANS-LES modelling.

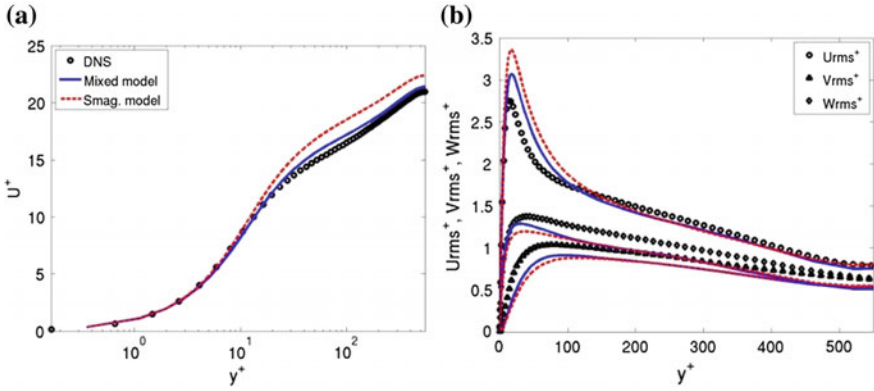


**Fig. 7** LES with the two-term algebraic SGS model for turbulent channel flow ( $Re_\tau = 550$ ), in comparison the Smagorinsky model. **a** Mean streamwise velocity; **b** Resolved velocity fluctuations

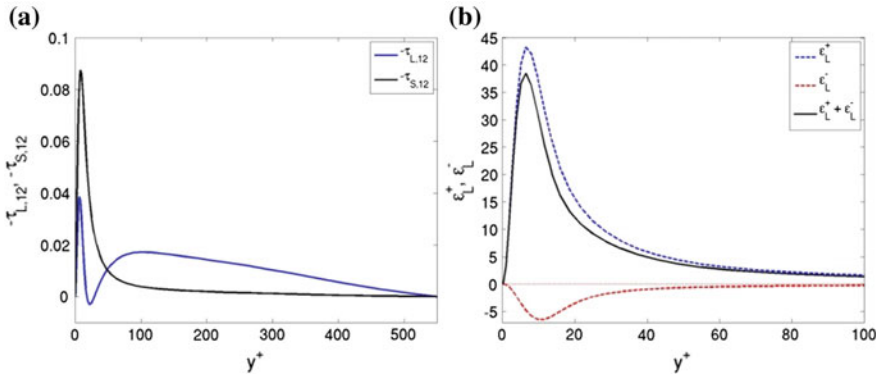


**Fig. 8** LES with the two-term algebraic SGS model for turbulent channel flow  $Re_\tau = 550$ . **a** Modelled turbulent shear stress for the Leonard term and the Smagorinsky term; **b** Modelled energy transfer due to the Leonard term

### 3.6 Algebraic Hybrid RANS-LES Formulation (HYB0M Model)

With appropriate calibration and validation, the SGS model of mixed-type given in the above equation can be used as the LES mode in hybrid RANS-LES formulation, in which the function of energy-backscatter can be exploited to enhance the LES-resolved large-scale turbulent fluctuations. In the FOI work, an algebraic hybrid RANS-LES model (HYB0) according to Peng (2005, 2006) has been taken as the baseline model, where the Smagorinsky-type model has been used for energy dissipation in the LES mode. Using the HYB0 formulation as the platform for testing, the two-term SGS model is then incorporated in the hybridized LES mode,

in which the energy-backscatter term is expected to support a more effective re-establishment of resolved turbulent fluctuations. After entering into the LES region immediately after the RANS-LES interface, this may to some extent mitigate so-called “grey area” problem. In conjunction with the Smagorinsky model, the SGS mixed model takes the form of

$$\tau_{ij} = \tau_{L,ij} + \tau_{S,ij} = (C_L \Delta)^2 f_L \frac{\partial \bar{U}_i}{\partial x_k} \frac{\partial \bar{U}_j}{\partial x_k} - 2f_D (C_S \Delta)^2 |\bar{S}| \bar{S}_{ij} \quad (31)$$

where  $f_L = \tanh(R_{sgs})$ ,  $f_D = f_w \tanh(R_{sgs}/5)$  with  $f_w = 1 - e^{y^+/10}$ ,  $R_{sgs} = v_{sgs}/\nu$ ,  $C_S = 0.12$  and  $C_L = \sqrt{1/12}$ .

For the hybrid RANS-LES modelling formulation, note that the Leonard term plays only a role in the LES mode. This term is thus shielded in the near-wall RANS region by introducing a “shielding” function,  $f_b$ , which complies with  $f_b = 0$  for the RANS mode and  $f_b = 1.0$  in the LES region. This has led to a formulation for the hybrid RANS-LES model, which reads

$$\tau_{ij} \approx -2\mu_h \bar{S}_{ij} + (C_L f_L \Delta)^2 f_b \frac{\partial \bar{u}_i}{\partial x_k} \frac{\partial \bar{u}_j}{\partial x_k} \quad (32)$$

The hybrid eddy viscosity,  $\mu_h$ , takes the same formulation as given by the baseline HYB0 model (Peng 2005, 2006). The shielding function is defined in terms of the ratio of the RANS length scale,  $\tilde{l}_\mu$ , and the SGS length scale,  $\Delta$ , namely,  $f_b = \tanh\left[(R_l/2)^8\right]$  with  $R_l = \tilde{l}_\mu/\Delta$ . The resulting model is termed the HYB0M model and the details of the modelling formulation can be found in Peng (2012).

The HYB0M model has been validated and verified in computations of 2D turbulent hill flow and for the flow over a backward-facing step (Peng 2012). As shown respectively in Fig. 9 (for 2D hill flow) and Fig. 10 (for the backward-facing step flow), the incorporation of the energy-backscatter function in the LES mode has induced some improvement in the prediction, having slightly enhanced the resolved turbulent energy. The formulation has been further verified and improved in computations of test cases defined in the project.

For better numerical treatment of the Leonard term, the energy-backscatter method has been formulated by introducing an effective eddy viscosity,  $\nu^*$ . Equation (32) is written as

$$\tau_{ij} = (C_L f_L \Delta)^2 f_b \frac{\partial \bar{u}_i}{\partial x_k} \frac{\partial \bar{u}_j}{\partial x_k} - 2\nu_h S_{ij} = L_{ij} - 2\nu_h S_{ij} \quad (33)$$

In Eq. (33), the first term on the right-hand side is the Leonard term, which may induce instantaneous energy backscatter. In the computation it was found that this term may trigger numerical instabilities when the instantaneous reverse energy transfer becomes large. This term needs thus to be limited. For an improved

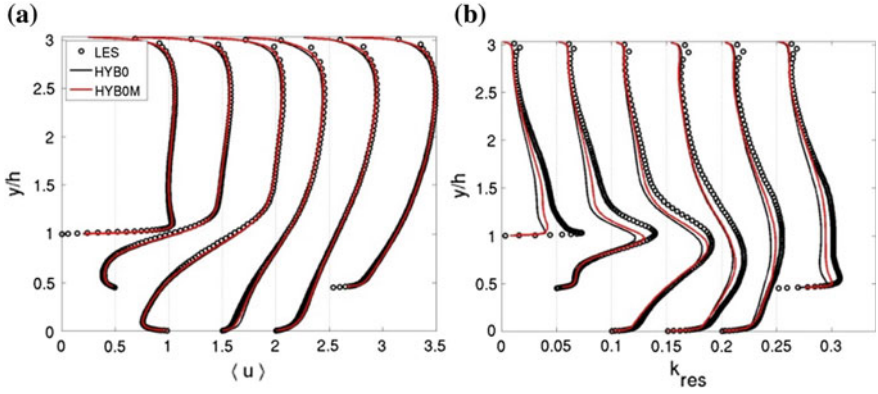


**Fig. 9** HYBO M computation for turbulent 2D periodic hill flow, in comparison the baseline HYBO model. **a** Mean streamwise velocity; **b** Resolved turbulent kinetic energy

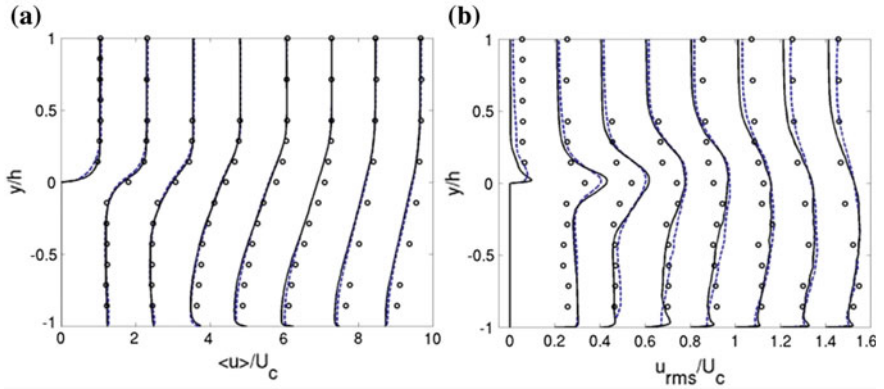


**Fig. 10** HYBO M computation (*solid line*) for turbulent backward-facing step flow in comparison the baseline HYBO model (*dashed line*). **a** Mean streamwise velocity; **b** Resolved turbulent fluctuations of streamwise velocity

numerical treatment, the Leonard term is split into two parts, viz.  $L_{ij} = L_{ij}^* + L_{ij}^d$ , where  $L_{ij}^*$  is assumed to be responsible for the energy transfer and  $L_{ij}^d$  is the deviatoric part. The first part,  $L_{ij}^*$ , is modelled using an effective eddy viscosity in terms of  $L_{ij}^* = -2\nu^*S_{ij}$ . Using  $S_{ij}$  to contract  $L_{ij}$ , and let  $L_{ij}^dS_{ij} = 0$ ,  $\nu^*$  can then be computed by

$$\nu^* = -\frac{L_{ij}S_{ij}}{2S_{ij}S_{ij}} \quad (34)$$

$L_{ij}^d$  is then computed by  $L_{ij}^d = L_{ij} - L_{ij}^*$ . With this formulation in the HYBOM computations, a negative value of  $v^*$  is limited by  $v^* \geq -(v_h + v)$  for numerical stability. This may to some extent have restricted the GAM function. In conjunction with HYB1 model, this is much alleviated, however, since the Leonard term enters also into the production term of the  $k$ -equation. Being incorporated in the HYB0 model (resulting the HYBOM model), it has been verified that a redefinition of the SGS turbulence length scale in the HYB0 model can further alleviate the grey-area problem. This is done by replacing the maximum local cell size,  $\delta_{max}$ , with the minimum one,  $\delta_{min}$ , namely, in the definition of  $\Delta$ ,

$$\Delta = \sqrt{(\delta_{min}^2 + \delta V^{2/3})/2} \quad (35)$$

where  $\delta_{min}$  has been used to replace  $\delta_{max}$  used in the original definition. With this definition of  $\Delta$ , both the HYB0 and HYBOM models have shown sensible improvement for mitigating the grey area in the initial stage of the mixing layer, for example.

## 4 Overview of Zonal Detached Eddy Simulation (ZDES) and Grid Scale Definitions for Modes I and II

### 4.1 Formulation

The Zonal DES (ZDES) approach was first proposed by Deck (2005a, b) and the complete formulation has been recently published in Deck (2012). The method is based on a fluid problem-dependent zonalisation and makes possible the use of various formulations within the same calculation.

In the framework of ZDES, three specific hybrid length scale formulations [see Eq. (36)], also called modes, are optimized to be employed on three typical flow field topologies as illustrated in Fig. 11. Though the method can be adapted to any turbulence model, in the framework of the underlying SA model (Spalart and Allmaras 1994),  $d_w$  is replaced with  $\tilde{d}_{ZDES}$  in the model according to:

$$\tilde{d}_{ZDES} = \begin{cases} d_w & \text{if } mode = 0 \text{ (i.e. RANS)} \\ \tilde{d}_{DES}^I & \text{if } mode = 1 \\ \tilde{d}_{DES}^{II} & \text{if } mode = 2 \\ \tilde{d}_{DES}^{III} & \text{if } mode = 3 \end{cases} \quad (36)$$

Mode 1 concerns flows where the separation is triggered by a relatively abrupt variation in the geometry; mode 2 is retained when the location of separation is induced by a pressure gradient on a gently curved surface, and mode 3 for flows

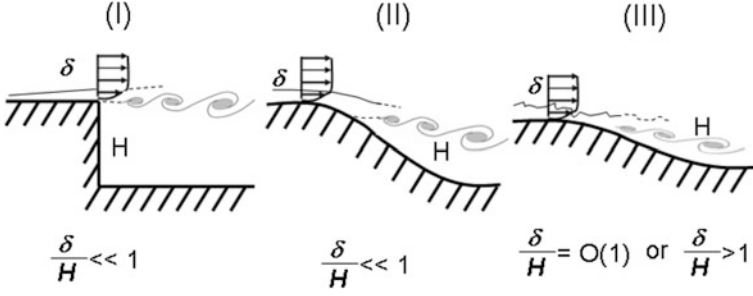


**Fig. 11** Classification of typical flow problems. *I* separation fixed by the geometry, *II* separation induced by a pressure gradient on a gently-curved surface, *III* separation strongly influenced by the dynamics of the incoming boundary layer

where the separation is strongly influenced by the dynamics of the incoming boundary layer (see Fig. 11). All these flow cases may be treated by the same ZDES technique in its different modes. An example where the three modes of ZDES are used at the same time on a curvilinear geometry can be found in Deck (2013).

In practice, the formulas of ZDES differ from those of DES97 or DDES in the definition of the ZDES length scale, the subgrid length scale and the treatment of the near wall functions in the LES mode as detailed in the following.

- Mode I of ZDES (*mode* = 1), location of separation fixed by the geometry

$$\tilde{d}_{DES}^I = \min\left(d_w, C_{DES}\tilde{\Delta}_{DES}^I\right) \quad (37)$$

- Mode II of ZDES (*mode* = 2), location of separation unknown a priori:

$$\tilde{d}_{DES}^{II} = d_w - f_d \max\left(0, d_w - C_{DES}\tilde{\Delta}_{DES}^{II}\right) \quad (38)$$

- Mode III of ZDES (*mode* = 3), Wall-Modelled LES (WMLES):

$$\tilde{d}_{DES}^{III} = \begin{cases} d_w & \text{if } d < d_w^{interface} \\ \tilde{d}_{DES}^I & \text{otherwise} \end{cases} \quad (39)$$

It is important to note that with mode 2 of ZDES, which clearly borrows ideas from DDES (Spalart et al. 2006), it is permitted to operate in an “automatic” manner since  $\tilde{d}_{DES}^{II}$  employs the same protection function as DDES to maintain the RANS behaviour in the attached boundary layer. The improvement lies in the definition of the subgrid length scale  $\tilde{\Delta}$  as will be discussed in the following.

Concerning this latter mode devoted to WMLES (described in detail in Part II (Chapter “Improved Embedded Approaches”, Sect. 4: ZDES mode 3), the switching into LES mode occurs at a given altitude  $d_w^{interface}$  prescribed by the user. In this mode (see Deck et al. 2014; Chauvet et al. 2007), the solution has to be fed with turbulent inflow content.

A second important ingredient of ZDES is the definition of the subgrid length scale  $\tilde{\Delta}$  entering Eqs. (37), (38) and (39). Indeed, analogous to the classical LES exercise  $\tilde{\Delta}$  controls which wavelengths can be resolved as well as the eddy viscosity levels. Though physically justified in the frame of DES97/DDES (Spalart et al. 2006) aimed to shield the attached boundary layer from MSD, the slow delay in the formation of instabilities in free shear layers of DDES has been partly attributed to the use of the maximum grid extension  $\Delta_{max} = \max(\Delta x, \Delta y, \Delta z)$  as subgrid length scale. The use of the time-honoured cube root of the cell volume  $\Delta_{vol} = (\Delta x \Delta y \Delta z)^{1/3}$  decreases dramatically the level of predicted eddy viscosity because this latter value is proportional to the square of the filter width. Chauvet et al. (2007) proposed an efficient flow-dependent definition based on the orientation of the vorticity vector  $\vec{\omega}$  aimed at solving the slow LES development in mixing layers. A generalization of Chauvet et al. subgrid length scale has been proposed by Deck (2012) (especially for unstructured grids) and may read as:

$$\Delta_{\omega} = \sqrt{\bar{S}_{\omega}} \quad (40)$$

where  $\bar{S}_{\omega}$  is the average cross section of the cell normal to  $\vec{\omega}$ . More precisely; it introduces the notion that at any spatiotemporal point, if the vorticity is not zero, there exists one particular direction indicated by the vorticity  $\vec{\omega}$  (Fig. 12).

The subgrid length scale that enters Eqs. (37) and (38) is respectively given by:

$$\tilde{\Delta}_{DES}^I(\Delta x, \Delta y, \Delta z, U_{i,j}) = \Delta_{vol} \text{ and } \Delta_{\omega} \quad (41)$$

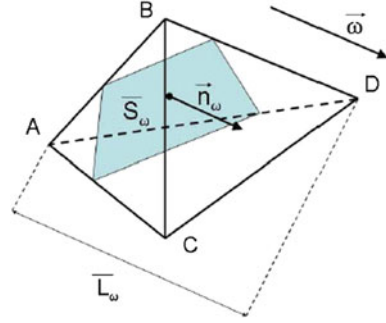
and

$$\tilde{\Delta}_{DES}^{II} = \begin{cases} \Delta_{max} & \text{if } f_d \leq f_{d0} \\ \Delta_{vol} \text{ or } \Delta_{\omega} & \text{if } f > f_{d0} \end{cases} \quad (42)$$

$\tilde{\Delta}_{DES}^{II}$  clearly borrows ideas from DDES in the sense that the  $f_d$  sensor is employed to determine whether  $\Delta_{max}$  or  $\Delta_{vol}$  (or  $\Delta_{\omega}$ ) is used. Equations (41) and (42) are not a minor adjustment in the DES framework since the modified  $\tilde{\Delta}$  length scales depend not only on the grid but also on the velocity and eddy viscosity fields. It is important to emphasize that the shielding of the boundary layer is still ensured



**Fig. 12** Definition of the subgrid length scale  
 $\Delta_\omega = \sqrt{\bar{S}_\omega \cdot \bar{S}_\omega}$  is the average cross section of the cell normal to the vorticity vector  $\vec{\omega}$



by the function  $f_d$  which behaves as standard DDES ( $\Delta = \Delta_{\max}$ ) as long as  $f_d < f_{d0}$ . The improvement lies in  $\Delta_\omega$  (or  $\Delta_{\text{vol}}$ ) becoming the new subgrid length scale when  $f_d > f_{d0}$  which solves the delay in the formation of instabilities (see Deck 2012).

## 5 NLR Approaches to Grey-Area Mitigation for Non-zonal Methods

### 5.1 Introduction

Two types of approaches are proposed to mitigate the grey-area issue for non-zonal DES methods, in particular the X-LES method:

- Triggering instabilities by introducing a stochastic subgrid-scale (SGS) model.
- Reducing the level of SGS stresses in initial shear layers, caused by high gradients of the mean velocity.

For both types, the baseline methods previously incorporated in X-LES, and used with some success to improve the capturing of free shear layers, are described below as well as a new method that has been investigated within the Go4Hybrid project. The baseline methods consist of a stochastic eddy-viscosity model (Kok and van der Ven 2009) and a high-pass filtered SGS model (Kok and van der Ven 2012), respectively. The new method incorporates a stochastic backscatter model (Kok 2016). Note that the approaches described can also be applied to other non-zonal DES methods.

## 5.2 The X-LES Method

In non-zonal DES methods such as X-LES (Kok et al. 2004), a single set of turbulence-model equations is used to model both the Reynolds stresses in RANS zones and the subgrid-scale (SGS) stresses in LES zones. An eddy-viscosity model is used for these stresses, which are then given by the Boussinesq hypothesis:

$$\tau_{ij} = 2\nu_t \left( S_{ij} - \frac{1}{3} \partial_k u_k \delta_{ij} \right) - \frac{2}{3} k \delta_{ij},$$

with  $\nu_t$  the eddy viscosity,  $S_{ij} = \frac{1}{2} (\partial_j u_i + \partial_i u_j)$  the rate-of-strain tensor, and  $k$  the turbulent or subgrid-scale kinetic energy.

The X-LES method in particular is based on the TNT  $k$ - $\omega$  model. The method switches to LES when the RANS length scale ( $l = \sqrt{k}/\omega$ ) exceeds the LES length scale ( $C_1 \Delta$ , with  $\Delta$  the filter width and  $C_1 = 0.08$ ). The RANS length scale is then replaced by the LES length scale in the expression for the eddy viscosity as well as in the expression for the dissipation of turbulent kinetic energy  $\varepsilon$ :

$$\nu_t = \min\{l, C_1 \Delta\} \sqrt{k},$$

and

$$\varepsilon = \frac{\beta k^{3/2}}{\min\{l, C_1 \Delta\}},$$

with  $\beta = 0.09$ . The filter width  $\Delta$  is defined at each grid point as the maximum of the mesh width in all directions. Note that effectively a  $k$ -equation SGS model is used in LES zones (where  $l > C_1 \Delta$ ), as  $\omega$  drops out of the expressions for  $\nu_t$  and  $\varepsilon$ .

## 5.3 Stochastic SGS Models

The current baseline stochastic eddy-viscosity SGS model (Kok and van der Ven 2009) attempts to destabilize shear layers by introducing a stochastic variable  $\xi$  in the expression for the eddy viscosity in LES mode. The stochastic variable has a standard normal distribution with zero mean and unit variance:  $\xi = N(0, 1)$ . For the X-LES method, the expression for the eddy viscosity then becomes:

$$\nu_t = \begin{cases} k/\omega, & \text{if } l \leq C_1 \Delta, \\ \xi^2 C_1 \Delta \sqrt{k}, & \text{if } l > C_1 \Delta. \end{cases}$$

At each time step, a new, uncorrelated value of  $\xi$  is drawn for every grid cell. The stochastic term is not included in the expression for the turbulent dissipation  $\varepsilon$ .

This stochastic eddy-viscosity model was not aimed at modelling energy backscatter. Furthermore, when this model is combined with the high-pass filtered SGS models of the next section, then its effect is diminished due to (much) lower values of the rate-of-strain tensor.

As an alternative approach, a new stochastic SGS model (Kok 2016) is considered that models backscatter at the theoretically correct rate. It is based on the models of Leith (1990) and Schumann (1995). Its formulation is presented in detail here, but a more extensive explanation is given by Kok (2016). The subgrid stress tensor is defined as

$$\tau_{ij} = 2\nu_t \left( S_{ij} - \frac{1}{3} \partial_k u_k \delta_{ij} \right) - \frac{2}{3} k \delta_{ij} - R_{ij},$$

with  $R_{ij}$  a random stress tensor that is responsible for the backscatter. This tensor is not modelled directly, but, following Leith, its gradient is modelled as the rotation of a stochastic vector potential:

$$\nabla \cdot \mathbf{R} = \nabla \times (C_B k \boldsymbol{\xi}),$$

with  $C_B$  a model constant ( $C_B = 1$  by default) and  $\boldsymbol{\xi}$  a vector of three independent stochastic variables  $\xi_i = N(0, 1)$ . The stochastic variables are assumed to be uncorrelated in space over distances larger than the filter width  $\Delta$  and uncorrelated in time over time intervals larger than the subgrid time scale  $\tau \sim \Delta/\sqrt{k}$ .

The additional stochastic term  $\nabla \cdot \mathbf{R}$  is effectively a random acceleration that is added to the momentum equation. As it is solenoidal, it does not induce pressure fluctuations and therefore will not function as a noise source.

Note that the value of  $k$  in the initial shear layer will be high if the upstream boundary layer is turbulent, whereas it will be practically zero if the upstream boundary layer is laminar. In the former case, the stochastic model may destabilize the shear layer, whereas in the latter case the stochastic model will be effectively switched off, allowing a natural laminar-to-turbulent transition of the shear layer.

An essential modification that has been investigated for the stochastic backscatter model is to include non-zero spatial and temporal correlations of the stochastic variables  $\xi_i$ . These correlations are obtained by solving stochastic differential equations that are defined below, leading essentially to the following correlations of  $\xi_i$ —see Kok (2016) for more details:

$$\mathbb{E}(\xi_i(\mathbf{x}, t) \xi_j(\mathbf{y}, s)) = \delta_{ij} e^{-d^2/2} e^{-|t-s|/\tau},$$

with  $d^2 = \|\mathbf{x} - \mathbf{y}\|^2 / (C_\Delta \Delta^2)$  and  $\tau = C_\tau \Delta / \sqrt{k}$ . For the model to be Galilean invariant, this correlation should be interpreted in Lagrangian sense, i.e.,  $\mathbf{x}$  and  $\mathbf{y}$  are the time-dependent coordinates of fluid particles. The default values for the model constants are  $C_\Delta = 0.1$  and  $C_\tau = 0.05$ .

To obtain temporal correlations, a stochastic Langevin-type differential equation is solved for each component  $\xi_i$ , given by

$$\rho \xi_i dt + \tau \left( \frac{\partial \rho \xi_i}{\partial t} + \nabla \cdot (\rho \mathbf{u} \xi_i) \right) dt = \sqrt{2\tau} \rho dW_i,$$

with  $dW_i(\mathbf{x}, t)$  the differential of a Wiener process  $W_i(\mathbf{x}, t)$  with the properties

$$dW_i(\mathbf{x}, t) = N(0, dt)$$

and

$$E(dW_i(\mathbf{x}, t) dW_j(\mathbf{y}, s)) = \delta_{ij} e^{-d^2/2} \delta(t-s) dt ds.$$

This equation is discretized with second-order central schemes both in space and time (second-order finite-volume in space and mid-point rule in time):

$$(\rho \xi)_{i,j,k}^n + \frac{\tau}{\delta t} \left( (\rho \xi)_{i,j,k}^{n+1/2} - (\rho \xi)_{i,j,k}^{n-1/2} \right) + \tau \nabla_{i,j,k} \cdot ((\rho \mathbf{u})^n \boldsymbol{\xi}^n) = \sqrt{2\tau/\delta t} \rho_{i,j,k}^n \boldsymbol{\eta}_{i,j,k}^n,$$

with  $f^n = \frac{1}{2}(f^{n+1/2} + f^{n-1/2})$ ,  $\delta t$  the time step,  $n$  the time-step index,  $(i, j, k)$  the grid-cell indices, and  $\nabla_{i,j,k}$  the second-order central finite-volume discretization of the gradient operator. Thus, at each time step  $n$ , first a new value of the stochastic variable  $\boldsymbol{\eta}_{i,j,k}^n$  must be determined and then a new value of the stochastic variable  $\boldsymbol{\xi}_{i,j,k}^n$  can be determined by solving the equation above. The stochastic variable  $\boldsymbol{\eta}_{i,j,k}^n$  should be uncorrelated in time and should have, at each grid cell, three independent components with zero mean, unit variance, and spatial correlation  $\exp(-d^2/2)$ .

Note that the stochastic variable  $\boldsymbol{\xi}$  is a 3-component vector and therefore three temporal equations need to be solved. This can be done simultaneously with the main flow and turbulence-model equations. These three equations are solved in the complete flow domain, with  $\boldsymbol{\eta}_{i,j,k}^n = 0$  in the RANS zones and at all external boundaries.

The variable  $\boldsymbol{\eta}_{i,j,k}^n$  can be obtained by applying a spatial smoother to a stochastic variable  $\boldsymbol{\zeta}_{i,j,k}^n = N(0, 1)$  that is drawn independently at each grid cell  $(i, j, k)$  and at each time step  $n$ . To obtain the desired spatial correlation of  $\boldsymbol{\eta}_{i,j,k}^n$  on a structured grid, three implicit smoothing operators per computational direction are applied to the spatially uncorrelated variable  $\boldsymbol{\zeta}_{i,j,k}^n$ :

$$(I - \beta_i \delta_i^2) (I - \beta_j \delta_j^2) (I - \beta_k \delta_k^2) \boldsymbol{\eta}_{i,j,k}^n = \boldsymbol{\zeta}_{i,j,k}^n,$$

with  $I$  the identity operator,  $\beta_i = C_\Delta (\Delta / \delta_{ix})^2$  the smoothing coefficient in  $i$ -direction,  $\delta_{ix}$  the mesh size in  $i$ -direction, and  $\delta_i^2$  the second-order difference operator in  $i$ -direction. To ensure a unit variance, the smoothed variable is scaled as

$$\boldsymbol{\eta}_{i,j,k}^n = \frac{(1 + 4\beta_i)^{3/4} (1 + 4\beta_j)^{3/4} (1 + 4\beta_k)^{3/4}}{(1 + 2\beta_i)^{1/2} (1 + 2\beta_j)^{1/2} (1 + 2\beta_k)^{1/2}} \boldsymbol{\eta}_{i,j,k}.$$

The implicit smoothing requires solving a tridiagonal system per computational direction, which can be done efficiently using the Thomas algorithm. At the boundaries, Dirichlet boundary conditions ( $\boldsymbol{\eta}' = 0$ ) are applied.

#### 5.4 High-Pass Filtered SGS Models

As shear layers are initially very thin, they contain high gradients of the (mean) velocity, and therefore of the rate of strain, which leads to high values of the subgrid stresses. Any instability of the initial shear layer may then be damped by these high stresses, thus delaying the development of resolved turbulence. The approach to grey-area mitigation considered in this section attempts to reduce these high values of the stresses.

A high-pass filtered (HPF) SGS model (Kok and van der Ven 2012) has been included in X-LES to remove the dependency of the stresses on (high) mean velocity gradients. The SGS stresses are computed from the velocity fluctuations  $u'$  instead of the instantaneous velocity  $u$ :

$$\tau_{ij} = 2\nu_t \left( S'_{ij} - \frac{1}{3} \partial_k u'_k \delta_{ij} \right) - \frac{2}{3} k \delta_{ij}, \text{ if } l > C_1 \Delta,$$

with  $S_{ij} = \frac{1}{2} (\partial_j u'_i + \partial_i u'_j)$ . The velocity fluctuations  $u'$  are obtained by applying a temporal high-pass filter to the velocity field. This high-pass filter consists of subtracting the running time average of the velocity from the instantaneous velocity:

$$u'(x, t) = u(x, t) - \bar{u}(x, t),$$

with the running time average given by

$$\bar{u}(x, t) = \frac{1}{t} \int_0^t u(x, s) ds,$$

which is discretized as (dropping dependency on  $x$ )

$$\bar{u}(t_n) = \frac{n-1}{n} \bar{u}(t_{n-1}) + \frac{1}{n} u(t_n).$$

A possible disadvantage of this particular high-pass filter is that the running time average contains the complete time history, with equal weight, including the transient. In practice, however, this does not appear to lead to a significant slow-down of the statistical convergence or to a lengthening of the transient.

The baseline high-pass filter is less suitable when the flow contains some non-turbulent unsteadiness at a low frequency that should also be filtered out.

Alternatively, high-pass filters that filter out all frequencies below a certain cut-off frequency may be considered to overcome this disadvantage. In order to limit memory requirements, time-discrete (or digital) filters that can be computed recursively may be chosen, such as the Butterworth-type filters. A disadvantage of these filters is that the cut-off frequency must be chosen a priori. The cut-off frequency should be lower than the frequency of the smallest resolved turbulent structures and higher than the frequency of any non-turbulent unsteadiness. For the test cases considered in Go4Hybrid, which do not contain any non-turbulent unsteadiness, the baseline high-pass filter was found to be sufficient.

## **6 Alternative, Shear Layer Adapted, Subgrid Length-Scale for Non-zonal Hybrid RANS-LES Methods**

### ***6.1 Introduction***

A new definition of the subgrid length scale is proposed, which aims at a rapid destabilising the separated shear layers and accelerating RANS-to-LES transition within non-zonal RANS-LES hybrid methods. In a sense, the proposed approach which underlying physics is outlined in detail in a recent publication of Shur et al. (2015), is similar to that of CFDB (see Sect. 2, above), since both approaches take advantage of the peculiarities of the flow and/or grid topology in the early shear layers. However, implementation of this idea in the two approaches is quite different: the CFDB approach relies upon an alternative SGS model formulation that discerns between quasi 2D and developed 3D flow states, whereas NTS uses for this purpose an alternative subgrid length-scale definition. This definition includes two ingredients, both involving specially designed kinematic criteria accounting for the abovementioned peculiarities of the early shear regions. Although so far this definition has been applied only with the Delayed DES (DDES) approach (Spalart et al. 2006), it is expected to be transferrable to any non-zonal hybrid RANS-LES method employing the grid scale as the LES filter width definition and to pure LES models as well. Below we outline both ingredients of the proposed definition and present its final formulation.

## 6.2 Formulation of Vorticity-Adaptive Grid Scale Measure

In the following, we consider, e.g., jet shear layers or trailing edges and define  $x$ ,  $y$  and  $z$  to be aligned with the streamwise direction, across the shear layer, and in the spanwise or azimuthal direction, respectively. In such situations, efficient grids are fine in the  $y$  direction and perhaps also in  $x$ , but coarse in  $z$ . This creates “pencil” or “ribbon” grid cells. The maximum cell size definition of  $\Delta$  normally used with DES is

$$\Delta_{\max} = \max(\Delta_x, \Delta_y, \Delta_z). \quad (43)$$

Although this is a rational and robust choice for archetypal LES in the inertial range with near-cubic cells, it turns out to be too “conservative” in the initial region of shear layers resolved by such anisotropic grids.

Chauvet et al. (2007) introduced the promising concept of sensitising  $\Delta$  to the orientation of the vorticity vector with the grid. The formulation was subsequently generalised for unstructured meshes by Deck (2012). In regions where the flow is essentially 2D with the vorticity axis aligned with the coarse  $z$  direction, their  $\Delta_\omega$  quantity reduces to  $\sqrt{\Delta_x \Delta_y}$ , thus removing the dominance of  $\Delta_z$ . Although this is helpful, we consider the strong influence of the smallest grid direction in this formulation troublesome. This is the same as our objection to the commonplace use of the cubic root of the cell volume, which was introduced by Deardorff (1970) without logical justification. We therefore propose an alternative concept that reduces to  $\max(\Delta_x, \Delta_y)$ .

Considering a cell with its centre at  $\mathbf{r}$  and vertices at  $\mathbf{r}_n$  ( $n = 1, \dots, 8$  for hexahedra), the proposed definition reads as:

$$\tilde{\Delta}_\omega = \frac{1}{\sqrt{3}} \max_{n,m=1,8} |(\mathbf{I}_n - \mathbf{I}_m)|, \quad (44)$$

where  $\mathbf{I}_n = \mathbf{n}_\omega \times (\mathbf{r}_n - \mathbf{r})$  and  $\mathbf{n}_\omega$  is the unit vector aligned with the vorticity vector. Thus, the quantity  $\tilde{\Delta}_\omega$  is the diameter of the set of cross-product points  $\mathbf{I}_n$  divided by  $\sqrt{3}$ .

As intended, in the shear layer situations outlined above it reduces to  $\frac{1}{\sqrt{3}} (\Delta_x^2 + \Delta_y^2)^{1/2}$ , i.e. is  $O(\max\{\Delta_x, \Delta_y\})$ . In 3D cases,  $\tilde{\Delta}_\omega$  is of the order of  $\Delta_{\max}$  except for the situation when the vorticity vector is aligned with one of the grid coordinate directions (e.g.,  $k$ ), when it reduces to  $O(\max\{\Delta_i, \Delta_j\})$ . Therefore, the smallest grid-spacing never rules.

Another improvement over the original proposal (Chauvet 2007; Deck 2012) occurs when the shear layer is skewed so that the vortex cores are not aligned with the  $z$  direction. In such a case, the Kelvin–Helmholtz instability cannot be resolved well, yet the original definition does not recognise this situation rapidly enough and keeps  $\Delta$  excessively small.

Testing for isotropic turbulence on an isotropic grid has shown that  $\tilde{\Delta}_\omega$  indeed adopts on average 97.5% of the value of  $\Delta_{max}$ . To balance this,  $\tilde{\Delta}_\omega$  can be multiplied by a factor 1.025. The influence of this is however very minor.

### 6.3 Testing for Backward-Facing Step

In order to evaluate a performance of the length-scale and  $\tilde{\Delta}_\omega$  versus the conventional DES length-scale  $\Delta_{max}$ , DDES has been conducted of the flow over a backward-facing step with the use of both length-scales. The grid resolution in the homogeneous spanwise direction has furthermore been varied between  $\Delta_z/H = 0.1$  and  $\Delta_z/H = 0.05$ , where  $H$  is the step height.

The grid used in the simulations and visualisation of the activity of the  $\tilde{\Delta}_\omega$  quantity are shown in Fig. 13a, b, respectively. In the very early shear layer, where

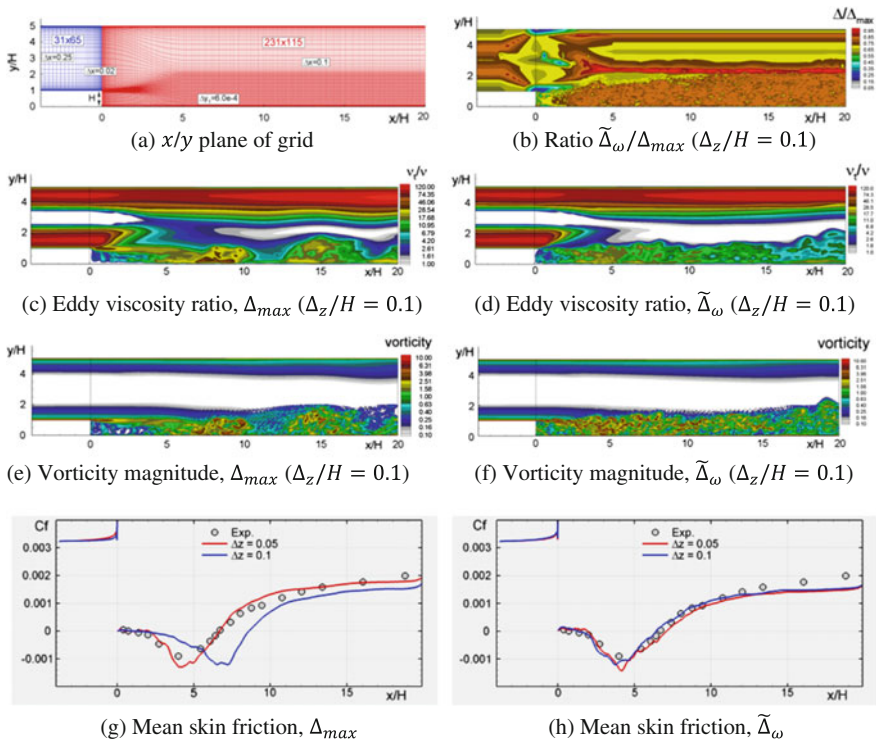


**Fig. 13** Visualisation and results for SA-DDES comparing the  $\Delta_{max}$  and  $\tilde{\Delta}_\omega$  grid scale measures for backward-facing step flow; experimental data of Vogel and Eaton (1985)



the grid cells are highly anisotropic and the vorticity vector is aligned with the  $z$  direction,  $\tilde{\Delta}_\omega$  gives significantly reduced values relative to  $\Delta_{max}$ . Further downstream, where three-dimensional resolved turbulence has developed, values of between around 70 and 85% of  $\Delta_{max}$  are seen. Correspondingly, eddy viscosity levels (Fig. 13c, d) are strongly reduced in the early shear layer, enabling a significantly accelerated development of resolved structures (Fig. 13e, f). Note also, that owing to the DDES shield function, the eddy viscosity levels in the attached boundary layers (treated with RANS) are unaffected, as intended.

As seen from the distributions of mean skin friction coefficient on the lower wall (Fig. 13g, h), the agreement with experiment is improved significantly by the  $\tilde{\Delta}_\omega$  formulation for the coarser  $\Delta_z/H = 0.1$  mesh. Furthermore, the strong sensitivity of the  $\Delta_{max}$  results to the spanwise mesh resolution is dramatically reduced using the  $\tilde{\Delta}_\omega$  expression, which is a highly desirable result.

#### 6.4 Extension of Formulation with “Vortex Tilting Measure” (VTM)

On a nearly isotropic (cubic) grid the effect of replacing  $\Delta_{max}$  with  $\tilde{\Delta}_\omega$  is marginal. So, provided that the isotropic grid is not sufficiently fine to ensure a proper resolution of the initial nearly-2D region of a shear layer,<sup>2</sup> one needs an additional, purely kinematic, measure allowing the identification of quasi-2D flow regions in which nearly Implicit LES treatment is desirable for facilitating the Kelvin-Helmholtz instability and accelerating transition to developed turbulence.

Such a measure called Vortex Tilting Measure (VTM) has been proposed. The measure presents a normalized upper bound of the cross product of the vortex-changing term  $S_{ij}\omega_j$  and the vorticity vector  $\omega_i$  and reads as:

$$\text{VTM} \equiv \frac{\sqrt{6} |(\hat{\mathbf{S}} \cdot \boldsymbol{\omega}) \times \boldsymbol{\omega}|}{\omega^2 \sqrt{3 \text{tr}(\hat{\mathbf{S}}^2) - [\text{tr}(\hat{\mathbf{S}})]^2}} \quad (45)$$

where  $\hat{\mathbf{S}}$  is the strain tensor,  $\boldsymbol{\omega}$  is the vorticity vector and  $\text{tr}(\cdot)$  means trace.

Thus defined measure varies in the range  $[0, 1.0]$ , is small (close to zero) in the quasi-2D flow regions (where the vorticity vector is an eigenvector of the strain tensor), and mostly close to 1.0 in the developed 3D turbulence.

With the use of the VTM quantity, the length-scale  $\tilde{\Delta}_\omega$  (Spalart et al. 2006) may be further modified as:

---

<sup>2</sup>Note that this is the case in all practically meaningful simulations, since “fine enough” actually means unaffordable.

$$\Delta_{SLA} = \tilde{\Delta}_\omega F_{KH}(\langle VTM \rangle). \quad (46)$$

Here the subscript SLA stands for Shear Layer Adapted,  $\langle VTM \rangle$  denotes the average of the VTM quantity over neighboring cells, which is needed to eliminate strong downward excursions experienced by the local values of VTM in the developed turbulence flow regions, and the function  $F_{KH}$  is aimed at unlocking Kelvin-Helmholtz instability in the initial part of shear layers.

To achieve this, the function should be designed so that it remains small at the  $\langle VTM \rangle$  values less than some prescribed threshold value and then rapidly increases up to 1.0 with the  $\langle VTM \rangle$  increase. One possible type of such a function is a simple piecewise-linear function defined as:

$$F_{KH}(\langle VTM \rangle) = \max \left\{ F_{KH}^{min}, \min \left\{ F_{KH}^{max}, F_{KH}^{min} + \frac{F_{KH}^{max} - F_{KH}^{min}}{a_2 - a_1} (\langle VTM \rangle - a_1) \right\} \right\} \quad (47)$$

Here  $F_{KH}^{max} = 1.0$  and  $F_{KH}^{min}$ ,  $a_1$  and  $a_2$  are adjustable empirical parameters which were set equal to 0.1, 0.15, and 0.3 respectively.

Considering that in the inviscid flow regions the quantity  $\langle VTM \rangle$  strongly oscillates in space, in order to avoid possible numerical issues this may cause, the definition of VTM (Chauvet et al. 2007) is further modified as follows:

$$VTM \equiv \frac{\sqrt{6} |(\hat{\mathbf{S}} \cdot \boldsymbol{\omega}) \times \boldsymbol{\omega}|}{\omega^2 \sqrt{3tr(\hat{\mathbf{S}}^2) - [tr(\hat{\mathbf{S}})]^2}} \max \left\{ 1, \frac{0.2v}{\max\{(v_t - v_{t,\infty})10^{-6}v_{t,\infty}\}} \right\} \quad (48)$$

which results in large values of  $VTM$  in the inviscid flow region and, therefore, deactivation of the  $F_{KH}$ , (at large values of  $VTM$ ,  $F_{KH}(\langle VTM \rangle) = 1.0$ ).

Finally, in the DDES approach the  $F_{KH}$  function (1) has to be deactivated also in attached boundary layers, where DDES should work in RANS mode. So, for the wall-bounded flows the function is further modified as follows Shur et al. (2015):

$$F_{KH}^{lim} = \begin{cases} 1.0, & \text{if } f_d < (1 - \varepsilon) \\ F_{KH}, & \text{if } f_d \geq (1 - \varepsilon) \end{cases} \quad (49)$$

where  $f_d$  is the delay function of DDES (Spalart et al. 2006) and  $\varepsilon$  is an empirical constant.

Based on the numerical experiments carried out in Shur et al. (2015) for the zero pressure gradient boundary layer, this constant was set equal to 0.01.

Thus, a final relation for the proposed length-scale reads as:

$$\Delta_{SLA} = \tilde{\Delta}_\omega F_{KH}^{\text{lim}} \left( \langle \text{VTM} \rangle \max \left\{ 1, \frac{0.2\nu}{\max\{(v_t - v_{t,\infty}), 10^{-6}v_{t,\infty}\}} \right\} \right) \quad (50)$$

Results of simulations illustrating a high efficiency of the thus modified subgrid length-scale within SA DDES of the spatially evolving plane shear layer (test case F.2), wall-mounted 2D hump (test case I.4), and round jet (test case I.5), and are presented in Part III (Chapter “[Free Shear Layer](#)”), Part IV (Chapter “[2D Wall-Mounted Hump](#)”) and Part IV (Chapter “[Single-stream Round Jet at M = 0.9](#)”), respectively.

# Improved Embedded Approaches

M. Shur, M. Strelets, A. Travin, A. Probst, S. Probst, D. Schwaborn,  
S. Deck, A. Skillen, J. Holgate and A. Revell

## 1 Introduction

In contrast to the non-zonal, DES-like, hybrid approaches, in which a transition from RANS to LES relies upon a natural instability of separated shear layers in massively separated flows, the zonal RANS-LES (actually, RANS—Wall Modelled LES or RANS-WMLES) hybrids imply the presence of a sharp interface between the flow regions treated by RANS and LES. The location of this interface may be arbitrarily specified by the user based on their understanding of the flow physics, available computational resources or the objectives of the simulation, e.g., a need for unsteady flow characteristics. Thus, the embedded approaches are capable of predicting not only massively separated flows but also flows with shallow separation and fully attached flows and in this sense they are more general than the non-zonal ones.

However, in such methods the issue of delayed RANS-to-LES transition also exists, and a necessary prerequisite of their success is “injecting” turbulent content at the RANS-LES interface, needed to trigger as rapid as possible transition from fully modelled turbulence in the RANS region to mostly resolved turbulence in the LES region. Obviously, the only possible way to decrease the length of this “grey area” or “adaptation region” required to establish mature turbulence downstream of

---

M. Shur (✉) · M. Strelets · A. Travin  
New Technologies and Services (NTS), St.-Petersburg Polytechnic University,  
Petersburg, Russia  
e-mail: mshur@cfds.spbstu.ru

A. Probst · S. Probst · D. Schwaborn  
DLR (German Aerospace Center), Göttingen, Germany

S. Deck  
ONERA, The French Aerospace Lab, 92190 Meudon, France

A. Skillen · J. Holgate · A. Revell  
The University of Manchester, Manchester, UK

the interface, is an improvement of the “quality” of artificial turbulent content injected at the interface, i.e., making it as close to real turbulence as possible.

Note also that a sudden formation of energetic vortical structures at the RANS-LES interface leads to the generation of strong spurious noise. Therefore, when applied to aeroacoustics, any basic “purely aerodynamic” algorithm for imposing unsteady turbulent content at the LES inflow should be supplemented with some means of suppressing this spurious noise.

Considering that a primary objective of the Go4Hybrid project is the grey area mitigation, the efforts of the partners involved in zonal RANS-LES approaches (DLR, NTS, ONERA, and UniMan) were focused exactly on resolving this issue, i.e., improving the tools for creating turbulent content at the RANS-LES interface. However, a considerable amount of work was performed in order to improve some other aspects of the zonal approaches used by the partners. This work is also reflected in this section, which is organized as follows.

The DLR contribution (Sect. 2, Embedded-LES methods for the DLR-TAU code) outlines an embedded LES approach, based on the IDDES approach of Shur et al. (2008), using different underlying RANS models and coupling it with both the original Synthetic-Eddy Method (SEM) of Jarrin et al. (2006) and its divergence-free variant (DF-SEM) of Poletto et al. (2011). A source-term based method to locally inject the turbulence at planes inside the flow domain, as well as the numerical prerequisites for accurate embedded LES in the form of a low-dissipation, low-dispersion (LD2) scheme for unstructured flow solvers are described. Moreover, steps towards an automatic embedded-LES approach are presented using algebraic RANS/LES sensors (Probst et al. 2011) to place the hybrid interface without user input.

An NTS contribution (Sect. 3, Acoustically adapted versions of STG) presents two techniques aimed at generating inflow synthetic turbulence. The first one presents an improved (“acoustically adapted”) variant of previously developed Synthetic Turbulence Generator (STG) for aerodynamic applications of Shur et al. (2014) ensuring suppression of spurious noise created by synthetic turbulence at the RANS-LES interface. The second technique, Volumetric STG (VSTG), heavily relies upon the original STG but is implemented via introducing of empirically designed volume sources into the momentum- and turbulent kinetic energy transfer equations rather than via a direct injection of fluctuating velocity at the RANS-LES interface, thus being more flexible in terms of grid structure and topology.

The ONERA contribution (Sect. 4, ZDES mode 3) presents Zonal DES (ZDES) methodology of Deck (2012), based on a problem dependent partitioning of the computational domain, thus making possible the use of various formulations within one simulation. Particularly, three types of flows are distinguished, which are treated by ZDES differently via the use of different turbulence length-scales: (1) flows with fixed separation i.e., those where the separation is caused by an abrupt variation of the geometry; (2) flows with unfixed (adverse pressure gradient induced) separation on smooth curved surfaces, and (3) flows where the separation is strongly influenced by the state of the incoming boundary layer. For the third

class of flow, an inflow turbulent content is injected with the use of the modification of SEM proposed by Pamiès et al. (2009) and extended to ZDES.

Finally, in Sect. 5 (Improvements to SEM and DFSEM), the UniMan contribution is presented which contains a detailed outline of newly proposed versions of the SEM and DFSEM tools for generating LES inflow turbulent content. These include re-defining the normalisation procedure with respect to the original formulations in order to better handle inhomogeneous length scale distributions, demonstrated to improve downstream accuracy and overall efficiency of the algorithms.

## 2 Embedded-LES Methods for the DLR-TAU Code

### 2.1 Summary

In the course of the Go4Hybrid project, DLR worked on extending its unstructured compressible finite-volume solver TAU (see Schwaborn et al. 2006) by methodologies to allow for reliable and accurate applications of embedded LES. The challenges to extend an unstructured 2nd-order flow solver by embedded-LES capabilities are twofold: First, a rather general method for computing synthetic turbulence has to be implemented, which does not require structured grid information (i.e., an  $ijk$ -metric) and works on grids with arbitrary cells (hexahedra, tetrahedra, prisms, etc.). Second, the numerical scheme for discretizing the flow equations, especially the turbulence-inducing momentum equations, has to meet the accuracy requirements of scale-resolving simulations of wall-bounded flows.

For the former purpose, the Synthetic-Eddy Method has been implemented in its original and a divergence-free version using either a Dirichlet-type inflow boundary condition or volume-source terms in the momentum equations to inject synthetic turbulence on unstructured grids. For the latter, a low-dissipation, low-dispersion 2nd-order central scheme has been developed and implemented into TAU, which allows for accurate simulations of the plane channel flow using either wall-resolved or wall-modelled LES, see Probst et al. (2015).

Another important prerequisite for the industrial application of embedded LES is a (widely) automatic, sensible placement of the embedded-LES region. For example, in flows with local separation, the method should automatically place the embedded zone around the separated region, without a-priori knowledge or manual intervention by the user. To this end, DLR worked on extending its “Algebraic Delayed DES” (see Probst et al. 2011) by wall-modelled LES capabilities (i.e., “Algebraic Improved Delayed DES” or AIDDES) and combining it with automatic synthetic-turbulence injection at the RANS/LES interfaces, which are placed according to algebraic boundary-layer criteria. Note that while the model formulation and most parts of the implementation have been completed, a full demonstration of the automatic embedded LES has not been achieved during the Go4Hybrid project.

## 2.2 Implementation of Synthetic-Turbulence Methods in DLR- TAU

As basic approach for generating synthetic turbulence, the Synthetic-Eddy Method (SEM) of Jarrin et al. (2006) has been selected for its limited complexity and possibility to be implemented without structured-grid information. Moreover, in order to remedy the generation of spurious noise due to non-zero divergence of the synthetic fluctuation field (especially in compressible solvers like TAU), the divergence-free SEM (DF-SEM) of Poletto et al. (2011) has been implemented as well.

### 2.2.1 Synthetic-Eddy Method (Jarrin et al. 2006)

Basically, the Synthetic-Eddy Method (SEM) generates a number of vortices at random locations inside a rectangular domain and with random rotational directions, which induce unsteady synthetic velocity fluctuations at the RANS/LES interface in accordance with given RANS input statistics. The induced fluctuation components at the location  $\vec{x} = x_i = (x, y, z)^T$  are given by:

$$u'_i = \frac{1}{\sqrt{N}} \sum_{k=1}^N a_{ij} \varepsilon_j^{(k)} f_\sigma \text{ with } f_\sigma = \sqrt{V_B} \cdot \sigma^{2/3} \prod_{i=1}^3 f_i,$$

where  $N$  is the total number of vortices in the domain,  $a_{ij}$  is the Cholesky decomposition of the Reynolds-stress input tensor taken from RANS data (either from external input or extracted from somewhat upstream of the interface), and  $\varepsilon_j^{(k)}$  is the randomly computed intensity of the  $k$ th vortex in  $j$ -direction (where  $\varepsilon_j$  needs to obey  $\langle \varepsilon_j \rangle = 0$  and  $\langle \varepsilon_j^2 \rangle = 1$ ). The shape function  $f_\sigma$  depends on the total volume of the rectangular domain  $V_B$ , the local vortex radius  $\sigma$ , and the 1D-shape functions  $f_i$  for each coordinate direction. In the basic approach these are given by:

$$\sigma = \max\{\min[l_{RANS}, \kappa\delta], \Delta\} \text{ and } f_i = f\left(\xi_i = \frac{x_i - x_i^{(k)}}{\sigma}\right) \\ = \begin{cases} \sqrt{3/2}(1 - |\xi_i|) \text{ if } |\xi_i| < 1 \\ 0 \text{ if } |\xi_i| \geq 0 \end{cases},$$

where  $l_{RANS}$  is the integral RANS length scale,  $\kappa = 0.41$  the von-Karman constant, and  $\Delta = \max\{\Delta x, \Delta y, \Delta z\}$  the LES filter width.

The synthetic vortices are convected through the rectangular domain with the ‘‘bulk’’ velocity of the local boundary layer, and they are randomly re-generated at the inflow of the domain as soon as they reach the outflow. Note that the streamwise

extent of the domain is given by  $\pm \max(\sigma)$  around the interface, whereas height and span are given by the size of the interface plane, all together determining  $V_B$ . The constant number of synthetic eddies is computed from  $\max(V_B/\sigma^3)$ .

### 2.2.2 Divergence-Free Synthetic-Eddy Method (Poletto et al. 2011)

Like many other synthetic-turbulence generators, the original SEM computes a fluctuation field with non-zero divergence, which induces spurious density and pressure oscillations in the compressible flow equations. This behavior is clearly unphysical in incompressible flows and thus may cause an additional delay in the development to realistic turbulence. Moreover, the sound source associated with the artificial pressure fluctuations may interfere with acoustic predictions.

The Divergence-free SEM (DF-SEM) of Poletto et al. (2011) aims to minimize the divergence of the synthetic velocity field by applying first the original SEM to the vorticity field, where the divergence-free condition can be easily imposed, and then transforming the result back to the velocity. This approach yields the following final expression for the velocity fluctuations:

$$u'_i = \frac{1}{\sqrt{N}} \sum_{k=1}^N \frac{q_\sigma(\bar{r}^{(k)}/\sigma)}{(\bar{r}^{(k)}/\sigma)^3} \frac{\bar{r}^{(k)}}{\sigma} \times \left[ R_L^G \left( \sqrt{2(k' - \lambda_i)} \varepsilon_i^{(k)} \right)^L \right],$$

where  $\bar{r}^{(k)} = \vec{x} - \vec{x}^{(k)}$  is the local distance vector from the current eddy ( $k$ ), and  $k'$  and  $\lambda_i$  are the turbulent kinetic energy and the eigenvalues of the Reynolds-stress input tensor, respectively. Unlike in the original SEM, the eddy size  $\sigma$  is assumed to be constant.  $R_L^G$  is a rotational matrix that transforms vectors from a local coordinate system  $L$  (given by the principal axes of the Reynolds-stress tensor) to the global coordinate system  $G$ . The shape function  $q_\sigma$  is defined as:

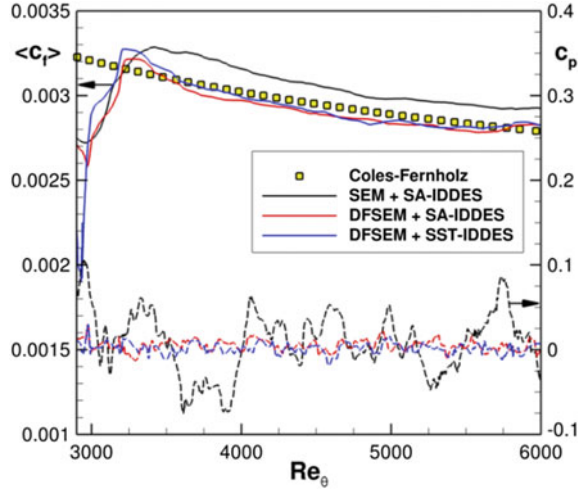
$$q_\sigma \left( \frac{|\bar{r}^{(k)}|}{\sigma} \right) = \begin{cases} \sqrt{\frac{V_B}{\pi\sigma^3}} \cdot \left[ \sin \left( \pi \frac{|\bar{r}^{(k)}|}{\sigma} \right) \right]^2 \cdot \frac{|\bar{r}^{(k)}|}{\sigma} & \text{if } \frac{|\bar{r}^{(k)}|}{\sigma} < 1 \\ 0 & \text{otherwise} \end{cases}$$

All other quantities correspond to the original SEM (see above). Note that this version of Divergence-free SEM (Poletto et al. 2011) is not able to reproduce all possible anisotropy states of the Reynolds-stress input tensor, i.e., it covers only a limited region of Lumley's anisotropy triangle. Note that the newer version considered by UniMAN (Poletto et al. 2013) extends the possible anisotropy range.

In Fig. 1 the differences between original SEM and DF-SEM (2011) are illustrated for flat-plate test case, where synthetic turbulence is injected at the inflow plane. The DF-SEM not only reduces the (instantaneous) pressure oscillations along the whole flow domain, but also improves the skin-friction prediction of the developed boundary layer.



**Fig. 1** Mean skin-friction and instantaneous surface-pressure coefficients on the surface of the flat-plate test case using different synthetic turbulence methods in the DLR-TAU code



### 2.2.3 Injection of Synthetic Turbulence into the Flow Domain

Two different methods to inject the synthetic velocity fluctuations from SEM or DF-SEM have been implemented: First, if the flow domain directly starts with the LES region as, e.g., in internal channel flows, the time-dependent fluctuations are simply added to the Dirichlet-type inflow boundary condition that is typically used in TAU for such flows. Second, in the more general case of an arbitrary interface plane in the (structured or unstructured) grid, a forcing source term in the momentum equations suitable for 2nd-order dual-timestepping schemes is applied. To this end, the grid points lying in the interface plane are flagged according to manual coordinate input by the user or the automatic procedure described in Sect. 2.4. In the flagged forcing region, a source term  $\vec{Q}$  is activated which is derived from a consistent expansion (i.e., on both LHS and RHS) of the implicit dual-time discretization for the fluctuating components of the velocity vector  $\vec{W}'$  at different time levels ( $n + 1$ : next time step,  $n$ : current time step, ...):

$$\frac{3(\vec{W}'^{n+1} + \vec{W}'^{n+1}) - 4(\vec{W}'^n + \vec{W}'^n) + (\vec{W}'^{n-1} + \vec{W}'^{n-1})}{2\Delta t} = \frac{1}{V}\vec{R}^* + \vec{Q}$$

with:

$$\vec{Q} = \frac{3(\vec{W}'^{n+1} - \vec{W}'^n) - (\vec{W}'^n - \vec{W}'^{n-1})}{2\Delta t}.$$

Here  $V$  is the local cell volume and  $\vec{R}^*$  the modified (dual-time) residual. Note that only the *target* fluctuations at the next time level  $\vec{W}'^{n+1}$  are directly taken from the synthetic turbulence generator, whereas the previous values are given by the

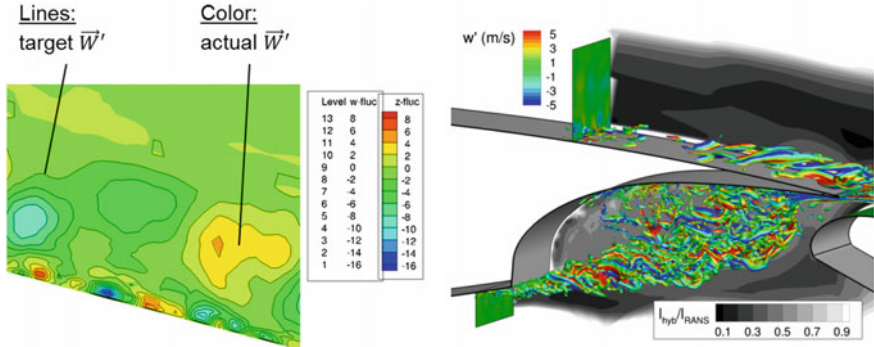


**Fig. 2** *Left* Comparison of actual and target fluctuations when using momentum source terms to inject synthetic turbulence. *Right* Demonstration of multiple forcing planes

actual fluctuations  $\vec{W}'^m = \vec{W}^m - \langle \vec{W} \rangle$  and  $\vec{W}'^{m-1} = \vec{W}^{m-1} - \langle \vec{W} \rangle$ , respectively. This is important to avoid decoupling of the actual flow solution from the target synthetic field, but adds the requirement of well-converged time averages  $\langle \vec{W} \rangle$ .

With this approach, the synthetic fluctuations from SEM/DF-SEM are accurately injected at the interface, as illustrated in Fig. 2 (left) for a zero-pressure-gradient boundary-layer flow. Note that the agreement between the target and the actual fluctuations may degrade, if too large a physical time step is used, which is however, unlikely to occur in typical hybrid RANS/LES computations. Figure 2 (right) illustrates the application of the source term in two independent interface planes on the 3-element-airfoil test case.

### 2.3 Low-Dissipation Low-Dispersion (LD2) Numerical Scheme

For accurate predictions of wall-bounded flows using scale-resolving approaches, the main types of numerical discretization errors in the main flow equations have to be minimized, namely *dissipation* and *dispersion*. To this end, a two-step approach was pursued and implemented in TAU:

- (1) *Low-Dissipation (LD) scheme*:

The LD-scheme relies on the skew-symmetric 2nd-order central discretization operator of Kok (2009) for the main-flow equations, which is energy-conserving, i.e., non-dissipative, on curvilinear grids. For general structured or unstructured meshes, matrix-valued 4th-order artificial dissipation needs to be added to guarantee stability. However, the amount of dissipation could be minimized to an adequate level for scale-resolving simulations by

conducting sensitivity studies on the dissipation parameters in decaying isotropic turbulence and for a plane channel flow. Moreover, low-Mach preconditioning is used to adapt the dissipation in low-speed (incompressible) flows.

(2) *Low-Dissipation low-dispersion (LD2) scheme:*

Following the ideas of Kok (2009), who derives a low-dispersion 4th-order scheme, an additional gradient-based extrapolation of the 2nd-order convective main-flow fluxes has been implemented in TAU. The extended central flux at a cell face  $ij$  reads

$$\phi_{ij,\alpha} = \frac{1}{2}(\phi_i + \phi_j) + \frac{1}{2}\alpha(\nabla_0\phi_i + \nabla_0\phi_j) \cdot \vec{d}_{ij}$$

where  $\phi$  is a general main-flow variable,  $\vec{d}_{ij}$  is the distance vector between two adjacent grid points, and  $\alpha$  is a free extrapolation parameter. This parameter has been numerically optimized in 1D- and 2D-wave propagation problems for a reduction of the dispersion error, yielding  $\alpha = 0.36$ . The combination of the low-dissipation settings (1) with the low-dispersion flux is denoted *LD2-scheme*.

The performance of both schemes in TAU is illustrated in Fig. 3 for channel-flow computations using wall-modelled LES (i.e., SST-IDDES). Apart from a slight log-layer mismatch at the RANS/LES interface for the high Reynolds number ( $Re_\delta = 98,300$ , corresponding to  $Re_\tau = 4200$ ), the LD2-simulations agree well with the reference data.

For more complex hybrid RANS/LES applications, where a suitable grid quality is not guaranteed throughout the whole flow domain, the LD2-scheme has also been

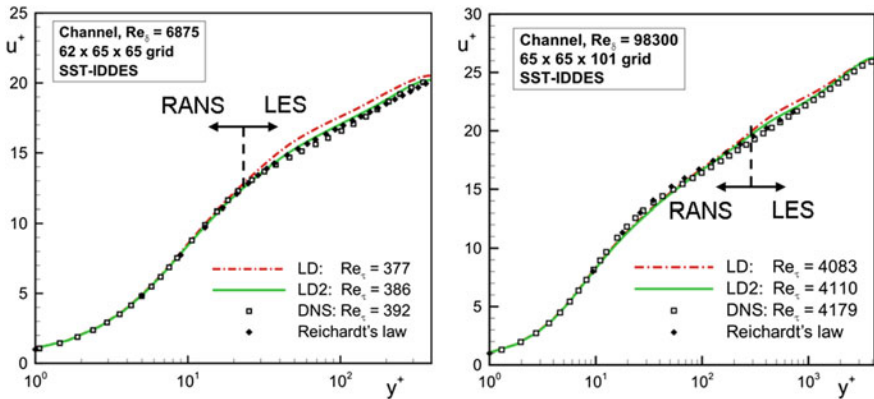


**Fig. 3** Channel flow computations at different Re-numbers using the LD- and LD2-schemes in TAU with SST-IDDES

implemented in a hybrid framework. Here, the numerical weighting function by Travin et al. (2004) is used to activate the LD2-scheme only in resolved (LES) regions, whereas the unresolved (RANS) region is treated by a more dissipative and dispersive standard central scheme. For more details, refer to Probst et al. (2015).

## 2.4 Towards Automatic Embedded LES Using Algebraic RANS/LES Sensors

The Algebraic DDES (ADDES) of Probst et al. (2011) employs algebraic boundary layer quantities to redefine the switch between RANS and LES regions instead of using the  $f_d$  function of classic Delayed DES (DDES). It aims to ensure RANS mode throughout the whole attached boundary layer even for strong adverse pressure gradients, and to reliably shift the RANS/LES interface towards the wall in separation regions, in particular for thin separation bubbles on smooth surfaces.

For this purpose, the flow solver is extended by an additional data structure: For every wall node (of the relevant boundaries) it provides a list of points lying on an approximate wall-normal ray in order to store and process local BL profiles in each time step. Search operations (e.g., for the BL edge) as well as line integrations (for integral BL quantities) are introduced. Moreover, the implementation allows to flag regions above the walls as attached or detached, depending on the evaluated criteria along each wall-normal ray.

The method can be most easily implemented in structured solvers by exploiting the  $ijk$ -metric. For unstructured solvers it is most suited for meshes whose structured layer fully contains the boundary layer, but TAU can also find wall-normal rays in hybrid meshes containing triangular elements.

### Detection of the Boundary-Layer Thickness

For determining the boundary-layer thickness  $\delta$ , the primary choice is to use  $\delta_{99}$ , being the wall distance where the local velocity  $U$  along a wall-normal profile reaches for the first time 99% of the boundary-layer edge-velocity  $U_{edge}$ . We compute  $U_{edge}$  from the pressure  $p_w$  at the corresponding wall node using the compressible Bernoulli equation:

$$U_{edge} = U_{\infty} \sqrt{1 + 0.5 \frac{1 - (p_w/p_{\infty})^{(\gamma-1)/\gamma}}{(\gamma-1)Ma_{\infty}^2}}$$

As this approach may fail in certain flow conditions, e.g., involving strong flow acceleration, two other methods for approximating the boundary layer thickness can be used as fallback (see Probst et al. 2011).

### Criteria for Flow Separation

In several publications, the value of the shape factor  $H = \delta^*/\Theta$ , with:

$$\delta^* = \int_0^{\delta} (1 - u/U_{\infty}) dy \text{ and } \Theta = \int_0^{\delta} \frac{u}{U_{\infty}} (1 - u/U_{\infty}) dy$$

is used as an empirical criterion for pressure-induced separation of subsonic turbulent boundary layers. In Castillo et al. (2004) the separation criterion  $H_{crit} \geq 2.76 \pm 0.23$  (obtained via similarity analysis) is shown to be in good agreement with existing experimental data (note that in the zero pressure gradient boundary layer  $H \approx 1.3-1.4$ ).

This criterion is adopted in ADDES, but requires adjustments to the respective underlying RANS model. Based on different flow cases with pressure-induced separation (a diffuser, an airfoil, and an engine nacelle at stall) which cover a broad range of flow conditions (2D/3D, Re-number, angle of attack) the following model-dependent separation criteria have been derived so far:

Spalart-Allmaras 1-eq model (Spalart, Allmaras 1992)	$H_{crit} = 2.4$
SST 2-eq model (Menter 1993)	$H_{crit} = 3.3$
$\varepsilon^h$ -Reynolds-stress model (Jakirlic, Hanjalic 2002):	$H_{crit} = 3.2$

In TAU's ADDES implementation the values of  $\delta^*$  and  $\Theta$  are computed by simple numerical integration (trapezoidal rule) along the wall-normal rays, where the detected boundary-layer edge  $\delta$  serves as upper integration boundary.

#### Determination of RANS and LES Regions

The boundary-layer thickness  $\delta$  and the shape factor  $H$  can now be used to decide locally whether the flow is attached or separated. This determines the new delay function  $f_{d,ADDES}$ , which basically replaces  $f_{d,\psi}$  in DDES, i.e.  $f_{d,ADDES} = 0$  for attached and  $f_{d,ADDES} = 1$  for separated regions.

Denote  $\delta_w$  and  $H_w$  the values of  $\delta$  and  $H$  at the wall node  $\vec{x}_w$ . Then we set this value for all nodes on the corresponding wall-normal ray  $\lambda(\vec{x})_w$ . Now, given a node  $\vec{x} \in \lambda(\vec{x}_w)$  with wall distance  $d_w$ , set:

$$f_{d,ADDES} = 0, \quad \text{if } d_w < \delta_w \text{ and } H_w < H_{crit}$$

$$f_{d,ADDES} = 1, \quad \text{if either } d_w > \delta_w \text{ or } H_w > H_{crit}.$$

#### Coupling with IDDES

For embedded LES of wall-bounded flows, the hybrid approach has to act as Wall-Modelled LES (WMLES) in the resolved flow regions. For this the ADDES is combined with Improved DDES (IDDES) of Shur et al. (2008), which adds an additional WMLES branch in the hybrid length-scale compared to DDES. The IDDES definition of  $l_{hyb}$  reads:

$$l_{hyb} = \tilde{f}_d(1 + f_e)l_{RANS} + (1 - \tilde{f}_d)l_{LES} \text{ with } \tilde{f}_d = \max\{(1 - f_{dt}), f_B\}.$$

Now, to preserve both the ADDES detection mechanisms for attached/separated flow and the WMLES capability of IDDES (which is basically controlled by the functions  $f_e$  and  $f_B$ ), the ‘‘Algebraic IDDES’’ (AIDDES) sensor replaces only the function  $f_{dt}$  inside  $\tilde{f}_d$ . Then,  $f_{d,AIDDES} = 0$  ensures RANS mode throughout the boundary layer, whereas  $f_{d,AIDDES} = 1$  yields WMLES close to walls or classic DES behavior in off-wall regions.

Exemplarily, Fig. 4 illustrates the essential ingredients of the approach for the 2D hump flow (based on a steady flow field computed with SST-RANS). It is shown that the local flow separation can be accurately detected and automatically treated in WM-LES mode. Together with a suitable treatment at the RANS/LES interfaces, e.g., (DF-)SEM, a fully automatic embedded-LES method has come into reach.

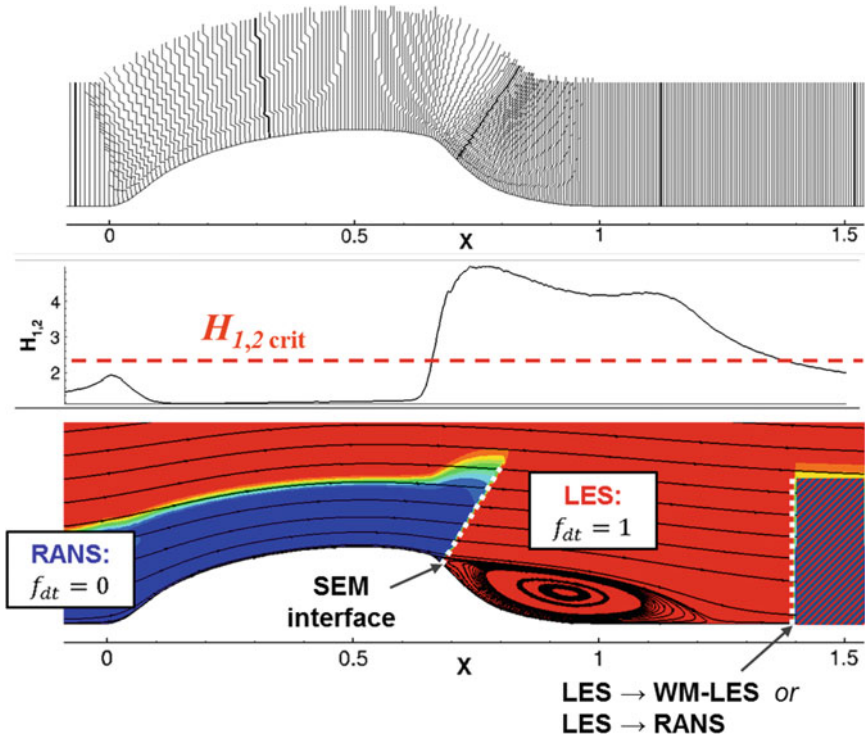


**Fig. 4** Outline of automatic embedded-LES approach for 2D-hump flow. *Top* Wall-normal rays. *Center* Computed shape factor and critical value (separation criterion). *Bottom* Resulting RANS and (WM-)LES regions and possible treatments at the interfaces

## 3 Acoustically Adapted Versions of STG

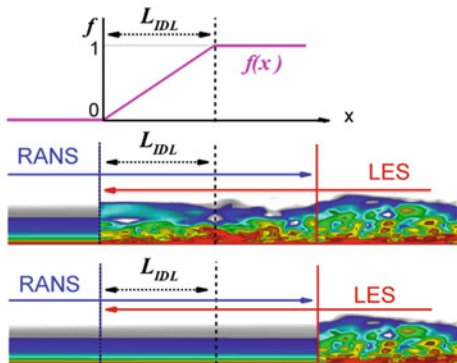
### 3.1 Summary

It is firmly established now that injection of the turbulent content at the RANS-to-LES interface is a powerful tool for the Grey Area Mitigation (GAM). A few approaches to creating such content are currently available. One of them developed by Shur et al. (2014) presents a modification of a simple and robust procedure for generating synthetic turbulence in the framework of embedded RANS-LES of attached and mildly separated wall-bounded flows as well as free shear flows (Adamian et al. 2011). This synthetic turbulence generator (“NTS STG”) has been validated on a range of canonical flows (developed channel flow, zero pressure gradient boundary layer, plane spatially developing mixing layer), as well as on a more complex flow over a wall-mounted hump with non-fixed separation and reattachment and shown to ensure a rapid conversion from modeled to resolved Reynolds stresses, i.e., a short “relaxation” region needed for establishing of mature LES-resolved turbulence. However, the procedure assumes the use of structured multi-block grids with the RANS-LES interface coinciding with a grid surface hampering its incorporation into industrial unstructured CFD solvers. Other than that, similar to all other available STGs, it results in creation of spurious noise sources at the RANS-LES interface caused by an abrupt appearance of unsteady vortical structures. This precludes application of the STG to aeroacoustic problems, i.e., to problems in which the need for Embedded LES approaches is especially severe.

In this section we briefly present two approaches aiming at diminution of these deficiencies of the STG of Shur et al. (2014) proposed and validated in the course of the Go4Hybrid project. The first approach presents a combination of this STG with an “Internal Damping Layer” (IDL) technique and the second one is a new, Volumetric STG (VSTG hereafter). Unlike the NTS STG and many other similar turbulence generating tools, VSTG is based on introducing specially designed volume sources (“body forces”) into the momentum—and turbulent kinetic energy transport equations. A major advantage of such an approach over the injection of turbulent fluctuations at the RANS-LES interface is a higher flexibility in terms of grid-structure, which facilitates implementation in different CFD codes. In addition, as demonstrated below, with a sufficiently stretched source region, VSTG provides also an efficient way of suppressing spurious noise generated by synthetic turbulence.

For the sake of completeness, we first present below the formulation of the already published IDL technique (Shur et al. 2014) and then dwell upon the VSTG. Note that all the developed methods are intended for working within zonal/embedded RANS-LES approaches with either wall resolved LES (WRLES) or LES with near-wall modeling (WMLES). The latter capability is supported by examples of the performance of DDES with improved wall-modelling capabilities (IDDES) with underlying  $k-\omega$  SST RANS turbulence model (Menter 1993).

**Fig. 5** Design of internal damping layer



### 3.2 “Acoustically Adapted” Version of STG (IDL Technique)

To suppress the spurious noise created by synthetic turbulence imposed at the RANS-LES interface it is proposed to insert an “internal damping layer” (IDL) in the LES sub-domain of zonal RANS-LES approaches. The idea and design of the damping layer is clarified by Fig. 5.

The IDL is placed within the overlapping region of the RANS and LES sub-domains. Inside this layer, at each time step a “preliminary” (computed by LES) pressure field is modified by “weighting” it with the URANS pressure also available in the overlapping region:

$$p_{LES}^{mod} = f(x) \cdot p_{LES} + [1 - f(x)] \cdot p_{RANS},$$

where the empirical weight function  $f(x)$  is defined as  $f = \max\{\min[(x - x_0)/L_{IDL}, 1], 0\}$ ,  $x_0$  is the streamwise coordinate of the (WM) LES inlet, and  $L_{IDL}$  is the user-specified length of the damping layer (typically, it is set equal to  $\sim 2\delta_{BL}$ ). The velocity and temperature fields within the IDL region remain unchanged, and the density is re-computed with the use of the modified pressure to satisfy the equation of state.

A drastic positive effect of this simple modification is illustrated by Fig. 6, which compares acoustic pressure fields in the trailing edge flow predicted with the use of the original (purely aerodynamic) and the modified versions of the STG within the  $k-\omega$  SST based zonal RANS-IDDES (details of this simulation can be found in Shur et al. 2014). One can see that the acoustic field predicted by the simulation using the original STG is dominated by intensive spurious sound waves radiated from the RANS-IDDES interface, whereas the simulation with the IDL results in a radical weakening, if not a complete elimination of these waves and in revealing the real sound waves generated by the physical noise source located near the trailing edge.

At the same time, the simulation with the use of the IDL does not reveal any negative side effect on the prediction of the mean flow characteristics and velocity



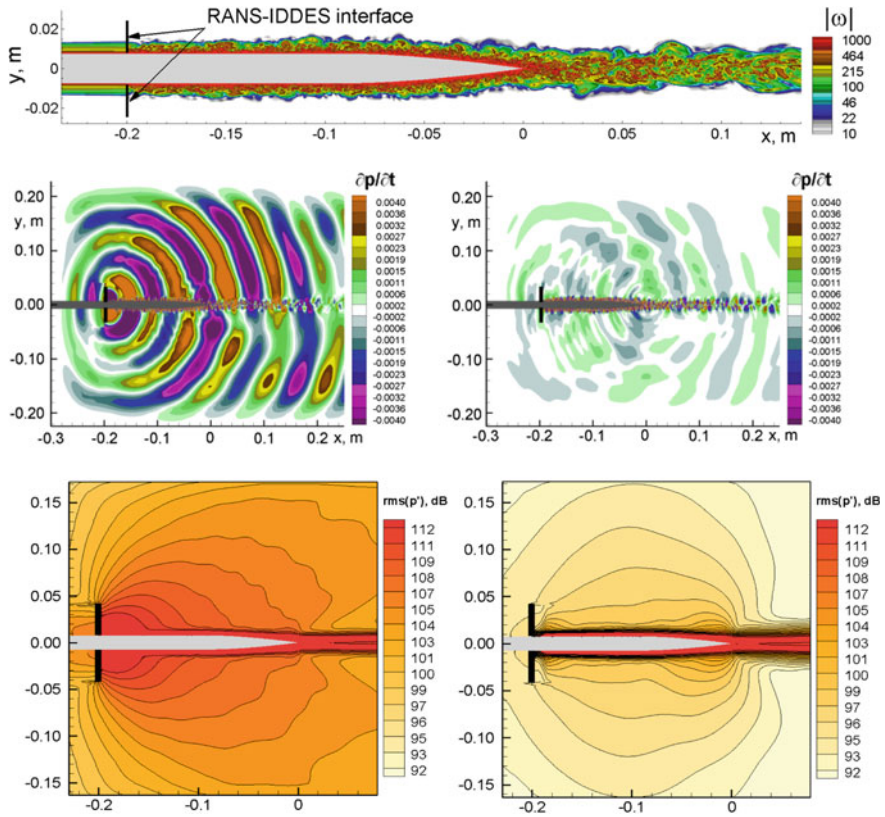


**Fig. 6** Snapshot of vorticity (*upper frame*), instantaneous acoustic pressure fields (*second row*) and *rms* of pressure fluctuations (*third row*) from zonal RANS-IDDES of trailing edge flow (Shur et al. 2014) performed with the use of purely aerodynamic STG (*left column*) and STG with IDL (*right column*)

spectra (not shown), at least at low Mach numbers typical of airframe noise problems. Note also that the intensity of the wall pressure fluctuations in the IDL region (i.e., in the close vicinity of the RANS-LES interface) predicted by the original (without the IDL) STG turn out to be strongly overestimated. In contrast to this, the simulation carried out with the use of the modified (with IDL) STG predicts both this intensity and spectral characteristics of the unsteady wall-pressure in the IDDES sub-domain fairly accurately (see Fig. 7). Finally, the IDL does not prevent capturing sound waves generated by noise sources located downstream of the end of the RANS sub-domain and propagating upstream (within the damping layer, they propagate through the RANS area).

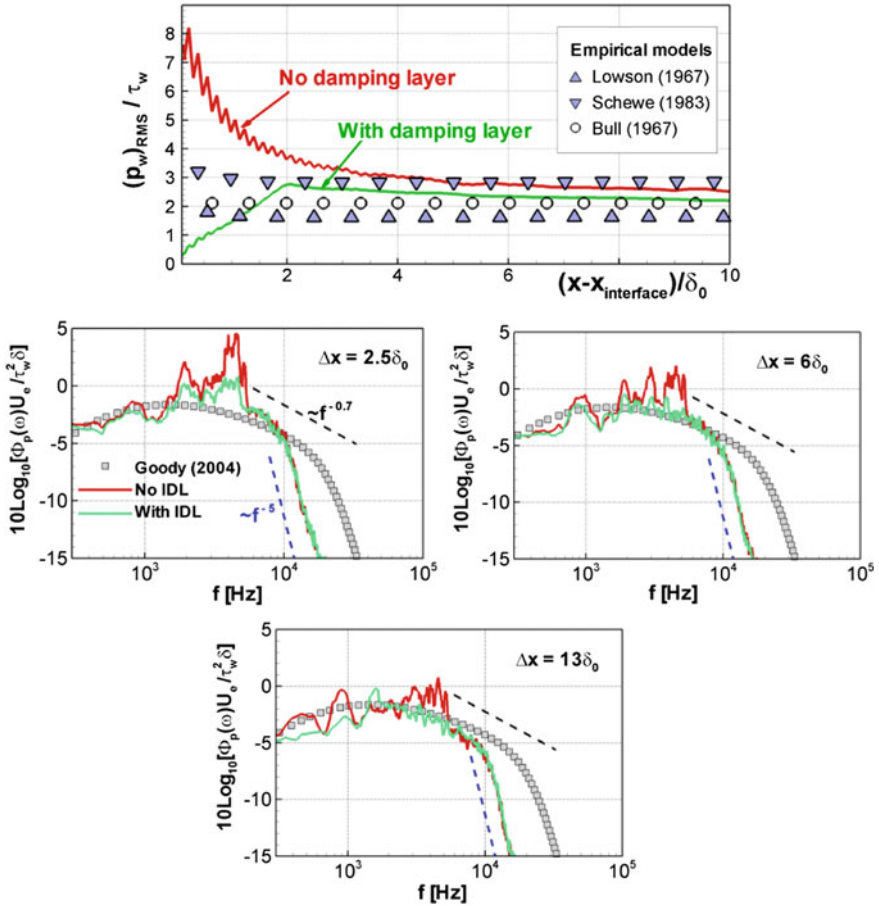


**Fig. 7** Effect of IDL on *rms* of wall-pressure fluctuations in IDDES sub-domain of RANS-IDDES (*upper frame*) and on power spectra of wall pressure (*lower frames*). Empirical correlations shown by symbols are taken from the works of Bull (1967), Lowson (1967), Schewe (1983) and Goody (2004)

### 3.3 STG Based on Spatially Distributed Volume Source Terms (V-STG)

As mentioned in the introduction, this approach to creating the inflow turbulent content for the (WM)LES sub-domain in the framework of embedded RANS-(WM) LES methods is in principle more tolerant to the grid structure than the STGs, in which the RANS-LES interface must coincide with some grid surface.

The approach presented below assumes that the WMLES model is IDDES with the underlying  $k$ - $\omega$  SST RANS model. It is based on introducing specially designed volume source terms (“Body Force”—BF) in the momentum and turbulent kinetic energy transport equations. These source terms are non-zero in some (user-specified) region, whose configuration relies only upon a priori known “streamwise” flow direction and is not anyhow “tied” to the used computational grid.

Other than that, the VSTG approach has a high potential in terms of adaptation to aeroacoustic problems without using any supplementary tools (like the IDL described in the previous sub-section) due to the possibility to gradually increase the strength of the volume sources in the downstream direction, which allows reducing the spurious noise caused by the abrupt emergence of turbulence typical of the “surface” STGs.

### 3.3.1 VSTG Formulation

Let us, for definiteness, assume that the mean flow within the source area is parallel to the  $x$ -axis and that the source region starts at  $x = x_0$  (RANS-LES “interface”) and has the streamwise width of  $L_{BF}$ , i.e. is located at  $x_0 < x < x_0 + L_{BF}$ .

Initially, we have attempted to design the VSTG so that assuming a frozen RANS velocity within the source region, it would produce the same velocity fluctuations field (synthetic turbulence) at its “downstream end”  $x = x_0 + L_{BF}$  as that provided by the “surface” STG at the RANS-LES interface. However, after a set of numerical experiments, we have arrived at the following, much more simple, purely empirical formulation, which, however, still satisfies the demand of closeness of turbulence produced by the VSTG and the original “surface” STG. In this formulation the source term in the momentum equation reads:

$$\mathbf{F}_{momentum} = C_{BF} \rho U_0 \mathbf{u}'(x, y, z) \alpha(x), \quad (1)$$

where  $C_{BF} = 1.1$  is an empirical constant,  $\mathbf{u}'(x, y, z)$  is the vector of velocity fluctuations within the source region computed with the use of the surface NTS STG based on the fields of mean velocity and Reynolds stresses from the current RANS solution at the flow section located slightly upstream of  $x = x_0$ , and  $\alpha(x)$  is the user-specified function controlling the spatial distribution of the source intensity, which satisfies the normalization condition  $\int_{x_0}^{x_0 + L_{BF}} \alpha(x) dx = 1$ .

Finally,  $U_0$  in Eq. (1) is a macro-scale velocity (e.g., the maximum or bulk velocity) which is involved in the formulation of the surface STG (Shur et al. 2014).

The sink term introduced into the  $k$ -transport equation of the  $k$ - $\omega$  SST model is defined as follows:

$$F_k = -\rho U_0 \alpha(x) \omega \max\{v_t^{IDDES} - v_t^{Smag}, 0\}, \tag{2}$$

where  $v_t^{IDDES}$  and  $v_t^{Smag}$  are the eddy viscosities computed with the use of IDDES and Smagorinsky SGS models, respectively, and  $\omega$  is the specific dissipation rate involved in the SST IDDES model. This sink term results in a rapid drop of  $k$  and, therefore, of  $v_t^{IDDES}$  at  $x > x_0$ , until  $v_t^{IDDES}$  gets equal to  $v_t^{Smag}$  thus zeroing the sink, i.e., ensuring a rapid transformation of the RANS SST eddy viscosity at  $x = x_0$  into the SGS viscosity within the source region.

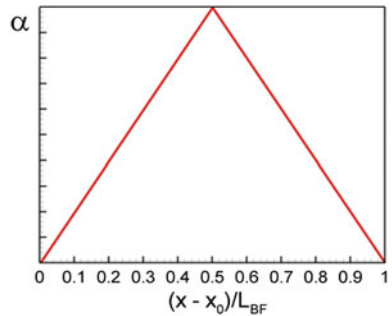
Note in conclusion that in principle the simulation can be initialized from an arbitrary flow-field but in order to reduce the transient period it is recommended to use a converged or at least reasonably mature RANS solution at  $x < x_0$  for this purpose. In addition, it is recommended to fix in time the value of the length-scale  $l_e^{max} = \max_{\mathbf{r}}\{l_e(\mathbf{r})\}$  used in the “surface” STG.

### 3.3.2 Validation of VSTG

In the course of the Go4Hybrid project the approach outlined above was tested on the compressible subsonic ( $M = 0.5$ ) ZPG BL at the Reynolds number based on the momentum thickness at  $x = x_0 = 0$  equal to  $2 \times 10^3$ . The function  $\alpha(x)$  in Eqs. (1) and (2) was defined as a simple piecewise linear function shown in Fig. 8. A comparison of RANS-IDDES predictions obtained for this flow with the use of the original STG and its acoustically adapted (with IDL) version versus a similar prediction obtained with the use of the VSTG is presented in Figs. 9, 10 and 11.

Figure 9 compares flow visualizations computed with the use of the STG and STG with IDL with those from simulations with VSTG at different values of the parameter  $L_{BF}$ . The figure suggests that all the considered methods of creating turbulent content ensure forming of realistic turbulent structures somewhat downstream of the RANS-IDDES interface or the end of the non-zero volume sources region.

**Fig. 8** Plot of the function  $\alpha(x)$  used in simulation of ZPG BL



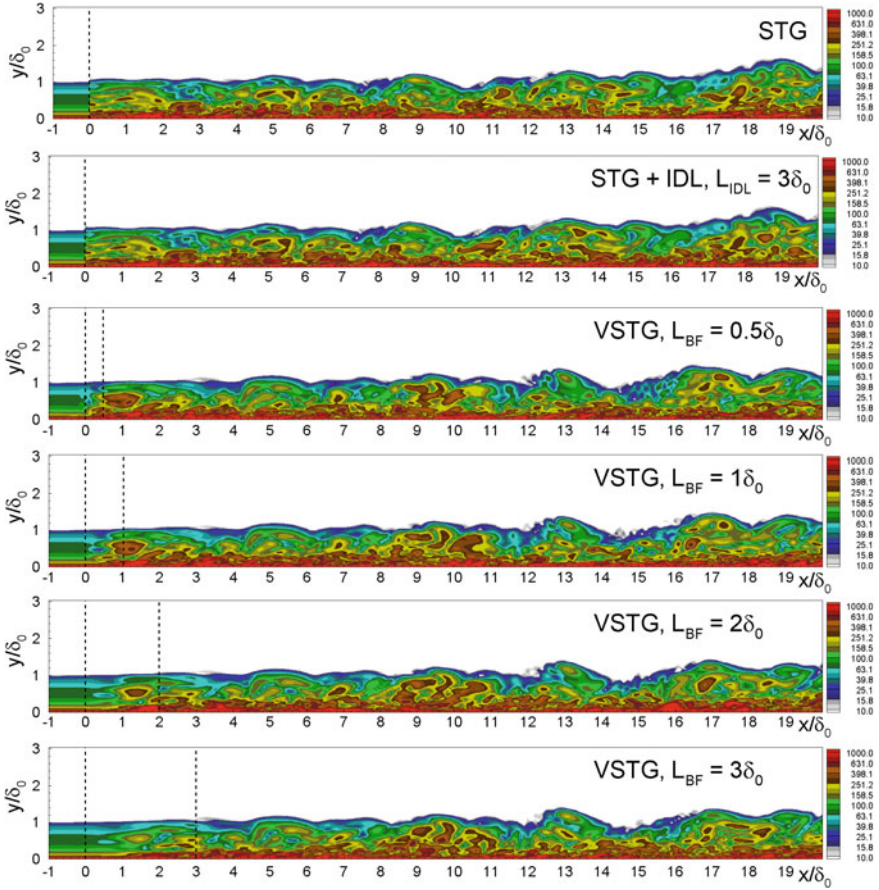


**Fig. 9** Comparison of instantaneous vorticity fields from simulations with the use of surface STG, surfaces STG with IDL, and VSTG at different values of the parameter  $L_{BF}$ . Dashed vertical lines shows locations of RANS-IDDES interface or boundaries of the non-zero volume sources in the momentum- and  $k$ -transport equations

Figures 10 and 11 give an idea on the quantitative capabilities of all the three approaches. Namely, it clearly demonstrates a fairly accurate performance of the surface STG combined with the IDL in terms of both predicting the mean flow (skin-friction) and unsteady (wall-pressure) flow characteristics. As for the simulations using VSTG, at small values of the parameter  $L_{BF}$  they result in a considerable deviation of the skin-friction and wall-pressure fluctuations from the “target” distributions but with increase of this parameter up to about  $(2-3)\delta_{BL}$ , they become quite competitive with the STG-IDL approach.

Hence it can be concluded that the STG-IDL approach is preferable for the solvers accepting multi-block structured overlapping grids, whereas for the industrial unstructured codes the VSTG can be recommended.

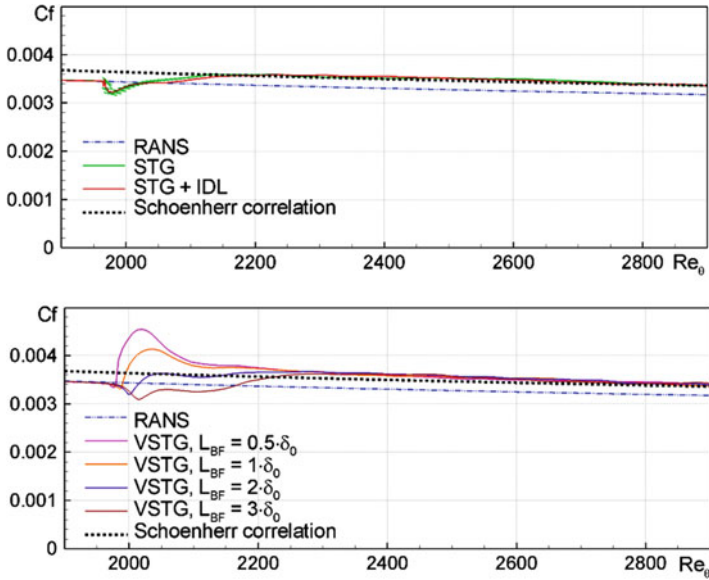


**Fig. 10** Comparison of distributions of mean skin-friction in compressible ZPG BL predicted by zonal RANS-IDDES with the use of original (surface) STG, STG combined with IDL, and VSTG at different values of parameter  $L_{BF}$  with SST RANS solution and Schoenherr empirical correlation

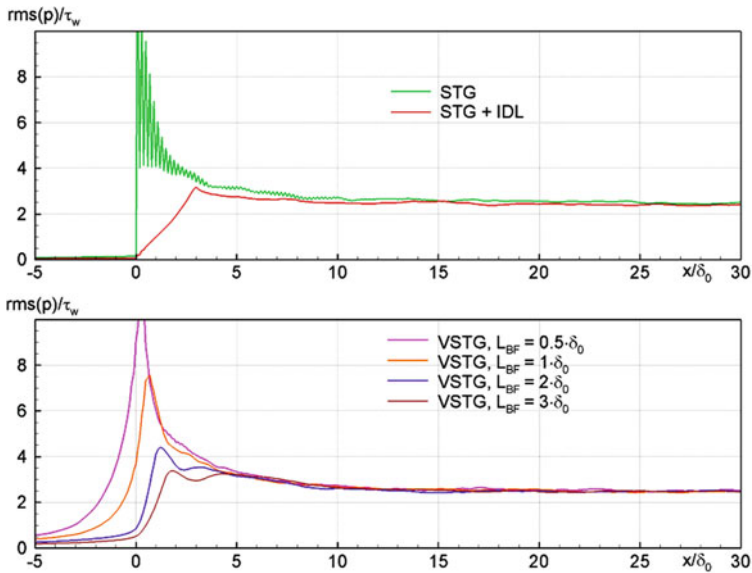


**Fig. 11** Comparison of distributions of *rms* of wall pressure fluctuations predicted by zonal RANS-IDDES with the use of original STG, STG combined with IDL, and VSTG at different values of the parameter  $L_{BF}$

## 4 ZDES Mode 3

### 4.1 Zonal DES

The ZDES was first proposed by Deck 2005a, b and the complete formulation has been recently published in Deck 2012. The method is based on a fluid problem-dependent zonalisation and makes possible the use of various formulations within the same calculation.

In the framework of ZDES, three specific hybrid length scale formulations [see Eq. (3)], also called modes, are optimized to be employed on three typical flowfield topologies as illustrated in Fig. 12. Though the method can be adapted to any turbulence model, in the framework of the underlying SA RANS model,  $d_w$  is replaced with  $\tilde{d}_{ZDES}$  in the model according to:

$$\tilde{d}_{ZDES} = \begin{cases} d_w & \text{if } \text{mod } e = 0 \text{ (i.e. RANS)} \\ \tilde{d}_{DES}^I & \text{if } \text{mod } e = 1 \\ \tilde{d}_{DES}^{II} & \text{if } \text{mod } e = 2 \\ \tilde{d}_{DES}^{III} & \text{if } \text{mod } e = 3 \end{cases} \quad (3)$$

Mode 1 concerns flows where the separation is triggered by a relatively abrupt variation in the geometry; mode 2 is retained when the location of separation is induced by a pressure gradient on a gently curved surface, and mode 3 for flows where the separation is strongly influenced by the dynamics of the incoming boundary layer (see Fig. 12). All these flow cases may be treated by the same ZDES technique in its different modes. An example where the three modes of

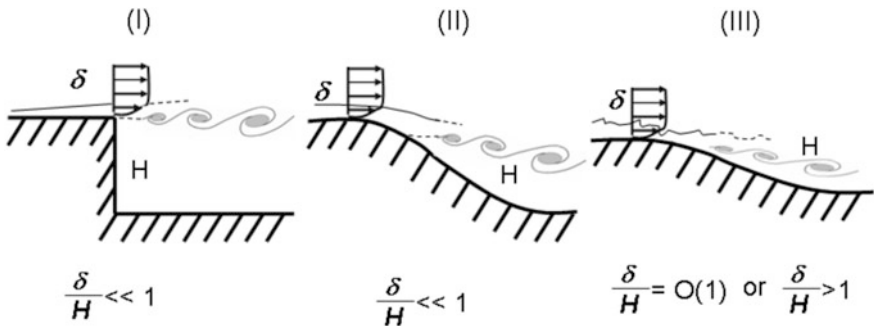


**Fig. 12** Classification of typical flow problems. *I* separation fixed by the geometry, *II* separation induced by a pressure gradient on a gently-curved surface, *III* separation strongly influenced by the dynamics of the incoming boundary layer

ZDES are used at the same time on a curvilinear geometry can be found in Deck and Laraufie (2013).

The ability of ZDES mode 3 to operate in both Wall Resolved Large Eddy Simulation (WRLES) and Wall-Modelled Large Eddy Simulation (WMLES) has been exercised in Deck et al. (2014a), Deck et al. (2011) and in Deck et al. (2014b), Láraufie et al. (2011), Láraufie and Deck (2013) (Fig. 13).

In the framework of Work package WP3, only the mode 3 of the ZDES approach in its WMLES branch will be used (see Fig. 14). The location of the interface results from the length scale used for mode 3 which reads as:

$$\tilde{d}_{ZDES}^{III} = \begin{cases} d_w & \text{if } d_w < d_w^{interface} \\ \min(d_w, C_{DES}\Delta) & \text{otherwise} \end{cases} \quad (4)$$

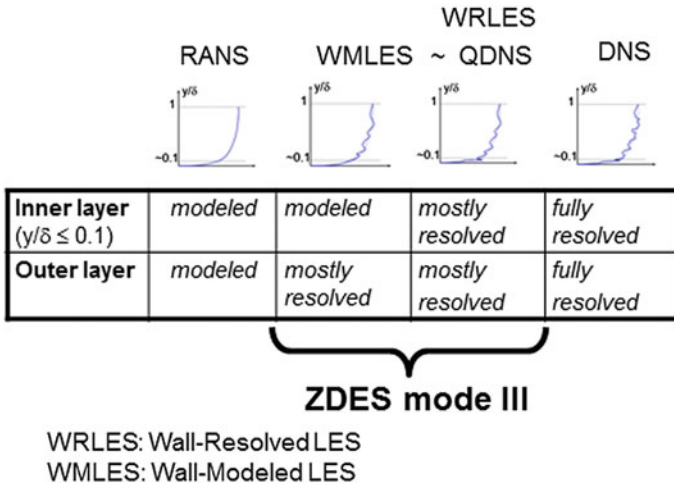


Fig. 13 Main Wall-bounded turbulence simulation strategies

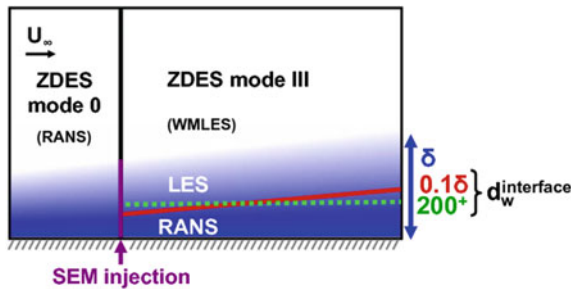


Fig. 14 ZDES simulation set up in the case of the flat plate turbulent boundary layer



with  $C_{DES} = 0.65$  and  $\Delta$  is the subgrid length scale entering the model and is defined by  $\Delta = (\Delta x \Delta y \Delta z)^{1/3}$ .

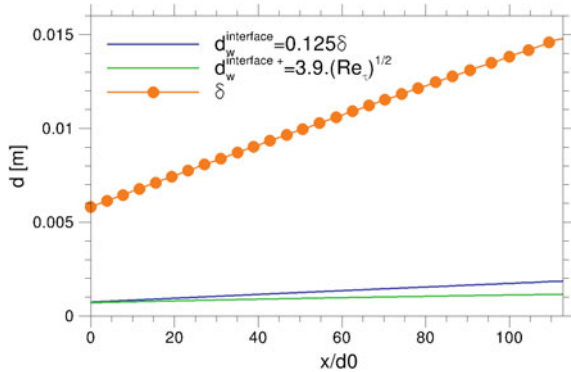
## 4.2 Location of the Interface

According to Eq. (4), the switching into LES mode occurs at a given altitude  $d_w^{interface}$  prescribed by the user as sketched in Fig. 14. In the frame of the project, the effect of a prescribed RANS/LES interface by forcing the treatment of the inner layer of the boundary layer in URANS mode has been investigated. Two interface positions are considered:

- $d_w^{interface} = 0.12\delta$  which is slightly higher than the one used in Deck et al. (2014b) (namely  $0.1\delta$ )
- $d_w^{interface+} = 3.9 \cdot (Re_\tau)^{1/2}$  which has been recently proposed by Renard and Deck (2015)

The first one has a constant outer-scaled height, i.e. it evolves proportionally to the local boundary layer thickness. The second interface corresponds to the geometric center of the logarithmic layer in a zero-pressure gradient turbulent boundary layer. The expected advantage of this interface is that it remains at the same location with respect to the physical phenomena driving the boundary dynamics when the Reynolds number increases. The interface positions are shown in Fig. 15. One can notice that the second interface (green line) penetrates more deeply into the boundary layer.

**Fig. 15** RANS/LES interface positioning within ZDES mode 3



### 4.3 Turbulence Generation Method Adapted to ZDES (Mode 3)

As soon as part of the boundary layer is resolved in LES mode, a turbulent content has to be injected at the inlet of the domain in order to match the low-order statistics given for example by a RANS calculation as well as to prevent turbulence decay, which may lead to re-laminarization.

An adaptation of the synthetic eddy method by Jarrin et al. (2006), proposed by Pamiès et al (2009) and extended to ZDES by Deck et al. is adopted for this purpose.

The basis is to generate a velocity signal with prescribed first and second order moments as follows

$$u_i(x, y, z, t) = U_i(y) + \sum_j A_{ij} \sum_{p=1}^P \tilde{v}_{jp} \quad i, j = 1, 2, 3 \quad (5)$$

The instantaneous velocity component  $u_i$  is built with a time average part  $U_i(y)$  and a random sequence  $\tilde{v}_{jp}$  defined as the superposition of turbulent structures with prescribed time and length scales and geometrical shape (i.e. vorticity content) which are randomly positioned in the inlet plane.  $A_{ij}$  denotes the Cholesky decomposition of the Reynolds stress tensor. The method M2 of Larauie and Deck 2013 (based on Wilcox’s hypothesis) has been retained to generate the inlet profiles from a RANS calculation using the SA model.

As wall-bounded flows are populated with eddies, which sizes depend on their distance to the wall, an adaptation of the Synthetic Eddy method to such flows has been proposed by Pamiès et al. (2009), which consists in taking into account the various coherent structures which populate turbulent boundary layers. Thus, one is able to specify the shape, the time scale as well as the length scale of the injected structures according to their altitude. In practice, it consists in the specification of  $P$  modes (typically  $P \leq 4$ ), each of which are scaled depending on their wall distance. The time ( $l_p^t$ ) scale as well as wall-normal and transverse length scales ( $l_p^y, l_p^z$ ) are assigned to each structure depending on their wall distance. In other words, one is able to specify the shape, the time scale as well as the length scale of the injected structures according to their altitude.

The synthetic velocity field is defined as follows:

$$\tilde{v}_{jp} = \frac{1}{N(p)} \sum_{k=1}^{N(p)} \varepsilon_k \underbrace{\Theta_{jp} \left( \frac{t - t_k - l_p^t}{l_p^t} \right) \Phi_{jp} \left( \frac{y - y_k}{l_p^y} \right) \Psi_{jp} \left( \frac{z - z_k}{l_p^z} \right)}_{g_{jp}(\bar{t}, \bar{y}, \bar{z})} \quad (6)$$

$\varepsilon_k = \pm 1$ . The number of structures per mode is given by  $N(p) = \frac{S_p}{S_S}$  where  $S_p$  is the area of the region in which mode  $p$  is defined and  $S_S$  is the cross-section of the vortex associated to mode  $p$ .

The random time of appearance  $t_k$  of each vortex as well as the coordinates  $y_k$  and  $z_k$  of the vortex are randomly chosen within the domain  $\left[t, t + l_p^t\right] \times \left[y_p^{low}, y_p^{up}\right] \times [-Lz/2, Lz/2]$  where  $Lz$  is the spanwise size of the domain. With these definitions, the surface of the transverse plane may be computed as  $S_p = Lz(y_p^{up} - y_p^{low})$  while the transverse surface of the support of the shape function is  $S_S = 4l_p^y l_p^z$ .  $\Theta_{jp}$ ,  $\Phi_{jp}$  and  $\Psi_{jp}$  denote respectively the shape functions of mode  $p$  in time and in the wall-normal and wall-transverse directions. Besides, Taylor's frozen hypothesis is used to define the time scale  $l_p^t = l_p^x / c_p$  where  $l_p^x$  is the stream-wise length scale of the structure and  $c_p$  its convection velocity.

All these parameters must be tuned to mimic physical coherent structures. The novelty of this modified SEM is that physical information concerning the coherent vortical structures are extracted from the literature and used in the definition of the modes. An example of set of kinematic and associated geometric parameters used within ZDES mode 3 is gathered respectively in Tables 1 and 2. This set of parameters needs a degree of adjustment in the frame of WMLES grids. Note also that one of the interesting aspects of this method is that a same eddy (like hairpin) can populate several regions of the boundary layer as observed in experiments.

**Table 1.** Locus of the center, sizes and convection velocity of turbulent structures associated with the 4 modes, expressed in wall units.  $\delta_0^+$  and  $U_\infty$  denote respectively the boundary layer thickness and the external velocity at the inlet

Mode	$(y_p^{low})^+$	$(y_p^{up})^+$	$(l_p^y)^+$	$(l_p^x)^+$	$(l_p^z)^+$	$c_p^+$
$p = 1$	20	40	20	100	30	15
$p = 2$	40	$0.188\delta_0^+$	40	80	40	18
	$(y_p^{low})$	$(y_p^{up})$	$(l_p^y)$	$(l_p^x)$	$(l_p^z)$	$c_p$
$p = 3$	$0.188\delta_0^+$	$0.72\delta_0^+$	$0.125\delta_0^+$	$0.125\delta_0^+$	$0.125\delta_0^+$	$0.76U_\infty$
$p = 4$	$0.4\delta_0^+$	$1.7\delta_0^+$	$0.227\delta_0^+$	$0.227\delta_0^+$	$0.227\delta_0^+$	$0.76U_\infty$

**Table 2.** Analytical expression of the shape functions ( $g_{jp}$   $j = 1, 2, 3$ ), see Eq. (6)

	$g_{1p}$	$g_{2p}$	$g_{3p}$
$p = 1, 2$	$G(\tilde{t})G(\tilde{y})H(\tilde{z})$	$-G(\tilde{t})G(\tilde{y})H(\tilde{z})$	$G(\tilde{t})G(\tilde{y})H(\tilde{z})$
$p = 3, 4$	$\varepsilon_1 * G(\tilde{t})G(\tilde{y})G(\tilde{z})$	$\varepsilon_2 * G(\tilde{t})G(\tilde{y})G(\tilde{z})$	$\varepsilon_3 * G(\tilde{t})G(\tilde{y})G(\tilde{z})$

Here  $H$  is defined by  $H(\xi) = \frac{1 - \cos(2\pi\xi)}{2\pi\xi\sqrt{C}}$  and  $C = 0.214$  is a normalization factor.  $G$  is the Gaussian function  $G(\xi) = A(\sigma)e^{-\frac{\xi^2}{2\sigma^2}}$ , where  $A(\sigma) = \frac{1}{\sqrt{\sigma\frac{\sqrt{\pi}}{2}\text{erf}(\frac{1}{\sigma})}}$ ,  $\sigma = \frac{1}{3}$  being the reference scale parameter.

The extension of this method to ZDES (mode 3), where an unsteady eddy viscosity has to be specified, has been proposed by Deck et al (2011). The eddy viscosity field is reconstructed from the synthesized velocity field as follows:

$$v_t(t) = \begin{cases} l^2 D^2 \langle S \rangle & \text{if } d_w < C_{DES} \Delta \\ (C_S \Delta)^2 & \text{if } d_w \geq C_{DES} \Delta \end{cases} \quad (7)$$

where  $C_S = 0.1$  is the Smagorinsky constant and  $S(t)$  (respectively  $\langle S \rangle$ ) the magnitude of the instantaneous vorticity built from the synthetic velocity field given by Eq. (6), respectively the vorticity calculated from the mean inflow velocity profile,  $l$  is the mixing length valid over the entire boundary layer which was proposed by Michel et al. 1969:

$$l = 0.085\delta \cdot \tan h\left(\frac{\kappa}{0.085} \cdot \frac{d_w}{\delta}\right) \quad \kappa = 0.41, \quad (8)$$

$D$  is the Van Driest Damping function given by  $D = 1 - \exp\left(-\frac{d_w^+}{26}\right)$ .

The pseudo eddy viscosity field  $\tilde{\nu}$  can be computed explicitly from the turbulent one  $\nu_t$ . This comes from the Spalart-Allmaras turbulence model which allows to get the following fourth order polynomial equation in  $\rho\tilde{\nu}$ :

$$(\rho\tilde{\nu})^4 - \mu_t(\rho\tilde{\nu})^3 - \mu\mu_t c_{v1}^3 = 0 \quad c_{v1} = 7.1 \quad (9)$$

An analytic solution of this fourth-order polynomial equation is detailed in Deck et al. (2011). As an example, Fig. 16 presents the contours of the streamwise component of the velocity and pseudo-eddy viscosity generated at the inlet of a ZDES mode 3 computation as described in the previous sections.

To further limit the adaptation distance, the Dynamic Forcing Method (DF) proposed by Laraufie et al. (2011) can be used together with the ZDES and SEM formulations. The DF method is based on the introduction of source terms in the wall-normal velocity momentum equation to trigger the production of resolved turbulent kinetic energy. An example of turbulent content generated with the ZDES mode 3 methods for the two interfaces investigated within the project are given in Fig. 17.

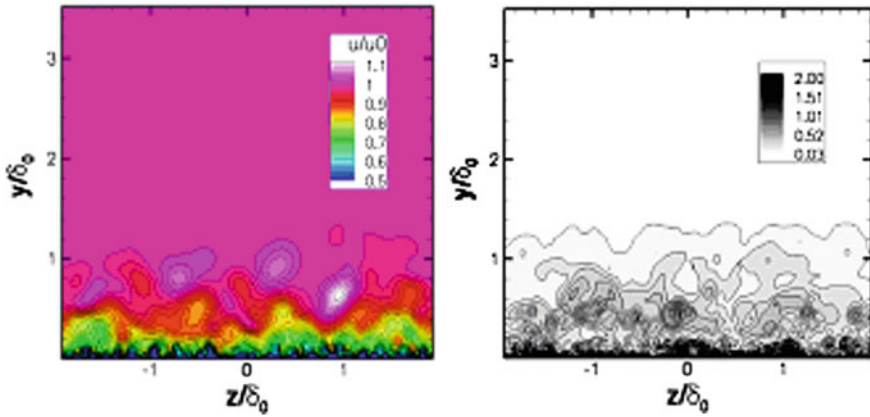


**Fig. 16** Instantaneous streamwise velocity (*left*) and instantaneous pseudo-eddy viscosity field  $\tilde{\nu}/\nu$  (*right*) in the inlet in the framework of ZDES mode 3

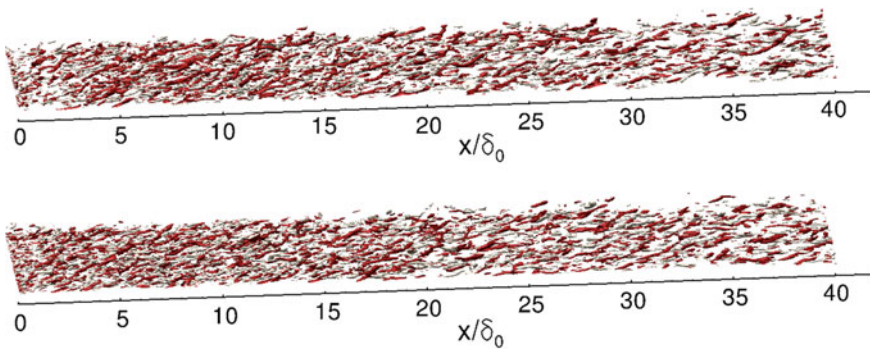


**Fig. 17** Turbulent structures educed by the Q criterion (iso surface  $Q^*(\delta_0/U_0)^2 = 0.3$ ). *Left* interface at  $d_w^{interface} = 0.12\delta$ ; *Right* interface  $d_w^{interface} = 3.9 \cdot (Re_\tau)^{1/2}$

## 5 Improvements to SEM and DFSEM

### 5.1 Summary

In the framework of the Go4Hybrid project UniMAN have focused on bringing performance improvements to the two variants of synthetic turbulence generation developed previously within the group at The University of Manchester; the original Synthetic Eddy Method (SEM) of Jarrin et al. (2006) and the Divergence Free Synthetic Eddy Method (DFSEM) from Poletto et al. (2013). In recent work, it became apparent to the authors that the original formulations were not strictly valid

for inhomogeneous eddy sizes or distributions due to the manner in which the eddy averaging process was implemented. In practice this is almost always the case, since it is realized wherever a non-uniform variation of turbulence kinetic energy or Reynolds stress tensor is prescribed. It seems unavoidable that the errors introduced by these discrepancies are transmitted downstream of the inlet, effectively polluting the downstream prediction and increasing the development length, the distance over which the flow adjusts from synthetic to ‘real’ turbulence. This has been identified to be particularly problematic where internal flows are examined. In general, these errors translate to loss of accuracy in the reproduction of second order statistics. This is demonstrated in the next section. Subsequently we illustrate ongoing work on the improvement of the DFSEM formulation.

## 5.2 New Formulation of SEM

In this section, we start with a brief overview of the Synthetic Eddy Method, as proposed in Jarrin (2006) before outlining our improvements to the method. In essence, the algorithm consists of defining a fixed number of synthetic eddies of compact support, generated at random within a virtual Cartesian box enclosing the inlet. These eddies contribute towards a preliminary (un-scaled) fluctuating velocity field as follows:

$$u'_j(\mathbf{x}, t) = \sqrt{\frac{V_{eddy}}{V_{eddy}N}} \sum_1^N \varepsilon_j f(\mathbf{x} - \mathbf{x}_{eddy}, \sigma_{eddy}) \quad (10)$$

where  $\varepsilon$  is an integer representing the ‘direction’ or sign of the eddy ( $\varepsilon = \pm 1$ ),  $V_{box}$  and  $V_{eddy}$  are the volumes of the Cartesian box and eddies respectively,  $N$  is the total number of eddies, and  $f$  is a shape function (a weighting based on the distance from the eddy centre). The shape function is chosen to satisfy the normalisation condition

$$\frac{1}{V} \iiint f^2(\mathbf{x}', \sigma) d\mathbf{x}' = 1 \quad (11)$$

The shape function has compact support on  $\mathcal{R}^3$  space, with extents defined by the associated eddy length-scale,  $\sigma$ . A truncated Gaussian function is used in the present study.

The inner product of the preliminary fluctuating field with the Cholesky decomposition of the prescribed Reynolds stress tensor is then assumed to yield a velocity field with the prescribed second order statistics and zero mean. This is then superimposed onto the mean velocity,  $U$ :

$$u_i(\mathbf{x}, t) = u'_j(\mathbf{x}, t)L_{ij} + U_i \quad (12)$$

where  $L$  is the Cholesky decomposition of the prescribed Reynolds stress tensor, given as follows, and  $R_{ij}$  are the Reynolds stresses.

$$L_{ij} = \begin{bmatrix} \sqrt{R_{11}} & 0 & 0 \\ \frac{R_{21}}{L_{11}} & \sqrt{R_{22} - L_{21}^2} & 0 \\ \frac{R_{31}}{L_{11}} & \frac{R_{32} - L_{21}L_{31}}{L_{22}} & \sqrt{R_{33} - L_{31}^2 - L_{32}^2} \end{bmatrix} \quad (13)$$

At each time-step, the position of all eddies is updated by advecting them by the bulk velocity of the inflow. If an eddy leaves the box as a result of this advection step, that eddy is regenerated at a random location on the opposite face to which it left. The size of the box is set such that any eddies generated on a face of the box do not (initially) intersect with any faces of the flow domain inlet. The minimum sized box that satisfies this constraint is selected for efficiency reasons.

### 5.2.1 Limitation to Homogeneous Turbulence

We now proceed to analyze the statistical properties of the synthetic signal generated by the original SEM. In order to yield the correct statistics, it is essential for the preliminary field given by Eq. (10) to have zero mean, unit variance and zero covariance. Since  $\varepsilon$  is positive or negative with equal probability, it can readily be seen that the zero mean condition,  $\langle u'_j \rangle = 0$ , is satisfied automatically. To assess the variance condition, we multiply Eq. (10) by itself, and average, to obtain the following:

$$\langle u_j'^2(\mathbf{x}, t) \rangle = \sqrt{\frac{V_{eddy}}{V_{eddy}N}} \sum_1^N \langle f^2(\mathbf{x} - \mathbf{x}_{eddy}, \sigma_{eddy}) \rangle \quad (14)$$

We note that *under* the assumptions of a statistically homogeneous spatial distribution and uniform eddy size, the ratio of the total volume of all eddies ( $NV_{eddy}$ ) to the volume of the virtual Cartesian box within which the eddies reside ( $V_{box}$ ) can be thought of as the ‘eddy density’ or ‘eddy concentration’—a measure of the statistical coverage level by the eddies. Similarly, since the eddies are convected through the inlet with fixed speed and with a random regeneration location, the time-average of the square of the shape function at a point for a single eddy,  $\langle f^2 \rangle$ , is equivalent to a numerical integration of Eq. (11), weighted by the time-fraction that that particular eddy is active at that point. Since the shape function is normalised such that the integral in Eq. (11) is unity, the summation of these contributions from all the eddies is also a measure of the statistical coverage level, and the terms balance. Therefore, under the stated assumptions (i.e. statistically uniform

distribution, uniform convection velocity, and homogeneous eddy size), Eq. (14). will indeed satisfy the unit variance condition,  $\langle u_j'^2 \rangle = 1$ .

Finally, the covariance condition can trivially be demonstrated to hold by noting that  $\langle \hat{a}_i \hat{a}_j \rangle = 0$  for  $i \neq j$ , and hence the cross-correlations are zero. Where the initial distribution of eddies is random, and all eddies are advected by the same velocity, the spatial distribution of eddies within the box will remain statistically uniform throughout the simulation. However, the inlet conditions are of course often needed perpendicular to a physical boundary, and should therefore be applied with an inhomogeneous eddy size. Indeed, for best results this is generally the recommended practice, as it improves the correlation statistics; both two-point and auto-correlations. The price to pay is in the form of errors introduced in the reproduction of the second order statistics, due to this violation of the assumption of homogeneous turbulence.

### 5.2.2 Improved Normalization for the SEM

Here, we propose an alternative, general normalisation factor, which can be found by taking the running average of the eddy concentration:

$$u_j'(\mathbf{x}, t) = \frac{\sum_1^N \varepsilon_j f^2(\mathbf{x} - \mathbf{x}_{eddy}, \sigma_{eddy})}{\sqrt{\langle \sum_1^N f^2(\mathbf{x} - \mathbf{x}_{eddy}, \sigma_{eddy}) \rangle^{AVG}}} \quad (15)$$

The operator  $\langle \cdot \rangle^{AVG}$  is a form of averaging. An exponential weighted average (EWA) has been used here since any initial transient is quickly eliminated. The EWA is defined as

$$\langle \phi \rangle^{AVG}(t) = \int_{-\infty}^t \left( \frac{1}{T} \phi(t') e^{-(t-t')/T} dt' \right) \quad (16)$$

which is a solution of

$$\frac{d\langle \phi \rangle^{AVG}}{dt} = \frac{1}{T} (\phi - \langle \phi \rangle^{AVG}) \quad (17)$$

where  $T$  is the averaging scale. Using a first order explicit Euler method to discretise Eq. (17), we obtain

$$\langle \phi \rangle^{AVG}(t^{n+1}) = \alpha \phi(t^n) + (1 - \alpha) \langle \phi \rangle^{AVG}(t^n) \quad (18)$$



where  $\alpha = \Delta t/T$ . In the present study,  $T$  is taken as one eddy turnover time for the largest eddy, for reasons to be explained below. The advantage of this formulation over the original SEM is that the desired statistical properties,  $\langle u_j' \rangle = 0$  and  $\langle u_j'^2 \rangle = 1$  are obtained independent of the eddy spatial distribution and length-scale. This can easily be seen by multiplying Eq. (15) by itself, and averaging, giving

$$\langle u_j'^2(\mathbf{x}, t) \rangle = \frac{\langle \sum_1^N f^2(\mathbf{x} - \mathbf{x}_{eddy}, \sigma_{eddy}) \rangle}{\langle \sum_1^N f^2(\mathbf{x} - \mathbf{x}_{eddy}, \sigma_{eddy}) \rangle^{AVG}} \quad (19)$$

which satisfies the unit variance condition precisely, provided the exponential weighted average is consistent with the averaging used to gather the statistics (e.g. a simple time average). For statistically steady inflow, this is the case provided  $T$  is large enough.

In determining a suitable timescale  $T$ , on one hand, we require  $T$  to be sufficiently large as to minimise spurious variance in the averaging operator (i.e. the EWA should return a steady value for statistically steady flows), while on the other hand, we wish for  $T$  to be small so as to minimise the duration of the initial transient. Values of  $T$  greater than one eddy turnover times (for the largest synthetic eddy) were found to suitably satisfy the former constraint, and hence the minimum suitable value of one eddy turnover time was used herein. For statistically unsteady flows, where there is a scale separation between the large-scale unsteadiness and the turbulence time-scale, a suitable value of  $T$  would be expected to be of the same order as the large-scale unsteadiness, although such an extension is left as future work.

### 5.3 Results for Improved SEM

It has been demonstrated in the previous section that the original SEM does not, in general, completely satisfy the unit variance condition on the preliminary velocity field, Eq. (9). For the purposes of demonstration, we define a simple test in which both the original SEM and the new SEM are used to generate the preliminary fields given by Eqs. (10) and (15), respectively. A rectangular planar inlet is defined of height  $H$ . The length-scale is set to  $\sigma = 0.06H$  for  $y < 0.5H$  and  $\sigma = 0.12H$  otherwise (see Fig. 18). We plot the variation of the value  $\langle u_j'^2 \rangle$  obtained from the two methods across the inlet as Fig. 19. From the figure it is apparent that in this case, there is a discrepancy of around 15% in the variance condition for the original SEM around the location where the length-scale prescription is changed. This would, of course, be translated into an error in the reproduced Reynolds stresses, were they to

**Fig. 18** Sketch of 'two-scale' test. Large eddies are used on the *upper half*, smaller eddies in the *lower half* (ratio of lengthscales is 1:2)

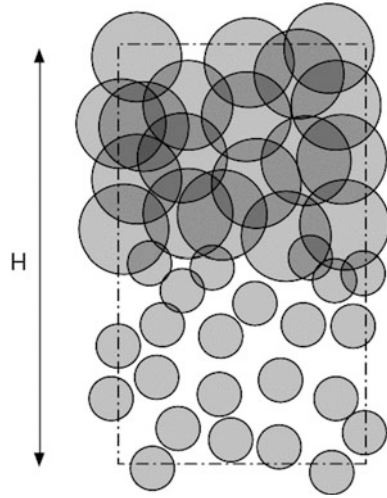
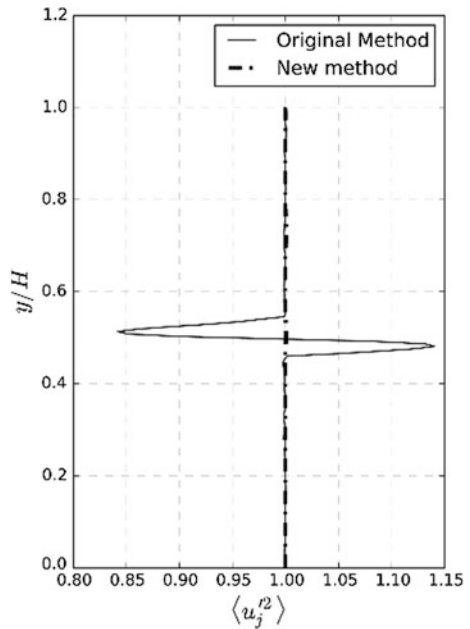
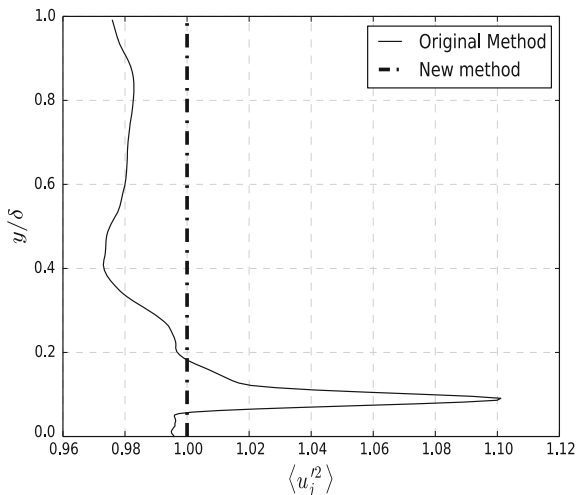


**Fig. 19** Plot of  $\langle u_j'^2 \rangle$  for the isolated inlet test



be computed. To understand better the origin of the discrepancy, consider first a point at the maxima in  $\langle u_j'^2 \rangle$  from Fig. 19. In this region, the length-scale is small, and the point is completely surrounded by small eddies. The correct statistics would therefore be obtained by considering the contributions from these small eddies only. However, there are also contributions from some larger eddies from

**Fig. 20** Channel Inlet. Plot of the preliminary stress using length scales obtained from RANS of channel flow at  $Re_\tau = 590$



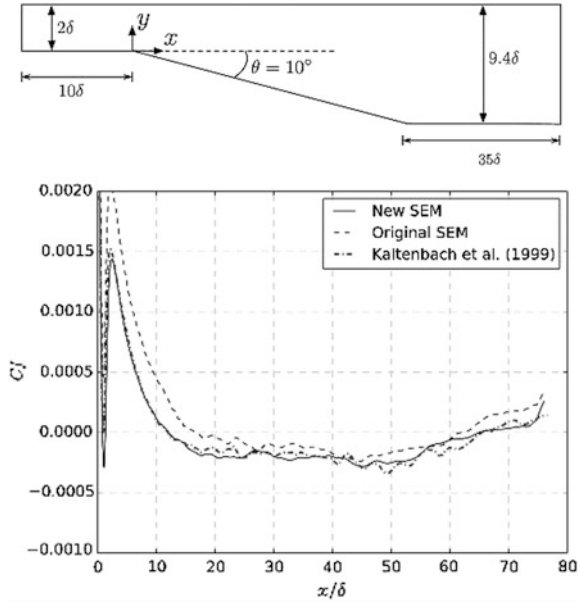
above, which overlap the region, and hence the stress is over-predicted. At the minima in  $\langle u_j'^2 \rangle$ , the opposite effect is happening. Since the support domain of the smaller near-wall eddies is insufficient to reach this region, the statistics are driven primarily by a one-sided subset of the eddies—hence the under-prediction.

### Application to a turbulent channel and a two-dimensional asymmetric diffuser

We first demonstrate the impact of the normalization on the inlet profile for a turbulent channel at  $Re_\tau = 590$ . Figure 20 shows the resulting profile of the preliminary stress  $\langle u_j'^2 \rangle$ , obtained from the averaged instantaneous velocity when using RANS results as input data. It can be seen that the discrepancy in the unit variance condition using the original SEM is significant (up to 10%) for this case where realistic length-scales have been employed following recommended practice, while the new method matches the desired unit variance condition precisely.

We now proceed to apply the above SEM formulation to predict the flow through a planar asymmetric diffuser, for which the inlet condition has been applied at the location  $x/\delta = -10$ , where  $2\delta$  is the inlet channel height, and the coordinate system's origin is located at the upstream corner (see Fig. 21). This geometry has been used in previous experimental and computational studies, and is a well-documented test case. The inclined surface is set at  $10^\circ$  so that the flow separation occurs along this section itself, rather than at the upstream corner; as such, the case is particularly challenging for synthetic inflow methods. Shortly following the pressure induced separation on the sloped wall, there is a reattachment in the tail section. In a detailed LES study of the same case, a strong sensitivity of the flow field to the inlet conditions was reported. If a flow is to be correctly simulated the flow must recover quickly downstream of the inlet. Any inaccuracies to the incoming turbulence levels (for example, due to the inlet section

**Fig. 21** (top)  
Two-dimensional diffuser  
case (bottom) Wall shear  
stress for inclined wall



being shorter than the development length), would act to alter the turbulent momentum transfer in the separating boundary layer, as well as the fluid entrainment into the shear layer; both effects would change the size, shape and position of the recirculation zone, which would be likely to have a dramatic global effect on the flow.

We have computed this case with both the new SEM, and the original SEM. In both cases, the same mesh density as that employed by Kaltenbach et al. (1999) was used (their finest mesh). The flow evolves according to the filtered Navier-Stokes equations, with discretisation schemes and turbulence closure the same as that reported in the previous section. The Reynolds number,  $Re_b = U_b H / 2\nu = 9000$ , and the computational domain extended  $8\delta$  in the span-wise direction, where periodic boundary conditions were employed. The size of the mean separation region can be ascertained precisely from plots of the skin-friction coefficient, reported in Fig. 21. It is seen that the prediction of the new SEM is significantly closer to the reference than that of the original, and corroborates our expectation that while mean flow quantities at the inlet may appear to be similar, small errors introduced at this location can play a major role in downstream flow development.

### 5.4 Improvements to the DFSEM

In the Divergence-free synthetic eddy method (DFSEM), virtual eddies are created and convected through a virtual Cartesian box in a similar fashion as for the SEM.

Herein we start by reviewing the original method, and in the following we adopt standard tensor notation, noting that implied summation is not performed over repeated sub-indices within parenthesis. In the DFSEM, a fluctuating velocity field can be found by working with the vorticity field before converting the result back to velocity fluctuations. The interested reader is referred to Poletto et al. (2013) for details. Here we simply state the result:

$$u_i(x) = C_1 \sum_{k=1}^N q_{(i)}(x, x^k, \sigma_{(i)}^k) \varepsilon_{(i)lm} r_l^k \alpha_m^k \quad (20)$$

In Eq. (20)  $C_1$  is a normalisation constant, necessary to account for the “density” of eddies (to be defined presently);  $\varepsilon$  is the Levi-Civita symbol;  $\sigma_k$  and  $\alpha_k$  are the length-scale and intensity of the  $k$ -th eddy, respectively; and  $q$  is a “shape function” (a weighting based on the distance from the eddy centre), defined as:

$$q_i = \begin{cases} \sigma_{(i)} [1 - r_j^k r_j^k] & \text{if } r_j^k r_j^k < 1 \\ 0 & \text{otherwise} \end{cases} \quad (21)$$

where  $r_j$  is the normalised distance from the eddy centre, given by:

$$r_j \equiv (x_{(j)} - x_{(j)}^k) / \sigma_{(j)}^k \quad (22)$$

For convenience, we work in the principle coordinate system, where the Reynolds stress tensor is diagonal. The fluctuations generated in the principle coordinate system are then transformed back to the local system. The intensity,  $\alpha$ , is set such that the prescribed first and second order statistics will be realized, and is given by:

$$\alpha_{(i)}^2 = \gamma \frac{\lambda_j / \sigma_j^2 - 2\lambda_{(i)} / \sigma_{(i)}^2}{2C_2} \quad (23)$$

where  $\lambda$  are the eigenvalues of the target Reynolds stress tensor (equal to the normal stresses in the principle coordinate system),  $\gamma$  is a random integer equal to 1 or  $-1$  with equal probability, and  $C_2$  is an additional normalisation constant.

The eddy length-scale is initially set to

$$\max\{k^{3/2} / \varepsilon, \Delta x, \Delta y, \Delta z\} \quad (24)$$

where  $k$  and  $\varepsilon$  are the turbulent kinetic energy and dissipation rate respectively, and  $\Delta$  is the mesh size. It can be seen from Eq. (23) that the eddy length scale is linked to the intensity. Since we require a real value for the eddy intensity, the right hand side of Eq. (23) must be positive. However, the length scale given by Eq. (24) will

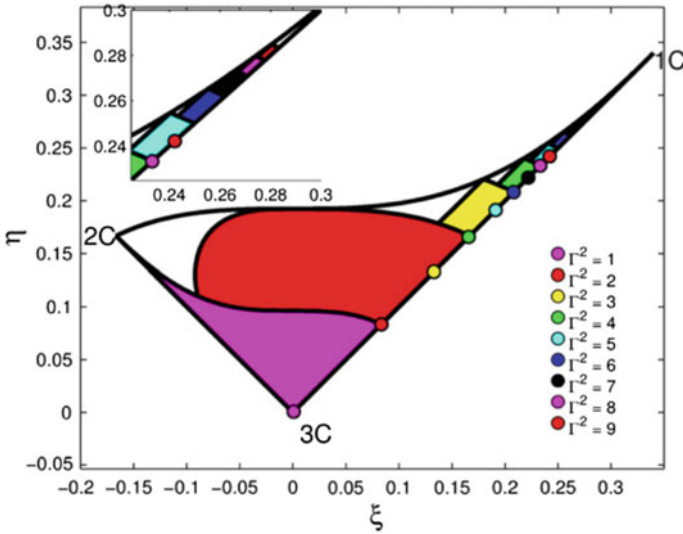


**Fig. 22** Regions of the Lumley triangle mapped with 9 different ratios

not, in general, satisfy this requirement; particularly where there is a disparity between stress components, as is typically the case close to a wall.

As such, the length-scale of an eddy whose intensity has an imaginary component is stretched (in the direction of the largest eigenvalue), while preserving its volume. The stretching ratio is arbitrarily set until a suitable stretching ratio is found such that all components of the intensity vector are real. This gives realisable stress states that cover the majority of the Lumley triangle (Fig. 22). A different set of ratios can be selected to cover more of the triangle if desired, though this was not found to be beneficial for channel flow test cases presented in Poletto et al. (2013).

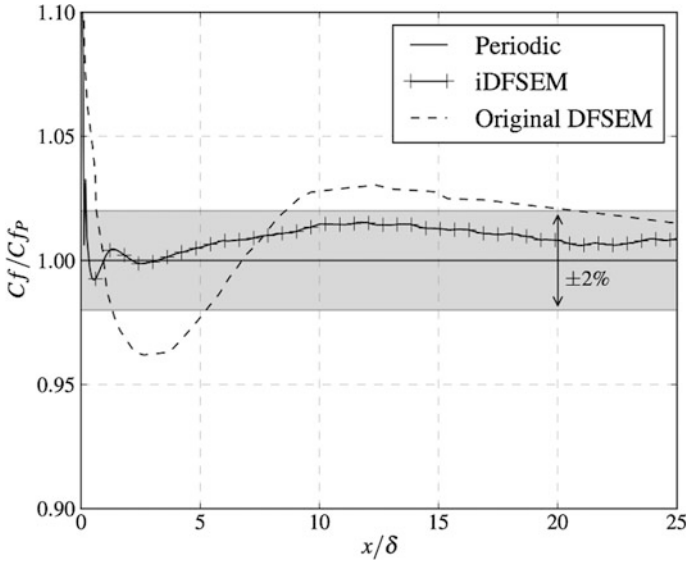
**Removal of the normalization constants**

In the original formulation, the normalization constants  $C_1$  and  $C_2$  involved into the Eqs. (20) and (24), respectively, are defined as follows. The first constant  $C_1$  is used to account for the “density” of eddies, and is given as follows, where  $V_0$  is the volume of the eddy box. Equation (25) is strictly valid only under the assumptions of a uniform eddy distribution and a constant eddy size.

The second normalisation constant,  $C_2$ , is used to account for the fact the magnitude of integral of the shape function is altered with changing  $\Gamma$  (effectively giving a different eddy intensity for different  $\Gamma$ ;  $C_2$  corrects for this spurious effect). Suitable values of  $C_2$  over a selection of  $\Gamma$  are given by Table 3.

**Table 3.** Values of  $C_2$ 

$\Gamma$	$\sqrt{1}$	$\sqrt{2}$	$\sqrt{3}$	$\sqrt{4}$	$\sqrt{5}$	$\sqrt{6}$	$\sqrt{7}$	$\sqrt{8}$
$C_2$	2.0	1.875	1.737	1.75	0.91	0.825	0.806	1.5

**Fig. 23** Evolution of skin friction coefficient downstream of inlet condition for channel flow simulations; impact of improved normalization

$$C_1 = \frac{\sqrt{10V_0} \sum_{i=1}^3 \sigma_i / 3}{\sqrt{N} \prod_{i=1}^3 \sigma_i} \min \sigma_i \quad (25)$$

In the new formulation, we have been motivated by the need to generalize these values, and as such we redefine the eddy intensity as:

$$\alpha_{(i)}^2 = 4 \frac{\lambda_j}{\langle q_i^2 \rangle} - 2 \frac{\lambda_{(i)}}{\langle q_{(i)}^2 \rangle} \quad (26)$$

where  $\langle q_i^2 \rangle$  is a running average of the shape function, based on the contribution from all eddies at the same  $\Gamma$ . A separate running average is evaluated for each  $\Gamma$  considered (a total of 8 in the present study). In this way, constants  $C_1$  and  $C_2$  are eliminated. We have also redefined the shape function as follows, where the

modification is required in order to render the shape function dimensionless; a necessary feature of the present formulation in order to maintain the correct overall normalisation.

$$q_i = \begin{cases} \frac{\sigma_{(i)}}{\sum_{k=1}^3 \sigma_k/3} [1 - r_j^k r_j^k] & \text{if } r_j^k r_j^k < 1 \\ 0 & \text{otherwise} \end{cases} \quad (27)$$

The performance of the new formulation is demonstrated in Fig. 23, which displays the skin-friction,  $C_f$  development along the channel walls at  $Re_\tau = 590$ . The improvement of the new DFSEM relative to the old is readily apparent and it returns to the periodic solution in a distance of one delta downstream of the inlet. There is a subsequent departure from the periodic solution which suggests that there remains further room for improvement, although this is beyond the scope of the present project.



**Part III**  
**Results for Fundamental Test Cases**

# Free Shear Layer

Shia-Hui Peng

## 1 Introduction

Mixing layer is an important and fundamental building block in engineering flows. A mixing layer usually originates from a wall-bounded flow that is detached from the wall surface and evolves in the form of a free shear layer, which is in many cases associated to flow separation. Typical free shear layers can be observed, for example, in flows over a backward step, detached from a bluff body and in jets. The overall accuracy in numerical simulation of a complex flow system may significantly be affected by the prediction of local mixing-layer flow properties nestled in the system. In the Go4Hybrid project, a turbulent spatial mixing-layer flow was selected as a fundamental test case (TC F2) to serve the primary objective targeting the development of methods to mitigate the so-called “grey area” problem for non-zonal hybrid RANS-LES methods.

It is known that the development of an initially laminar (with no inlet turbulent content) spatial shear layer is characterized by intrinsic vortex rolling structures (quasi-2D related to Kelvin–Helmholtz instabilities), accompanied with increasing 3D vortex pairing phenomena when developing further downstream and eventually leading to a fully turbulent shear layer. In Go4Hybrid, the plane incompressible mixing layer is formed from the confluence of two turbulent boundary layers emanating from the trailing edge of a thin flat plate. In non-zonal hybrid RANS-LES modelling, the upcoming boundary layers are usually treated with the RANS mode, whereas the free shear layer, forming immediately after the trailing edge of the thin flat plate, is handled with the LES mode while receiving no resolved turbulent contents from upstream RANS modelling. The initial shear layer immediately emanating from the wall layers is thus a typical grey area in hybrid RANS-LES computations.

---

S.-H. Peng (✉)

FOI (Swedish Defence Research Agency), Stockholm, Sweden  
e-mail: peng@foi.se

In relation to the grey-area problem, the resolved initial shear-layer instabilities are often delayed and, consequently, the re-establishment of the fully developed shear layer is unphysically delayed compared to experimental observation. The focus in the computation of this test case is on the verification of the predictive capabilities of hybrid RANS-LES modelling incorporated with developed Grey-Area Mitigation (GAM) methods in resolving the initial development of the spatial shear layer.

The plane mixing layer has been taken as a test case with primary purpose to verify non-zonal hybrid RANS-LES methods. In this chapter, the emphasis is thus placed on the computations using non-zonal modelling approaches with contributions from, respectively, CFDB, FOI, NLR, NTS and ONERA. It is noted that this test case may also be well adopted in verification of zonal hybrid RANS-LES modelling approaches provided that a prescribed RANS-LES interface is set across the incoming boundary layers at or before the location where the mixing layer starts to form.

## 2 General Setup of Test Case

The mixing layer was a fundamental test case in the GARTEUR AG49 project (Peng et al. 2014), in which several partners in the Go4Hybrid project were actively involved. The experimental data set was reported in the thesis of Delville (1995), and was further summarized in AGARDograph 345, Test identification SHL04 (1998). The experiment was performed in the E300 open-loop wind tunnel of the C. E.A.T. Poitiers, see Fig. 1. It is composed of the following parts from upstream to downstream: filters to avoid probe contamination, a converging part (contraction ratio is 16) with a square section, the test section ( $0.3 \text{ m} \times 0.3 \text{ m}$  with a length of 1.2 m), the lower and upper walls can be slanted to adjust pressure gradients, a diffuser, an axial fan and a silencer.

A flat plate of 1 m separates the converging part of the wind tunnel into two symmetrical parts. The thickness of this plate is 3 mm. Towards the trailing edge, the plate is tapered symmetrically to a sharp beveled edge with a slope of about 3%

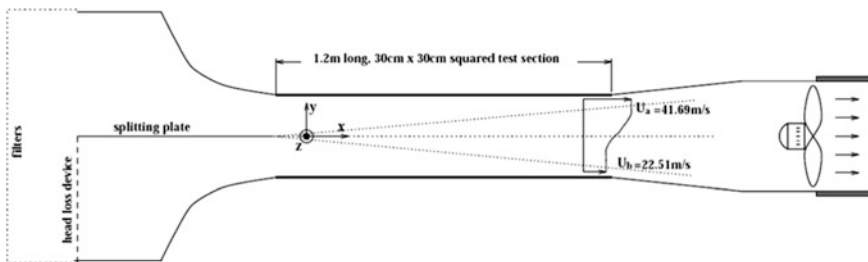


Fig. 1 Schematic of the experimental setup (Delville 1998)

over a length of 50 mm. The experimental data include, at various downstream locations, time-averaged velocities and turbulence statistics.

The mean (freestream) velocity of the high-speed boundary layer (on the upper side of the plate) is  $U_a$  ( $= 41.69$  m/s) and the low-speed velocity (on the lower side of the plate) is  $U_b$  ( $= 22.51$  m/s), giving a velocity ratio of  $U_b/U_a = 0.6$ . The measurement, taken at  $x = -10$  mm upstream from the plate trailing edge where  $x = 0$ , has been used to verify in the prediction the two boundary layers approaching the formation of the mixing layer. The characteristic parameters of the boundary layers are summarized in Table 1.

The mean velocity profiles at  $x = 0.5$  mm have been adopted for the verification to ensure that the formation of the mixing layer has been started with two well-predicted boundary layers. RANS computations of precursor type were conducted to set the location of inflow sections of upper and lower boundary layers as well as the transition locations. Following Deck (2012), the inflow locations have been specified, respectively, at  $xU = -0.82$  m for the upper layer and  $xL = -0.46$  m for the lower layer, as shown in Fig. 2, while the transition locations being set at  $x = -0.708$  m and at  $x = -0.388$  m, respectively. The flow domain has a downstream extension of  $x = 2$  m from the plate trailing edge and a relatively large vertical extension of  $L_y = \pm 1.0$  m (Deck 2012).

A focus region,  $x \in [0, 1]$ , is defined for modelling assessment and appraisal, for which a mandatory 2D structured mesh was provided to all involved partners, as shown in Fig. 2, with a uniform distribution of 640 cells in the  $x$ -direction. Adapting to the modelling method used, partners were permitted to generate their own meshes in reference to this 2D mandatory mesh by imposing the same or very similar resolution in the focusing zone. The size in the spanwise direction is  $L_z = 0.15$  m for the 3D computational domain (cf Fig. 2), over which 96 cells are distributed uniformly, giving the same mesh spacing as in the  $x$ -direction.

It is noted here that, using the same computational domain, partners have made additional computations for preliminary modelling verification and validation. The results included in this chapter have been those made by partners with the mandatory resolution in the focusing region. This has thus ensured that the assessment and verification can be undertaken by means of model-to-model and code-to-code comparisons.

**Table 1** Parameters of the two incoming boundary layers (measured at  $x = -10$  mm)

Measured at $x = -10$ mm	Notation	High-velocity BL	Low-velocity BL
Velocity	$U_a, U_b$	41.54 m/s	22.40 m/s
Thickness (99%)	$\delta$	9.6 mm	6.3 mm
Displacement thickness	$\delta_\theta$	1.4 mm	1.0 mm
Momentum thickness	$\theta$	1.0 mm	0.73 mm
Shape factor	H	1.35	1.37
Re number based on $\theta$	$Re_\theta$	2900	1200
Turbulence level	$u'/U$	$\sim 0.3\%$	$\sim 0.3\%$

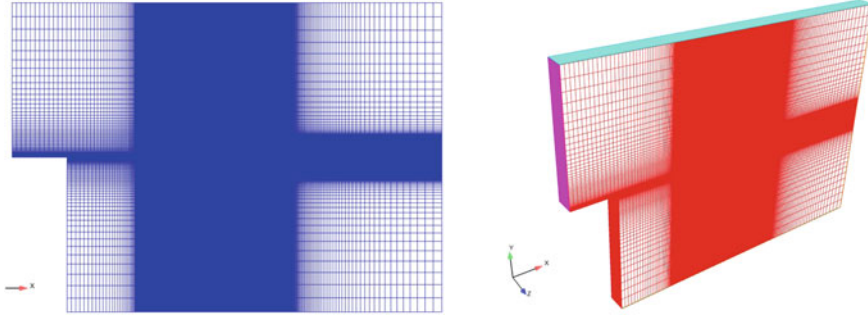


**Fig. 2** Mandatory grid (*left* 2D mesh with a focus region of  $x = 1$  m after the plate trailing edge; *right* 3D schematic) for the mixing-layer case

It is further noted that, in all computations contributed by involved partners, the plate thickness was assumed to be zero, whilst being treated as two flat wall boundaries. With the mandatory simulation setup, shown in Fig. 2, constant velocity profiles were imposed at the upper and lower inflow sections over the flat plate, with magnitudes equal to the respective experimental freestream velocities. Also, the freestream air temperature of  $20\text{ }^{\circ}\text{C}$  is prescribed. The turbulence intensity at the inflow section is set as given in Table 1. At the outflow boundary, free-stream static pressure is prescribed for compressible solvers. For incompressible solvers, convective outflow boundary condition can be specified. On the upper and lower boundaries, Euler wall or symmetric boundary conditions are applied. In the spanwise direction, periodic boundary conditions are imposed.

### 3 Computational and Modelling Approaches

As mentioned, the mixing-layer test case has been intended primarily for verification of GAM methods supporting non-zonal modelling approaches. All involved partners have used the mandatory setup described in the previous section in terms of the computational domain and the grid resolution in the focus region. The details of the GAM methods used by partners can be found in Part II. A brief statement is given here for the GAM method used by each partner.

CFDB has used the SA-DDES-based formulation (Spalart et al. 2006), in which the LES mode is adapted to take the form of the  $\sigma$  (Nicoud et al. 2011) SGS model. The SA-based  $\sigma$ -DDES is further re-calibrated using a modified constant in the SA-DDES shielding function (see Part II, Non-Zonal Approaches for Grey Area Mitigation, Sect. 2). Additionally, the approach is combined with the  $\tilde{\Delta}_{\omega}$  vorticity-adaptive grid scale proposal of NTS (see Part II, Non-Zonal Approaches for Grey Area Mitigation, Section 6), and further tested by Fuchs et al. (2014) and Fuchs et al. (2015), in relation to the orientation of vorticity vector. CFDB has used

the pressure-based incompressible OpenFOAM solver, which adopts 2nd-order central scheme in space and a 2nd-order implicit Euler scheme in time.

FOI has verified with this test case an improved SGS modelling for non-zonal hybrid RANS-LES methods. The approach is based on an energy-backscatter function incorporated in the LES mode, for the purpose of enhancing the resolved large-scale turbulent contents in the LES region. In conjunction with a conventional SGS eddy-viscosity formulation, the energy-backscatter part is formulated in terms of velocity gradients and functions as a scale similarity model (Peng and Davidson 2002, 2009). The energy-backscatter function was previously examined using an algebraic non-zonal hybrid RANS-LES (HYB0) model (Peng 2006) as the baseline model for fundamental flows (Peng 2012). In the computation, the modelling formulation (HYB0 M) has been further refined and the SGS length scale has been re-examined using an alternative length scale in the baseline HYB0 model by replacing the maximum cell size,  $\Delta_{\max}$ , with  $\Delta_{\min}$ , in combination with the conventional control-volume-based length scale  $(\delta V)^{1/3}$  (see Part II, Non-Zonal Approaches for Grey Area Mitigation, Sect. 3). In the computation, FOI has used their in-house unstructured Edge solver, which is finite volume based using the 2nd-order central scheme in space and a 2nd-order implicit Euler backward scheme in time.

NLR has used the X-LES method as baseline model (Kok et al. 2004, 2009). To improve the turbulence-resolving capability in predicting free shear layers, two modifications have been added to the X-LES method (see Part II, Non-Zonal Approaches for Grey Area Mitigation, Sect. 5). The first modification consists of a stochastic backscatter model (Kok 2016), in which a spatially and temporally correlated random stress tensor is added to the subgrid stress tensor, modelling backscatter from the subgrid to the resolved scales at the theoretically correct rate. The second modification consists of a high-pass filtered (HPF) SGS model (Kok et al. 2012). In order to avoid high subgrid stresses in the initial shear layer, the subgrid stresses are computed from the velocity fluctuations  $u'$  instead of the instantaneous velocity, which are obtained by applying a temporal high-pass filter to the velocity field. NLR has used its in-house structured ENSOLV solver, adopting a 4th-order low-dispersion skew-symmetric finite-volume method (Kok 2009) combined with the 2nd-order midpoint-rule scheme in time.

NTS has used SST-based DDES (Travin et al. 2002) as the baseline model in combination with a new subgrid length scale in their GAM method (see Part II, Non-Zonal Approaches for Grey Area Mitigation, Section 6). The new, Shear-Layer-Adapted, LES length scale,  $\Delta_{SLA}$ , aims at a rapid destabilisation of the separated shear layers and acceleration of RANS-to-LES transition within non-zonal RANS-LES hybrid methods (Shur et al. 2015). This length scale has employed a vorticity-based length scale similar to that proposed by Chauvet et al. (2007), but being redefined so that the LES length scale  $\tilde{\Delta}_\omega$  reduces to the order of  $\max(\Delta_x, \Delta_y)$  in regions where the flow is essentially 2D with the vorticity axis aligned with the coarse  $z$  direction. The NTS definition may further improve the scale-resolving capability over the original proposal (Chauvet et al. 2007 and Deck

2012) when the shear layer is skewed so that the vortex cores are not aligned with the  $z$  direction. Other than that, the length scale  $\Delta_{SLA}$  includes an empirical function of specially designed kinematic criterion VTM (Vortex Tilting Measure) for automatic identification of the quasi-2D flow regions, which further facilitates transition to developed fully 3D turbulence. NTS uses the incompressible branch of their in-house code, which invokes 4th order central scheme for inviscid fluxes and 2nd order central scheme for viscous fluxes. The temporal advancement employs an implicit three-layer 2nd-order scheme. It is noted that the NTS mesh has a streamwise grid step  $\Delta x$  stretching proportional to mixing-layer thickness.

ONERA has used the SA-based Zonal DES (ZDES) approach by Deck (2005a, b, 2012). The method is based on a problem-dependent zonalisation and makes it possible to use various formulations within the same calculation. In the framework of ZDES, three specific hybrid length scale formulations (see Part II, Non-Zonal Approaches for Grey Area Mitigation, Sect. 4), also called modes, are optimized to be employed upon typical flow field topologies. In non-zonal modelling verification using the mixing-layer test case, mode 2 of ZDES has been employed, which adopts the DDES formulation (Spalart et al. 2006) and thus operates in an “automatic” non-zonal manner. The GAM improvement lies in the vorticity-based subgrid length scale,  $\Delta_{\omega}$ , which takes a generalized form of Chauvet et al. (2007) especially for unstructured grids (Deck 2012; see also Part II, Non-Zonal Approaches for Grey Area Mitigation, Sect. 4). The ONERA structured solver FLU3 M has been used in the computation, which employs the AUSM + (P) scheme in space and an implicit 2nd-order backward scheme in time.

As mentioned above, all involved partners have generated their own mesh with particular attention paid to the focusing zone, where the grid resolution is the same as, or very similar to, the mandatory grid resolution. Different time steps have been used by different partners, however, as summarized in Table 2, where the modelling approaches used by partners are also briefly summarized.

**Table 2** Summary of simulation methods used by partners

Partner	Hybrid model	GAM method	Mesh	$\Delta t$ [sec]
CFDB	SA-DDES	LES-mode adapted to WALE/ $\sigma$ SGS models, $\Delta_{LES}$ re-adapted to a vorticity-based length scale $\Delta_{(\omega)}$	Mandatory 12.7 M	$1.0e^{-5}$
FOI	HYB0	Energy backscatter in LES mode, $\Delta_{LES}$ reformulated in terms of $\Delta_{min}$ and $\delta v$	Mandatory 10.8 M	$2.0e^{-5}$
NLR	X-LES	Stochastic backscatter model and high-pass filtering (HPF) incorporated in LES mode	Mandatory 13.7 M	$1.0e^{-5}$
NTS	SST-DDES	Shear-Layer-Adapted definition of subgrid length scale $\Delta_{SLA}$	Mandatory 16 M	$1.0e^{-6}$
ONERA	ZDES mode 2	ZDES mode2, $\Delta_{LES}$ re-adapted to a vorticity-based length scale $\Delta_{(\omega)}$	Mandatory 16 M	$1.0e^{-6}$

It is noted here that the note “mandatory” in Table 2 for the mesh refers to the mandatory grid resolution in the focusing region, whereas the difference in the total number of nodes has been due to the grid arrangement in other regions of the computational domain. Note that also different time steps have been used, where the largest time step (by FOI) is 20 times large than the smallest (by NTS and ONERA).

## 4 Results and Discussion

The initial part of the mixing layer, emanating from two RANS-modelled boundary layers after detaching from the trailing edge of the flat plate, is a typical “grey area”. Without GAM treatment, conventional hybrid RANS-LES methods may often render delayed shear-layer instabilities in the initial stage with significantly under-resolved turbulent content by the LES mode. The assessment of GAM methods has thus been conducted by means of comparative studies of the LES-resolved mixing layer in the initial stage of the focus region over  $x \in [0, 1]$ , including available experimental data in the comparison.

The effectiveness of the GAM method is reflected in the development of the mixing layer thickness. The momentum thickness of the mixing layer,  $\theta_m$ , is defined by

$$\theta_m = \int_{-\infty}^{+\infty} \frac{U - U_b}{U_a - U_b} \left( 1 - \frac{U - U_b}{U_a - U_b} \right) dy \quad (1)$$

where  $U$  is the local mean (time-averaged) velocity in the mixing layer. The vorticity thickness,  $\theta_\omega$ , of the mixing layer takes the following form

$$\theta_\omega = \frac{U_a - U_b}{(\partial U / \partial y)_{y=0}} \quad (2)$$

Moreover, mean velocity profiles and resolved turbulence statistics at two stations,  $x = 200$  and  $800$  mm, respectively, have also been used in the verification in comparison with experimental data wherever available. It is noted that, of all the numerical data contributed by partners, only the most promising results obtained with their respective methods have been included in this summary.

### 4.1 Resolved Instantaneous Flow Structures

The GAM methods have been incorporated respectively in three baseline hybrid RANS-LES models for verification and assessment. In order to highlight the



improvement due to grey-area mitigation over the base models, the turbulent structures resolved in the mixing layer are first visualized in Fig. 3 for the base models, namely, the SST-DDES, the SA-DDES and the HYB0 model using iso-surfaces of the Q-criterion (second invariant of velocity gradients). The failure of the baseline hybrid RANS-LES models is clearly demonstrated in resolving the initial instabilities and turbulent vortex structures of the mixing layer. All the three models have resolved only 2D rolling structures far downstream from the plate trailing edge. The RANS-modelled boundary layers have fed no resolved turbulent content in the mixing layer that is handled by LES mode, which is consequently unable to allow in the simulation a quick development of a three-dimensional turbulent mixing layer.

Using the above three models as base model, the GAM methods proposed by partners are then verified by illustrating a snapshot of resolved instantaneous turbulent structures in the initial stage of the mixing layer, as given in Fig. 4, where a normalized iso-surface of the Q-criterion,  $Q \cdot (U/L)^2 = 100$ , is illustrated and colored with the magnitude of vorticity. Also shown in the same figure (right-hand side) is the contour of the normalized magnitude of vorticity. The function of different GAM methods has been demonstrated in mitigating the grey area in the initial stage of the mixing layer. In comparison with the resolved turbulent structures with the base models, illustrated in Fig. 3, all GAM methods have shown rather effective GAM capabilities resolving much richer turbulent structures. The formation of the mixing layer starts with two turbulent boundary layers modelled with the RANS mode, relying essentially on the LES mode to resolve the turbulent development of the mixing layer.

The GAM methods incorporated here are all targeting a modified SGS modelling formulation by means of either re-defining the LES length scale and/or introducing other inherent modelling mechanisms. Of all the GAM methods, which have all

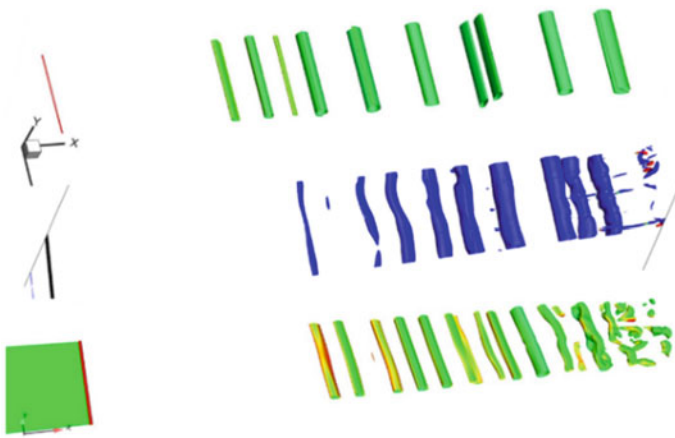


**Fig. 3** Resolved turbulent structures by the baseline hybrid RANS-LES modes for the mixing layer (flow from *left to right*). SST-DDES (*upper*), SA-DDES (*middle*) and HYB0 (*lower*)

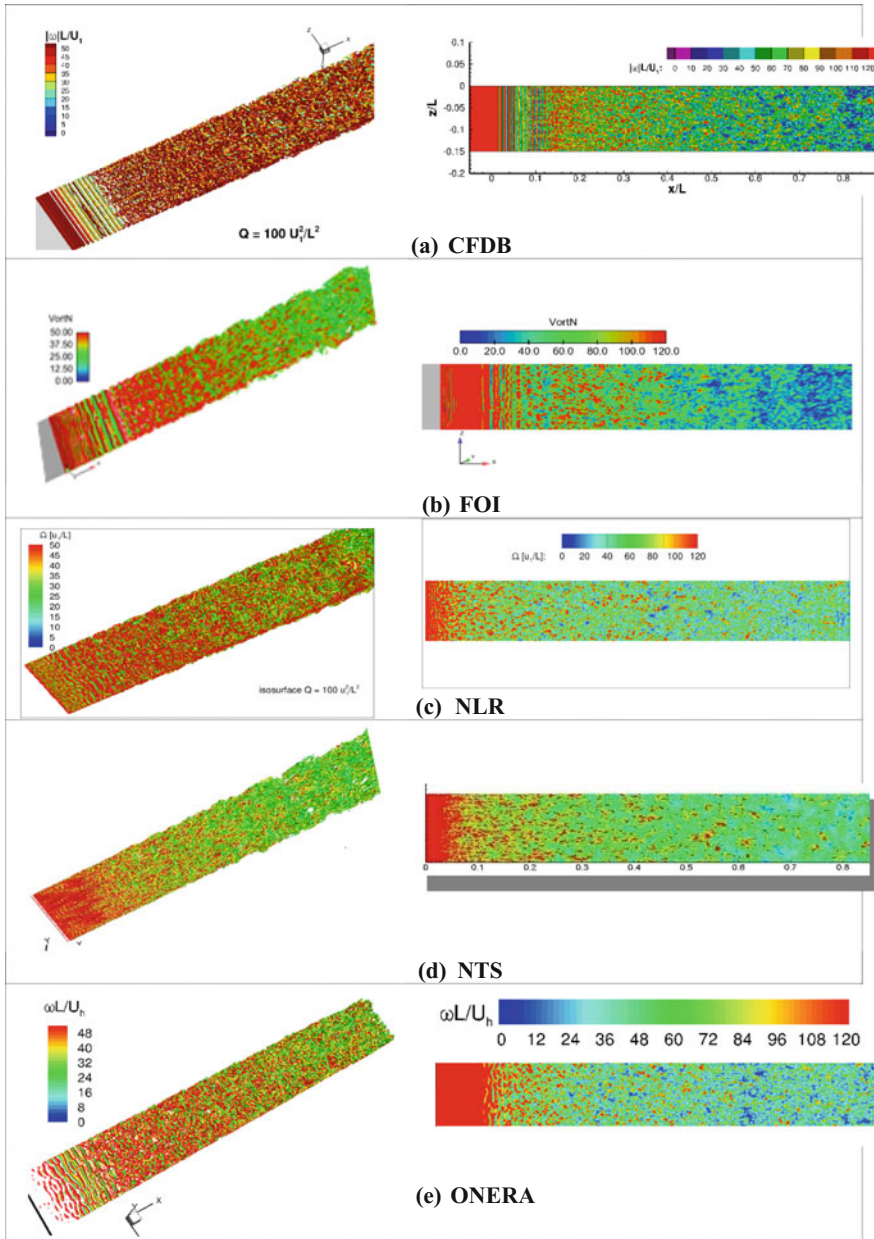


**Fig. 4** Resolved turbulent structures using iso-surfaces of the Q-criterion, with  $Q \cdot (U/L)^2 = 100$  by incorporating the GAM methods proposed by partners

shown promising improvement in capturing the initial shear-layer instabilities, the NLR and NTS methods have shown a particularly quick response to the formation of three-dimensional mixing-layer structures.

## 4.2 Mean Flow and Resolved Turbulent Quantities

A snapshot of resolved instantaneous turbulent structures, shown comparatively in Figs. 3 and 4, has verified illustratively that all the GAM methods, to different degrees, are able to mitigate the grey area and enrich turbulent content in the initial stage of the mixing layer. The methods in this subsection are further examined by plotting mean flow and turbulent quantities in the mixing layer. The statistical analysis of time-averaged flow and turbulent data was performed by averaging the flow variables over a sufficient time period and additionally by a spatial averaging in the homogeneous spanwise direction. The mean flow and turbulent data plotted below are extracted from two stations across the mixing layer at, respectively,  $x = 200$  mm located in the initial grey area and  $800$  mm in the fully-developed region downstream (see Fig. 5).

The computed mean streamwise velocity profile at  $x = 0.5$  mm from the TE is present in Fig. 6 from partners' computations using different methods. Also present in the same figure is the time-averaged turbulent eddy viscosity (normalized by the molecular dynamic viscosity),  $\langle \mu_t \rangle / \mu$ . In comparison with measured boundary-layer velocities, some discrepancies are observed in the outer edge (particularly for the high-speed boundary layer), where the streamwise velocity was over-predicted in all computations. The models by CFDB, NLR, NTS and ONERA have produced relatively large values of  $\langle \mu_t \rangle / \mu$  at  $x = 0.5$  mm. Note that the GAM method adopted in the FOI computation has incorporated an additional term for instantaneous energy backscatter, which plays *statistically* a role in energy dissipation and has supported in part the rather small value of  $\langle \mu_t \rangle / \mu$  present in the Smagorinsky term. It is further noted that the base model, HYB0, in the FOI computation has been adapted to a reduced LES length scale (see Part II, Non-Zonal Approaches for Grey Area Mitigation, Sect. 3). This has made a large

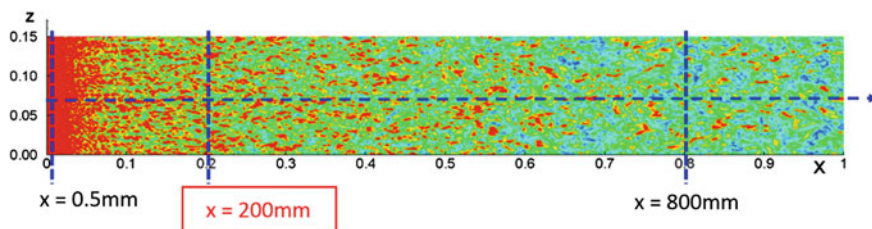


**Fig. 5** Locations where data extracted for time-averaged flow and turbulent quantities in a comparative plotting

part of the wall layer covered in the band of RANS-LES transition and in part by the LES mode, due also partly to the grid stretching in the streamwise direction, when the two boundary layers are approaching to the plate TE. Consequently, the modelled eddy viscosity is rendered with small values even in the incoming boundary layers (with values of  $\langle \mu_t \rangle / \mu$ ) in the order of 10 or smaller). In spite of the additional velocity-gradient term for instantaneous reverse energy transfer in the SGS model, the intervention of the LES mode to the approaching wall boundary layers may have caused “modelled-stress depletion” similar to the DES model with its LES mode penetrating in the wall layer. This has led to the near-wall discrepancy observed in the FOI mean velocity profile at  $x = 0.5$  mm (illustrated in Fig. 6). As shown below, nonetheless, this undesirable behavior in the upstream boundary layers does not support resolving any relevant near-wall turbulent contents towards the formation of the mixing layer after the plate TE.

In Fig. 7, the profiles of resolved turbulent stresses are plotted at  $x = 0.5$  mm, which is located within the first grid cell after the trailing edge (streamwise mesh width equals 1.56 mm). Note that only the normal stress  $\langle u'u' \rangle$  was measured and thus the experimental data were used for a comparison in Fig. 7a. None of the GAM methods adopted by partners have proven capable of resolving turbulent stresses comparable with the measured values at this location. The CFDB result presents the highest level of resolved stresses, however only in peaks at the centre line (at  $y = 0$ ), while the flow field is locally two-dimensional, since  $\langle w'w' \rangle = 0$ . The only method capable of producing three-dimensional turbulent flow properties here is that of NLR, evidenced by the relatively intensive spanwise fluctuations, which is a result of the correlated stochastic backscatter incorporated. These results highlight the inevitable grey area behavior of non-zonal approaches: Despite best efforts to mitigate the grey area, the resulting prediction of the immediate RANS-LES interface region would remain inevitably non-physical, due to the lack of upstream resolved turbulent content. Indeed, this is an inherent weakness in non-zonal hybrid RANS-LES modelling of free shear layers detached from wall

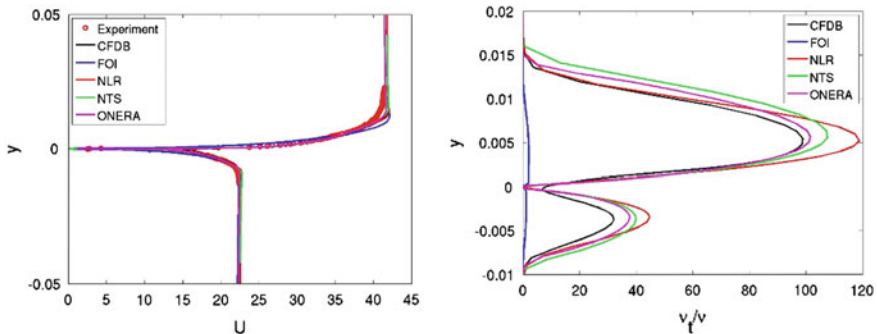


**Fig. 6** Profiles of time-averaged quantities at  $x = 0.5$  mm. Mean streamwise velocity (*left*); Time-averaged turbulent eddy viscosity normalized by molecular dynamic viscosity,  $\langle \mu_t \rangle / \mu$  (*right*)

surface, where the large-scale turbulence is not sufficiently resolved by the LES mode in the immediate RANS-LES interface region as would otherwise be reproduced in a full LES.

The mean streamwise velocity profiles at  $x = 200$  mm and  $800$  mm are then presented in Fig. 8a and c, respectively, in comparison with the measured data. It is noted that the kink, as shown in the computations by CFDB and ONERA in the velocity profile at  $x = 200$  mm (and  $y = 0$ ) is an indication of insufficient turbulent diffusion in the shear layer. The FOI computation, on the other hand, has somewhat over-predicted the velocity in the outer part of the mixing layer on the high-speed side. Note that the GAM approach of NLR works in a different way from the others: it reduces the SGS stresses by high-pass filtering, whereas the other approaches essentially reduce the eddy viscosity, as can be seen in Fig. 8b. At  $x = 800$  mm, the FOI computation presents a slightly more extensive turbulent mixing with large values of modelled turbulent eddy viscosity in the outer part of the mixing layer. Overall, all the computations have produced reasonable mean velocity profiles across the mixing layer in the developing region ( $x = 200$  mm) and when approaching the developed region ( $x = 800$  mm), whereas the NLR and NTS computations give the results closest to the measured profiles.

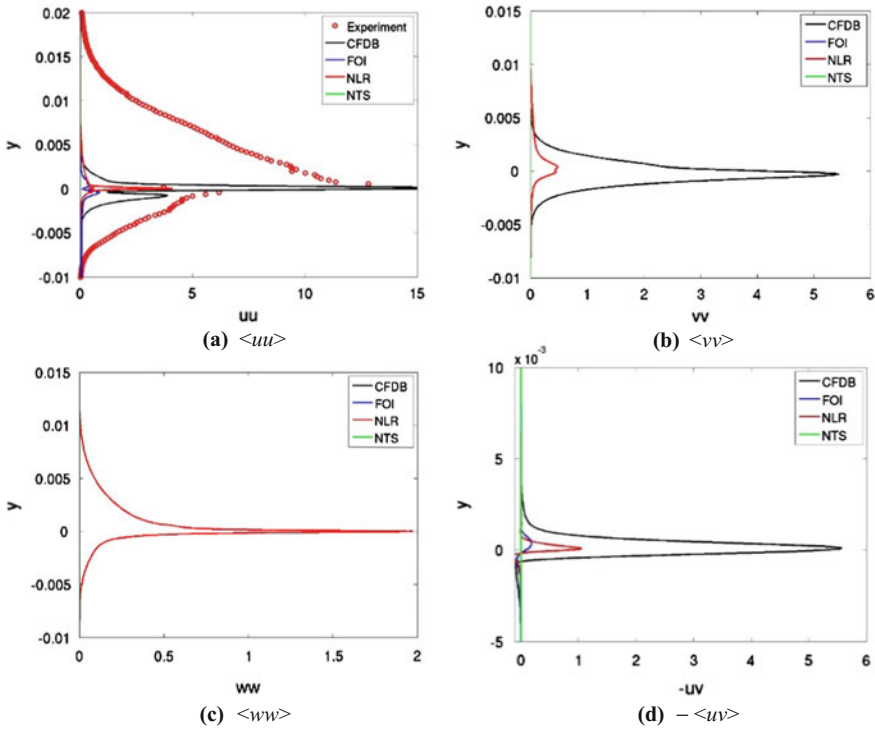
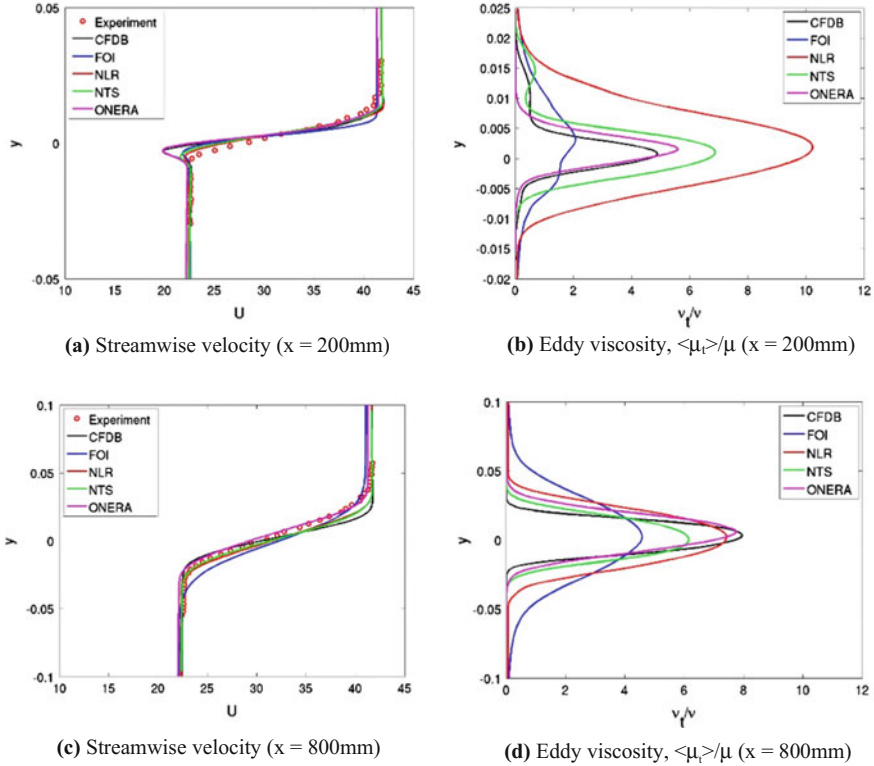


Fig. 7 Profiles of time-averaged resolved turbulent quantities at  $x = 0.5$  mm



**Fig. 8** Time-averaged (mean) streamwise velocity profiles (*Left*) and turbulent eddy viscosity,  $\langle \mu_t \rangle / \mu$  (*Right*), at  $x = 200$  and  $800$  mm, respectively

In Fig. 9, the resolved turbulent stresses are displayed in comparison with the measured data for the two stations. At  $x = 200$  mm, Fig. 9a, c, e and g, all the computations have under-estimated the resolved turbulent stresses on the high-speed side of the mixing layer, suggesting an incorrect prediction of the spreading rate of the mixing layer at this location. For the normal stresses at  $x = 200$  mm in Fig. 9a, c and e, the other computations have under- or over-predicted the peak values in the mixing layer, whereas the NLR and NTS computations have claimed peak values closer to the measurement for the streamwise normal stress.

Both the NLR and ONERA computations have over-predicted  $\langle vv \rangle$  and  $\langle ww \rangle$ , indicating an exaggerated prediction of turbulent fluctuations in the vertical and spanwise directions, whereas the other computations have under-predicted these stresses. The NLR results show reasonable agreement with the measured  $\langle uu \rangle$ ,  $\langle ww \rangle$  and  $-\langle uv \rangle$  on the low-speed side of the mixing layer, see Fig. 9a, e and g, respectively.

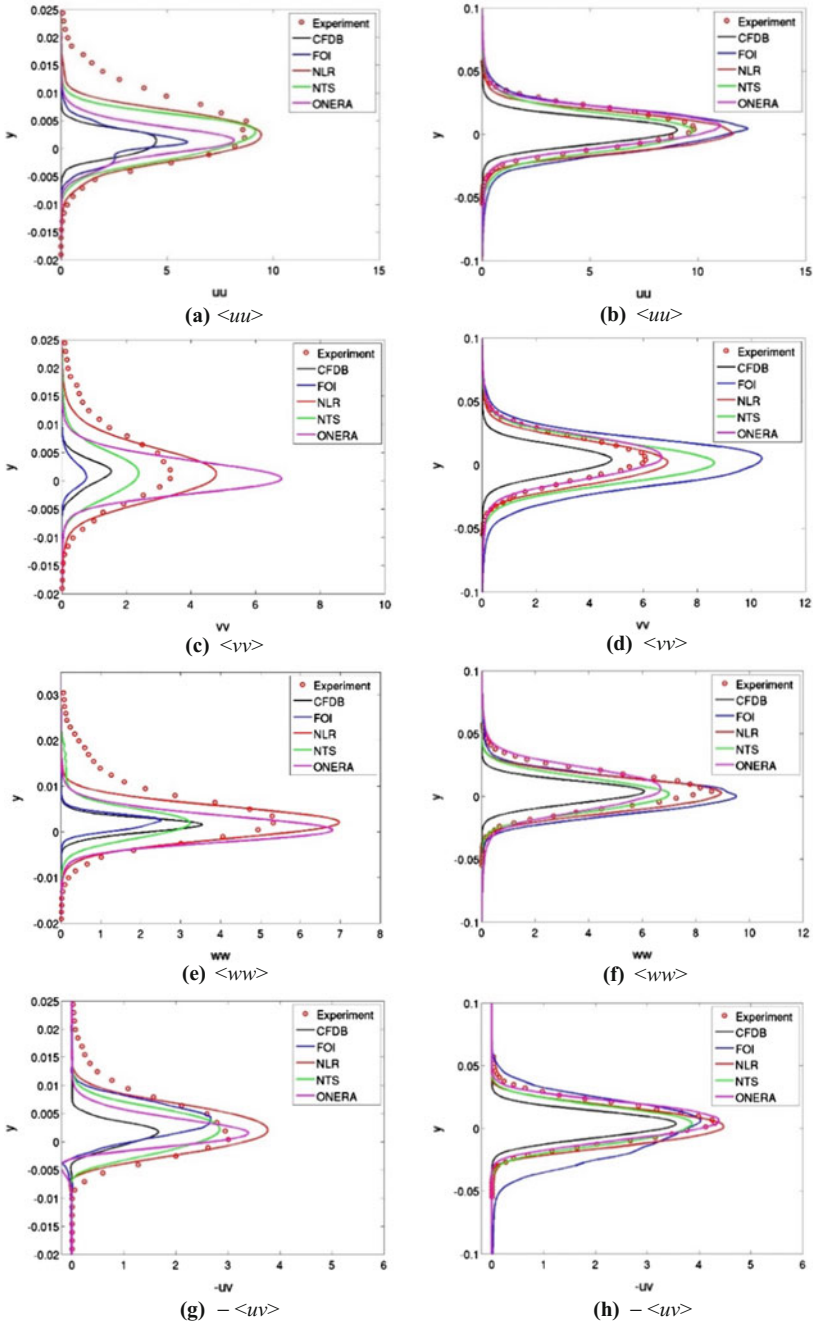
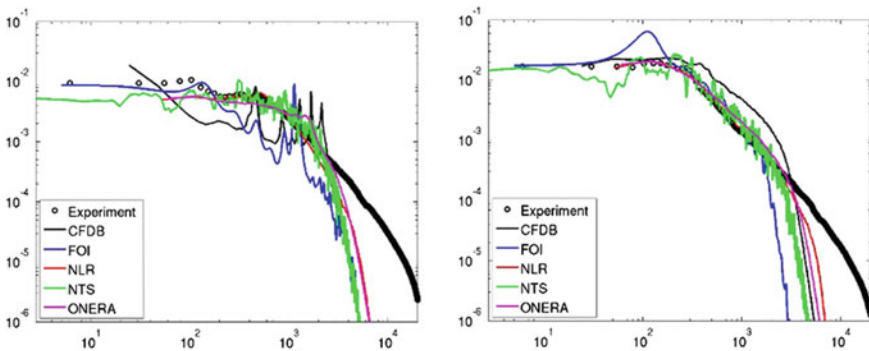


Fig. 9 Resolved turbulent stresses at  $x = 200$  mm (left column) and  $x = 800$  mm (right column)

Moving downstream at  $x = 800$  mm, where the mixing layer is expected to be fully developed, all computations have resolved the streamwise velocity fluctuations reasonably well, the NTS prediction being somewhat closer to the data than the other ones, see Fig. 9b. For the other two normal stresses,  $\langle vv \rangle$  and  $\langle ww \rangle$  in Fig. 9d and f, the results due to different modelling approaches are more diverse, however, but the NLR results agree reasonably well with the measured data. The peak of  $\langle vv \rangle$  was predicted fairly well in the NLR and ONERA computations, while being over-predicted in the computations by FOI and NTS and under-predicted by CFDB. Both the CFDB and ONERA computations have under-predicted the peak values of  $\langle ww \rangle$ . The turbulent shear stress,  $-\langle uv \rangle$  in Fig. 9h, was over-predicted in the low-speed side of the mixing layer by the FOI computation. This has probably been caused by the modelled part of SGS  $\tau_{ij}$  based on velocity gradients with an over-estimated instantaneous reverse diffusion in the modelling. The CFDB computation, on the other hand, has under-predicted the resolved turbulent stresses at  $x = 800$  mm, which suggests that the mixing layer remains undergoing a relatively intensive development.

Overall, it should be emphasized that, compared to the base model, which renders hardly any resolved turbulence at  $x = 200$  mm, the GAM methods incorporated by involved partners have played a significant role in mitigating the grey area and in facilitating an earlier re-establishment of resolved turbulent mixing layer over the initial stage.

The power spectral density (PSD) for the resolved streamwise velocity fluctuations is plotted in Fig. 10, of which the data have been sampled with time in the computation at  $x = 200$  and  $800$  mm on the central line ( $y = 0$ ), respectively. Corresponding approximately to the peak of resolved turbulent normal stress  $\langle uu \rangle$ , Fig. 9a for  $x = 200$  mm and b for  $x = 800$  mm, the level of the PSD at  $x = 200$  mm is predicted well by NLR, NTS and ONERA, while it is under-predicted by CFDB and FOI. At  $x = 800$  mm, the computed PSD shows an overall reasonable agreement with the experiment at frequencies below 3 kHz.



**Fig. 10** Power spectral density (PSD) for the streamwise velocity fluctuations at  $x = 200$  mm (left) and  $x = 800$  mm (right)



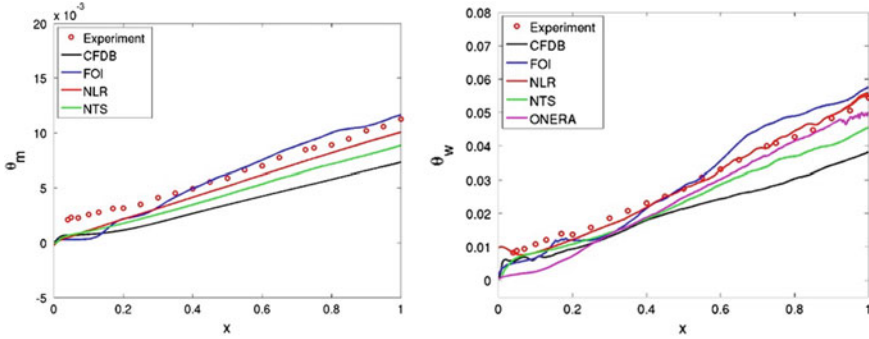


**Fig. 11** Computed momentum thickness,  $\theta_m$  (*left*) and vorticity thickness,  $\theta_w$  (*right*) of the mixing layer, both are in meter

The FOI computation presents an earlier damping at high frequencies, which is probably due in part to a large time step adopted in their computation (see Table 2).

An overall observation of the resolved turbulent mixing layer in its development can be made by plotting its momentum and vorticity thickness, defined respectively in Eqs. (1) and (2), as shown in Fig. 11.

Overall, the NLR result gives the best agreement with the measured data. For the momentum thickness,  $\theta_m$ , the FOI computation has returned a slight over-prediction of the downstream mixing layer, while the other computations have under-predicted this quantity (no data was provided by ONERA because of the high sensitivity of their assessment in the numerical bounds of the integral defining  $\theta_m$ ). The NLR result shows a slope of  $\theta_m$  consistent with the experiment data and, for the vorticity thickness,  $\theta_w$ , the NLR computation agrees very well with the measured data. The ONERA results shows also a good agreement with the experiment in the downstream part, whereas the FOI result has over-predicted  $\theta_w$ . In general, the results shown in Fig. 11 suggest that the GAM methods examined have, although to different degrees, effectively mitigated or alleviated the grey area problem in resolving the mixing layer emanating from RANS-modelled boundary layers.

## 5 Summary and Conclusions

As a fundamental test case, the mixing layer has been used in Go4Hybrid project work to verify the grey-area mitigation (GAM) methods incorporated in non-zonal hybrid RANS-LES modelling approaches. Five partners have contributed to this test case. It is noted here that a number of additional computations have been performed, including numerous computations on different grids and computations with zonal methods supported with synthetic turbulence. For relevant comparison, nonetheless, only one set of results from each involved partner is included for the comparison summarized in this section. It is further noted that, in spite of the

mandatory grid resolution required in the focusing region targeting the initial part of the mixing layer, partners have generated their own grid to comply with the implementation of selected modelling approaches and, moreover, different numerical settings have been adopted due partly to different solvers adopted.

The GAM approaches, used in dealing with grey-area problem inherent in hybrid RANS-LES computations of this test case, include: (a) Redefined LES length scales oriented perpendicular to the vorticity vector, triggering earlier mixing layer instabilities and 2D vortex structures breakup (CFDB, NTS and ONERA); (b) Stochastic energy-backscatter and high-pass filtering (HPF) LES modelling formulation (NLR); (c) Energy backscatter based on velocity gradients in LES mode, enhancing resolved turbulent fluctuations (FOI). These GAM approaches have been examined using, respectively, SA- or SST-based DDES (or modified variant), X-LES, or HYB0 as base models.

In general, all the GAM methods are, to different extents, able to mitigate or alleviate the grey area in the initial shear layer, which has been well reflected in the resolved turbulent structures and statistics, as well as in the predicted mixing layer thickness. More specifically, the following conclusions can be derived from the assessment based on the computations contributed.

- All methods achieve an initial re-establishment of turbulence, but showing different ways and “re-establishing rates” towards a well-resolved turbulent mixing layer, leading consequently to different degrees of GA mitigation.
- Of all the verified GAM methods, the approach by NLR has shown a more effective adaption to “true” (measured) turbulence with a relatively large amount of three-dimensional turbulence resolved already at the plate trailing edge.
- The formation of the mixing layer starts with two RANS-simulated turbulent boundary layers in the absence of resolved turbulence, for which the grey area is usually characterized by two-dimensional spanwise “rolling” structures. All the GAM methods have shown capabilities of re-establishing three-dimensional turbulent structures. No evidence has been present in the computations, however, to show distinguishable three-dimensional “pairing” structures as a consequence of mitigating the grey area in the presence of initial “rolling” structure breakup.
- In spite of improved effectiveness of mitigation using different GAM approaches, the mixing-layer thickness is often under-predicted in the (very) initial stage due to under-resolved turbulent mixing/diffusion.

In summary, the computation of a mixing layer for verification of the GAM methods incorporated in non-zonal hybrid RANS-LES modelling represents significant progress with successful demonstration. Nonetheless, further studies are required towards fully eliminating the “grey-area” problem. It seems reasonable to indicate that targeting only on improving LES mode might not be enough to “purge” the grey area in non-zonal hybrid RANS-LES modelling.

# The Spatially Developing Flat Plate Turbulent Boundary Layer

Sébastien Deck

## 1 Introduction—Physical Phenomena and Modelling

Spatially developing boundary layers at high Reynolds numbers play a key role in many engineering applications e.g. for determining friction drag on a body moving relative to a fluid. This enables performance prediction (e.g. fuel consumption).

Natural use of DES-type methods (or more generally any “weak-coupling” method) induces that the attached boundary layers are systematically treated in RANS mode. Such methods may not be adequate in situations where the flow is sensitive to the history of the upstream turbulence like a shallow separation bubble on a smooth surface induced by a moderate adverse pressure gradient (see Fig. 1). As a consequence, the simulation has to be fed with turbulent fluctuations to match the low-order statistics given for example by a RANS calculation. In this framework, the hybrid RANS/LES model can be considered as a LES where the RANS model plays the role of a wall-layer model.

In contrast to the rich literature concerning channel flows, there exists only very few publications where hybrid RANS/LES results are compared with experimental/DNS data in the case of a spatially developing flat plate boundary layer. This may appear surprising since the capability to simulate a spatially developing boundary layer is a mandatory milestone of a hybrid RANS/LES method intended to simulate complex flows of practical interest. Nevertheless, the capability to simulate accurately such flows in WMLES mode is definitely a challenging issue.

The problem of zonal or embedded hybrid coupling is equivalent to a multi-resolution decomposition of the problem and can take several forms as illustrated in Fig. 2:

---

S. Deck (✉)

ONERA, the French Aerospace Lab, 92190 Meudon, France  
e-mail: sebastien.deck@onera.fr

**Fig. 1** Illustration of flow situations where a WMLES approach might be useful. **a** Turbulent boundary layer–trailing edge noise. **b** Boundary layer under a strong adverse pressure gradient on the upper surface of a flap in a three-element high-lift airfoil. **c** Mild separation near the trailing edge of a flap, with the incoming boundary layer thickness of the same order of magnitude as the height of the separated flow region. Adapted from Deck et al. (2014)

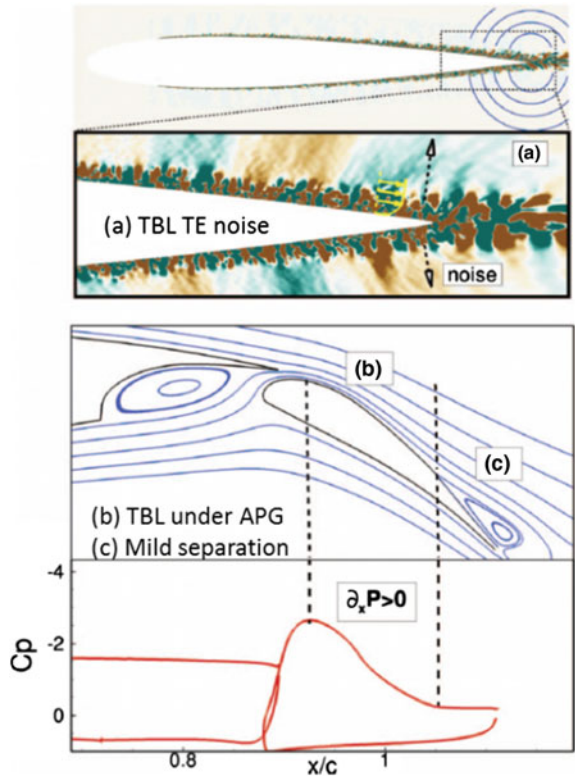
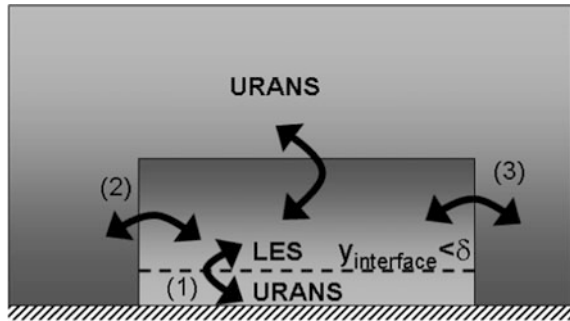


**Fig. 2** Several configurations of zonal RANS/LES coupling: (1) Wall-Modelled LES (WMLES)—(2) Turbulent inflow condition—(3) Embedded (adapted from Sagaut et al. 2013)



1. Whilst non-zonal methods aim at covering the entire boundary layer in the URANS mode, embedded methods aim at covering only the inner part of the boundary layer. Consequently, LES content has to be generated in the outer part of the boundary layer. This first type of problem is sometimes referred to as Wall-Modelled LES (WMLES).

2. The second type of RANS/LES coupling aims at representing a turbulent inflow especially when a LES domain is located downstream a RANS domain. In this case, synthetic turbulent structures have to be generated to match statistical characteristics provided by the RANS side.
3. The most general multi-domain/multi-resolution problem concerns the case where a local LES simulation is embedded into a global RANS simulation.

In some cases, the spatial derivatives of the averaged flow field are discontinuous across the RANS/LES interface and synthetic turbulence must be generated at the inflow of the LES domain when it is located downstream a RANS region.

For the purposes of the Go4Hybrid project, a turbulent flat plate boundary layer test case has been designed to address the aforementioned issues. The common flow and inflow conditions as well as the grid are presented first. An overview of the different partner calculations including the underlying hybrid model, the turbulence inlet method as well as some salient numerical parameters are then given. Both instantaneous fields together with global and local statistical quantities are then thoroughly assessed.

## 2 Test Case

### 2.1 Flow and Inflow Boundary Conditions

The test case is a spatially developing zero-pressure gradient turbulent boundary layer over a smooth flat plate. The free-stream velocity is  $U_0 = 70 \text{ m}\cdot\text{s}^{-1}$ , the static pressure is set to  $P_0 = 99,120 \text{ Pa}$ , the temperature equals  $287 \text{ K}$  leading to a Reynolds number per meter  $\text{Re} = 4.72 \times 10^6 \text{ m}^{-1}$  and a Mach number  $M_0 = 0.2$ .

The initial boundary layer thickness is  $\delta_0 = 5.8 \text{ mm}$  so that the Reynolds numbers based respectively on the momentum thickness  $\theta_0$  and the friction velocity  $u_{\tau_0}$  at the inlet are respectively:

$$\text{Re}_{\theta_0} = \frac{U_0 \theta_0}{\nu} = 3040 \quad \text{and} \quad \delta_0^+ = \text{Re}_{\tau_0} = \frac{u_{\tau_0} \delta_0}{\nu} = 1065$$

Implementation of inflow conditions for LES is a serious and still open problem. Indeed, using the RANS field alone to generate inflow data for the LES domain cannot be sufficient: additional modelling which includes further assumptions on local length scales, time scales and energy distribution is required to recover an efficient inlet condition for LES.

As the knowledge of the whole Reynolds stress tensor is often lacking, Laraufie and Deck (2013) assessed several methods to generate these quantities from a RANS calculation providing only the velocity and eddy viscosity profiles. The method M2 of Laraufie and Deck (2013), (based on Wilcox's hypothesis) has been

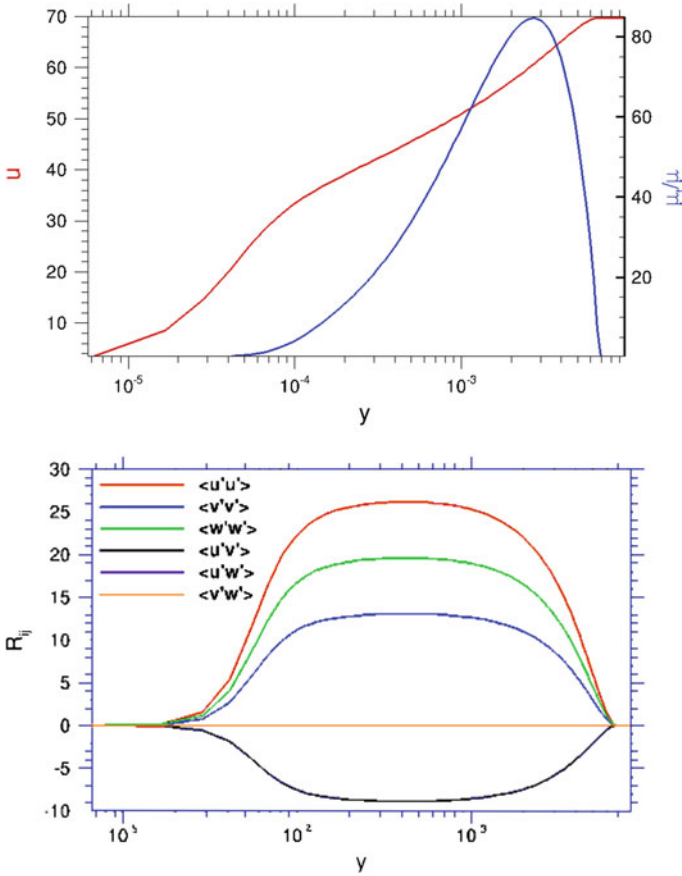


**Fig. 3** *Top* Velocity and eddy viscosity profiles; *Bottom* Reconstructed Reynolds stresses profiles at the inlet

retained to generate the inlet profiles plotted in Fig. 3. Let us be reminded that the description of the inner peak of  $\langle u'u' \rangle$  (near  $y^+ \approx 15$ ) is not needed in the frame of a WMLES approach where the inner-layer is modeled.

## 2.2 Geometric Description and Mandatory Grid

A mandatory structured grid was designed for the purposes of the project. The computational domain sizes in the streamwise, spanwise and wall-normal directions are respectively  $L_x = 113 \delta_0$ ,  $L_z = 5 \delta_0$  and  $L_y = 52 \delta_0$  so that the range of Reynolds number covered by the simulation is  $3040 \leq Re_\theta \leq 6100$  (or  $1065 \leq Re_\tau \leq 2095$ ) thus permitting comparison of numerical results with both

**Fig. 4** Computational domain of the mandatory grid

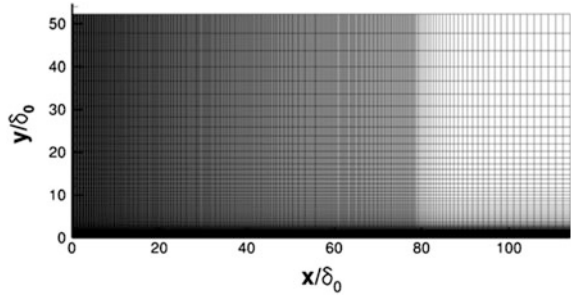


**Table 1** Parameters of the mandatory grid.  $N_x$ ,  $N_y$  and  $N_z$  are the grid sizes along the axes and the  $\Delta s$  are the corresponding resolutions expressed in both wall unit  $\cdot^+$  and inlet boundary layer thickness unit ( $\delta_0$ )

$\Delta x^+$	$\Delta y^+$	$\Delta z^+$	$\Delta x/\delta$	$\Delta z$	$N_x \times N_y \times N_z$	$N_{xyz}$
$100^+ - 200^+$	2	50	0.092–0.1	$\Delta x_{\min}/2$	$587 \times 127 \times 1030$	$7.7 \times 10^6$

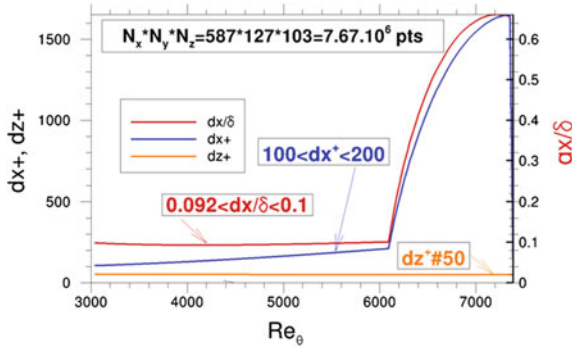


**Fig. 5** Streamwise evolution of the mesh resolutions

DNS (Schlatter and Örlü 2010) and experimental (DeGraaff and Eaton 2000; Österlund et al. 2000) datasets. A visualisation of the computational domain is displayed in Fig. 4. Note that for  $x/\delta_0 > 77$ , mesh cells are stretched in order to progressively damp the turbulent fluctuations. This procedure is common to ensure that the domain of interest is free from wave reflections.

The major parameters of the grid resolution are gathered in Table 1 as well as in Fig. 5 and correspond to classical grid resolutions (though somewhat fine) used in the framework of WMLES approach whose objective is to describe the outer part of the boundary layer. Note that the first cell is at  $y^+ = 1$  in the framework of a cell-centred code (i.e.  $y^+ = 2$  in the framework of a cell-vertex code). The grid distribution in the streamwise direction is not uniform in order to maintain  $\Delta x/\delta \approx 0.1$  in the region of interest. Conversely, the grid in the spanwise direction is constant so that  $\Delta z = \Delta x_{\min}/2$ . Finally, the total number of points is  $N_{xyz} = 7.7 \times 10^6$  points.

**Table 2** Overview of partner contributions

Partner	Solver (incomp/comp)	Model	Spatial scheme	Time step (s)	Comments
DLR	TAU compressible	IDDES-SA <sup>a</sup>	Central +LD2 <sup>1</sup>	$8 \times 10^{-7}$	SEM <sup>f</sup> DFSEM <sup>c</sup>
NTS	NTS compressible	IDDES-SA & SST <sup>a</sup>	Hybrid 4th Center/3rd Upwind	$3 \times 10^{-6}$	NTS-STG <sup>d</sup> and VSTG <sup>d</sup>
ONERA	FLU3M compressible	ZDES-SA mode 3 <sup>b</sup>	Modified AUSM+P	$3.2 \times 10^{-7}$	SEM <sup>g, h</sup> +Dynamic Forcing <sup>c</sup>
UNIMAN	OPENFOAM-EXTEND 3.1 incompressible	IDDES-SA <sup>a</sup>	Central	$1 \times 10^{-6}$	DFSEM <sup>c</sup> with new normalisation <sup>c</sup>

<sup>a</sup>Shur et al. (2008), <sup>b</sup>Deck (2012), <sup>c</sup>Poletto et al. (2013)

<sup>d</sup>Shur et al. (2014), <sup>e</sup>Laraufie et al. (2011), <sup>f</sup>Jarrin et al. (2009)

<sup>g</sup>Pamiès et al. (2009), <sup>h</sup>Deck et al. (2011), <sup>i</sup>Löwe et al. (2015)

### 3 Overview of Partner Contributions

A list of the partners who computed this flow as well as the salient information of the different simulations on the numerical method, the time-step, the hybrid model as well as the inlet method are gathered in Table 2. It is worth noting that both incompressible and compressible industrial codes have been assessed on a fair set of representative numerical methods (central and upwind).

## 4 Results—Discussion

### 4.1 Flow Visualization

A snapshot of the instantaneous spanwise velocity at the computational inlet is shown in Fig. 6. Small intense vortices close to the wall and larger scales in the outer part of the boundary layer can be discerned. One can notice that the instantaneous velocities generated near the wall are seemingly close, while some differences of the largest scales can be observed in the outer layer.

The turbulent content downstream from the inlet is quickly generated as highlighted by showing a positive value of the Q criterion (see Fig. 7). Though a possible damping at the inlet can be noticed for some methods, the turbulent content is sustained further downstream.



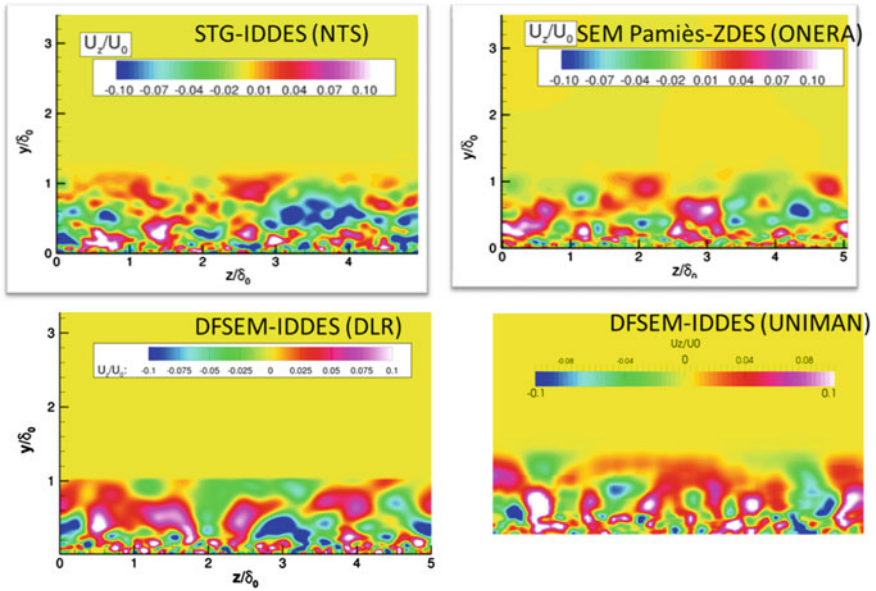


Fig. 6 Instantaneous spanwise velocity

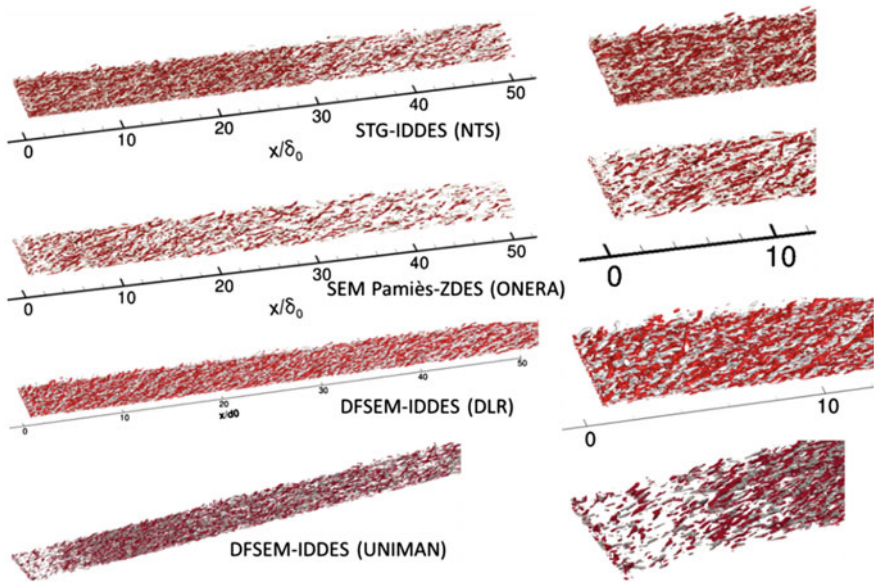
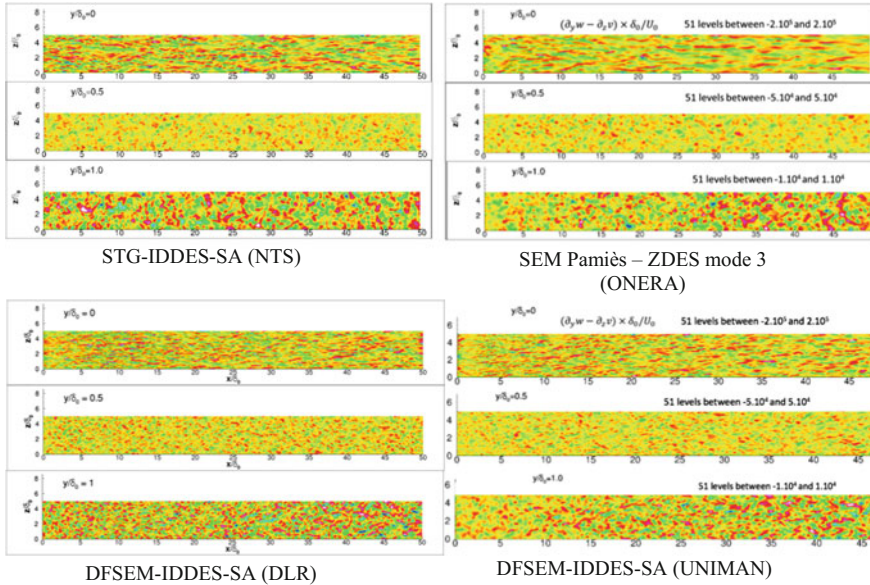


Fig. 7 Turbulent structures educed with  $Q. (\delta_0/U_0)^2 = 0.3$  iso-surface and colored by the sign of the streamwise vorticity (red  $\omega_x < 0$ ; white  $\omega_x > 0$ ). A zoom of the inlet is given in the right part



**Fig. 8** Instantaneous streamwise vorticity component  $(\partial_y w - \partial_z v) \times \delta_0 / U_0$

An alternate visualization of the instantaneous field is provided in Fig. 8 showing the streamwise vorticity component in several XZ planes at several distances to the wall namely  $\frac{y}{\delta_0} = 0, 0.5, 1.0$ .

Some “streak-like” structures are visible at the wall. This result may appear surprising since the very-wall region is treated in URANS mode indicating that this URANS region is very permeable to the resolved fluctuations further away from the wall. This will be discussed in the following.

### 4.2 Skin Friction

The skin friction constitutes a primary quantity of interest and its assessment deserves particular attention.

Numerical results are compared with the available experimental and DNS data as well as with the widely acknowledged Coles-Fernholz correlation (see Nagib et al. 2007) given by

$$C_f^{CF} = 2 \left( \frac{1}{0.384} \ln(\text{Re}_\theta) + 4.127 \right)^{-2}$$

Based on the Coles-Fernholz correlation, one can define the error on the skin friction as follows

$$Err = \frac{|C_f^{CF} - C_f|}{C_f^{CF}}$$

The streamwise evolution of the skin friction coefficient  $C_f$  as a function of the Reynolds number as well as the evolution of the Error coefficient as a function of the distance from the inlet is shown in Fig. 9. It is worth noting that the skin friction coefficient is well predicted (<5%) with both IDDES and ZDES mode 3. The divergence-free version (DFSEM) of SEM improves the prediction of the skin friction coefficient compared with the original SEM. Besides for most calculations, the adaptation distance  $L_R$  is lower than 10 initial boundary layer thicknesses which

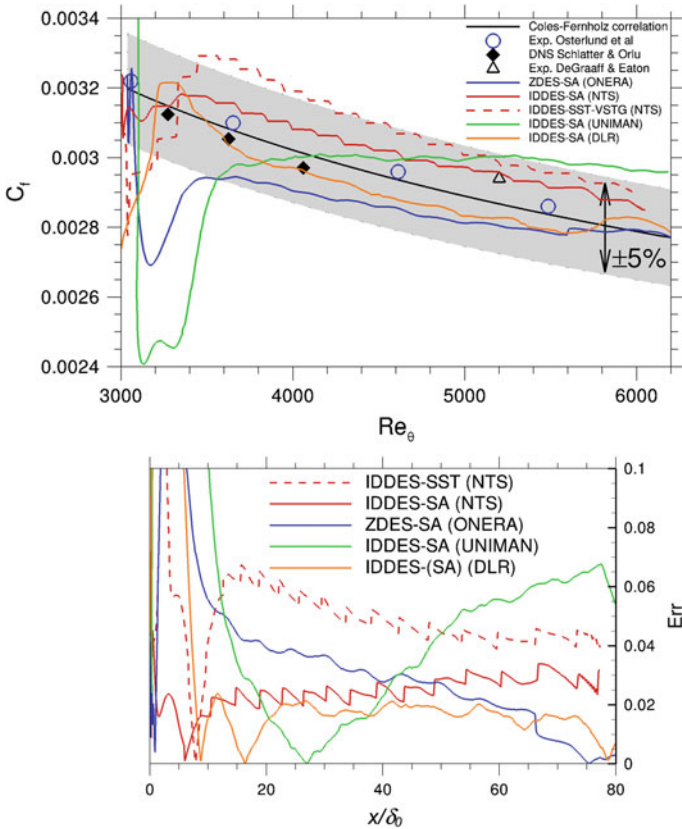


**Fig. 9** *Top* Streamwise evolution of the skin friction coefficient. *Bottom* Streamwise evolution of the error coefficient as a distance from the inlet  $x/\delta_0$

can be considered as a very positive achievement since the present WMLES is performed on a coarse grid compared with those classically used in WRLES.

### 4.3 Velocity and Reynolds Stresses Profiles

In this section, the salient properties of the first and second order statistical properties of the velocity field are assessed. Two stations, namely  $Re_\theta = 4060$  and  $5200$ , are investigated. First, Fig. 10 shows the mean velocity profile plotted in both inner and outer scales. While quite similar velocity profiles are obtained between all methods when plotted in outer scales (i.e.  $U/U_0(y/\delta)$  plots), some differences can be highlighted in the profiles plotted in inner scales (i.e.  $u^+(y^+)$  plots). Indeed, the velocity is too high in the vicinity of the interface in the frame of the ZDES calculation which can be attributed to the limit of the use of a passive interface. A similar trend is observed with IDDES but with a lesser extent since the ‘‘RANS region’’ is smaller as can be seen in Fig. 11 showing the Reynolds stresses. Indeed, the lower interface position featured with IDDES vs ZDES leads to a higher amount of resolved turbulence close to the wall as will be discussed later in Fig. 13. It is also worth noting the dramatic effect of the inlet method [e.g. IDDES-DFSEM (DLR) vs. IDDES-STG (NTS)] on the outer layer properties. This result highlights that turbulent inflow can have a ‘‘long-lasting’’ impact further downstream. The effect of the turbulence generating method can still be seen at a distance of  $30\delta_0$  downstream from the inlet independently of the hybrid model since both latter calculations resort on IDDES with low dissipative numerical schemes.

In Fig. 12, the Reynolds stresses are plotted in inner scales for  $Re_\theta = 5200$ . This figure shows the robustness of the self-similar behavior of the outer-layer (if normalized by  $u_\tau$ ) since no significant difference can be depicted using this scaling. Besides, one can notice that the inner layer, though treated in URANS mode, is very permeable to fluctuations since no sudden jump in the *rms* quantities can be depicted in the vicinity of the RANS/LES interface. Of interest, the outer layer is

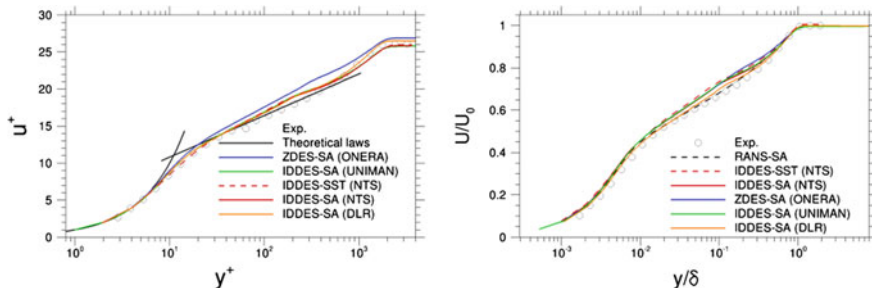


Fig. 10 Streamwise velocity profiles at  $Re_\theta = 4060$

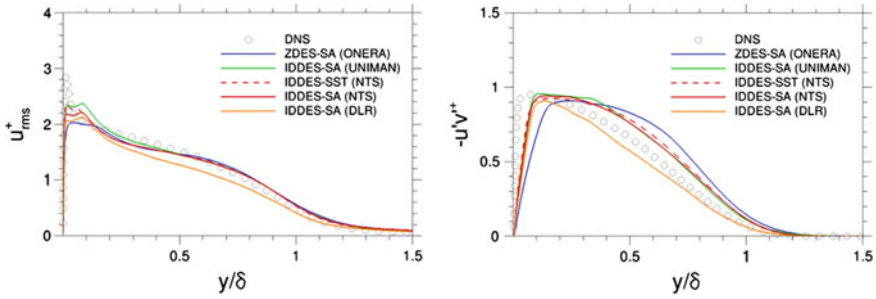


Fig. 11 Resolved Reynolds stresses profiles at  $Re_0 = 4060$

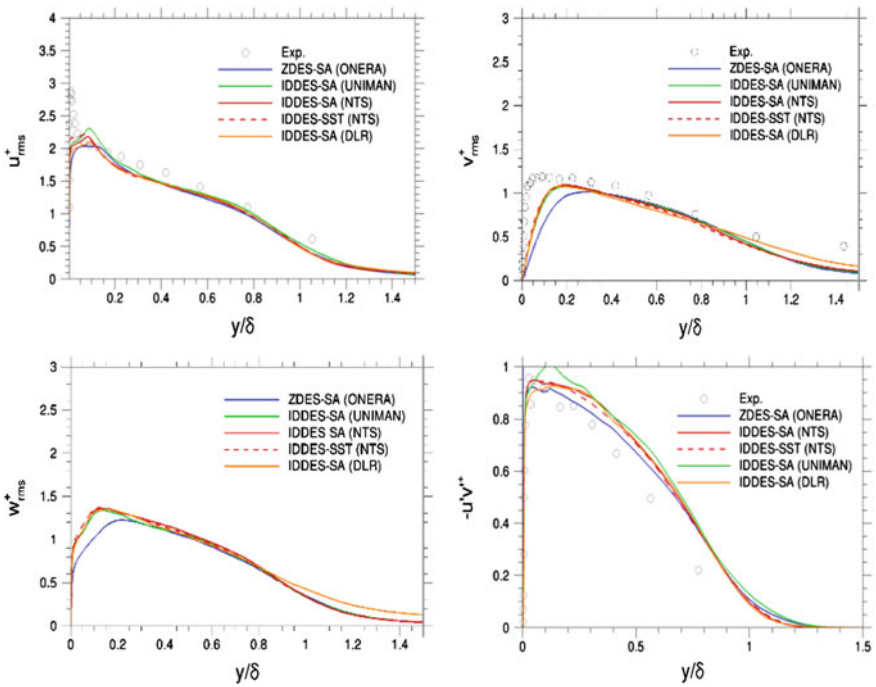
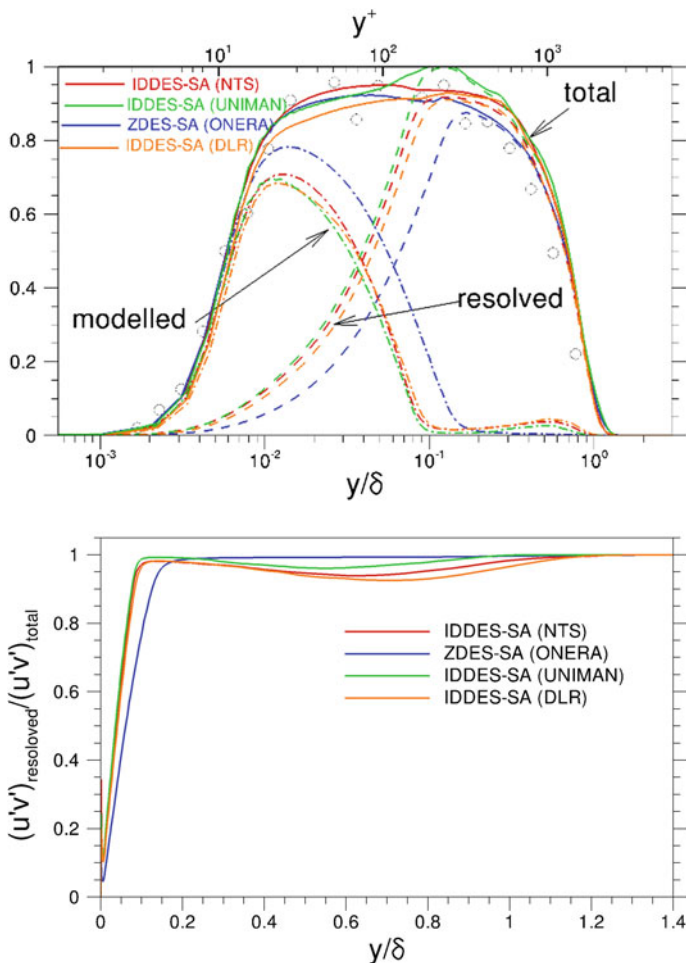


Fig. 12 Resolved Reynolds stresses profiles at  $Re_0 = 5200$

well simulated though a small deficit in the  $u'^{2+}$  and  $v'^{2+}$  profiles above the RANS/LES interface can be observed for all calculations.

Figure 13 presents an example of the wall-normal profiles of the terms contributing to the Reynolds shear stress at  $Re_0 = 5200$ . The additional part  $\mu_t \left( \frac{\partial \bar{u}'}{\partial y} + \frac{\partial \bar{v}'}{\partial x} \right)$  has not been considered here since it has been shown in Deck et al.



**Fig. 13** Decomposition of the total Reynolds shear stress profiles into modeled and resolved parts at  $Re_\theta = 5200$

2014 that its contribution to the total shear stress  $-qu'v'$  can be neglected compared with the resolved part  $-\rho\bar{u}'v'$  and the modeled part  $\mu_t \left( \frac{\partial \langle u \rangle}{\partial y} + \frac{\partial \langle v \rangle}{\partial x} \right)$ .

Figure 13 shows that the total Reynolds shear stress (solid line) is well assessed over the entire boundary layer thickness with both IDDES-(NTS/DLR) & ZDES mode 3. The difference between UNIMAN and DLR calculations (e.g. overestimation of the total shear stress near the interface) may be explained by the “long-lasting” impact of the turbulent inflow as discussed above.

Finally, the ratio resolved/total Reynolds shear stress (Renard and Deck 2015) highlights that the modeled shear stress is negligible (IDDES: <5–10% and ZDES:

<1.5%) in the outer layer. The behavior of this ratio is not monotonous with IDDES but it does not disturb the total stress behaviour.

## 5 Conclusion

In the course of Go4Hybrid, a series of Wall-Modelled Large Eddy Simulations has been carried out by four partners (DLR, NTS, ONERA, UNIMAN) with the use of different approaches (IDDES, ZDES mode 3), turbulence generating methods and codes.

All methods developed within the project have been thoroughly assessed and compared with available DNS and experimental data. It has been shown that most synthetic turbulence methods have reached a good level of maturity in the sense that the skin friction coefficient is mostly predicted within 5%. Besides, the adaptation distance is mostly lower than 10 initial boundary layer thicknesses which can be considered as a very positive achievement since the present WMLES are performed on a coarser grid than those classically used in WRLES.

The analysis also highlights that the synthetic turbulent inflow methods can have a somewhat “long-lasting” impact further downstream since the effect of the turbulence generating method can still be seen at a distance of  $30\delta_0$  downstream the inlet independently of the underlying hybrid method.

The generalization of these methods to three-dimensional curvilinear geometries at high Reynolds numbers with emphasis on aero-acoustic sources prediction will constitute one of the next challenges in this field.

**Part IV**  
**Results for Complex Test Cases**



# Single-Stream Round Jet at $M = 0.9$

M. Fuchs, C. Mockett, M. Shur, M. Strelets and J.C. Kok

## 1 Introduction

As a major source of aviation noise, the prediction of jet noise is a key engineering application of CFD. Carefully-conducted Large-Eddy Simulations (LES) have been demonstrated to give accurate predictions of jet noise, however the computational cost is unfeasibly high within the thin turbulent boundary layers present in the nozzle flow at practical Reynolds numbers. Neglecting the boundary layer turbulence has been shown to lead to excessive flow separation on the nacelle and central bullet (Khalighi et al. 2011). Such considerations become even more important when wing and pylon geometries are included.

Hybrid RANS-LES methods provide the necessary means to tackle such problems with a feasible computational expense. Efficient treatment of attached turbulent boundary layers is achieved using a Reynolds-Averaged Navier–Stokes (RANS) model, whereas the turbulence-resolving power of LES is applied to predict acoustic sources in the jet plume.

---

M. Fuchs (✉) · C. Mockett  
CFD Software Entwicklungs- und Forschungsgesellschaft mbH (CFDB),  
Bismarckstr. 10-12, 10625 Berlin, Germany  
e-mail: marian.fuchs@cfdb-berlin.com

M. Shur · M. Strelets  
New Technologies and Services (NTS), 14 Dobrolyubov Ave.,  
197198 St.-Petersburg, Russia

M. Shur · M. Strelets  
St.-Petersburg Polytechnic University, 28 Grazhdansky Ave. 28,  
195220 St.-Petersburg, Russia

J.C. Kok  
Netherlands Aerospace Centre NLR, Anthony Fokkerweg 2,  
1059 CM Amsterdam, The Netherlands

Despite nominally providing all necessary features to handle complex installed jet noise prediction, the Grey Area problem is strongly pronounced for standard DES approaches applied to jets: In the important early shear layer region, excessive levels of eddy viscosity lead to a sluggish generation of resolved LES turbulence following the RANS boundary layers.

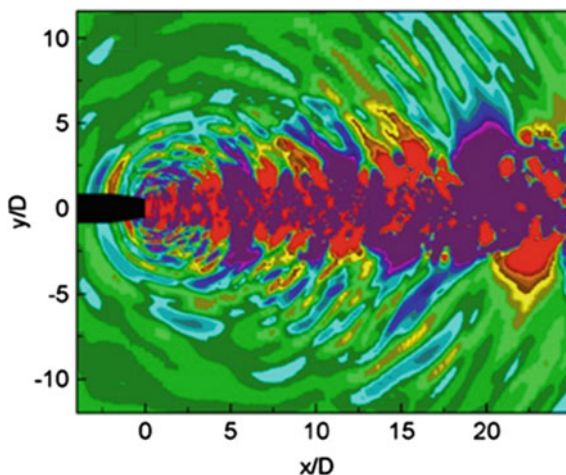
The round jet is therefore studied within Go4Hybrid as an ideal case for assessing the improvements achieved by the developed GAM approaches and their scope for application for this important industrial problem.

## 2 Flow Case, Simulation Setup and Experimental Reference Data

An unheated, compressible, round jet at  $M = 0.9$  is investigated, which issues into quiescent fluid. The Reynolds number based on the nozzle diameter of  $D = 0.06223$  m is  $Re_D = 1.1 \times 10^6$ . Prior to Go4Hybrid, this jet was extensively studied by NTS (e.g. Shur et al. 2005, 2011), who kindly provided their existing grids and reference (zonal RANS-ILES) results to the consortium. An impression of the resolved acoustic simulation from those reference simulations is given in Fig. 1.

To assess the predictive accuracy of aerodynamics quantities, a variety of different experimental data is available from literature. In Bridges and Wernet (2010), different experimental data sets from NASA have been evaluated and a “consensus” data set is proposed which includes mean velocity and RMS profiles along the jet centreline and lip line as well as profiles of these quantities at different downstream locations  $x/D = 4.0, 8.0, 12.0$  and  $16.0$ . As a rather large scatter of results is found in literature, further data sets of Lau (1981), Arakeri et al. (2003) and Simonich et al. (2001) are additionally used for comparison here. Despite the observed scatter

**Fig. 1** Instantaneous pressure contours in the acoustic range of ILES simulation for round jet test case (Shur et al. 2005)



in the experimental measurements, the selected data sets are considered sufficient to judge the relative improvement achieved by the proposed GAM methods over conventional hybrid RANS-LES approaches.

For comparison of farfield sound, the measurements of Viswanathan (2004) are utilized. Here, farfield SPL spectra at different observer angles ( $\Theta = 50^\circ, 90^\circ, 130^\circ, 150^\circ$ ) at a distance of  $R/D = 98$  away from the nozzle are provided as well as overall sound pressure levels (OASPL) for different observer angles  $50^\circ \leq \Theta \leq 155^\circ$ . All data accounts for sound absorption at standard day conditions according to the correction detailed in Shields and Bass (1977).

### 3 Grids

The grids provided by NTS (Shur et al. 2011) are all of O/H topology, with a Cartesian inner block to avoid the centreline singularity surrounded by a cylindrical outer block. Four meshes, ranging from between 1.6 M cells (G1) to 23 M cells (G4) were provided, which are summarised in Table 1. Since the previous simulations of NTS showed near-converged results for G3, this was defined as the mandatory grid for all partners.

The computational domain is meshed from  $10D$  upstream to  $70D$  downstream of the nozzle exit, and varies radially between  $15D$  near the nozzle to  $30D$  near the outlet (see Fig. 2). Streamwise and radial stretching of grid cells is used in the outer domain part to naturally damp fluctuations and to weaken wave reflections at the boundaries.

### 4 Simulations Performed and Numerical Setup

Three partners computed results for the test case, where an overview about the different GAM techniques applied and the respective CFD codes used is given in Table 2.

**Table 1** Summary of grid parameters (all dimensions normalised with  $D$ )

	G1	G2	G3	G4
Outer block size $N_x \times N_r \times N_\phi$	$308 \times 81 \times 64$	$515 \times 101 \times 80$	$515 \times 101 \times 160$	$601 \times 158 \times 240$
Total cell count	1.6 M	4.2 M	8.4 M	23 M
$\Delta x$ at nozzle exit	0.011	0.008	0.008	0.005
Min $\Delta r$ in shear layer	0.033	0.022	0.022	0.016
$r\Delta\phi$ in shear layer	0.05	0.04	0.02	0.013

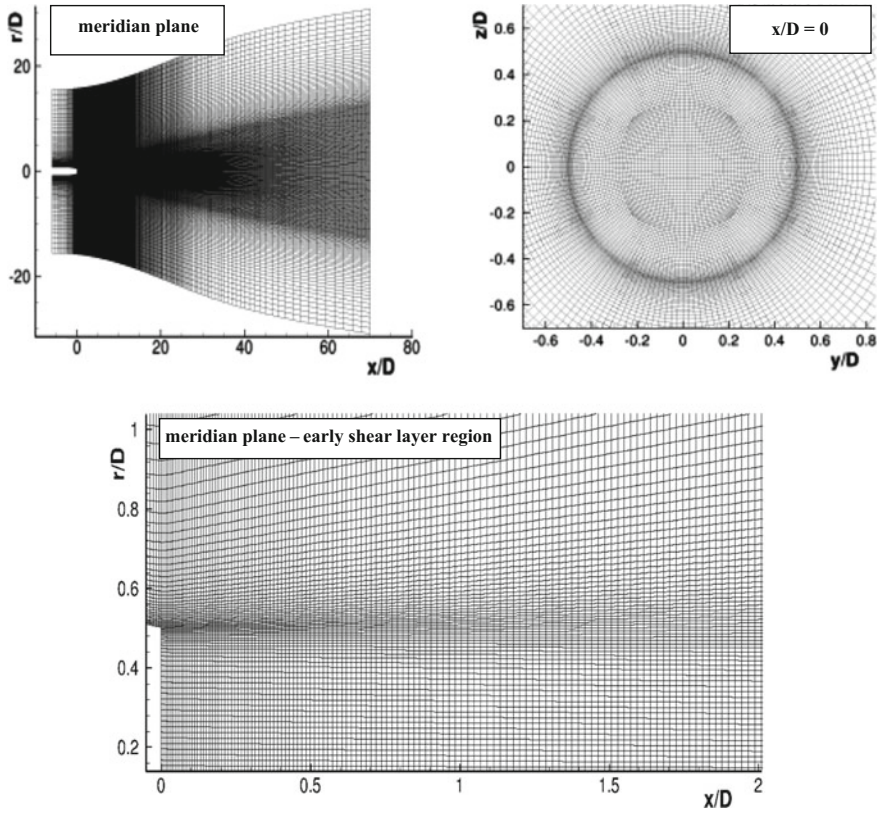


Fig. 2 Different views of mandatory grid G3 (see Table 1)

Table 2. Summary of GAM approaches and CFD codes used for jet simulations

Partner	Type of hybrid approach	GAM technique	CFD Code
CFDB	Non-zonal	$\sigma$ -DES+vorticity-adaptive length scale $\Delta_{\omega}$	Compressible branch of OpenFOAM® code (2nd order in space and time)
NTS	Non-zonal	Shear layer adapted length scale $\Delta_{SLA}$	Compressible branch of NTS code (Shur et al. 2004) (4th order in space and 2nd order in time)
NLR	Non-zonal	High-pass filtered SGS stresses + temporally and spatially correlated stochastic backscatter forcing	ENSOLV code (Kok 2009) (4th order in space and time)

CFDB applied their non-zonal GAM formulation (Mockett et al. 2015) based on the  $\sigma$  model of Nicoud et al. (2011) in conjunction with SA-DDES and the  $\tilde{\Delta}_\omega$  vorticity-adaptive grid scale definition, denoted SA- $\sigma$ -DDES +  $\tilde{\Delta}_\omega$ . Simulations were conducted using the unstructured OpenFOAM solver, in which the hybrid convection scheme of Travin et al. (2000) was used to blend between 2nd order accurate central differences in the turbulent region and a 2nd order upwind-biased scheme in the irrotational region.

NTS assessed their shear layer adapted grid scale definition  $\Delta_{SLA}$  (Shur et al. 2015) as grey area mitigation method for the jet, where 4th order centred and 5th order upwind schemes were used in their code in conjunction with the hybrid scheme of Travin et al.

Finally, NLR employed their delayed X-LES with a high-pass filtered (HPF) SGS model and a spatially correlated backscatter approach, where the exact model formulation can be found in Part II (Presentation of Approaches, Chapter “Non-Zonal Approaches for Grey Area Mitigation”). In their ENSOLV code, a 4th order low-dispersion skew-symmetric finite-volume method (Kok 2009) is used to ensure low numerical dissipation in the jet region.

CFDB and NTS used a 2nd order accurate implicit time integration scheme, whereas NLR used a 4th order explicit Runge–Kutta scheme.

This test case is primarily intended for the assessment of non-zonal methods in Go4Hybrid. For such methods, a coupled simulation of nozzle and plume is assumed, however only the plume is meshed and incorporated into the simulation. A RANS solution (including eddy viscosity) is imposed at the nozzle exit plane to mimic a coupled approach. In this study, CFDB and NTS used prescribed profiles computed via standard SA-RANS for the nozzle interior, whereas NLR used profiles extracted from SST-RANS for their  $k$ - $\omega$ -based background model.

## 5 Results—Performance of Best Methods on Mandatory Grid G3

First, the performance of the three different GAM approaches in terms of aerodynamics prediction is assessed on the mandatory grid G3 (see Table 2). Results are subsequently compared to both experimental data and a reference computation (conducted by NTS) using SA-based DDES and the standard grid scale definition  $\Delta_{max}$ , but on the coarser grid level G2. Results for all 3 GAM methods on grid G2, which enable a direct comparison to standard DES, are presented in the subsequent section.

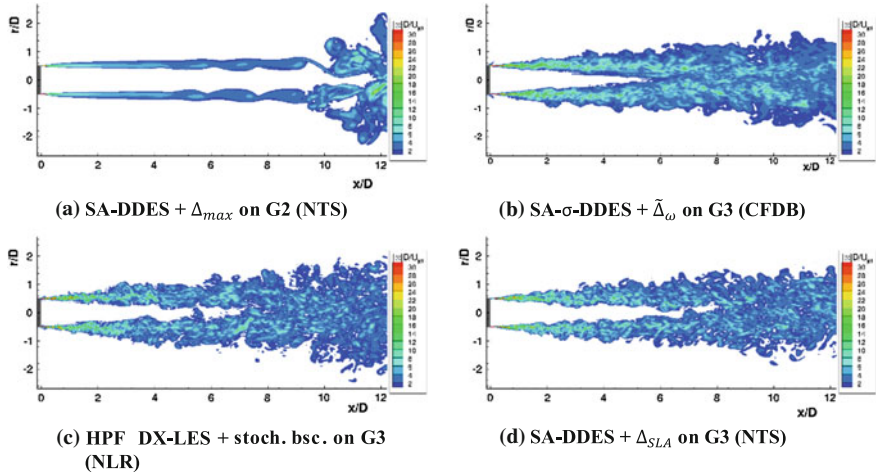


**Fig. 3** Contours of instantaneous vorticity magnitude on meridional plane, comparison of benchmark SA-DDES (on grid level G2) and three different non-zonal GAM approaches (on mandatory grid G3)

## 5.1 Instantaneous Flow

In Fig. 3 instantaneous snapshots of normalised vorticity magnitude are visualised for the entire jet region until far downstream of the nozzle ( $x/D \sim 12$ ). For the standard DES model, transition from the steady-state RANS nozzle profile to resolved turbulent content is visibly delayed by many diameters, where the early shear layer remains relatively stable. This behaviour of standard DES for jets comes without surprise and has been reported in numerous publications in the past (e.g. Shur et al. 2005). In contrast, all new GAM approaches show much improved behaviour and rapid transition from RANS to fully three-dimensional LES downstream of the nozzle. The simulations of NLR and NTS appear to resolve somewhat more fine-grained turbulent content, which could be due to the higher order discretisation schemes used in these two codes compared to the 2nd order OpenFOAM solver employed by CFDB.

A magnified view of the very important early shear layer region is presented in Fig. 4, where vorticity magnitude and eddy viscosity ratio contours are displayed. For standard SA-DDES, very high levels of SGS stresses can be identified in this region. This has a pronounced negative effect on the evolution of resolved scales, since natural Kelvin-Helmholtz instabilities in the shear layer are damped. All three novel GAM approaches succeed in freeing natural instabilities of the flow and thus promoting a fast transition to fully-resolved LES. Both the CFDB and NTS approach facilitate this by reducing the local grid length scale  $\Delta$  in this region as well as for the CFDB approach reducing the velocity gradient operator  $S^*$  entering the LES formulation (see Part II, Presentation of Approaches, Chapter “Non-Zonal

Approaches for Grey Area Mitigation”). Both modifications effectively result in reduced eddy viscosity levels in this region and as a consequence reduced SGS stresses, which is considered one of the core problems of standard DES with regard to the Grey Area issue for such flows. In contrast, the NLR approach reduces the SGS stresses by high-pass filtering the velocity entering the Boussinesq hypothesis (see Part II, Presentation of Approaches, Chapter “Non-Zonal Approaches for Grey Area Mitigation”) instead of reducing the eddy viscosity, obtaining the same effect without significant reduction of eddy viscosity in the early shear layer part. Furthermore, a direct promotion of flow instabilities is achieved via the stochastic forcing approach.

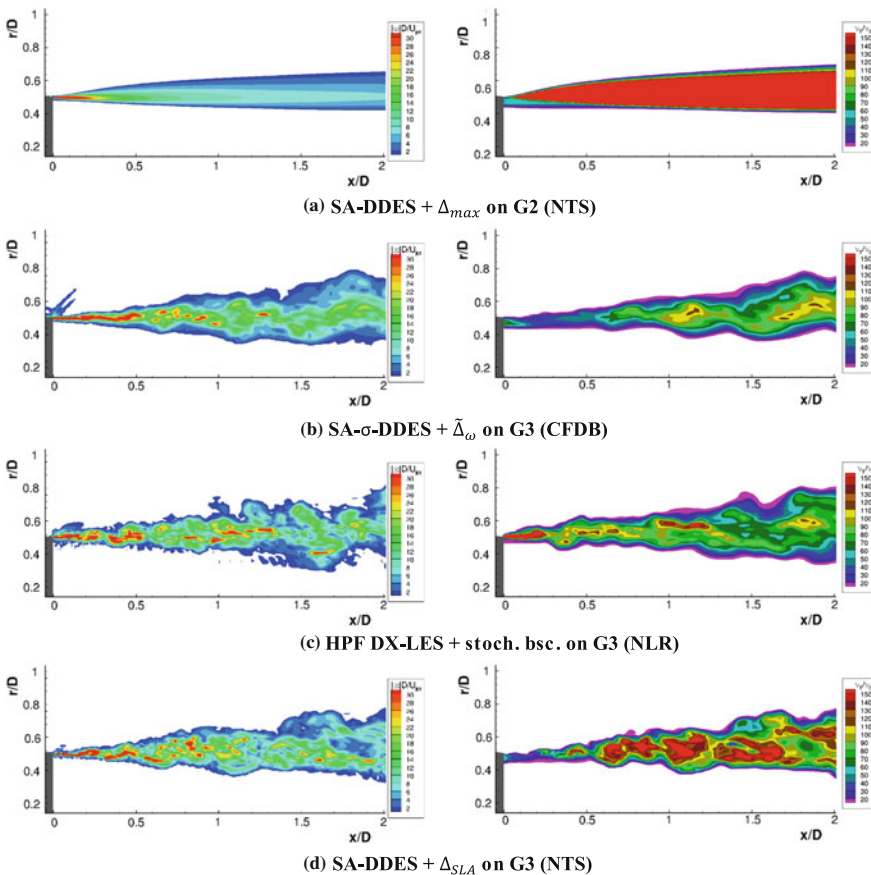


**Fig. 4** Contours of instantaneous vorticity magnitude and eddy viscosity ratio on meridional plane, comparison of benchmark SA-DDES (on grid level G2) and three different non-zonal GAM approaches (on mandatory grid G3), early shear layer region ( $x/D < 2.0$ ) is shown

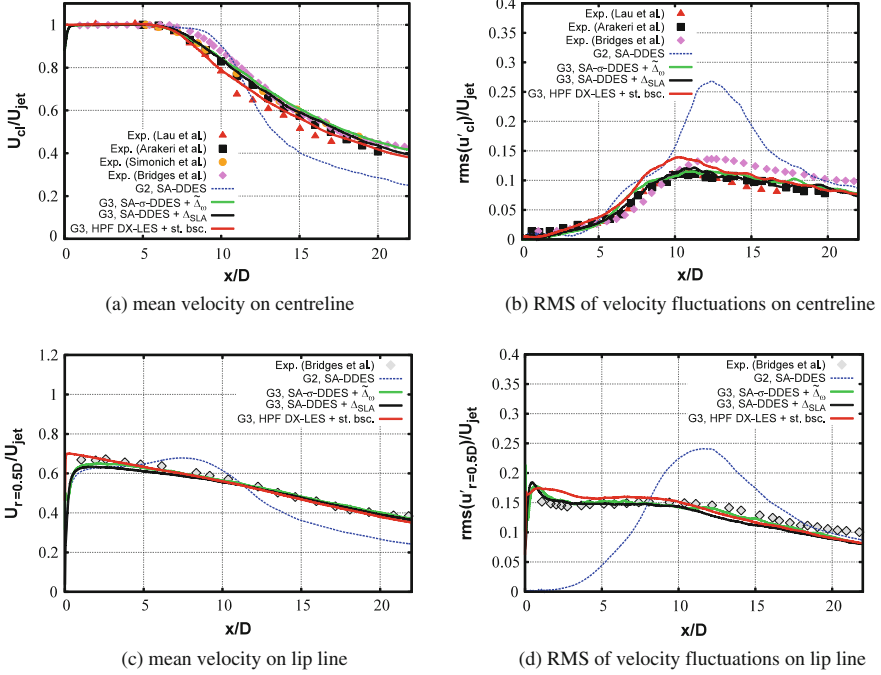


**Fig. 5** Comparison of results for different GAM techniques on mandatory grid G3, reference simulation using SA-DDES on G2 and experimental data, mean velocity and RMS fluctuations are shown on the jet centreline and lip line

## 5.2 Mean Flow

The very positive impact seen for all presented GAM approaches on the instantaneous flow field also translates to mean flow statistics. Figure 5 shows a comparison of results with different experimental data sets from literature for mean velocity and RMS fluctuations on the jet centre and lip line. The delay in RANS-to-LES transition seen for the standard SA-DDES causes an over-prediction of the jet core length. At the location where the stable shear layers finally disintegrate, the break-up of large scale structures is too strong and centreline velocity drops too rapidly. Centreline velocity fluctuations are also significantly over-predicted, which has a pronounced detrimental effect on noise prediction. The RMS profile on the lip line highlights the lack of resolved content predicted by the reference model, where again an over-shoot is seen once the shear layers break-up. In contrast, all three GAM methods deliver very good agreement compared to the measurements within the scatter of the experimental data and outperform standard DES. A slight over-shoot in RMS velocity fluctuations on the centreline is seen for the NLR model in the region  $7 < x/D < 10$ , corresponding to a mildly more rapid decrease of centreline velocity than seen in the CFDB and NTS simulations.



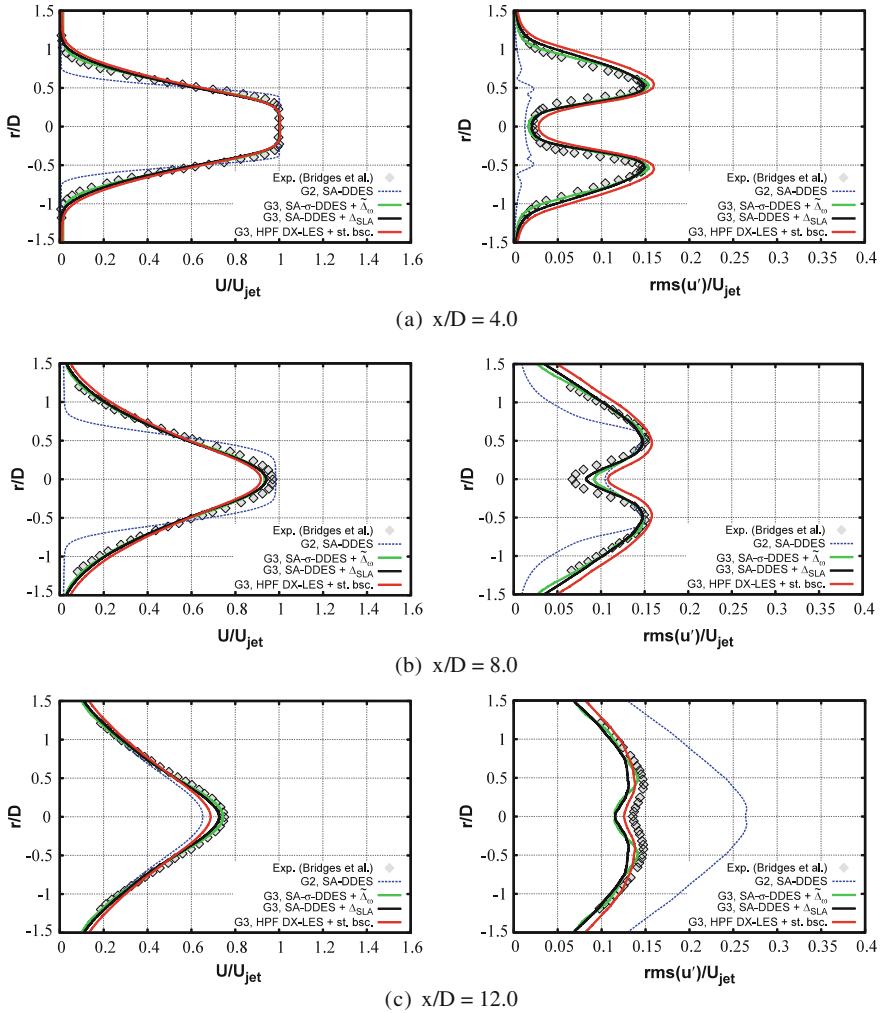


**Fig. 6** Mean velocity profiles and fluctuations at different positions downstream of nozzle

In Fig. 6, radial mean velocity and RMS profiles are shown for different downstream locations from the nozzle. Overall, an excellent agreement between the experimental data set and all three GAM methods is revealed at all displayed locations, where again standard DES under-predicts velocity fluctuations close to the nozzle at  $x/D = 4.0$  while over-predicting them further downstream.

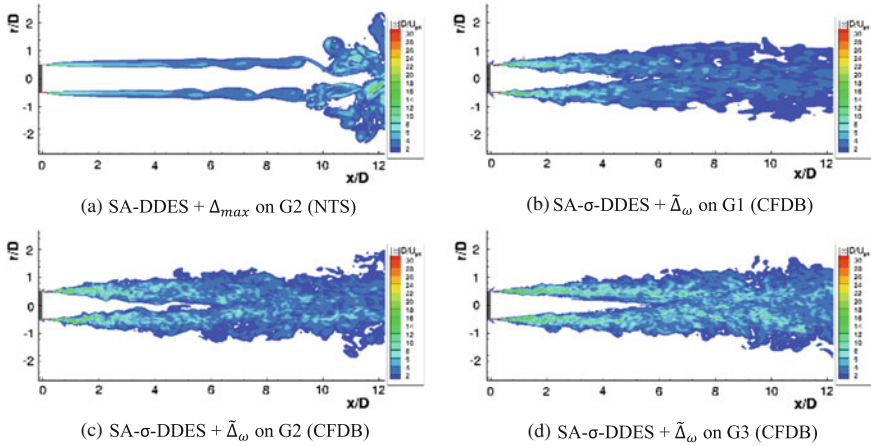


**Fig. 7** Assessment of grid dependency of SA- $\sigma$ -DDES approach (CFDB) on grids G1–G3, instantaneous vorticity magnitude is shown

## 6 Grid Resolution Study

To assess the grid resolution dependency of the respective new GAM approaches, all three partners conducted simulations on the grid levels G1–G3, where NTS additionally provided results for their method on G4. Figure 7 shows contours of instantaneous vorticity magnitude for the CFDB approach on the grids G1–G3.

The  $\sigma$ -DDES in conjunction with the vorticity-sensitised length scale  $\tilde{\Delta}_\omega$  seems to provide rapid transition to fully-resolved LES even on the coarsest grid level G1 and delivers clearly enhanced behavior on G2 compared to the reference simulation of NTS using standard DDES on the same grid.

The very favourable performance of the CFDB method on the coarser grids is also seen for the two other partner approaches of NTS and NLR, where centerline profiles are plotted in Fig. 8. All three GAM methods on all four grids outperform the benchmark model on G2. A slightly varying grid convergence behavior is seen though between the different partner simulations, where the CFDB simulations show a less pronounced grid refinement trend. We suspect that this is not model related, but due to different numerics. In particular, the spatial order of accuracy might be a factor here.

## 7 Acoustic Results (NTS)

In addition to the improvement of aerodynamics prediction, NTS conducted an extensive analysis of the farfield sound prediction, where their applied methodology is described in full detail in Shur et al. (2005). Results are presented here for the

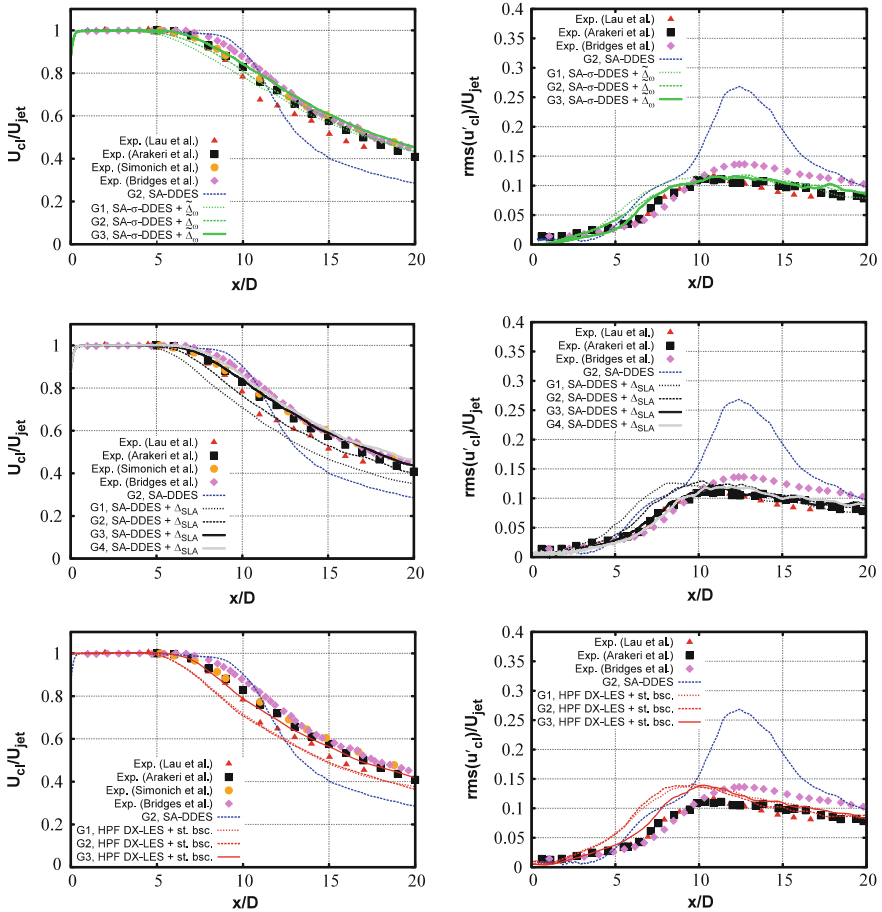


**Fig. 8** Comparison of results on all four grids G1–G4 for the new GAM methods and reference simulation on G2, mean velocity and RMS fluctuations on centreline is shown

NTS non-zonal GAM technique, i.e. the shear layer adapted length scale  $\Delta_{SLA}$ . In addition, NTS implemented the earlier CFDB approach of WALE-DDES (see Part II, Presentation of Approaches, Chapter “[Non-Zonal Approaches for Grey Area Mitigation](#)”) into their CFD code and assessed its performance in conjunction with the vorticity-sensitised length scale  $\tilde{\Delta}_\omega$ . Comparative simulations conducted by CFDB established that the  $\sigma$ -DES model is slightly superior to WALE-DES for this test case in terms of pure flow prediction, see Fuchs et al. (2014), so that the results presented in this section also give a good indication about the jet noise prediction capabilities of the  $\sigma$ -DES approach.

In Fig. 9, results are presented for farfield sound spectra at different observer angles. For all observer angles, standard SA-DDES significantly over-predicts farfield sound in the low frequency range up to  $St = 1$ . In contrast, both new GAM

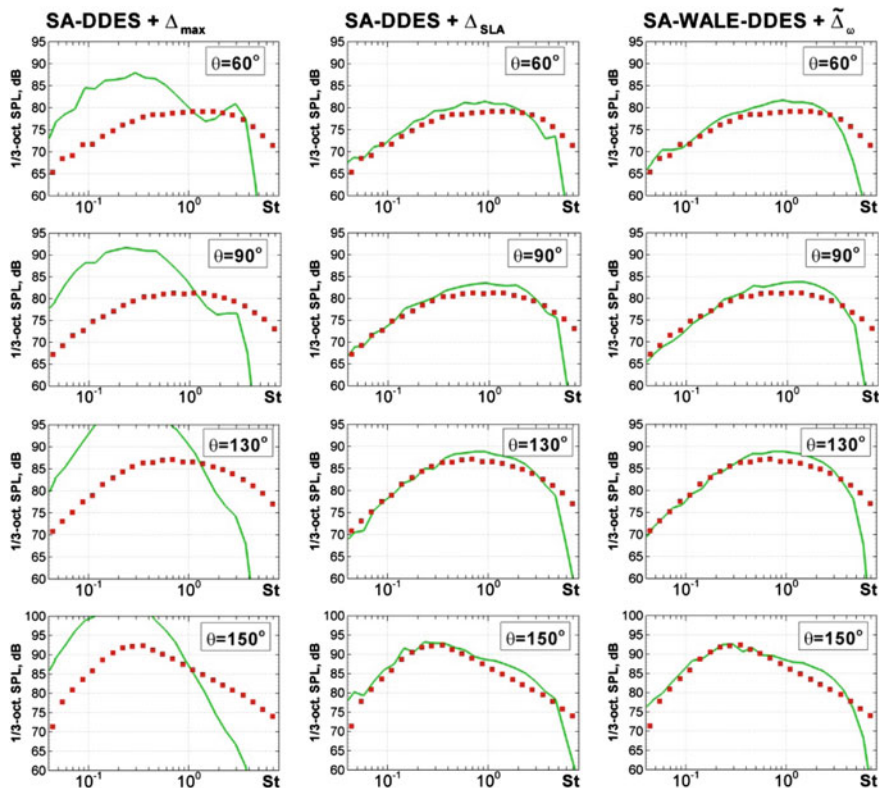


**Fig. 9** Farfield 1/3-octave noise spectra at different observer angles, comparison between experimental data (symbols), reference simulation and 2 GAM methods of NTS and CFDB in NTS code on grid G2

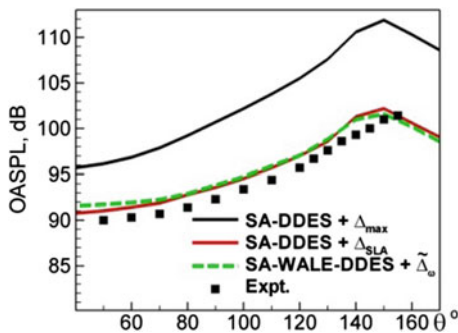


**Fig. 10** Overall sound pressure levels, comparison between experimental data and new GAM methods of NTS and CFDB in NTS code on grid G2

techniques deliver excellent results comparable to the quality of zonal approaches such as implicit LES [for which results have been published e.g. by NTS in Shur et al. (2011)], where both the shape of the experimental spectra as well as sound pressure levels are well reproduced almost up until the limit of grid resolution.

This also holds when inspecting overall sound pressure levels in dependence of the observer angle as shown in Fig. 10. Standard SA-DDES significantly over-predicts OASPL for every angle, whereas an agreement within 2–3 dB accuracy relative to the experimental data is achieved for both GAM approaches.

## 8 Conclusions and Outlook

Simulations for a single stream, unheated static jet configuration were carried out; a test case which was considered difficult to treat with DES-type methods prior to the Go4Hybrid project. In this project, three different non-zonal grey area mitigation techniques were assessed and subsequently compared with results obtained via the benchmark model standard SA-DDES. The following conclusions can be drawn from the study:

- Excellent results could be achieved by all partners with their respective GAM techniques, matching or even slightly improving those obtained with a zonal implicit LES approach in previous studies
- All methods converge towards the experimental data with grid refinement, where a very good performance is even seen on the coarsest grid level G1
- Minor differences in grid convergence behaviour are seen between the methods, which might be related to different numerical properties of the applied CFD codes (2nd order vs. 4th order discretisation)
- Noise evaluation by NTS demonstrates that the positive conclusions regarding flow prediction can be transferred to aeroacoustics results as well.

The success of the new GAM modifications to DDES-like methods now potentially enables commercial airplane engine jet-flap interaction simulations, which was previously difficult to achieve using e.g. implicit LES. The new methods offer shielded RANS behaviour for the boundary layers on wing, flap and nacelle while switching to scale-resolving LES-mode in the separated shear layer regions to capture the acoustic sources. As studying installation effects is an emerging field in CFD due to increasing fan diameters of commercial jet engines, the progress made in this project will have a significant impact on how such simulations are conducted in future industrial work.

# Delta Wing at High Angle of Attack

J. Kok, M. Fuchs and C. Mockett

## 1 Introduction

For a delta wing at high angle of attack, the flow at the suction side is fully separated and exhibits two large, turbulent vortices above the wing that are formed as the shear layers emanating from the leading edge roll up. Such a flow is a natural test case for hybrid RANS–LES methods and has been considered before in the literature, see e.g. Cummings et al. (2008), Lüdeke (2006), Morton (2009), and Schiavetta et al. (2007). Although successful computations are reported in the literature, experience in the previous EU-project ATAAC<sup>1</sup> showed that DES-type computations for a delta wing at high angle of attack can suffer from considerable grey areas where no resolved turbulence develops over much of the wing surface. Therefore, this test case has been considered further in the Go4Hybrid project. It is concerned in particular with the prediction of vortex breakdown above a delta wing with a sharp leading edge. The results obtained in ATAAC have been preserved in the ERCOFTAC QNET-CFD Wiki as an Application Challenge (Kok et al. 2015).

The same wing geometry as in ATAAC is considered: the NASA delta wing of Chu and Luckring (1996). This wing has been used extensively in the Vortex Flow Experiment 2 (VFE-2), see Lamar et al. (2009), which included both experiments and computations. The most detailed experimental results within VFE-2 are from the experiments of Furman and Breitsamter (2008, 2009), which include

---

<sup>1</sup>ATAAC project (Advanced Turbulence Simulation for Aerodynamic Application Challenges) funded by the European Union under Grant Agreement no. 233710.

---

J. Kok (✉)  
Netherlands Aerospace Centre NLR, Anthony Fokkerweg 2,  
1059 CM Amsterdam, The Netherlands  
e-mail: johan.kok@nlr.nl

M. Fuchs · C. Mockett  
CFD Software E+F GmbH, Bismarckstraße 10-12, 10625 Berlin, Germany

measurements of velocity fluctuations. Flow conditions from these experiments have been selected with an angle of attack that is large enough to exhibit vortex breakdown.

## 2 Test Case Definition

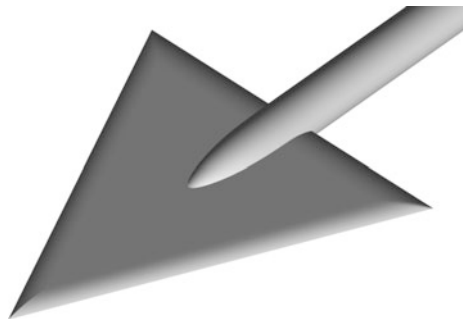
The NASA delta wing geometry has a  $65^\circ$  leading-edge sweep and a sharp leading edge. The geometry includes a sting. The analytic definition of the geometry (including sting) is given by Chu and Luckring (1996). An impression of the geometry is given in Fig. 1.

The considered flow conditions are a Mach number of  $M_\infty = 0.07$ , a Reynolds number of  $Re_{\text{mac}} = 1 \times 10^6$  based on the mean aerodynamic chord  $c_{\text{mac}}$ , and an angle of attack  $\alpha = 23^\circ$ . At these conditions, the vortex in the experiment breaks down between  $x/c_r = 0.6$  and  $x/c_r = 0.8$ . The mean aerodynamic chord equals  $2/3$  of the root chord ( $c_r$ ).

The flow around a delta wing at high angle of attack is characterized by the main vortex developing above the wing. The vortex is formed as the shear layer emanating from the leading edge rolls up, starting immediately at the apex in case of a sharp leading edge. At high Reynolds numbers, the shear layer rapidly becomes unstable and a turbulent vortex is formed. Between the main vortex and the leading edge, secondary separation may occur. At a sufficiently high angle of attack, the vortex breaks down: the high axial velocity in the vortex core drops rapidly to a value close to zero.

To properly capture this flow, it is essential to capture the shear layer separating from the leading edge and in particular, the instabilities developing in this shear layer. Experience from ATAAC showed that the shear layer may remain stable in DES-type computations over at least the first half of the wing. As a consequence, resolved turbulence may be completely absent in the main vortex over the same part of the wing. In other words, the computations may suffer from a severe grey-area problem that needs to be mitigated.

**Fig. 1** Impression of geometry of NASA delta wing



The complex, highly three-dimensional flow topology is of particular interest, since it represents a strong departure from the planar shear studied e.g. in the fundamental shear layer test case. As such, the delta wing provides an important test of GAM method generality.

### 3 Computational Set-up

The common multi-block structured grid from ATAAC is employed, which consists of 22 blocks and 6.3 million grid cells (see Fig. 2). Based on a grid dependence study performed in ATAAC, it was concluded that this grid is fine enough to capture the flow and resolve a significant part of the turbulence in the main vortex (Kok et al. 2015). The grid has a conical structure over a large part of the wing: the grid covering the main vortex is essentially isotropic at each chord-wise station (outside the boundary layer) and the mesh width grows in all directions together with the main vortex, going from approximately  $0.003c_{\text{mac}}$  to  $0.011c_{\text{mac}}$ . In other words, the grid resolution relative to the main vortex is kept constant. Only in a small region near the apex, the conical structure is not fully maintained, avoiding a grid singularity. The far-field boundary is located at three root chord lengths from the wing, which was also found to be sufficient in ATAAC.

Non-zonal DES-type computations have been performed by CFDB and NLR. As baseline, CFDB employed SA-DDES and NLR employed SST-DDES, both using the standard definition of the filter width ( $\Delta_{\text{max}}$ ). As grey-area mitigation (GAM) approach, CFDB extended SA-DDES with the Nicoud  $\sigma$  model (SA- $\sigma$ -DDES) and with the vorticity-sensitized filter width ( $\tilde{\Delta}_\omega$ ), while NLR employed delayed X-LES with a high-pass filtered SGS model and a spatially correlated backscatter model. See Part II (Presentation of Approaches, Non-Zonal Approaches for Grey Area Mitigation) for precise descriptions of these models.

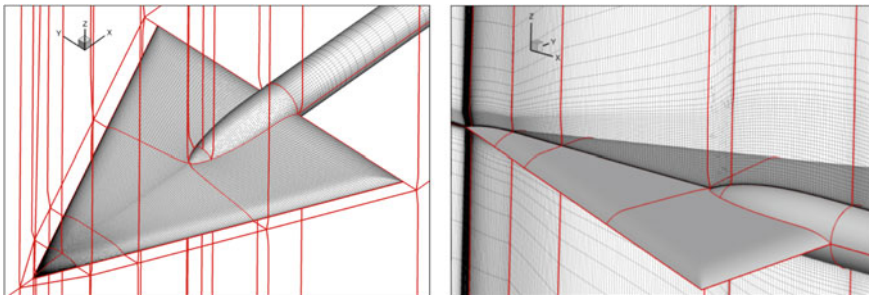


Fig. 2 Impression of multi-block structured grid



All computations have been performed on the mandatory grid with second-order implicit time integration. In terms of numerical methods, the main difference between the two partners is that CFDB employed a second-order blended central/upwind scheme of Travin et al. (2000), whereas NLR employed a fourth-order low-dispersion skew-symmetric finite-volume method (Kok 2009). Both partners used a time step of  $\Delta t = 3.75 \times 10^{-4} \text{CTU}$ , with the convective time unit defined as  $\text{CTU} = c_{\text{mac}}/u_{\infty}$ . This corresponds to a convective CFL  $\approx 1/8$  based on the free-stream velocity and a mesh width of  $0.003c_{\text{mac}}$ . Statistics were computed over a time period of approximately 13 CTU after an initial transient of 7 CTU.

The experiment reports a dominant frequency of  $St = fc_{\text{mac}}/u_{\infty} = 2$  implying 1333 time steps per period. Schiavetta et al. (2007) also report higher relevant frequencies, e.g., for shear layer instabilities  $St = 8-10$ . These frequencies are also well resolved by the time step.

## 4 Results

As a first impression of the results, instantaneous vortical structures are visualized by iso-surfaces of the Q-criterion as shown in Fig. 3. The baseline methods (sub-figures a and b) display only large-scale structures over the first half of the wing. In particular, helical sub-vortices can be recognized. Note that these sub-vortices are spatial instabilities of the main vortex, which are stationary in time. In contrast, the computations with GAM approaches (Fig. 3 subfigures c and d) display fine-scale time-dependent structures starting very close to the apex of the wing. Hence, the GAM approaches have a strong qualitative impact on the computational results.

The strong impact of the modelling approach on the flow above the first half of the wing can be assessed further by looking at the level of resolved turbulent kinetic energy at the station  $x/c_r = 0.4$  in comparison with the measured turbulent kinetic energy (Fig. 4). The baseline methods show practically no resolved turbulence at all, in stark contrast to the GAM methods, which give levels of resolved turbulence that are much more in line with the hotwire measurements, although they under-predict the level in the vortex core. At the two stations further downstream (Figs. 5 and 6), resolved turbulence has started to develop in the baseline computations, but its distribution still strongly differs from the experiment. The two GAM results show distributions that are quite similar, but now the level in the core is over-predicted compared to the experiment, which shows a local minimum. It should be stressed, however, that the hotwire measurements are intrusive and appear to have caused significantly earlier vortex breakdown compared to the non-intrusive PIV measurements (discussed further below). Most likely, this early vortex breakdown has altered the level and distribution of turbulent kinetic energy at the last two stations, especially in the vortex core.

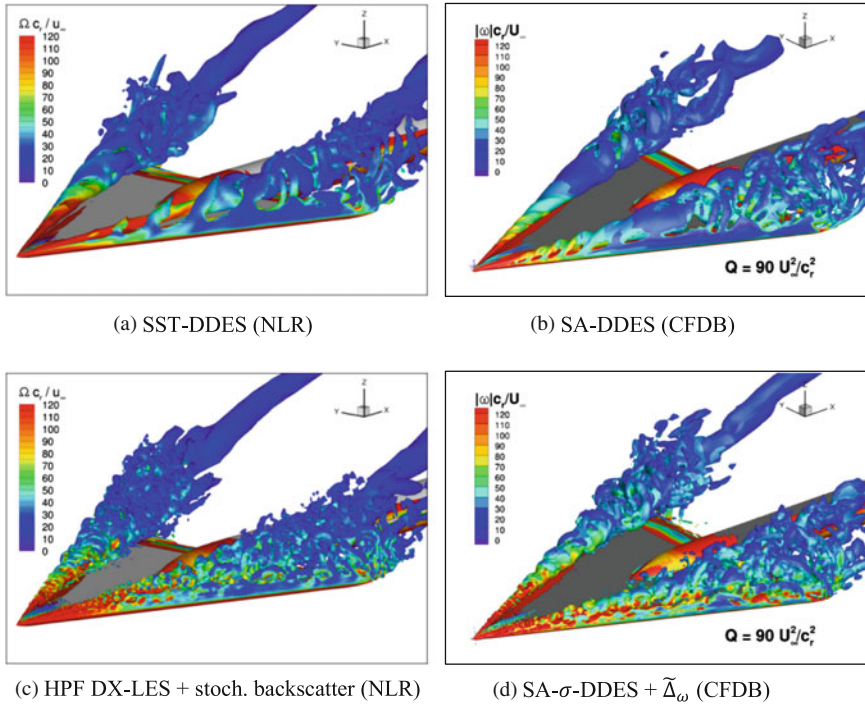


**Fig. 3** Instantaneous vortical structures (iso-surfaces of Q-criterion coloured with vorticity magnitude)

The distribution of the mean pressure coefficient at five chord-wise stations is compared to the experiment in Fig. 7. At most stations, the suction peak below the main vortex is higher and in closer agreement with the experiment for the GAM methods than for the baseline methods, especially at  $x/c_r = 0.6$  and  $x/c_r = 0.8$ . Also, the outboard pressure plateau for the GAM methods closely agrees with experiment, indicating a comparable level of secondary separation.

The SST-DDES result overpredicts the secondary separation at the first station ( $x/c_r = 0.2$ ), indicated by a clear second suction peak. At this station, all computational results show a strong main suction peak, contrary with the experiment. This suggest that in the experiment, a strong, detached vortex has not yet formed, which is unexpected for a wing with a sharp leading edge and resembles more the situation for a round leading edge. At a higher Reynolds number ( $2 \times 10^6$ ), the experiment does show a clear main suction peak (Furman and Breitsamter 2009). At the last station ( $x/c_r = 0.95$ ), the mean pressure distribution compare less well to the experiment; here, the geometry curves towards the sharp trailing edge and the flow has separated locally. This shallow separation from a smooth surface may be difficult to capture accurately with non-zonal DES methods.

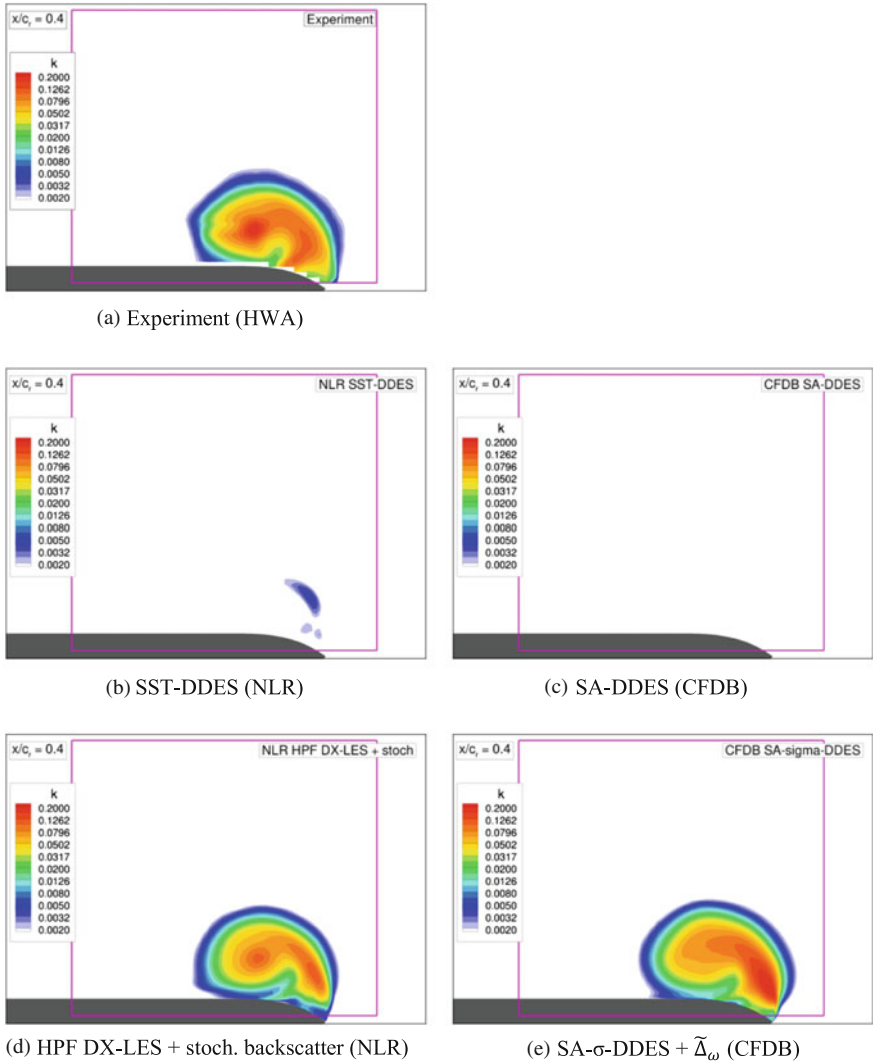


**Fig. 4** Measured and resolved turbulent kinetic energy at cross-stream plane

The strong difference between the baseline and GAM methods is again seen in the distribution of the RMS value of the pressure coefficient (Fig. 8). The baseline methods show practically no pressure fluctuations at the first two stations, whereas the GAM methods show high levels at these stations, that gradually decay going downstream. Clearly, the GAM results match the experiment more closely at all stations, especially for the HPF DX-LES computation at stations  $x/c_r = 0.4$  and  $x/c_r = 0.6$ .

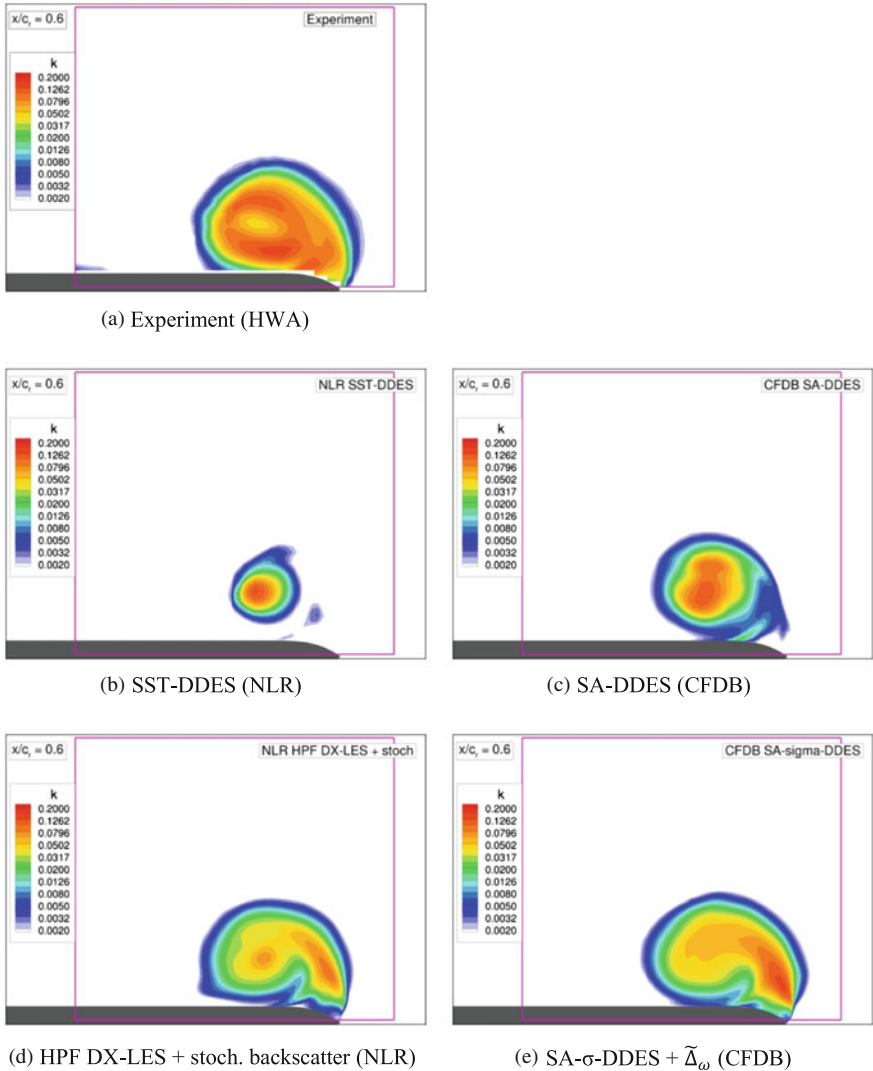


**Fig. 5** Measured and resolved turbulent kinetic energy at cross-stream plane

The mean velocity distribution is compared to two computational results: hot-wire (HWA) and PIV measurements (Figs. 9, 10, 11 and 12). These two measurement techniques show remarkably different results. For the HWA results, the velocity direction below the main vortex is not aligned with the wing surface, which cannot be correct. Hence, these measurements are considered less reliable than the non-intrusive PIV measurements. Furthermore, at  $x/c_r = 0.6$ , the vortex has clearly broken down in the HWA results, showing a large region in the vortex core with a

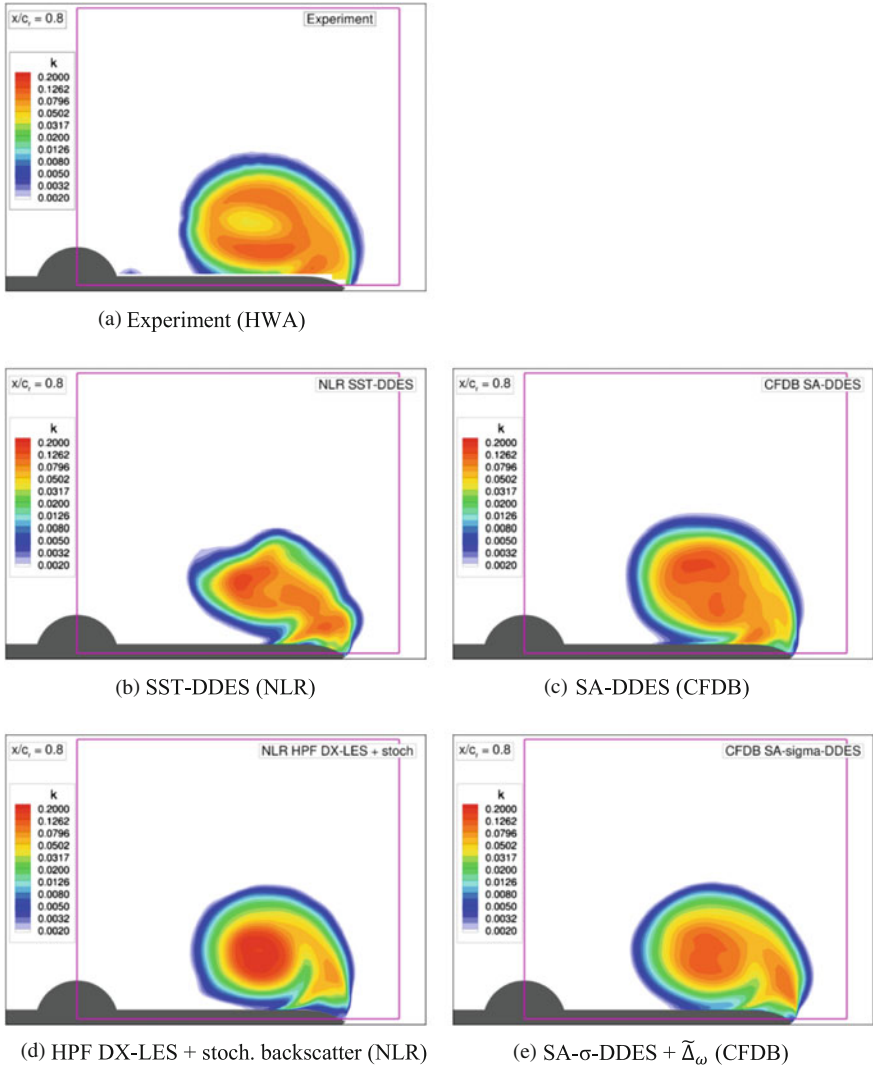
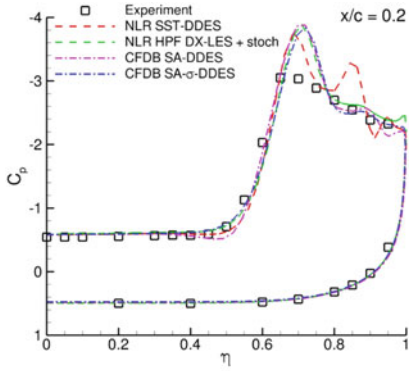


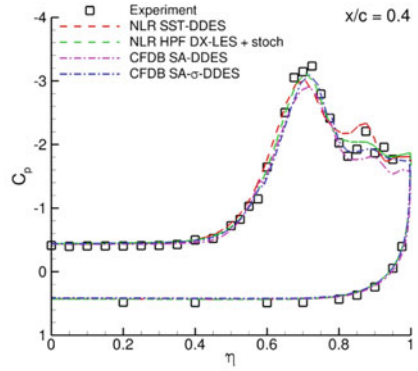
**Fig. 6** Measured and resolved turbulent kinetic energy at cross-stream plane

small chord-wise velocity component. The vortex in the PIV results, on the other hand, does not start to break down until the station  $x/c_r = 0.8$  and shows a large low-velocity region only at the last station. This strong difference in breakdown location may be attributed to the intrusive nature of the HWA measurements, which may have triggered the premature collapse of the vortex.

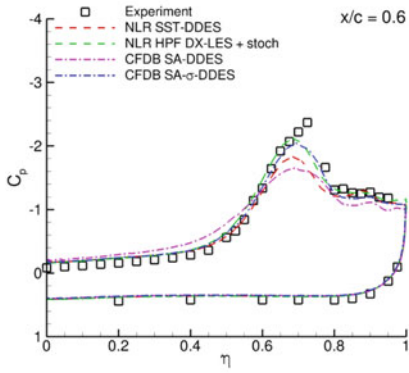
Taking the PIV measurements as reference, again the GAM methods correspond more closely to the experiment than the baseline methods. Especially SA-DDES



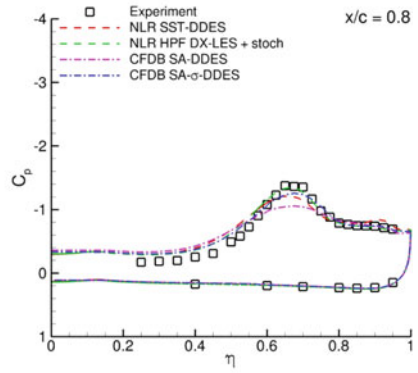
(a)  $x/c_r = 0.2$



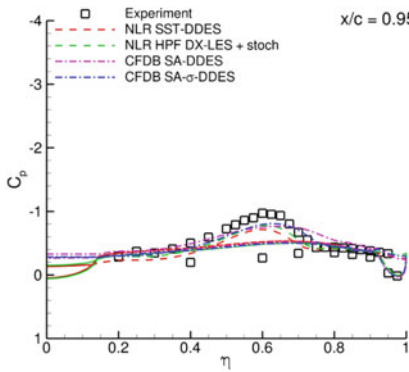
(b)  $x/c_r = 0.4$



(c)  $x/c_r = 0.6$

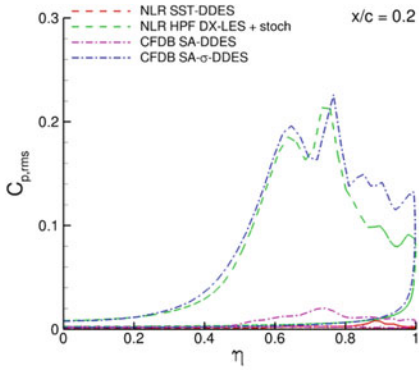


(d)  $x/c_r = 0.8$

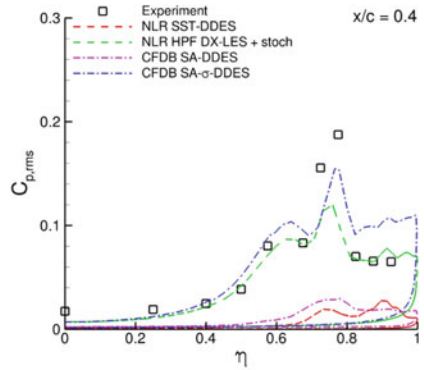


(e)  $x/c_r = 0.95$

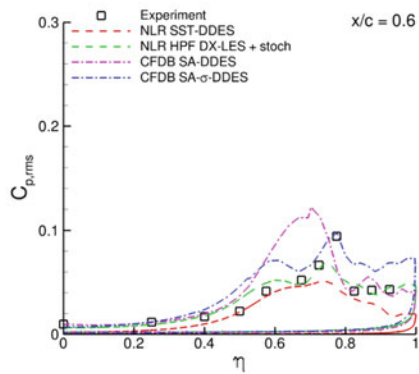
Fig. 7 Mean pressure coefficient at five chord stations



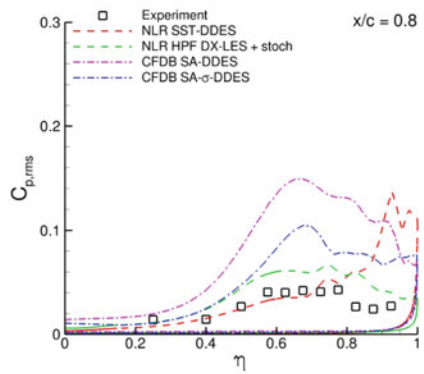
(a)  $x/c_r = 0.2$



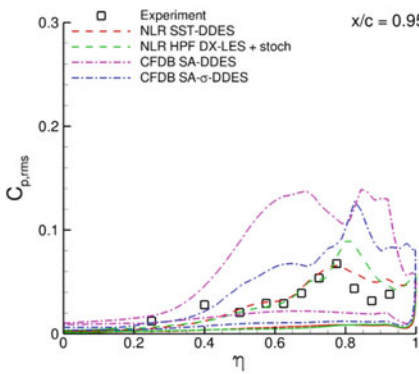
(b)  $x/c_r = 0.4$



(c)  $x/c_r = 0.6$



(d)  $x/c_r = 0.8$



(e)  $x/c_r = 0.95$

**Fig. 8** RMS of pressure coefficient at five chord stations

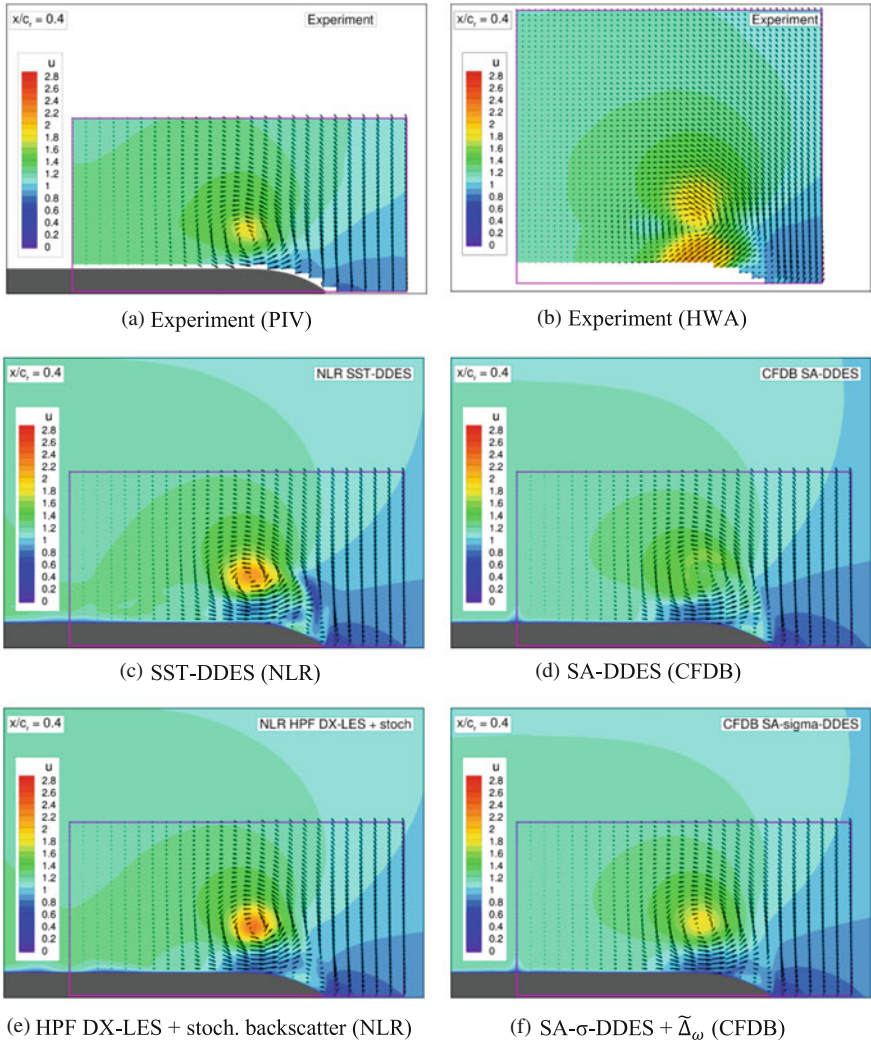


**Fig. 9.** Time-averaged velocity field at cross-stream plane  $x/c_r = 0.4$  (contour plots of x-component and vector plots of in-plane components)

predicts the vortex breakdown further upstream, but also SST-DDES already tends towards breakdown at  $x/c_r = 0.6$ . Apparently, under-prediction of upstream resolved turbulence by the baseline methods results in premature prediction of vortex breakdown, which is improved by the GAM methods. At  $x/c_r = 0.8$ , where the vortex in the PIV results has just started to break down, also the GAM results show smaller breakdown regions than the baseline methods (in particular



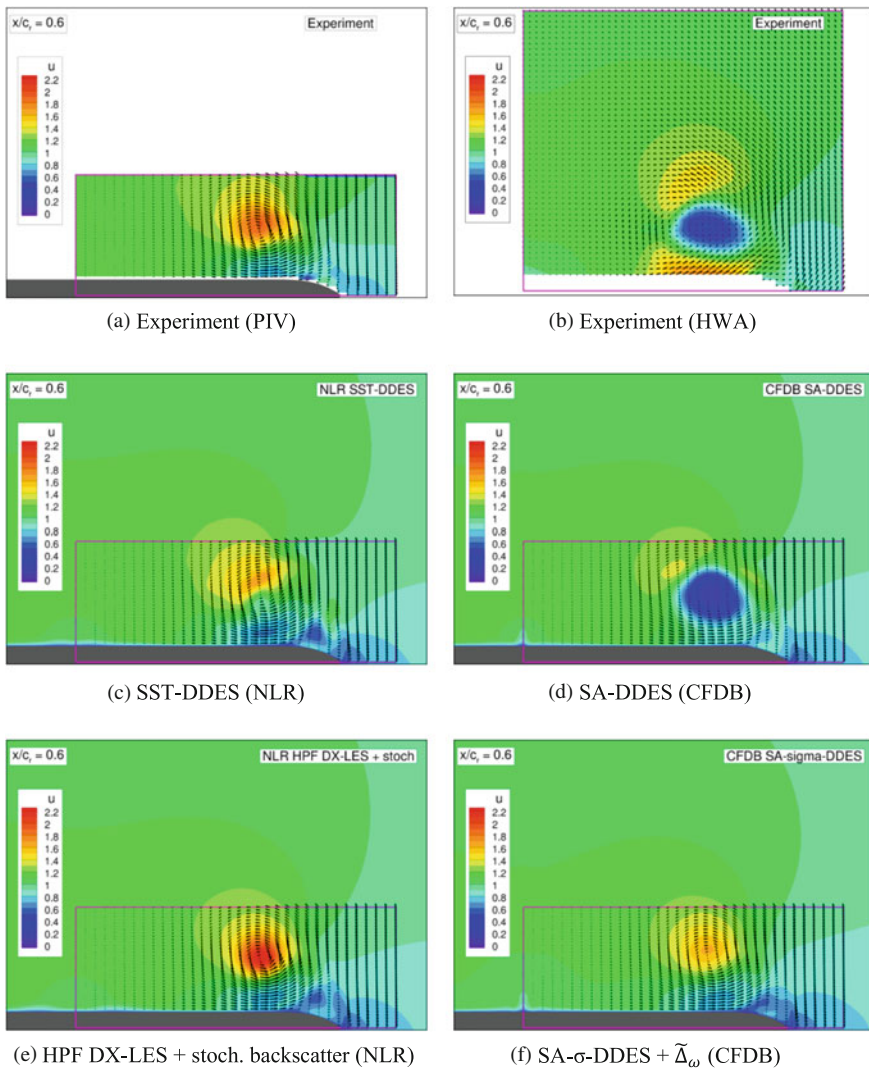


**Fig. 10** Time-averaged velocity field at cross-stream plane  $x/c_r = 0.6$  (contour plots of x-component and vector plots of in-plane components)

SA-DDES shows a very large breakdown region). Also at the last station, the size of the breakdown regions of the GAM results agrees with the experiment and again especially SA-DDES strongly overpredicts this region.

Finally, the PIV measurements show some secondary separation, but it is perhaps not fully resolved. Also, the computational results show secondary separation.

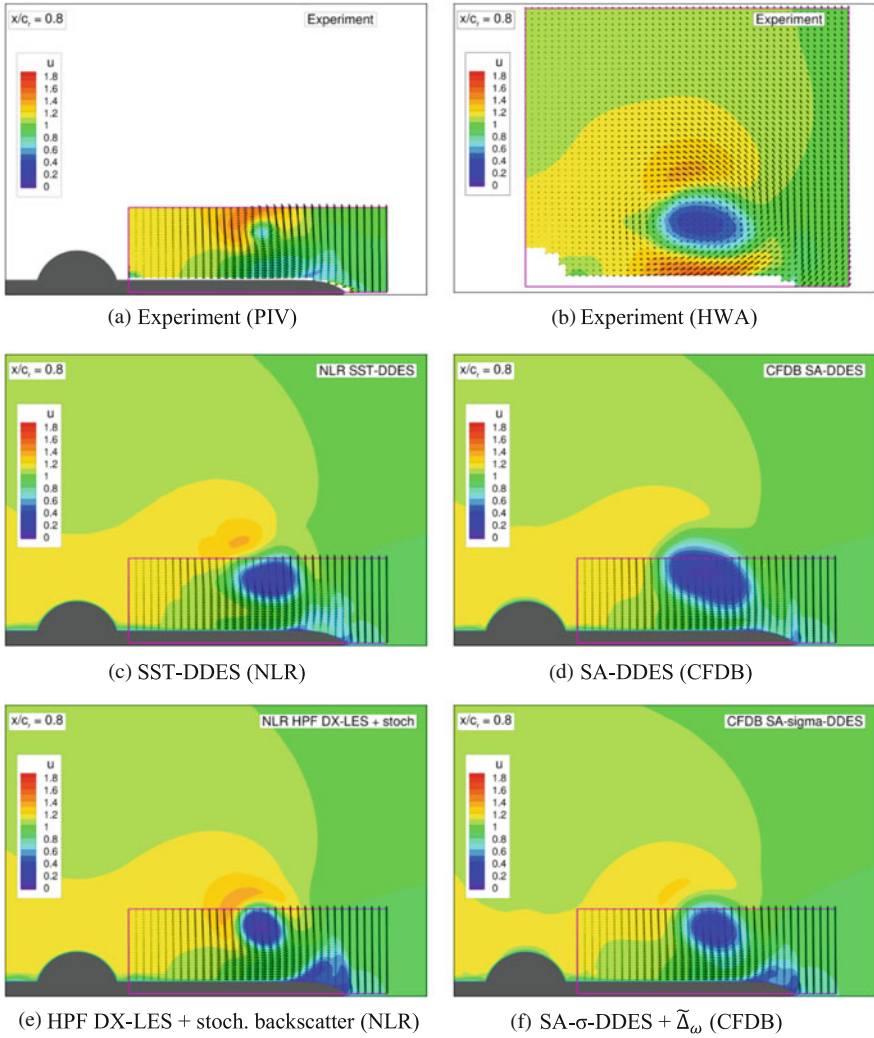


**Fig. 11** Time-averaged velocity field at cross-stream plane  $x/c_r = 0.8$  (contour plots of x-component and vector plots of in-plane components)

The impression is that the secondary separation is somewhat more pronounced in the GAM results than in the baseline results. It is hard to judge which agrees better with experiment, although the good correspondence of the pressure plateaus discussed above, indicates that the strength of the secondary separation is predicted well by the GAM methods.

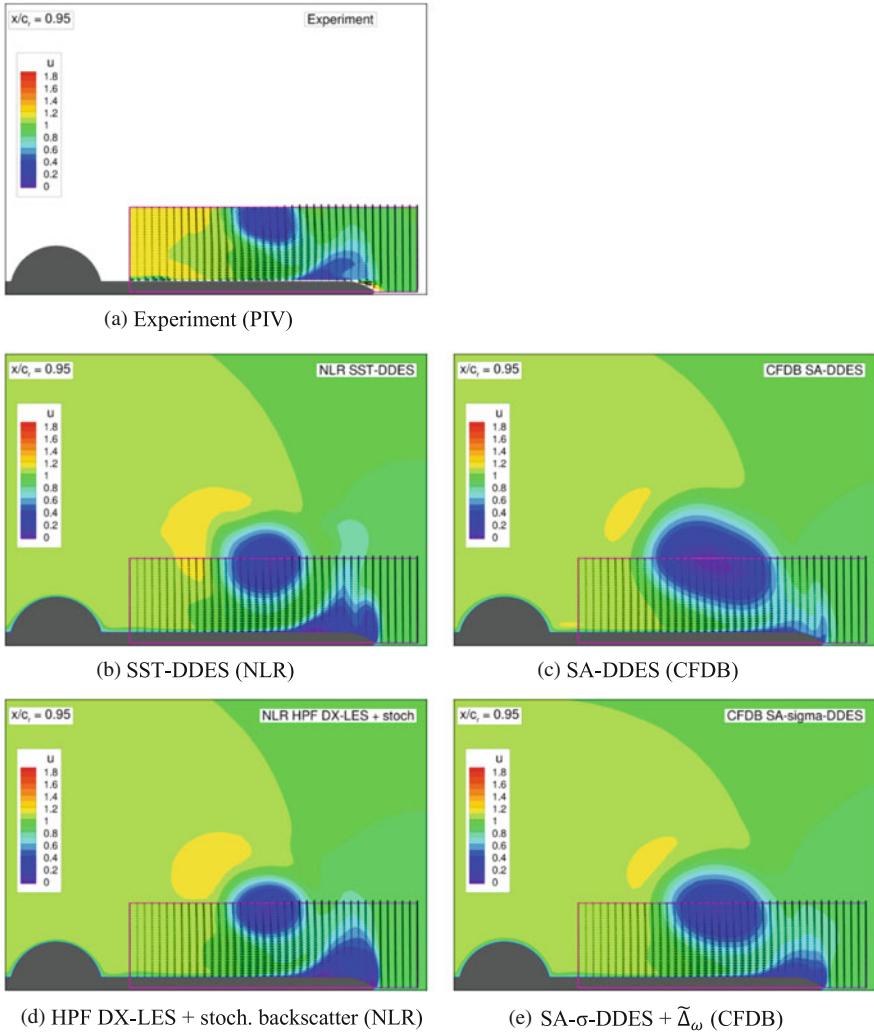


**Fig. 12** Time-averaged velocity field at cross-stream plane  $x/c_r = 0.95$  (contour plots of x-component and vector plots of in-plane components)

## 5 Conclusion

DES-type computations of the flow over the NASA delta wing with sharp leading edge at high angle of attack can suffer strongly from the grey area problem in which the turbulence is not resolved even though the computation is expected to be in LES mode. This grey area may cover the main vortex above the upstream half of the wing. This lack of resolved turbulence apparently results in a breakdown of the main vortex that is too far upstream compared to PIV measurements.

Two grey-area mitigation (GAM) methods have been tested for this case:

- SA-DDES extended with the Nicoud  $\sigma$  model and the vorticity sensitized filter width  $\tilde{\Delta}_\omega$ , and
- delayed X-LES extended with a high-pass filtered SGS model and a spatially correlated stochastic backscatter model.

Generally, these two GAM methods result in strong improvements over the baseline models and give very similar results that only differ in some minor respects. These methods predict high levels of resolved turbulence in the main vortex starting close to the apex of the wing as well as high pressure fluctuations over the upstream part of the wing, both matching much more closely with the experiments than is the case for the baseline methods. As a result, the location of vortex breakdown is shifted further downstream and both location and strength of the breakdown are found to be in closer agreement with PIV measurements.

**Acknowledgements** Experimental results have been kindly provided by Christian Breitsamter from TU Munich.

# 3-Element Airfoil

A. Probst, S. Probst and D. Schwamborn

## 1 Introduction

High-lift configurations are often a challenge for numerical simulation once it comes to the prediction of maximum lift. This is not so much a problem of the separated flow in the wing and slat coves, which are rather confined, but of the pressure induced separation taking place on the upper flap surface. With respect to a Scale-Resolving Simulation (SRS) this kind of separation is certainly prone to the grey area issue, while due to the recirculation of turbulent eddies the cove flow is mainly treatable by standard SRS approaches like DDES. Other important aspects in the frame of SRS and the grey area are the shear layers leaving the trailing edges of all airfoil elements contributing to noise (especially in the case of the slat) and the mixing of shear layers with wakes. As all these interactions together determine the global flow pattern (i.e., lift and drag), every single aspect has to be treated correctly to arrive at accurate flow and sound predictions of such high-lift configurations.

In order to build on pre-existing knowhow of the Go4Hybrid partners, the DLR-F15 (Wild et al. 2006) airfoil has been chosen as the 3-element airfoil in this study, as the same airfoil was already a test case in the ATAAC EU-project (Schwamborn et al. 2012). This airfoil originates from the DLR project LEISA (Low noise exposing integrated design for start and approach, 2005–2008), which combined activities in the research areas of high lift system design, flow control and aero-acoustic design methods. The geometry of the airfoil consists of three elements, i.e. slat, main wing and flap (see Fig. 1), where the position of slat and flap was optimized by DLR and is denoted by F15 3eOpt.

---

A. Probst (✉) · S. Probst · D. Schwamborn  
DLR (German Aerospace Center), Göttingen, Germany  
e-mail: Axel.Probst@dlr.de

D. Schwamborn  
e-mail: dieter.schwamborn@dlr.de

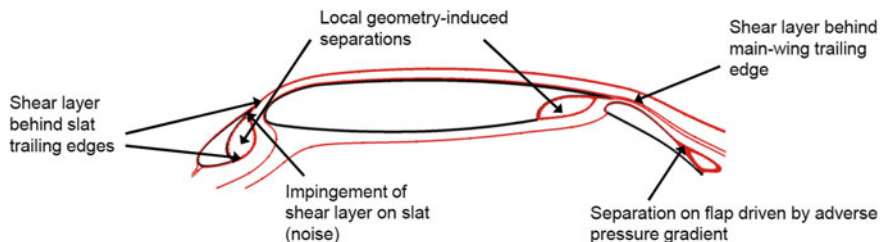


**Fig. 1.** Geometry and basic flow features of the considered 3-element airfoil

The inflow conditions for the considered test case are  $M = 0.15$  and  $Re = 2.094 \times 10^6$ , where  $Re$  is based on the retracted chord length  $c$  ( $= 0.6$  m in the experiment). The (corrected) angle of attack is  $\alpha = 6^\circ$ . At these conditions, a rather complex interaction of different flow phenomena and modelling challenges is expected, which is illustrated in Fig. 1 as well.

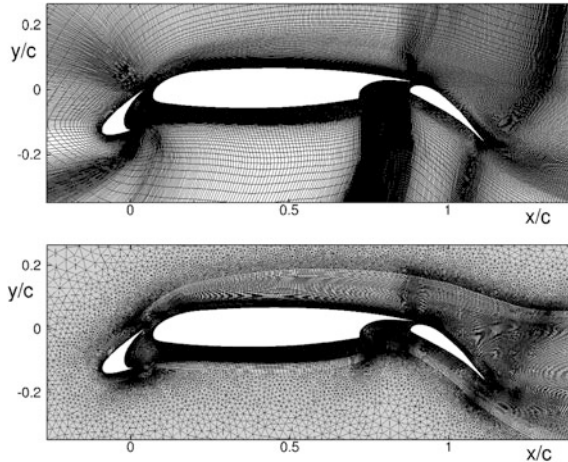
Experimental measurements at these flow settings were performed in the low-speed wind-tunnel Braunschweig (NWB), Germany. Experimental data comprise the mean surface pressure coefficient  $c_p$  in three span-wise sections, as well as profiles of the total pressure at around 80 mm downstream of the flap trailing edge. Acoustic data from microphone wall array are available, too. However, based on experience from the precursor EU-project ATAAC, the experimental uncertainties in the different wind-tunnel campaigns (comprising 3D- and side-wall effects, laminar/turbulent transition, angle-of-attack corrections etc.) are considered too numerous to use this case for detailed model validation. Accordingly, this test case has been chosen mainly as a relevant application and demonstration case rather than a validation case.

## 2 Basic Simulation Setup

Because of the large uncertainties in reproducing the experimental conditions, it was decided to keep the simulation setup rather simple and focus the assessment on model-to-model and code-to-code comparisons. Therefore, according to the mandatory simulation setup, the DLR-F15 is considered under free-air conditions using farfield boundaries, and fully-turbulent modelling is applied on all viscous airfoil surfaces.

A block-structured hexahedral mesh with  $27 \times 10^6$  points generated by NTS is provided as the mandatory ( $M$ ) grid, see Fig. 2. In spanwise direction, the grid is composed of 100 grid layers over a domain width of  $L_z/c = 8\%$ , which is considered sufficient to resolve the relevant turbulent scales in combination with spanwise periodic boundary conditions. Taken exemplarily from the center of the upper main-wing element ( $x/c = 0.5$ ), the grid exhibits normalized cell spacings of  $\Delta x^+ \approx 350$ ,  $\Delta y^+(1) \approx 1$ ,  $\Delta z^+ \approx 100$  (in wall units) and  $\Delta x/\delta = 0.23$  and

**Fig. 2.** Mandatory grids (*top* structured; *bottom* hybrid) for the 3-element airfoil



$\Delta z/\delta = 0.065$  (relative to the local boundary-layer thickness), respectively. With this resolution, the grid is considered suitable for different scale-resolving approaches, although any wall-modelled LES should be restricted to the upper sides of the main wing and the flap.

For partners using unstructured flow solvers, an alternative mandatory hybrid (*MH*) grid was derived from the structured grid by replacing the hexahedral cells in the outer flow field by prisms. Thus, while the two grids are identical in the critical viscous flow regions near the airfoil surface and in the wake (see Fig. 2), the hybrid grid saves around 1/3 of the grid points and relaxes the cell anisotropy of the block-structured grid near the farfield boundary.

Regarding temporal resolution, a mandatory physical time step of  $\Delta t = 2 \times 10^{-4} c/U_\infty$  is suggested for 2nd-order time-stepping schemes. The initial transient simulation phase should comprise at least  $4 c/U_\infty$  (i.e., 4 CTU = “convective time units”), while another 2–3 CTU for statistical averaging is considered sufficient to obtain meaningful mean values and Reynolds stresses.

Note that no mandatory interface positions for the embedded approaches were defined. This allows the partners to concentrate on the most promising setups for their respective methods, according to their own experience.

### 3 Partner-Wise Description of Numerical Setup

The 3-element airfoil case was considered by 5 different partners in the Go4Hybrid project, who mostly considered either non-zonal (NLR, FOI), or embedded approaches (DLR, ONERA). Only NTS conducted simulations with both types of grey-area mitigation (GAM) methods, thus allowing for a direct comparison of results from a single flow solver.

### 3.1 Non-zonal Methods

#### 3.1.1 NLR

NLR has performed delayed X-LES computations combining two non-zonal GAM approaches: a high-pass filtered SGS model (Kok and Van der Ven 2012) and a stochastic SGS model. The stochastic model captures energy backscatter at the correct rate and includes both spatial and temporal correlations of the stochastic sub-grid stresses (see Part II, Presentation of Approaches, Non-Zonal Approaches for Grey Area Mitigation). The approach is non-zonal in the sense that the RANS and LES regions are not explicitly fixed, but determined dynamically by the model, with the exception of some regions that are set to RANS a priori (such as the main wing and flap pressure sides as well as the main wing suction-side boundary layer). An impression of instantaneous RANS and LES regions is given in Fig. 3.

The computations have been performed on the mandatory, structured grid, using a fourth-order low-dispersion skew-symmetric finite-volume method (Kok 2009). The equations are integrated in time with the 2nd-order midpoint rule and a time step of  $\Delta t = 1 \times 10^{-4} c/U_\infty$ . After a transient period of 4.2 CTU, flow statistics have been gathered over a time period of 4 CTU.

#### 3.1.2 FOI

With this test case FOI has verified an improved SGS modelling for grey-area mitigation in non-zonal hybrid RANS-LES methods by resolving a 3-element high-lift flow. The approach is based on an energy-backscatter function incorporated in the LES mode for the purpose of enhancing the resolved large-scale turbulent contents in the LES region. In conjunction with a conventional SGS eddy-viscosity formulation, the energy-backscatter part is formulated in terms of velocity gradients and functioning as a scale similarity model (Peng and Davidson 2002, 2009). The energy-backscatter function was previously examined using an

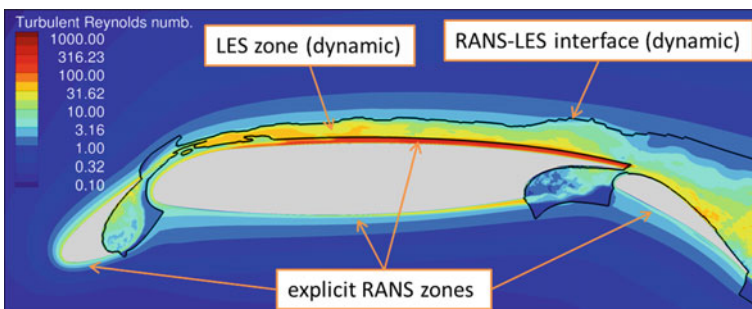


Fig. 3. Non-zonal setup of NLR



algebraic non-zonal hybrid RANS-LES (HYB0) model (Peng 2006) as the baseline model for fundamental flows (Peng 2012). In Go4Hybrid, the modelling formulation has been further refined and the SGS length scale has been re-examined using a vorticity-based length scale,  $\Delta_\omega$ , or an alternative length scale in the baseline HYB0 model by replacing the maximum cell size,  $\Delta_{\max}$ , with  $\Delta_{\min}$ , in combination with the conventional control-volume-based filter width  $(\delta V)^{1/3}$ .

In addition to the computation using the baseline HYB0 model, three computations have been conducted using, respectively, the energy-backscatter (HYB0 M),  $\Delta_\omega$  in HYB0 and  $\Delta_{\min}$  in HYB0 M. The results presented here are obtained using the HYB0 M model. In all simulations, the physical time step was set to  $\Delta t = 1 \cdot 10^{-3} c/U_\infty$  based on numerical analysis (Peng 2013), which is however larger than the recommended  $\Delta t$ . FOI has used their in-house unstructured CFD solver Edge for the computation based on the mandatory hybrid grid (*MH*) generated by DLR. A 2nd-order central scheme was used for spatial discretization, and an implicit 2nd-order backward scheme for physical time advancement. At each time step, the solution is converged using an explicit three-stage Runge-Kutta scheme accelerated by an efficient multigrid strategy and implicit residual smoothing. The numerical settings have been further summarized in Table 1 in comparison with those by other partners.

### 3.1.3 NTS

A non-zonal method used by NTS for computations of this flow is the SST-based IDDES combined with the shear-layer adapted subgrid length-scale  $\Delta_{SLA}$  outlined in detail in the paper of Shur et al. 2015. The simulation was carried out on the mandatory multi-block structured grid (see upper frame in Fig. 2) with the use of the incompressible branch of the NTS solver (see Shur et al. 2004 for details). The code employs implicit 2nd order in time flux-difference splitting scheme of Rogers and Kwak with a weighted (4th order centered—3rd order upwind biased) approximation of the inviscid fluxes controlled by an automatic (solution dependent) blending function (Strelets 2001).

## 3.2 Embedded Methods

### 3.2.1 ONERA

ONERA has investigated three complementary embedded-modelling setups for the 3-element airfoil. They utilize the Spalart-Allmaras-based Zonal DES (ZDES) and apply all available ZDES modes (0–3) in different parts of the flow domain. The simulations differ only in the modelling of the region near the trailing edge of the upper wing surface, marked by the grey box in Fig. 4.

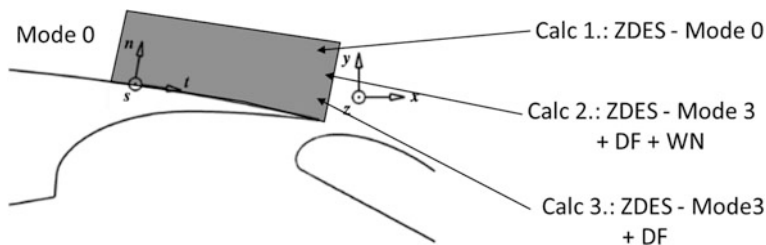


**Fig. 4.** Setup of the three ZDES simulations of the 3-element airfoil conducted by ONERA

While in the reference setup (Calc 1.), the Mode 0 (RANS modelling) is simply extended along the whole main wing down to the trailing edge, the other two simulations apply Mode 3 (wall-modelled LES) together with Dynamic Forcing + White Noise (Calc 2.) and just Dynamic Forcing (Calc 3.) in this region. Note that while only Calc 3 is included in the results section below, a preliminary comparison by ONERA has shown a very close agreement between the 3 different simulations in terms of mean-flow predictions. A further discussion of the fluctuating aerodynamic field around the airfoil together with its relation to aeroacoustic feedback mechanisms can be found in Deck and Larauie 2013. ONERA uses an own block-structured grid with 48.6 million grid points in order to manually set the ZDES modes as desired. The physical time step is  $\Delta t = 1.7 \times 10^{-5} c/U_\infty$ , i.e., one order of magnitude smaller than the mandatory one.

### 3.2.2 DLR

To realize embedded LES for the 3-element airfoil using the unstructured TAU code, DLR applies its implementation of the Synthetic-Eddy Method with volume-source terms in user-defined interface planes and combines this approach with a “zonal” SST-based IDDES. In particular, the flow regions upstream of the SEM planes are manually set to SST-RANS, whereas downstream the SST-IDDES is set to operate in wall-modelled LES mode.

Two embedded setups were investigated: The first one is similar to ONERA’s setup, as synthetic turbulence is injected into the upper-side boundary layer of the main wing, somewhat upstream of the trailing edge at  $x/c = 0.75$ . In the second setup, which is roughly sketched in Fig. 5 (left), another SEM plane is located just ahead of the wing cove on the lower side, at  $x/c = 0.7$ . Note that only the latter setup (two SEM planes) is included in the comparative assessment.

On the numerical side, DLR applies the mandatory hybrid grid (*MH*) which is additionally subjected to a spanwise coarsening outside of the structured region and upstream of the fixed interfaces, see Fig. 5. Apart from reducing numerical stiffness when using the unstructured TAU solver, a significant grid-point reduction ( $\sim 60\%$ ) could be achieved without losing any grid resolution in the LES regions. In those regions, a low-dissipation low-dispersion (LD2) 2nd-order central scheme

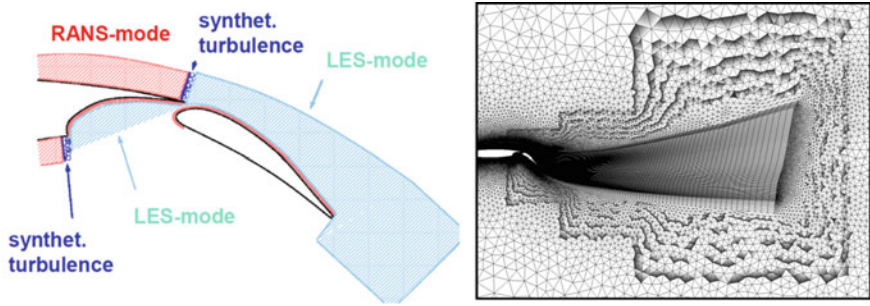


**Fig. 5.** Sketch of DLR’s extended embedded setup (*left*) and the mandatory hybrid grid with spanwise coarsening, where the coarsening steps are made visible by a suitable grid cut (*right*)

is applied to accurately resolve the turbulent structures. In both simulations, the mandatory physical time step of  $\Delta t = 2 \times 10^{-4} c/U_\infty$  is used.

### 3.2.3 NTS

NTS investigates almost the same two setups as DLR, in that they combine “zonal” SST-RANS/SST-IDDES with two different setups for the embedded interface locations. In the full setup, which is considered in the comparative assessment below, the interfaces are located at  $x/c = 0.7$  on the upper side and at  $x/c = 0.67$  on the lower sider of the main-wing element, see Fig. 6.

At the interface planes, the Synthetic Turbulence Generator (STG) is used to augment the transition from RANS to LES (a specific version of the STG is the purely aerodynamic STG described in detail in Shur et al. 2014). In those regions NTS refined the mandatory structured grid according to their best-practice knowledge on synthetic-turbulence injection, yielding a modified mandatory (*mM*) grid. For the physical time step, the exact mandatory settings are adopted. The flow is simulated using the incompressible version of NTS’ structured solver with a mixed 4th-order central/3rd-order upwind flux discretization.

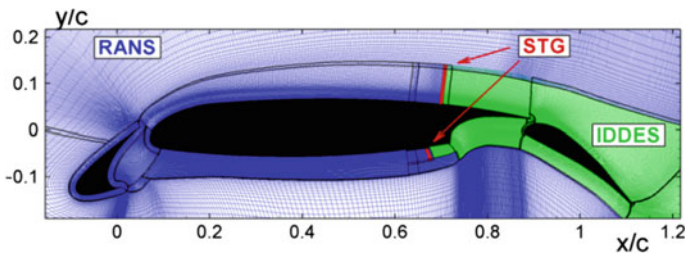


**Fig. 6.** NTS’ embedded setup with two interfaces for the 3-element airfoil

## 4 Results and Discussion

Due to the numerous partners contributing to this test case, only one result per partner and GAM type (non-zonal/embedded) is included in the comparative assessment. It comprises qualitative visualizations of the instantaneous flow fields, comparisons of the time- and span-averaged flow fields, as well as the evaluation of statistical quantities on the airfoil surface.

As experimental data is only available for the mean surface pressure and with a rather high uncertainty w.r.t. to the flow conditions (see above), the following assessment focuses on model-to-model and code-to-code comparisons. A summary of the considered simulations in this assessment and their respective settings is provided in Table 1.

### 4.1 Instantaneous Flow Visualizations

To illustrate the flow regions, where the different simulation approaches yield resolved turbulence, Figs. 7 and 8 provide views of the instantaneous airfoil flow for the non-zonal and embedded methods, respectively. The turbulent structures are visualized by iso-surfaces of the Q-criterion, which are colored by the normalized vorticity magnitude. In line with expectations, all simulations yield a similar amount and a decent resolution of turbulence on the flap, whereas the upstream flow history differs according to the modelling approach. The effect of the different numerical schemes ranging from 2nd-order unstructured to 4th-order structured plays no apparent role and becomes visible only in somewhat larger and fewer resolved structures in the FOI computation, at most, which may also to some extent be related to a larger time step used in the simulation.

For the non-zonal methods, resolved turbulence is generated in both coves of the slat and the main-wing element, and is convected downstream in the shear layers behind the respective trailing edges. While the hybrid models of NLR and FOI damp out most structures in the attached main-wing boundary layer, the IDDES used by NTS- $\Delta_{SLA}$  conserves this turbulence thanks to its wall-modelled LES mode. In the wing cove, the NLR computation shows the earliest breakup of the shear layer coming from the lower wing surface, which indicates a pronounced reduction of the local grey area.

For the embedded methods, the almost equivalent setups of NTS-STG and DLR lead to very similar distributions of resolved structures, which are only present downstream of the prescribed interfaces near the main-wing trailing edge. In contrast, the ONERA simulation treats the leading-edge region in a non-zonal manner (i.e., mode 1 of ZDES), leading to rich turbulent content in the slat cove. However, due to the RANS zone prescribed on the main wing, the resolved structures are damped out before interacting with the flap flow. The lack of synthetic turbulence

**Table 1.** Overview of conducted simulations considered in the comparative assessment (M: mandatory structured, MH: mandatory hybrid, mM: modified mandatory structured)

Partner	Solver order: space/time	Hybrid model	Non-zonal method	Embedded method	Grid	$\Delta t/CTU$	Sim. time: transient + statistics (CTU)
NLR	4th/2nd	DX-LES	Stochastic + HPF-SGS	-	M	$1 \times 10^{-4}$	4.2 + 4
FOI	2nd/2nd	HYB0	Energy back-scatter	-	MH	$1 \times 10^{-3}$	3.6 + 6.1
NTS	4th <sub>(hyb)</sub> /2nd	SST-IDDES	$\Delta_{SLA}$	-	M	$2 \times 10^{-4}$	5 + 3
NTS	4th <sub>(hyb)</sub> /2nd	SST-IDDES	-	STG	mM	$2 \times 10^{-4}$	5 + 3
DLR	2nd/2nd	SST-IDDES	-	SEM	MH	$2 \times 10^{-4}$	5 + 5
ONERA	2nd/2nd	SA-ZDES	-	DF + WN	own	$1.7 \times 10^{-5}$	5 + 5.6

*M*: mandatory structured, *MH*: mandatory hybrid, *mM*: modified mandatory structured

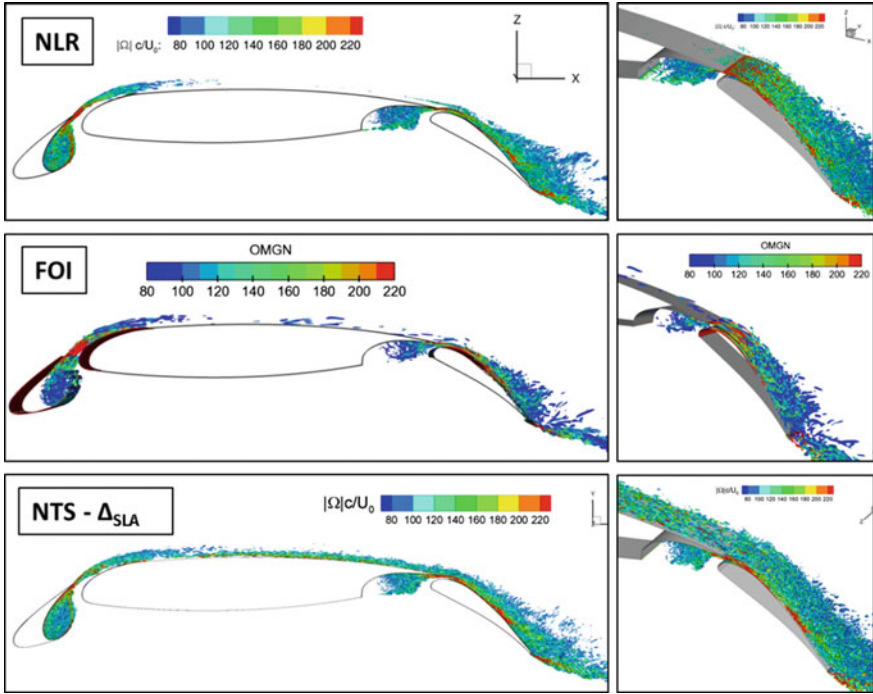


**Fig. 7.** Visualizations of turbulent structures in the non-zonal simulations using iso-surfaces of the Q-criterion, with  $Q(c/U_0)^2 = 1500$

on the lower wing in ONERA's simulation delays the formation of resolved structures in the wing cove, but this has no apparent effect on the flap flow.

Regarding the region just downstream of the embedded interfaces on the wing, DLR's SEM generates relatively large synthetic structures, which tend to dissipate before re-developing towards the trailing edge. While this behavior of SEM has partly been observed in other test cases as well, e.g., the flat plate boundary layer, it should also be noted that NTS and ONERA use a finer grid resolution in this area.

## 4.2 Mean Flow Field

The mean flow-field data were obtained by averaging the flow variables over appropriate time periods (see Table 1) plus additional spatial averaging in the homogeneous spanwise direction. The resulting flow topologies from all considered simulations are visualized by the mean streamlines in Fig. 9. All plots show the expected global behavior, i.e., attached flow on the outer surfaces of the slat and the main-wing element, as well as local geometry-induced separation regions in the coves. Regarding the pressure-induced separation on the flap, the non-zonal

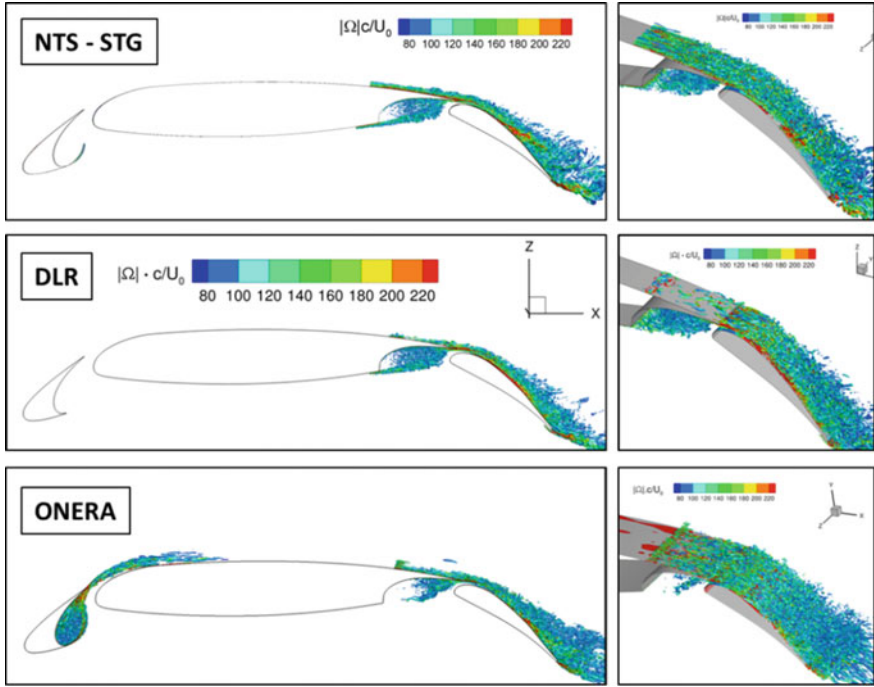


Fig. 8. Visualizations of turbulent structures in the embedded simulations using iso-surfaces of the Q-criterion, with  $Q(c/U_0)^2 = 1500$

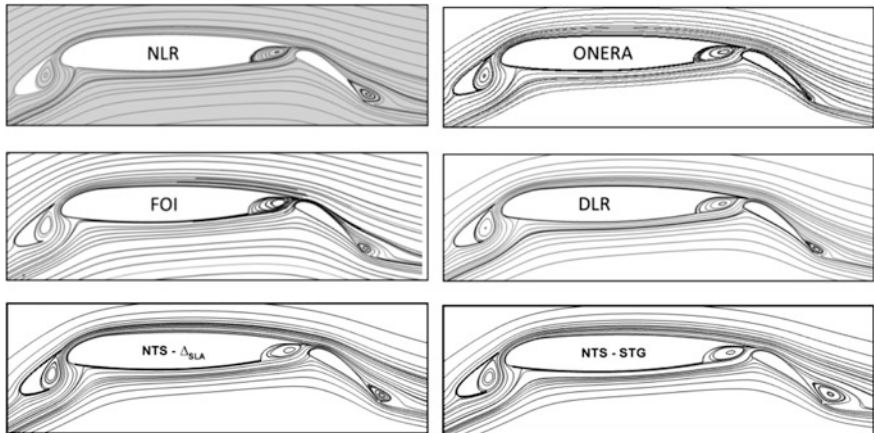


Fig. 9. Mean streamlines from the non-zonal (*left*) and embedded (*right*) simulations

simulations (Fig. 9, left) show a remarkable agreement, whereas for the embedded approaches both the smallest (ONERA) and the largest (NTS-STG) separation bubbles are observed.

Further information about the near-wall flow can be inferred from boundary-layer velocity profiles, which have been extracted at four positions along the upper airfoil surface as depicted in Fig. 10. The velocities in x- and y-directions ( $u$  and  $v$ ) are compared in Fig. 11 for the non-zonal and in Fig. 12 for the embedded simulations, respectively.

Again, for the non-zonal approaches a rather consistent behavior of the near-wall flow can be stated, note for example the almost identical profiles near the main-wing leading edge ( $x/c = 0.1$ ) and the very similar backflow regions predicted by NLR and NTS- $\Delta_{SLA}$  at  $x/c = 1.1$ .

Larger deviations are only observed near the trailing edge of the main wing ( $x/c = 0.8$ ), where the three simulations operate in rather different modelling modes, as already seen in Fig. 7, while NTS- $\Delta_{SLA}$  works as a (dynamic) wall-modelled LES (IDDES) and yields a smooth, well-developed velocity profile, the explicit near-wall RANS zone in the NLR simulation (see Fig. 3) seems to be mismatched with the resolved outer flow, causing a distinct ‘kink’ in the boundary-layer profile, which is probably responsible for some difference between NTS and NLR velocity profiles further downstream (at  $x/c = 1.0$  and  $x/c = 1.1$ ).

In contrast, the velocity profiles from the embedded simulations in Fig. 11 show a larger variation on the flap ( $x/c = 1$  and  $1.1$ ) which agrees with the different separation sizes inferred from the mean streamlines (see Fig. 3). At least for DLR and NTS-STG, which share an almost identical modelling setup (SST-IDDES), the profiles at  $x/c = 0.8$  are almost identical, though. This allows concluding that the separation behavior on the flap is strongly affected by the different synthetic turbulence methods, i.e., SEM and STG.

For the ONERA results the sensitivities are less clear, since additional factors may affect the flap region, e.g., the different hybrid model (SA-ZDES), or the finer grid resolution.

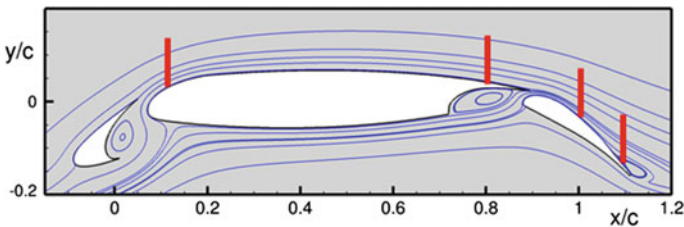
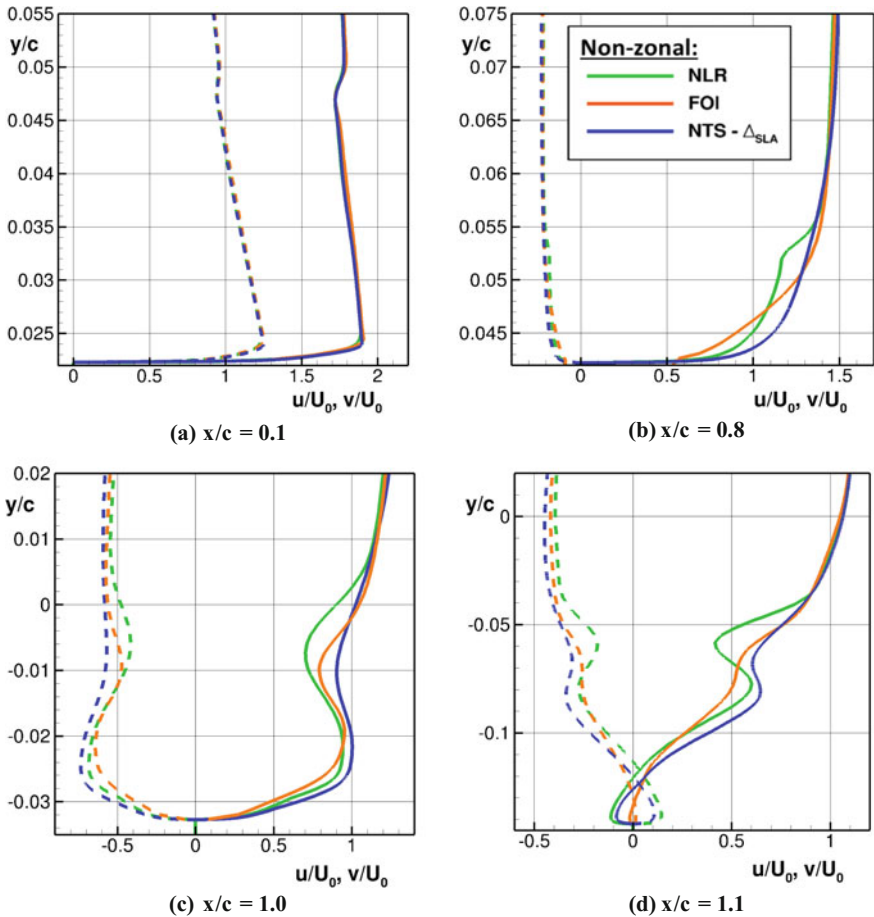


Fig. 10. Locations of analyzed velocity profiles





**Fig. 11.** Mean normalized velocity profiles in the locations shown in Fig. 10 (solid line:  $u$ ; dashed line:  $v$ ) from the non-zonal simulations

### 4.3 Mean Surface Data

Time- and span-averaged surface-pressure distributions are shown in Fig. 13, along with corrected experimental data from measurements in the NWB wind tunnel. As discussed above, this comparison with reference data is affected by large uncertainties in reproducing the experimental flow conditions. With that in mind it can merely be stated that all considered simulations yield plausible pressure distributions on the whole airfoil (including the interaction of  $c_p$  on the different elements), which equally lie within the uncertainty range of the comparison.

However, the results can well be used to confirm the findings from the analysis of the global mean flow fields: while the non-zonal simulations show a remarkable

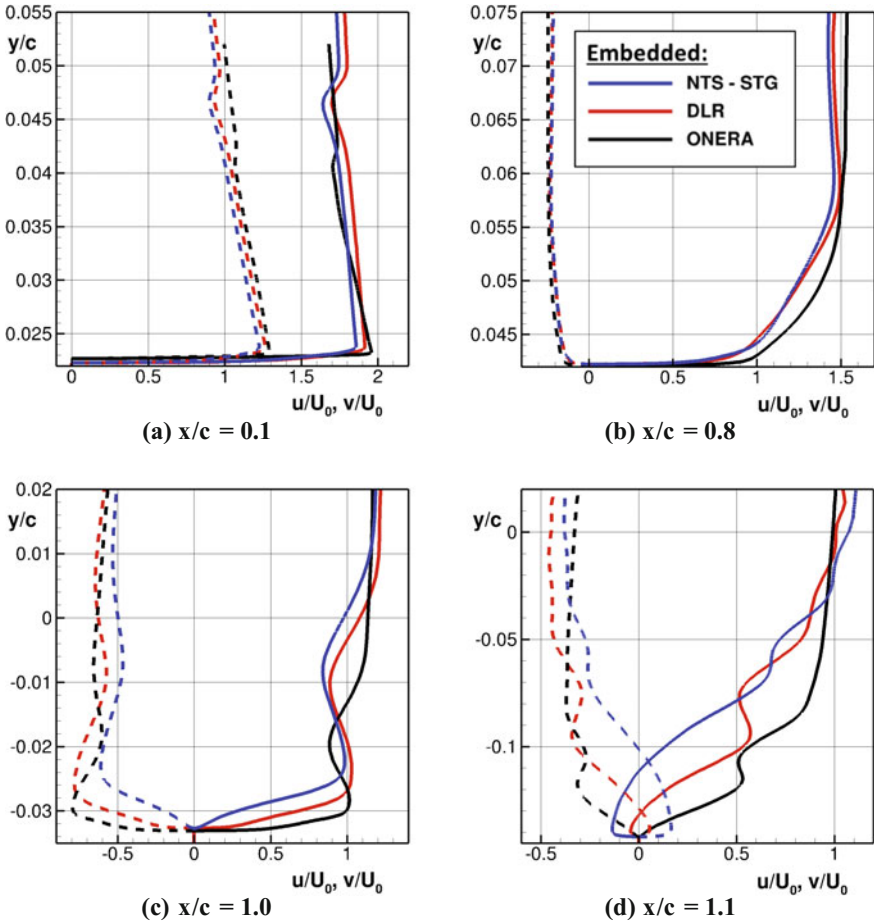


**Fig. 12.** Mean normalized velocity profiles in the locations shown in Fig. 10 (solid line:  $u$ ; dashed line:  $v$ ) from the embedded simulations

agreement in  $c_p$  despite rather different modelling approaches, the embedded simulations yield a similar strong variation in the whole  $c_p$ -distribution as already found in the velocity profiles on the flap. This highlights the rather global reaction of the flow (e.g., the height of all suction peaks) to the size of the flap separation, which in turn is sensitive to the respective synthetic-turbulence generator. Thus, it is not surprising that DLRs pressure distribution is close to those of the non-zonal methods, as also the sizes of the corresponding separations are very similar (see Fig. 9).

To analyze the viscous near-wall flow behavior, consider the absolute values of the mean skin friction in Fig. 14. On first glance somewhat surprisingly, the variation of simulation results is now larger for the non-zonal methods, than for the

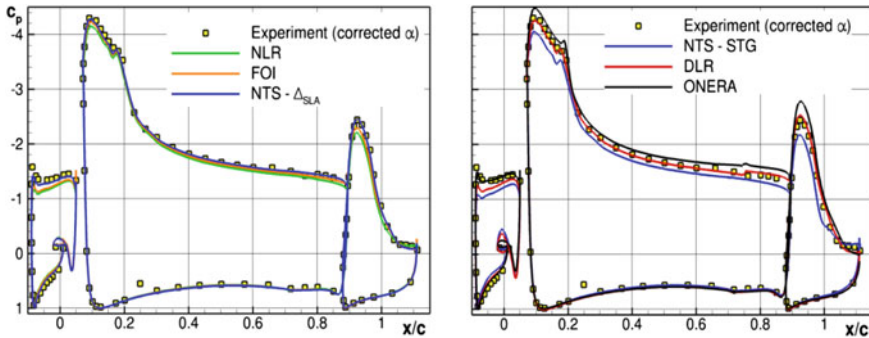


Fig. 13. Mean surface-pressure distributions non-zonal (left) and embedded simulations (right)

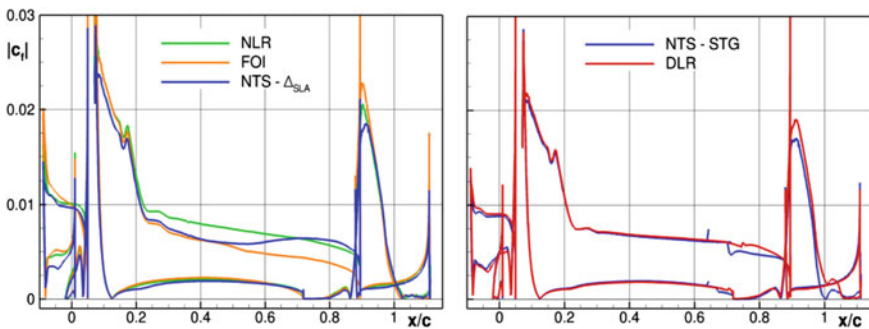


Fig. 14. Mean skin-friction distributions from non-zonal (left) and embedded simulations (right)

depicted embedded approaches, i.e., NTS-STG and DLR. However, the near-wall flow is strongly determined by the underlying RANS model, which differs for all three non-zonal simulations. The main deviations occur on the main wing, where a 30% offset between NLR and FOI (both resolving only parts of the turbulence, see Fig. 7) is observed, whereas the IDDES of NTS- $\Delta_{SLA}$  yields an unexpected  $c_f$ -minimum at the center of the main-wing element. Note that this ‘dent’ has also been found in basic SST-IDDES computations of this flow without any grey-area mitigation (Probst et al. 2014). Despite the different flow behavior on the main wing, the skin friction on the flap almost coincides for the non-zonal methods, which is well in line with the previous analysis.

Unlike the non-zonal results, both the embedded simulations of NTS-STG and DLR use SST-RANS upstream of respective interfaces near the main-wing trailing edge, which yields almost identical  $c_f$ -distributions up to this location. Here, the switch to LES induces disturbances in both simulations which, however, are less pronounced in the DLR simulation. This could be explained by the different synthetic-turbulence methods (SEM vs. STG), but also by implementation details of the zonal switch from RANS to LES. In line with previous findings, only the flap

region shows a wider variation in  $c_f$ , showing once again opposing sensitivities of the embedded methods in comparison with the non-zonal simulations.

The final assessment in Fig. 15 considers the root-mean-square (RMS) of the pressure oscillations on the surface which is related to the prediction of the acoustical properties of the flow (i.e., noise generation). Overall, the non-zonal simulations predict similar distributions and levels of  $c'_{p,RMS}$  and again appear less sensitive to the respective modelling approach than the embedded methods.

It is worth to note that despite the use of a stochastic SGS model, NLR computes the overall lowest  $c'_{p,RMS}$  levels among the non-zonal simulations in Fig. 15 (left). This confirms that the NLR approach is “passive” in terms of noise generation for a relevant aeronautical flow. NTS- $\Delta_{SLA}$  predicts slightly higher levels with an additional maximum on the main wing, which is due to IDDES resolving the boundary-layer turbulence in wall-modelled LES mode (see Fig. 7). Even higher maximum  $c'_{p,RMS}$  values—best visible in the peaks on the slat and on the flap—are computed by FOI. Referring to previous studies (Probst et al. 2014, 2015) using the rather similar DLR-TAU code, this is probably caused by somewhat larger numerical dissipation and dispersion in the 2nd-order unstructured Edge solver, when compared to the 4th-order structured codes of NLR and NTS.

Regarding the embedded methods in Fig. 15 (right), only ONERA resolves the lower slat shear layer impinging on the cove surface, as DLR and NTS simulate this part of the airfoil in RANS mode. The resolved impingement leads to the characteristic  $c'_{p,RMS}$ -peak around  $x/c = 0.05$ . That peak and the values on the flap are rather close to the non-zonal predictions in Fig. 15 (left), even though the synthetic turbulence injected at  $x/c = 0.75$  on the upper main-wing side induces strong local pressure oscillations ranging up to a maximum of  $c'_{p,RMS} = 0.6$ . This well-known issue of artificial sound generation by synthetic turbulence has an even stronger impact on DLR’s embedded simulation, where at the same location ( $x/c = 0.75$ ) a maximum of  $c'_{p,RMS} = 1.1$  is reached. For the DLR simulation, these local oscillations are strong enough to affect the whole airfoil surface, notably in the increased  $c'_{p,RMS}$ -levels on all three elements. This is possible because the compressible TAU solver simulates the unsteady propagation of acoustic waves.

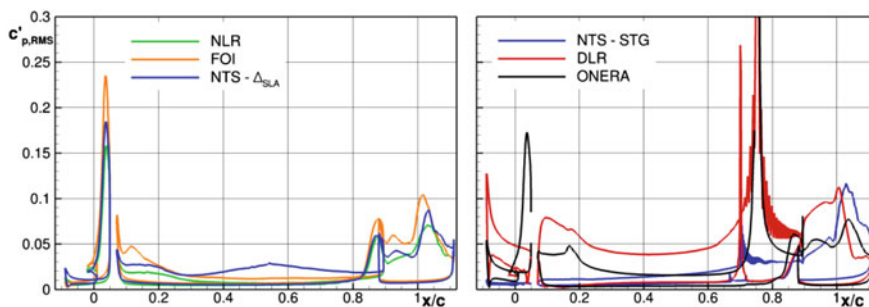


**Fig. 15.** Root-mean-square of the surface pressure from non-zonal (*left*) and embedded simulations (*right*)

This propagation mechanism is not resolved by the incompressible code used in NTS-STG, which results in almost negligible  $c'_{p,RMS}$  values in the RANS regions upstream of the embedded interfaces at  $x/c \approx 0.7$ . Moreover, with the STG used by NTS (see Shur et al. 2014), the artificial pressure fluctuations reach only rather low maximum amplitudes of  $c'_{p,RMS} = 0.11$ . It is worth to note, though, that NTS-STG computes the highest peak on the flap, which is presumably caused by the large size of the predicted separation, see Figs. 9 or 12.

## 5 Conclusions

Hybrid RANS/LES simulations of the flow around the 3-element high-lift airfoil DLR-F15 near stall conditions were conducted in the course of the Go4Hybrid project. Five (out of seven) project partners contributed to this relevant but challenging test case, providing results of three non-zonal grey-area mitigation (GAM) approaches and of three embedded simulations using synthetic turbulence. Note that even more simulations were performed, but only one per partner and GAM type was selected for the present comparison.

Chosen mainly as a relevant demonstration case, this test case suffers from a rather limited and uncertain reference data base, as the experimental flow conditions were found difficult to reproduce exactly enough for a detailed model assessment. Moreover, not all of the provided simulations were conducted using the mandatory settings and grids.

Despite of this, a number of conclusions can be drawn from the comparison:

- All partners successfully applied their GAM approaches to this highly-relevant aeronautical flow with rather complex flow interactions.
- Apart from a few ‘abnormalities’, an overall convincing level of plausibility and consistency between different methods and codes was achieved.
- The non-zonal simulations are in close agreement with each other, which indicates a rather weak effect of non-zonal GAM methods in this flow, at least w.r.t. the global airfoil behavior (separation size,  $c_p$ -distribution).
- The embedded simulations mainly differ in size of the pressure-induced separation on the flap, which appears to be a direct effect of the chosen method for generating synthetic turbulence just upstream of the flap.
- The synthetic turbulence in embedded methods may interfere with acoustic predictions, especially if compressible flow solvers are used.

In summary, the work on the DLR-F15 case represents a successful demonstration of various GAM methods using different numerical solvers for a complex and relevant aeronautical flow.

# 2D Wall-Mounted Hump

A. Garbaruk, E. Guseva, M. Shur, M. Strelets and A. Travin

## 1 Introduction

This configuration studied in the experiments of Greenblatt et al. (2006a, b) and by Naughton et al. (2006) had been specially designed as a CFD validation test case and was used for this purpose in numerous computational studies including those carried out in the framework of specially organized workshops<sup>1</sup> and in the course of the ATAAC EU project.<sup>2</sup>

The model presents a wall-mounted Glauert-Goldschmied type body, geometrically similar to that employed by Seifert and Pack (2002) mounted between two glass endplate frames with both leading and trailing edge faired smoothly with a wind tunnel splitter plate, as shown in Fig. 1.

A primary objective of the original test-case was to evaluate the capabilities of different CFD approaches to predict the effect of synthetic jets on turbulent boundary layer separation. However, a baseline experiment (with no jets) allows also a reliable assessment of these approaches in terms of prediction of pressure induced separation, reattachment of the separated shear layer to the splitter plate and relaxation of the reattached turbulent boundary layer further downstream. These complex flow phenomena are common for many industrial flows (e.g. wings/turbine blades near maximum loading) and present a serious challenge not only for RANS modelling but also for hybrid RANS-LES approaches. For the latter, the major

---

<sup>1</sup>Langley Research Center Workshop on CFD Validation of Synthetic Jets and Turbulent Separation Control, Williamsburg, Virginia, USA, March 29–31, 2004: <http://cfdval2004.larc.nasa.gov/case3.html>.

<sup>2</sup>Advanced Turbulence Simulation for Aerodynamic Application Challenges (ATAAC) EU Project <http://cfd.mace.manchester.ac.uk/twiki/bin/view/ATAAC/WebHome>.

---

A. Garbaruk (✉) · E. Guseva · M. Shur · M. Strelets · A. Travin  
New Technologies and Services (NTS) and St. Petersburg Polytechnic University,  
St. Petersburg, Russia  
e-mail: [agarbaruk@cfds.spbstu.ru](mailto:agarbaruk@cfds.spbstu.ru)

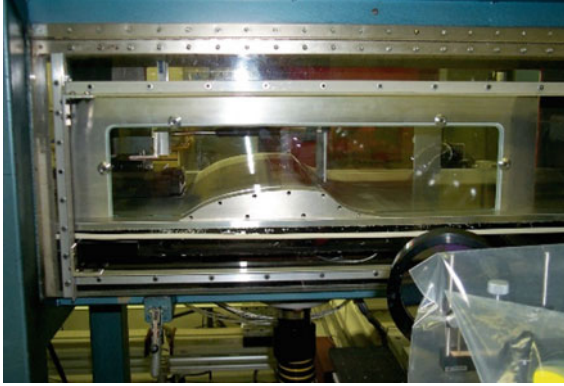


**Fig. 1** Experimental set-up for study of 2D wall-mounted hump flow

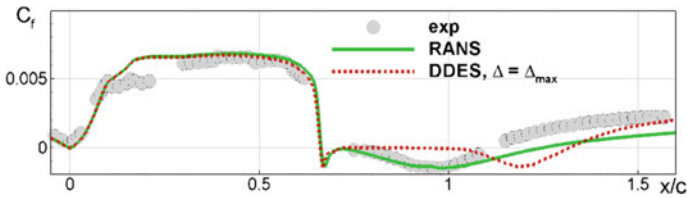


**Fig. 2** SA RANS and SA-based DDES predictions of skin-friction coefficient distribution over the 2D hump flow. Pre-project computations of NTS

difficulty in predicting the considered flow is associated with the grey area issue, which causes a strong delay of transition from RANS to LES in the separated shear layer resulting in a significant deviation of the predicted flow quantities from the experimental data (see an example in Fig. 2). Exactly for this reason, this flow has been included in the list of industrially relevant test cases (TC I.4) aimed at evaluating the grey-area mitigation tools developed in the course of the Go4Hybrid project.

In this section, we briefly present the flow configuration, the numerical set-ups used by the partners who computed this flow, and the primary outcome of the performed simulations.

## 2 Geometry, Flow Regime, and Available Experimental Data

A 3D view of the model is presented in Fig. 3 and the flow schematic is given in Fig. 4 which shows also its major geometric parameters.

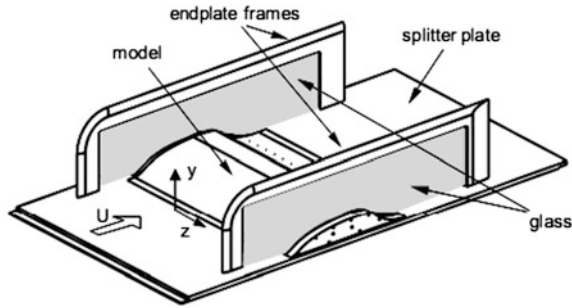


**Fig. 3** Perspective view of the experimental setup showing the model, endplates, and splitter plate (Greenblatt et al. 2006a)

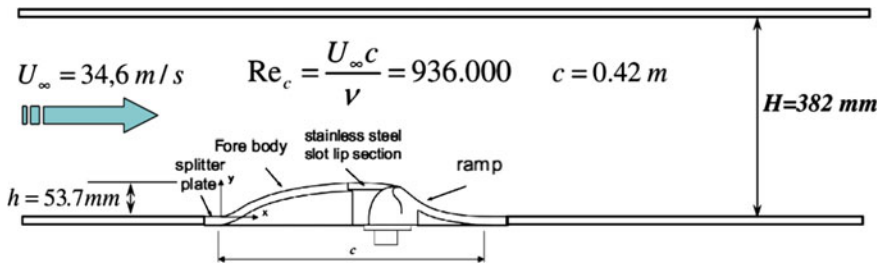


**Fig. 4** Flow schematic and geometrical parameters. The simulations performed correspond to the flow with closed slot for micro-jet injection (“baseline” experiment)

The hump chord length,  $c$ , is equal to 0.42 m, and the crest height is 0.0537 m. The hump is mounted on a splitter plate of thickness 0.0127 m, which extends 1.935 m upstream of the hump leading edge and 1.129 m downstream of the hump leading edge. The hump with the splitter plate is placed in a wind tunnel of 0.771 m width and 0.508 m height, but the nominal test section height (between the splitter plate and the top wall) is 0.382 m and the nominal hump width (between the two end plates) is 0.584 m. The characteristic Reynolds number based on the hump chord is about  $10^6$  and the Mach number is 0.1, which allows both incompressible and compressible simulations.

The experimental database for the considered flow is available at <http://cfdval2004.larc.nasa.gov/case3expdata.html>. It includes streamwise distributions of the surface pressure and skin-friction coefficients,  $C_p$  and  $C_f$ , as well as velocity and turbulence data along the tunnel center-plane, roughly covering the region  $0.63 < x/c < 1.39$ .

Uncertainties reported in the experimental studies are summarized in Table 1.

Other than that, there is an operational uncertainty associated with the endplates blockage effect, which should be compensated in the quasi-2D simulations (see next sub-section).



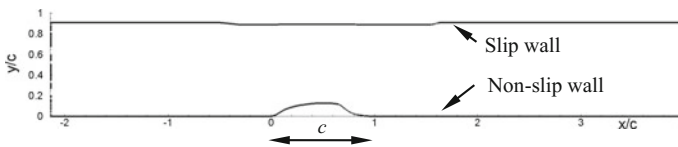
**Table 1** Experimental uncertainties

Quantity	Pressure coefficient, $C_p$	Reynolds shear stress, $\langle u'v' \rangle$	RMS of streamwise and wall-normal velocity fluctuations
Experimental uncertainty	$\pm 0.001$	up to 20%	up to 14%

**Table 2** Matrix of performed simulations

Partner	Type of hybrid approach	Scale-resolving approach	GAM technique	Location of RANS-LES interface	CFD Code
DLR	Zonal	SST-based IDDES <sup>a</sup>	SEM <sup>c</sup>	$x/c = 0.5$ $x/c = -1.0$	Compressible TAU code with hybrid LD2 scheme <sup>f</sup>
NTS	Zonal	SST-based IDDES <sup>a</sup>	NTS STG <sup>d</sup>	$x/c = 0.5$ $x/c = -1.0$	Incompressible branch of NTS code <sup>g</sup>
NTS	Non-zonal	SST-based DDES <sup>b</sup>	Shear Layer Adapted length-scale <sup>e</sup>	No	Incompressible branch of NTS code <sup>g</sup>

<sup>a</sup>M. Shur et al. (2008), <sup>b</sup>P. Spalart et al. (2006), <sup>c</sup>N. Jarrin et al. (2009), <sup>d</sup>M. Shur et al. (2014) <sup>e</sup>M. Shur et al. (2015), <sup>f</sup>A. Probst et al. (2015), <sup>g</sup>M. Shur et al. (2004)

**Fig. 5** Mandatory computational domain in XY-plane

### 3 Simulations Performed and Numerical Setup

A matrix of simulations of the considered flow carried out in the course of the project is presented in Table 2.

The mandatory computational domain in the XY-plane used in all simulations is shown in Fig. 5. The size of the domain in the homogeneous (spanwise) direction,  $L_z$ , was set equal to  $0.4c$ , which has been proven to be sufficient for getting a span-independent solution in the course of ATAAC project. As seen in the figure, the contour of the upper wall of the domain is modified (moved downwards) in the area above the hump in order to compensate the blockage effect of the endplates as suggested in [http://turbmodels.larc.nasa.gov/nasahump\\_grids.html](http://turbmodels.larc.nasa.gov/nasahump_grids.html).

Boundary conditions were specified as follows:

- At the bottom (hump) wall no slip conditions were imposed, whereas the upper wall was considered as an inviscid one, using free-slip boundary conditions.

- The inflow and outflow conditions in the DLR and NTS simulations were different since DLR used the compressible TAU code and NTS employed the incompressible branch of their in-house code (NTS code). In both cases velocity and turbulent quantities at the inflow boundary ( $x/c = -2.14$ ) were specified from a precursor SST RANS of the zero-pressure gradient boundary layer, carried out to match the experimental value of the momentum thickness based Reynolds number  $Re_{\theta_{inflow}} = \theta_{inflow} U_{\infty} / \nu = 7200$ . In the incompressible simulations (NTS) the inflow static pressure was defined by the linear extrapolation by its values in the nearby interior cells of the domain, whereas in the compressible simulations (DLR) flux boundary conditions are used together with an extrapolation of the pressure from the interior. The latter leads to conditions very similar to that of NTS. At the outflow boundary NTS specified a constant static pressure and defined all the other flow variables by linear extrapolation from the interior of the domain, which is also very similar to DLR's flux conditions with an imposed fixed exit pressure.
- Finally, in all the simulations the boundary conditions in the spanwise direction were periodic ones.

The grid in  $XY$ -planes used in all the simulations is shown in Fig. 6, which is a somewhat modified variant of the grid used for the 2D hump flow simulations in the course of the ATAAC project. In particular, the grid is normal to the walls and is refined in the  $x$ -direction at  $-1.0 < x/c < 0.5$  in order to provide a possibility of

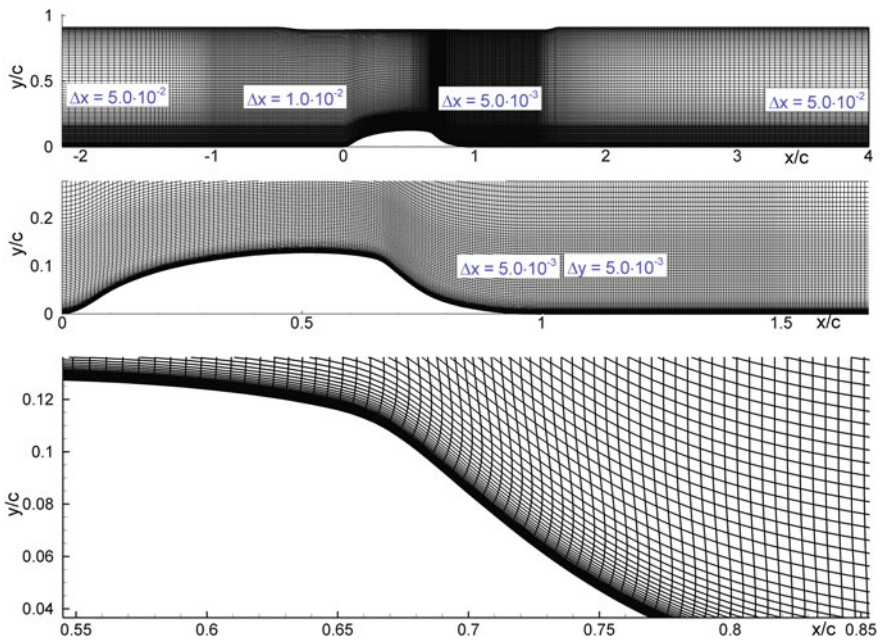


Fig. 6 Mandatory grid in  $XY$ -plane used in the simulations

placing the RANS-LES interface in any cross-section of this region. In the separation (“focus”) region ( $0.67 < x/c < 1.5$ ) both  $x$ - and maximum  $y$ -steps are equal to  $0.005c$ . Considering that the spanwise grid step is also equal to  $0.005c$ , the grid in this region is close to cubic. Finally, the first step size off the bottom wall in wall units ( $\Delta y_1^+$ ) is less than 1.0 in the whole domain. As a result, the total grid size is  $511 \times 127 \times 80$ , i.e. about 5.2 million cells.

## 4 Results and Discussion

### 4.1 Evaluation of the Performance of Zonal RANS-IDDES Approaches

Figures 7, 8, 9, 10 present flow visualizations in the form of instantaneous fields of the vorticity magnitude in an  $XY$ -plane at the bottom wall from all the zonal simulations, i.e., the zonal SST RANS—SST-based IDDES of DLR and NTS carried out for two locations of the RANS-IDDES interface,  $x/c = -1.0$  and  $0.5$ , respectively. A comparison of the figures allows two major conclusions.

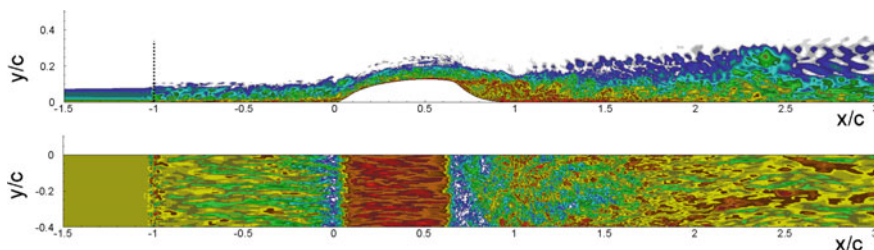


**Fig. 7** Snapshots of vorticity magnitude in  $XY$ -plane and on bottom wall from zonal SST RANS—SST-based IDDES of DLR with RANS-IDDES interface (*dashed vertical line*) located at  $x/c = -1.0$

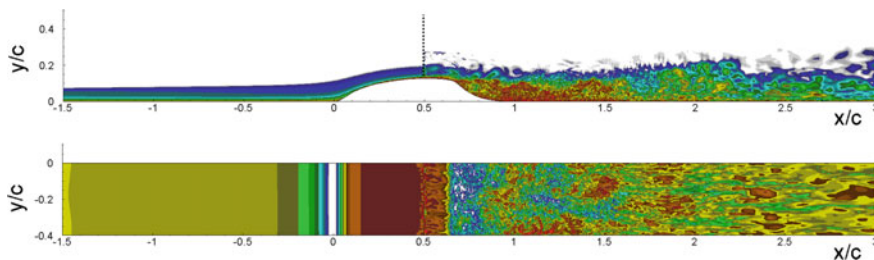


**Fig. 8** Same, as in Fig. 7, with RANS-IDDES interface located at  $x/c = 0.5$

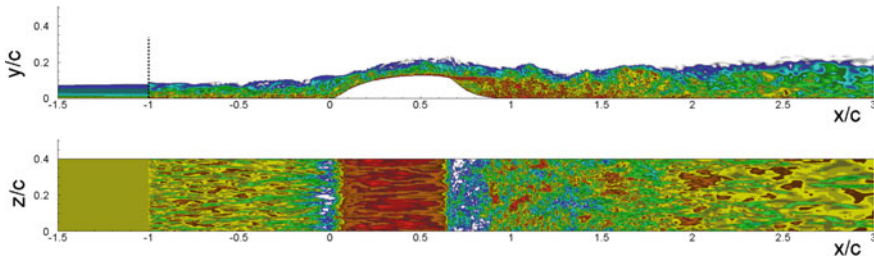


**Fig. 9** Snapshots of vorticity magnitude in  $XY$ -plane and on the *bottom* wall from zonal SST RANS—SST-based IDDES of NTS with RANS-IDDES interface (*dashed vertical line*) located at  $x/c = -1.0$

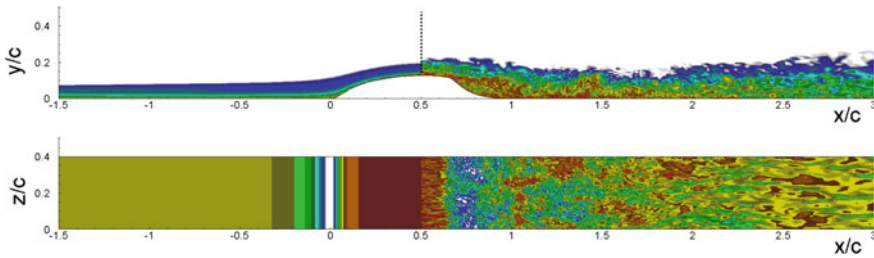


**Fig. 10** Same, as in Fig. 9, with RANS-IDDES interface located at  $x/c = 0.5$

Turbulence structures right downstream of the interface in the DLR and NTS simulations are somewhat different, which is not surprising considering the use of different turbulence generators in these simulations, i.e., SEM in the case of DLR and NTS STG in that of NTS. The figures do, however, not reveal any tangible difference of the turbulence structures further downstream, which means that at least for the flow considered, both approaches to create turbulent content at the inlet of the IDDES region are quite comparable and ensure relatively rapid transition from RANS to IDDES (short relaxation length).

Furthermore, both DLR and NTS simulations ensure very close resolution of turbulent structures in the “challenging” flow region located downstream of the separation line, with sizes of smallest resolved eddies compatible with the cells-sizes of the computational grid in the IDDES zone. This suggests that the TAU-LD2 unstructured code has a low numerical dissipation comparable with that of the high-order structured NTS code.

Figures 11 and 12 compare distributions of mean friction and wall-pressure coefficients predicted by the DLR and NTS simulations. As could be expected based on the analysis of the corresponding flow visualizations, these distributions are in a very close agreement with each other. This suggests a comparable performance of the two synthetic turbulence generators used in the simulations as well

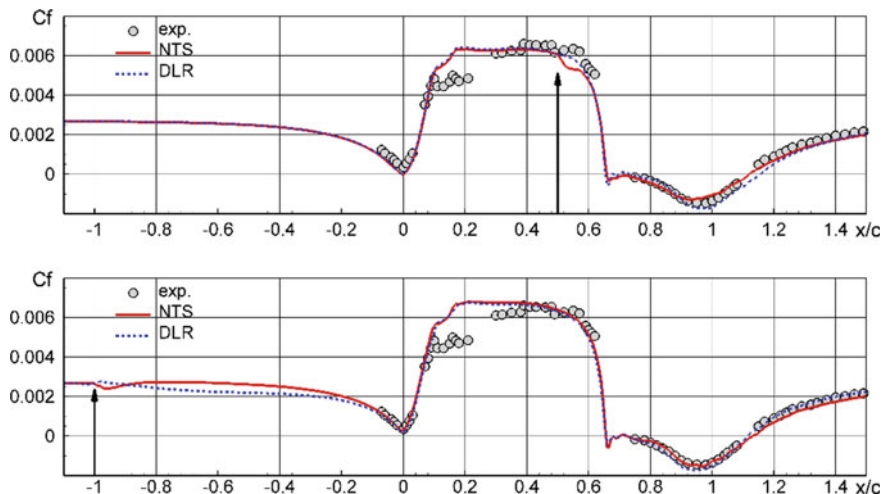


**Fig. 11** Comparison of mean skin-friction coefficient distributions predicted by TAU-LD2 and NTS codes with different locations of RANS-IDDES interface with experimental data. *Arrows* indicate locations of the interface

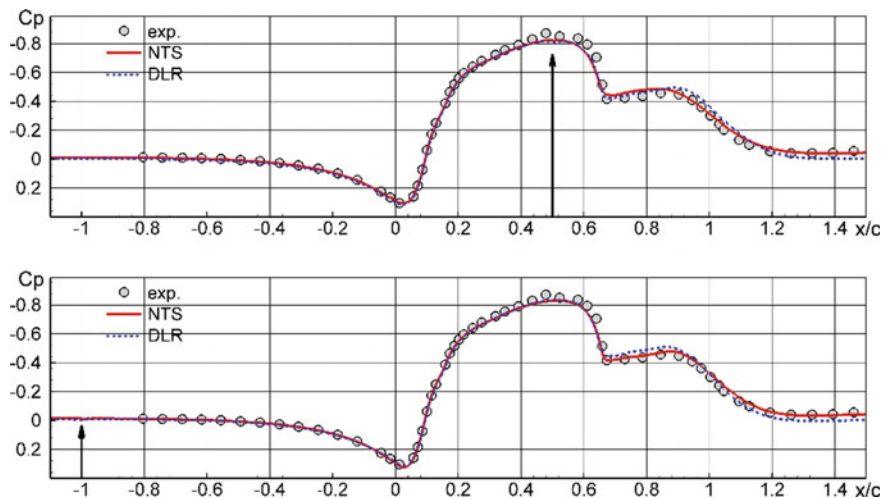


**Fig. 12** Same, as in Fig. 11, for wall-pressure coefficient distributions

as independence of the mean flow prediction on the code and on the location of RANS-IDDES interface. As far as agreement with the data is concerned, it turns out to be very good, thus supporting the credibility of the zonal RANS-IDDES approach.

Nearly the same conclusions can be drawn based on the comparison of the predicted profiles of the streamwise velocity component at different cross-sections of the flow with the corresponding experimental profiles presented in Figs. 13 and 14, respectively. Note, however, that at  $0.65 \leq x/c \leq 0.9$  these profiles turn out to be a bit more sensitive to the location of RANS-IDDES interface than  $C_P$  and  $C_f$ . In this respect the location of the interface farther upstream of the hump (at  $x/c = -1.0$ ) ensures a somewhat better agreement with the experiment than that close to the separation line (at  $x/c = 0.5$ ).

As seen from Figs. 15, 16, 17, 18, 19, 20, the agreement of the Reynolds stress profiles with the experimental data is not as good as that of the velocity profiles and, especially the  $C_f$  and  $C_P$  distributions, but it remains still quite acceptable. Note also that predictions of the stresses by the NTS code turned out to be somewhat more accurate than those of the DLR code at least in the simulations carried out with the RANS-IDDES interface located at  $x/c = -1.0$ .

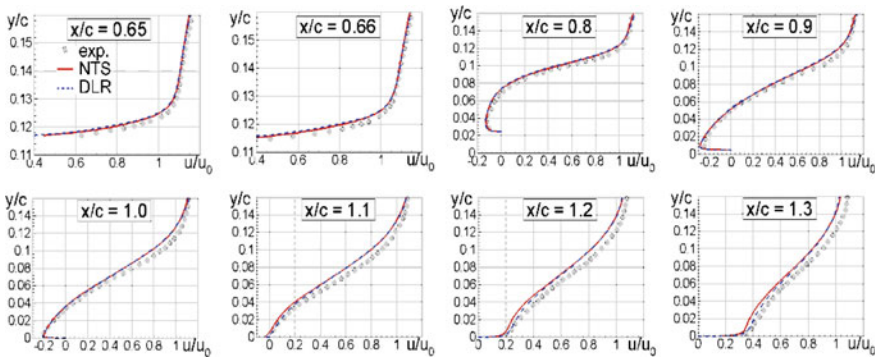


**Fig. 13** Comparison of mean streamwise velocity profiles at different flow sections predicted by TAU-LD2 and NTS codes with locations of RANS-IDDES interface at  $x/c = -1.0$  with experimental data

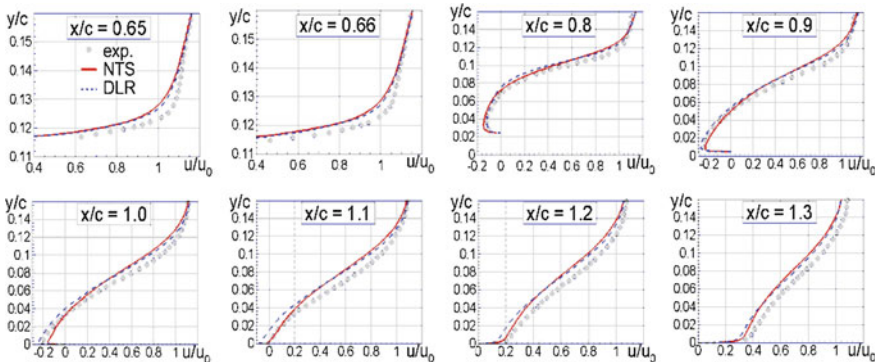


**Fig. 14** Same, as in Fig. 13, with the interface located at  $x/c = 0.5$

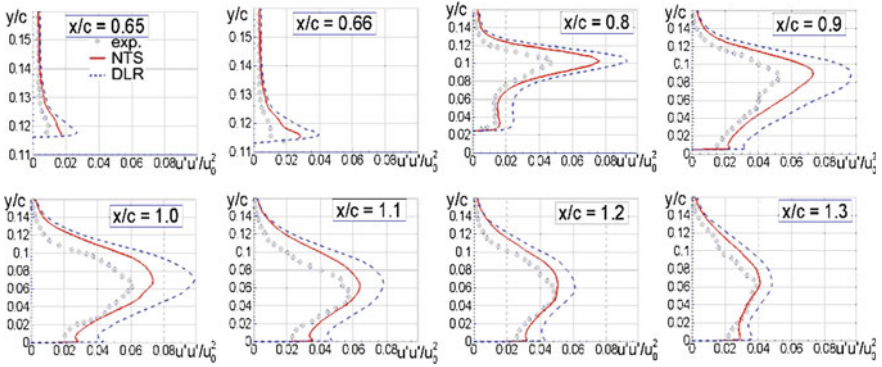


**Fig. 15** Comparison of  $\langle u'u' \rangle$  profiles at different flow sections predicted by TAU-LD2 and NTS codes with location of RANS-IDDES interface at  $x/c = -1.0$  with experimental data

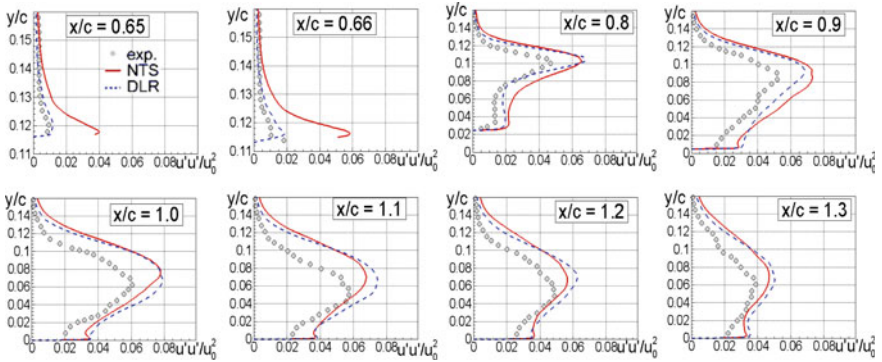


**Fig. 16** Same as in Fig. 15 with the interface located at  $x/c = 0.5$

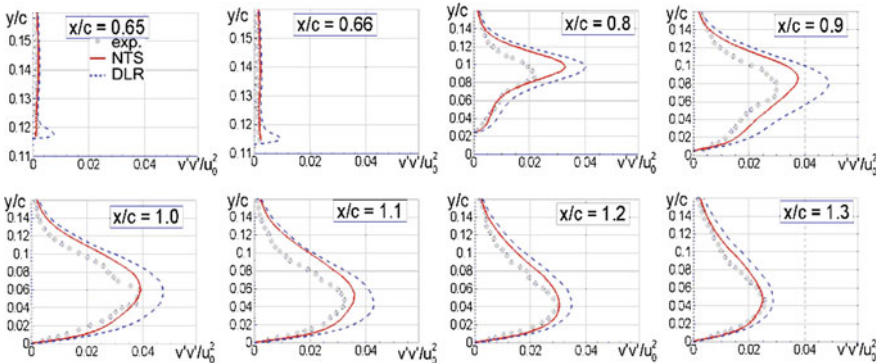


**Fig. 17** Comparison of  $\langle v'v' \rangle$  profiles at different flow sections predicted by TAU-LD2 and NTS codes with location of RANS-IDDES interface at  $x/c = -1.0$  with experimental data

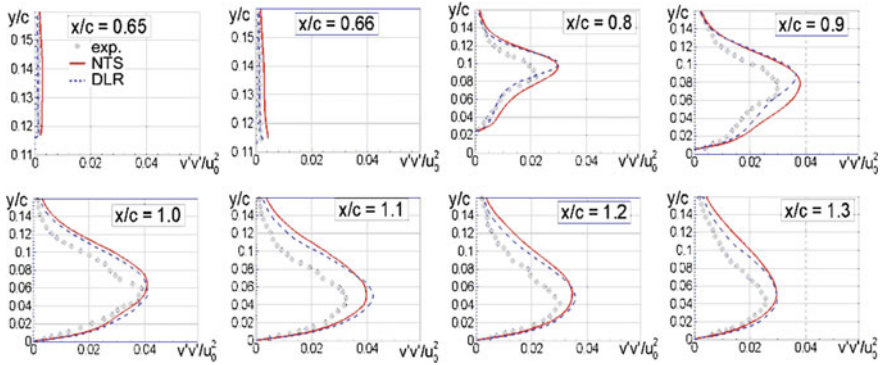


Fig. 18 Same as in Fig. 17 with the interface located at  $x/c = 0.5$

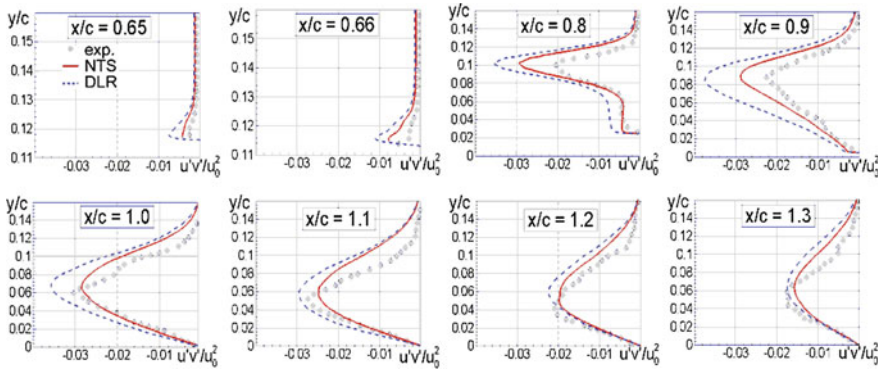


Fig. 19 Comparison of  $\langle u'v' \rangle$  profiles at different flow sections predicted by TAU-LD2 and NTS codes with location of RANS-IDDES interface at  $x/c = -1.0$  with experimental data

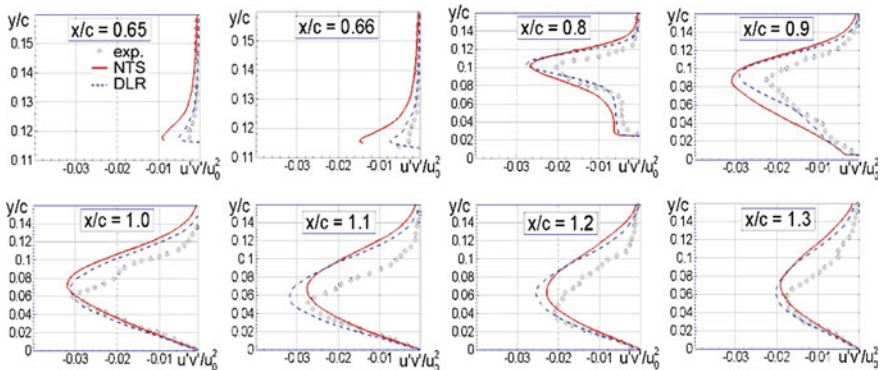


Fig. 20 Same as in Fig. 19 with the interface located at  $x/c = 0.5$

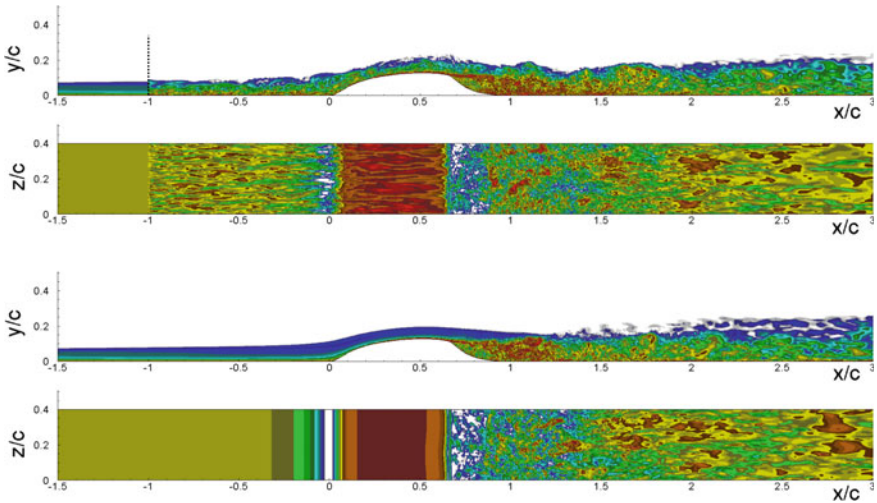


## 4.2 Evaluation of Non-zonal Versus Zonal Approaches

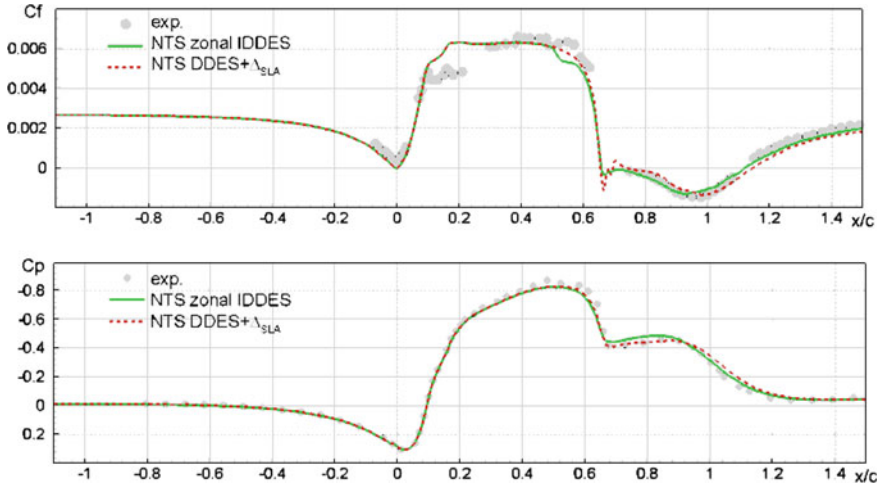
As mentioned in Sect. 3 (see Table 2), along with zonal SST-RANS—SST-based IDDES, NTS has carried out simulations of the hump flow using the non-zonal (“global”) SST-based DDES (Spalart et al. 2006) combined with a modified (shear-layer adapted) subgrid length-scale proposed by Shur et al. (2015). Below we present a comparison of results of these two simulations.

Figure 21 shows a comparison of the corresponding flow visualizations in the form similar to that in Fig. 7 above. One can see that the global DDES predicts steady flow upstream of the separation and automatically becomes unsteady further downstream where its prediction of the turbulent structures is very close to that of the zonal RANS-IDDES.

As a result, the mean flow and turbulence statistics computed in both simulations also turn out to be very close to each other and equally well agree with the experimental data (see Figs. 22, 23, 24, 25, 26). Thus, the comparison suggests that non-zonal hybrid DDES combined with the shear-layer-adapted definition of subgrid length-scale  $\Delta_{SLA}$  is quite competitive with the zonal RANS-IDDES approach.



**Fig. 21** Comparison of snapshots of the vorticity magnitude in the  $XY$ -plane and on the *bottom wall* from zonal SST RANS—SST-based IDDES (*upper frames*) and SST-based non-zonal DDES (*lower frames*). The *dashed line* shows the location of the RANS-IDDES interface in the zonal simulation



**Fig. 22** Comparison of mean skin-friction and wall pressure coefficient distributions predicted by zonal SST-RANS—SST-based IDDES and by non-zonal SST-based DDES combined with shear-layer adapted subgrid length-scale

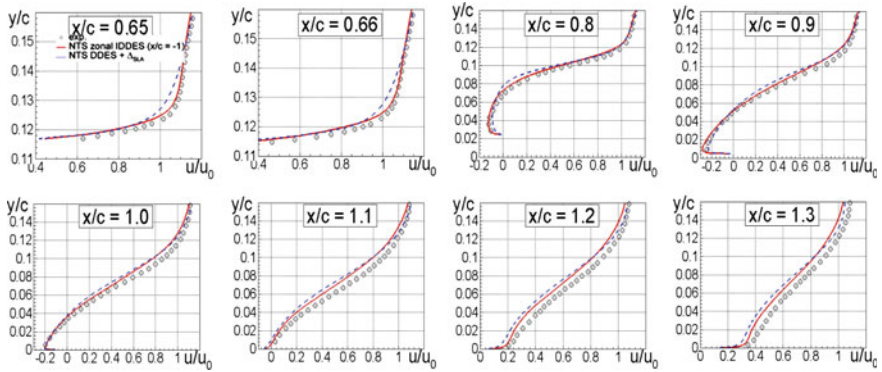


**Fig. 23** Comparison of mean velocity profiles in different flow cross-sections predicted by zonal SST-RANS—SST-based IDDES and by non-zonal SST-based DDES combined with shear-layer adapted subgrid length-scale

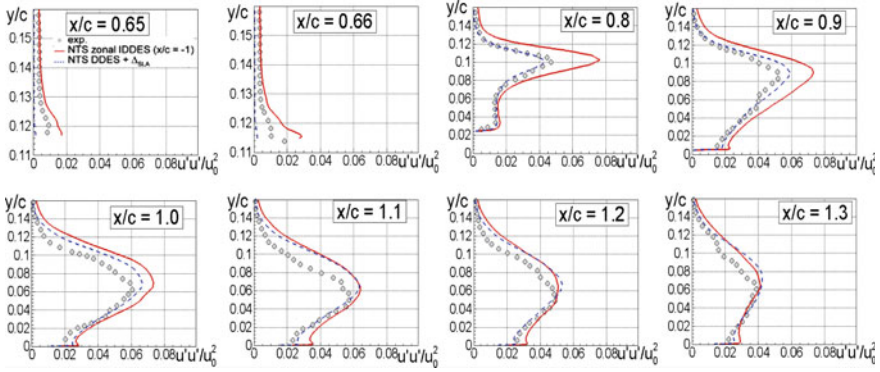


Fig. 24 Same, as in Fig. 23, for  $\langle u'u' \rangle$  profiles in different flow cross-sections

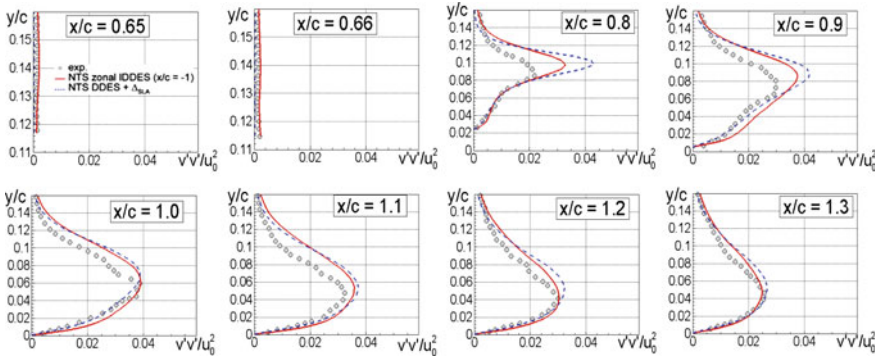


Fig. 25 Same, as in Fig. 23, for  $\langle v'v' \rangle$  profiles in different flow cross-sections

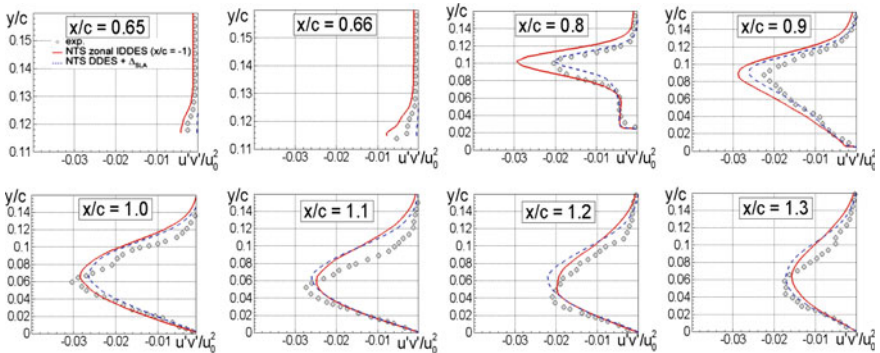


Fig. 26 Same, as in Fig. 23, for  $\langle u'v' \rangle$  profiles in different flow cross-sections

## 5 Conclusions

Simulations of the 2D wall-mounted hump flow carried out in the course of the project with the use of two grey area mitigation techniques (zonal RANS-IDDES with synthetic turbulence injected at their interface and non-zonal DDES combined with the shear layer adapted definition of the subgrid length-scale of Shur et al. 2015) allow drawing the following conclusions.

- For the flow in question, both grey area mitigation tools are proven to be nearly equally efficient and ensure a strong decrease of the delay of transition from the fully modeled (RANS) to mostly resolved (LES) turbulence in the separated shear layer, which in turn leads to a good agreement with the experimental data.
- Along with this, it is shown that the zonal technique implemented in two rather different industrial codes (the unstructured TAU code of DLR using the LD2 scheme and the multi-block structured code of NTS) provide close predictions thus supporting robustness of the approaches.
- No tangible difference is found in the performance of the two approaches to inject turbulent content at the RANS-IDDES interface, namely, the SEM of Jarrin et al. (2009) used in the DLR simulations and NTS STG of Shur et al. (2014) used by NTS.

To summarize, the work on the 2D wall-mounted hump flow (I.4 test case) turned out to be rather successful and giving a solid evidence in favor of high efficiency of the developed grey area mitigations tools.

# EC135 Helicopter Fuselage

N. Ashton, M. Fuchs, C. Mockett and B. Duda

## 1 Introduction

The EC135 helicopter fuselage represents a realistic and challenging test-case with a range of complex flow physics, such as 3D separation and an unsteady vortical wake. Whilst developing new turbulence models naturally begins with simple test-cases, the potential impact of any new approach for industry cannot truly be measured until they are assessed on such representative complex geometries. Accuracy is a key requirement of new approaches, however, robustness and stability are also crucial and can often be the deciding factor on their inclusion into an industrial CFD process.

This chapter presents work by the University of Manchester (UniMAN), CFD Software E + F GmbH (CFDB) and the Exa Corporation (EXA) to assess standard hybrid RANS-LES methods and a new Grey-Area Mitigation (GAM) DDES model, developed by CFDB for this industrially relevant test-case. Results for the pressure distribution, skin-friction, streamwise velocity and turbulent statistics are compared, in addition to power spectra density plots at several points on the helicopter to assess the unsteady dynamics of the flow-field.

---

N. Ashton (✉)  
School of MACE, University of Oxford, Manchester, UK  
e-mail: neil.ashton@oerc.ox.ac.uk

N. Ashton  
Oxford E-Research Centre, University of Oxford, Manchester, UK

M. Fuchs · C. Mockett  
CFD Software Entwicklungs- und Forschungsgesellschaft mbH (CFDB),  
Bismarckstr. 10-12, 10625 Berlin, Germany

B. Duda  
Exa GmbH, Landshuter Allee 8, 80637 Munich, Germany

## 2 Previous CFD Study and Issues with Experimental Comparability

Within the EU-funded FP7 Clean Sky project HELIDES (CSGA-2010-278415), a comparative study between steady-state RANS, unsteady RANS and DES has been conducted for two different geometrical configurations of an EC135 helicopter subjected to different angles of attack, see Fuchs et al. (2015). The primary goal of the study was to assess the feasibility of DES for simulation at full flight Reynolds number, i.e.  $Re = 4.7 \times 10^6/m$ , as well as the improvement in predictive accuracy compared to RANS and URANS. Two configurations were investigated, one consisting of the cabin and empennage and a second including also the landing skids. Both configurations excluded the main rotor and Fenestron<sup>®</sup> at the tail, so that the flow around the fuselage can be considered virtually incompressible. All simulations were conducted in fully turbulent mode, as little influence of laminar to turbulent transition is expected at full flight Reynolds number.

The CFD study was accompanied by experimental measurements conducted at the TU Munich by Grawunder et al. (2012), which were made available to the consortium after the completion of all simulations. Unfortunately, the experiments were not designed to directly match the physical and geometrical conditions of the CFD case, so that significant deviations between experiments and CFD exist:

- In contrast to CFD which was conducted at full flight Reynolds number, the experimental Reynolds number was constrained to values roughly an order of magnitude lower. Particularly for the landing skids laminar to turbulent transition has a strong influence. At the experimental Reynolds number range the cylindrical struts are clearly within the sub-critical (laminar separation) regime, giving rise to significantly wider wakes and increased drag compared to the super-critical (turbulent separation) flight/CFD Reynolds number.
- The experimental geometry used for integral force and surface pressure measurements featured a smoother cabin underbelly, for which roughness elements such as the landing skid mounting cavities were sealed. The comparably smoother underbelly geometry of the experiment significantly influenced the flow conditions towards the cabin backdoor and main separation region, which compromised comparability to the CFD for all local quantities in this region (e.g. mean and fluctuating surface pressure, wake topology and separation line). For a second measurement campaign where force coefficients on isolated parts of the helicopter and PIV measurements of the wake were investigated, a more realistic geometry including the underbelly roughness elements was used, which offered a better comparability to the CFD.

Despite these issues, some situations existed for which a reliable validation could be pursued, namely the force coefficient and wake flow measurements for the configuration without landing skids. In Fig. 1, the measured drag contribution of the isolated cabin (CABI), for which a weaker  $Re$  dependency than seen for the skids is expected, is compared to all CFD over a range of different angles of attack.

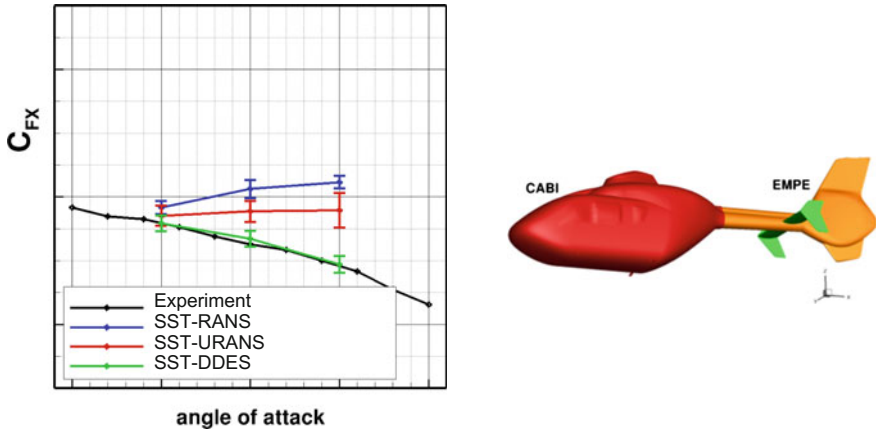


**Fig. 1** Drag coefficient on isolated cabin (CABI) for CFD simulations (Fuchs et al. 2015) and experiment (Grawunder et al. 2012)

In this situation, standard SST-based DDES was seen to perform very reliably in predicting the massively separated wake behind the fuselage, which is the main contributor to the overall drag. In contrast, RANS and URANS showed an inconsistent trend with angle of attack. The same conclusions could be drawn from comparing PIV data in the separated wake region to the CFD for the configuration without landing skids (see Fig. 2). Without the apparent Reynolds number effect of the skids and a comparable underbelly geometry in the experiment, very good agreement between measurements and DES was achieved, whereas both RANS and URANS significantly over-predict flow separation behind the cabin backdoor.

The previous HELIDES study therefore concluded that standard DDES offers significantly improved predictive accuracy for such helicopter fuselage aerodynamics applications.

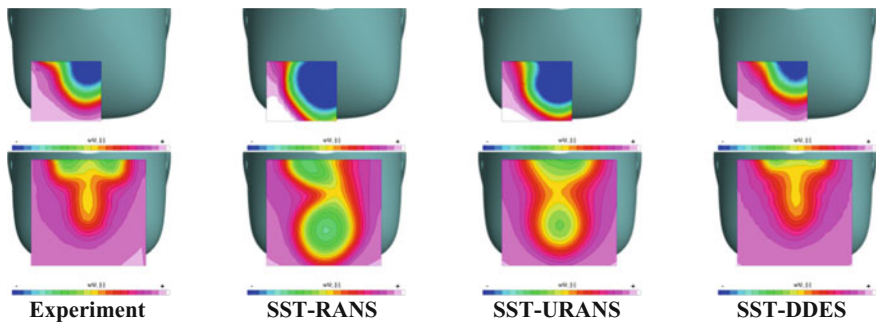


**Fig. 2** Comparison of streamwise velocity component for different scanning windows between CFD and experiment,  $\alpha = 0^\circ$ , configuration without landing skids

### 3 Motivation

Despite the comparability issues outlined above, the decision was nonetheless made to compute the configuration with landing skids. The higher geometrical complexity was considered valuable w.r.t. the goal to demonstrate robustness of new methods for a complex geometry. In particular, the landing skid struts protruding from the fuselage cause local separated wakes upstream of the main fuselage separation. This complication, which is typical for industrial geometries, presents a conceptual challenge regarding RANS/LES zone demarcation.

*The focus of this study is hence on comparison between CFD methods only and no experimental measurements will be shown.* The only exception made is for unsteady pressure measurements in the region above the tail boom, since the issues regarding the landing skids and underbelly are not expected to affect this region.

The goals of the study are therefore:

- To demonstrate whether the Grey-Area improved DDES formulation of CFDB is robust for such a complex geometry and applicable to unstructured grids.
- To assess whether the expected improvement in resolution of early shear layer turbulence is achieved with the GAM approach. Since the overall flow is not thought to be strongly dominated by the Grey Area, a significant change of global flow quantities is not expected.
- Comparison of std. DDES methods between different 2nd order finite-volume codes
- Comparison of std. DDES methods with different underlying RANS models (a strong sensitivity could be related to differing prediction of BL separation line from rear fuselage)
- Comparison between 2nd order finite volume codes and a Lattice-Boltzmann solver with a non-zonal hybrid RANS-LES model.

### 4 Geometric Description

Though the geometry retained is a simplification of the complete CATIA model, its sizing remains at full scale. All construction details have been removed and the outer contour is described by a watertight surface. This simplifies the meshing process whilst still keeping the main features that influence the main flow physics.

The fuselage comprises the *cabin*, the *landing skids* and the *empennage* shown in Fig. 3. To be noted is the high level of geometry details retained on the cabin and the landing skids such as, for instance, windows on the left and right sides, roughness elements on the bottom and clamps on cross-spars. Since a configuration without rotor-head is considered, the mast fairing has been closed by a surface tangential to the rim of the opening.





**Fig. 3** EC135 CFD Model

## 5 Partners and Numerical Tools

CFDB used the unstructured open-source flow solver OpenFOAM. An incompressible implicit transient solver, pimpleFoam was used (a blend between SIMPLE and PISO pressure-velocity coupling) with a time step of  $1 \times 10^{-4}$ . Convective fluxes were discretized using a hybrid numerical scheme, see Travin et al. (2000), which switches between a low-dissipation second order central differencing scheme and a robust second order linear upwind scheme based upon a blending function sensing regions of well-resolved vorticity dominated flow. The viscous fluxes were discretized using a 1st order upwind scheme. CFDB performed simulations using the SST-DDES model as well as a new GAM DDES method described later in this chapter.

UniMAN used the commercial unstructured flow solver STAR-CCM+ . A segregated implicit incompressible solver was used with dual time-stepping with a time of step of  $5 \times 10^{-5}$  and 5 inner iterations per time-step. The same hybrid numerical scheme as described for CFDB was used with a blend between a bounded second order CDS scheme and a 2nd order upwind scheme. The SA-DDES model was used for all simulations using a 2nd order upwind discretization scheme for the viscous fluxes.

Exa used their commercial Lattice-Boltzmann solver PowerFLOW. Contrary to standard CFD methods where a set of non-linear partial differential equations is solved, LBM methods rely on solving a velocity distribution function. The standard D3Q19 lattice scheme is employed, which allows 19 velocity states per mesh node in a three-dimensional discretization volume. It can be shown that this is sufficient for recovering the Navier-Stokes equations for an isotropic flow, yielding a low-dissipation second-order accurate scheme (Chen et al. 1998, 2003).

In order to account for unresolved turbulent flow structures, a variant of the RNG  $k-\varepsilon$  model is solved on the same underlying lattice. A swirl correction reduces eddy-viscosity in areas of high vorticity, allowing for the resolution of the unsteady large-scale vortices if the underlying grid is sufficiently fine. This approach is referred to as LBM-VLES. When benchmarked against other scale-resolving simulations such as DES variants or LES, LBM-VLES was found to be up to one order of magnitude faster, see Manoha and Caruelle (2015).

## 5.1 Grids

All the UniMan and CFDB simulations were conducted on the same mandatory mesh. This mesh shown in Fig. 4, was created by CFDB using the HEXPRESS software, resulting in an unstructured Cartesian-prismatic mesh of 32 million cells. The near-wall grid was designed to achieve a  $y^+$  of 40, thus all simulations by UniMan and CFDB utilized wall-functions.

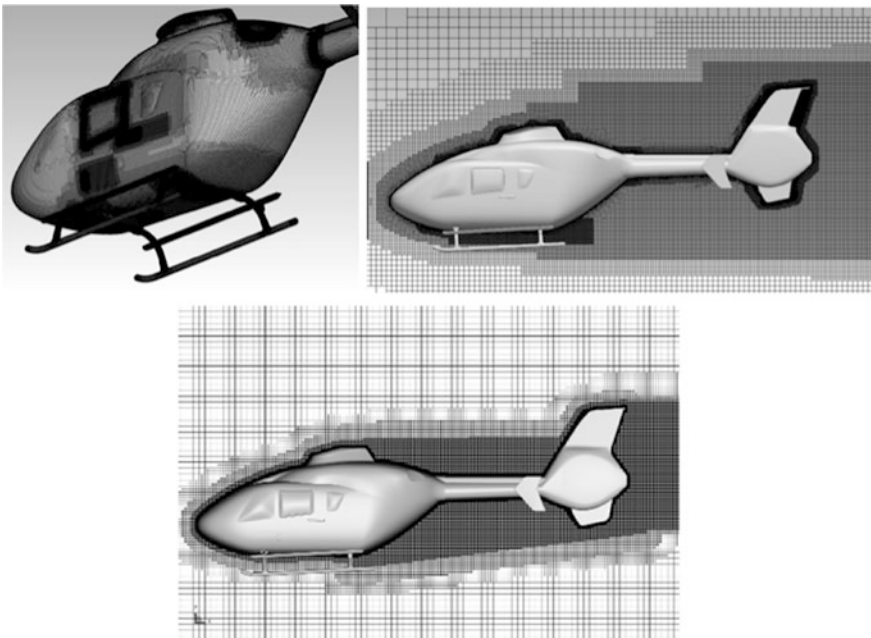


**Fig. 4** Mandatory unstructured mesh used by UniMAN and CFDB, and the grid used by EXA (*bottom*, every other line shown)

Exa generated their own grid, due to the differing requirements of their Lattice-Boltzmann code. A grid refinement study resulted in a final mesh consisting of 318 million volume elements (“voxels”) and 17.8 million surface elements (“surfels”). The explicit local time stepping procedure gives a time step of  $3.7 \times 10^{-6}$  s in the smallest cell. Due to the Cartesian cut-cell approach, wall-functions were also required in the near-wall region.

### 5.2 Boundary Conditions

The flight conditions retained correspond to a cruise flight at 140 knt at a height of 500 m in the standard atmosphere (ISA) and are listed in Table 1.

All surfaces of the helicopter geometry were treated as viscous (no-slip) walls. The flight conditions were imposed at the inlet to the computational domain and a suitable outflow condition was used at the outlet. At the vertical and lateral domain boundaries, suitable “non-blocking” conditions were applied, such as a mixed inlet/outlet condition depending on the flow direction into or out of the flow domain.

The computational domain boundaries were placed at a distance of approximately 200 m from the helicopter geometry, in line with the ‘free-flight’ type simulations

## 6 Results and Discussion

Due to the lack of experimental data at the desired Reynolds number, the focus of this study was to both assess the robustness of standard and GAM hybrid RANS-LES methods, as well as cross code comparison between OpenFOAM, STAR-CCM+ and Exa PowerFLOW. Such a code comparison aims to build confidence that DES-like methods can be used for complex industrial applications using main-stream CFD codes.

Thus, the results section is split into two sections, for the cross-code comparison and the testing of the GAM method developed by CFDB.

**Table 1** Flight conditions for CFD simulations

$T_{\infty} =$	284.9	K	Static temperature
$\rho_{\infty} =$	1.16727	kg/m <sup>3</sup>	Static density
$p_{\infty} =$	95,463	Pa	Static pressure
$\mu_{\infty} =$	$1.774 \times 10^{-5}$	kg m <sup>-1</sup> s <sup>-1</sup>	Dynamic viscosity
$V_{\infty} =$	72.02	m/s	Flight speed
$\alpha =$	0	deg	Angle of attack
$\beta =$	0	deg	Angle of side-slip

## 6.1 Cross-Code Comparison

In Fig. 5 we see a comparison of the mean skin-friction coefficient and surface pressure for the simulations conducted using OpenFOAM (SST-DDES), STAR-CCM+ (SA-DDES) and Exa PowerFLOW (LBM-VLES). Whilst the three simulations use different hybrid RANS-LES models and different codes, the separation line from the backdoor is similar between all simulations. Where there are differences in the skin-friction and surface pressure these are likely due to the differing underlying RANS models and wall-function approaches which will be active in the boundary layer.

Figures 6 and 7 show the mean streamwise velocity and mean turbulent viscosity ratio of the partners' computations on three planes behind the main cabin. It can be seen, that for the streamwise velocity there is good agreement, with only minor differences in the initial size of the cabin separation region. This difference is likely to have been affected by the separation prediction of the underlying RANS model as each partner's approach used a different RANS model. The difference between the partners is more noticeable for the turbulent viscosity ratio, where the larger turbulent viscosity ratio of the OpenFOAM simulation corresponds to the larger separation region. Most striking however is the extreme reduction of the turbulent viscosity in the PowerFLOW simulation. This implies that the leading order effect of turbulence is directly addressed in LBM-VLES by resolving large-scale structures and that the underlying turbulence model has only very little impact in the wake. This is achieved with the turbulence modelling strategy implemented in the standard release version of PowerFLOW.

Figure 8 shows the computed spectra downstream of the mast fairing for the OpenFOAM and Star-CCM+ results. It is considered highly encouraging that such

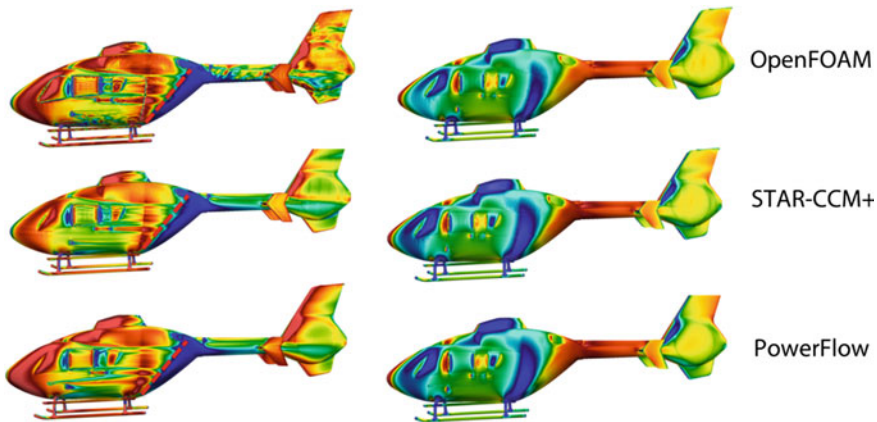


**Fig. 5** Surface skin-friction coefficient (Mean for STAR-CCM+ and Powerflow and instantaneous for OpenFOAM) (*left*) and mean surface pressure (*right*) for each code. Separation line marked with *dashed red line*

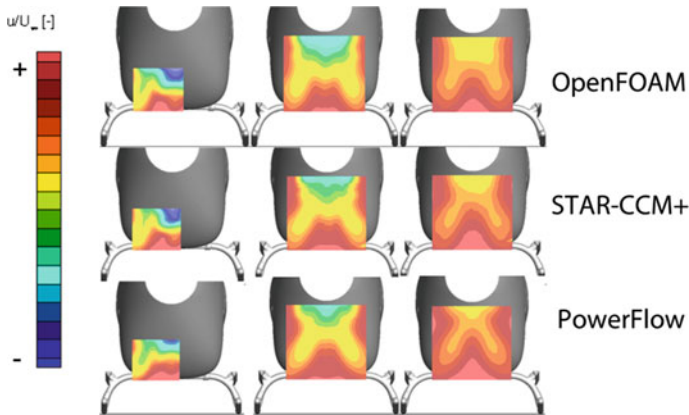


**Fig. 6** Comparison of the streamwise velocity behind the cabin at three locations using OpenFOAM, STAR-CCM+ and PowerFLOW

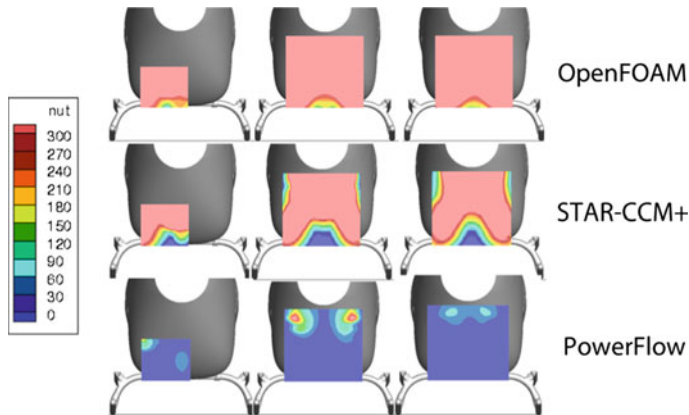


**Fig. 7** Comparison of the mean turbulent viscosity ratio behind the cabin at three locations using OpenFOAM, STAR-CCM+ and PowerFLOW

similar spectra are returned by different solvers using different DES variants on a common grid. Performance of GAM-improved DES.

In Mockett et al. (2012), the effect of different RANS background models on the flow prediction for a more generic EC145 helicopter geometry was thoroughly investigated, which resulted in the decision to select the  $k-\omega$  SST background model in the preliminary CFD study (described in an earlier subsection). To enable a clean comparison between the benchmark SST-DDES results and the GAM-improved  $\sigma$ -DES, the novel approach was implemented and validated based on the SST model (indeed, the  $\sigma$ -DES approach does not depend on a specific underlying RANS model). This guarantees equivalent DDES behaviour and

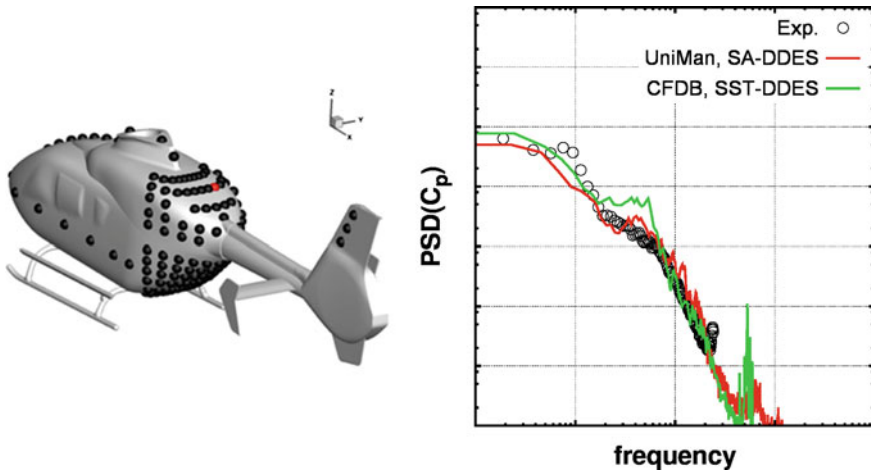


**Fig. 8** Computed and measured Power Spectral Density (PSD) of surface pressure coefficient time signals at the location shown in the *left* figure

prediction of wall shear stress upstream of the pressure-induced separation line. The same concepts as detailed in Part II (Presentation of Approaches, Non-Zonal Approaches for Grey Area Mitigation) for SA- $\sigma$ -DDES were applied, where the strain rate invariant  $S^* = \sqrt{2S_{ij}S_{ij}}$  as part of the SST model production term was replaced with the corresponding term  $B_\sigma S_\sigma$  of the  $\sigma$ -DES approach. The new variant denoted as SST- $\sigma$ -DDES was subsequently calibrated using the isotropic turbulence test case, where equivalent behaviour as standard SST-DDES was confirmed. In addition, the model was validated for the spatially evolving shear layer test case, where again comparable results to the SA-based  $\sigma$ -DDES model were achieved.

For the EC135 test case, SST- $\sigma$ -DDES was assessed in conjunction with the new LES filter width definition  $\tilde{\Delta}_\omega$  and equivalent numerics relative to the benchmark SST-DDES. The new model proved to be very robust for this complex application, showing equivalent convergence behaviour to SST-DDES. In Fig. 9, time histories of different contributions to the overall drag coefficient are plotted along with the time-averaged benchmark values from SST-DDES. In general, the new  $\sigma$ -DDES approach predicts very similar values of the different components with a deviation of max. 3%. This also translates to the other force coefficients and moments, indicating that the influence of the Grey Area issue is not very pronounced for this test case. Regarding the statistical error of the simulation, an isolated shedding effect at  $\sim 5t \times U_\infty/[m]$  can be observed in the drag coefficient time history, which originates from the cabin contribution. The selected time sample length might slightly over-represent the effect of this isolated event on the mean drag value.

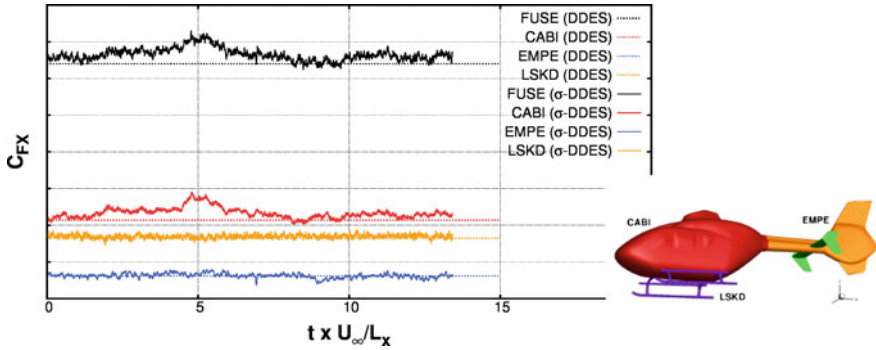


**Fig. 9** Time history (excluding initial transient) of overall drag coefficient (FUSE) and individual contributions from different components for GAM-improved  $\sigma$ -DES, dashed lines mark time-averaged values from standard DES

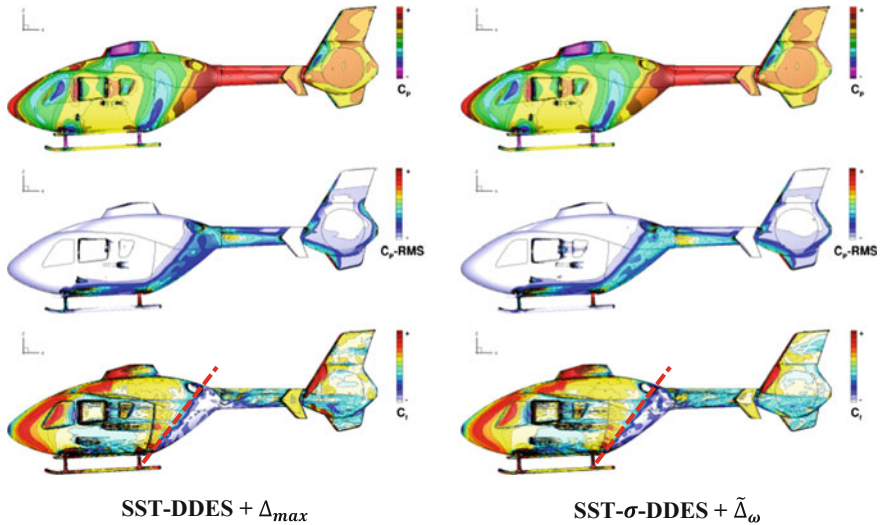


**Fig. 10** Contours of mean surface pressure coefficient (*top*), surface pressure coefficient RMS (*middle*), instantaneous wall friction coefficient (*bottom*). Main separation line on cabin marked with dashed red line

In Fig. 10, a comparison of different surface quantities is shown between standard DDES and the novel GAM-improved  $\sigma$ -DDES. Very similar surface pressure and wall friction levels are seen in the attached flow regime upstream of the cabin backdoor, indicating that both DDES variants provide sufficient shielding of the RANS boundary layer in this region. Likewise, the predicted location of the main separation line corresponds very well between the two DDES variants, but differences in the  $C_p$ -distribution are seen in the separation region, where flow separation

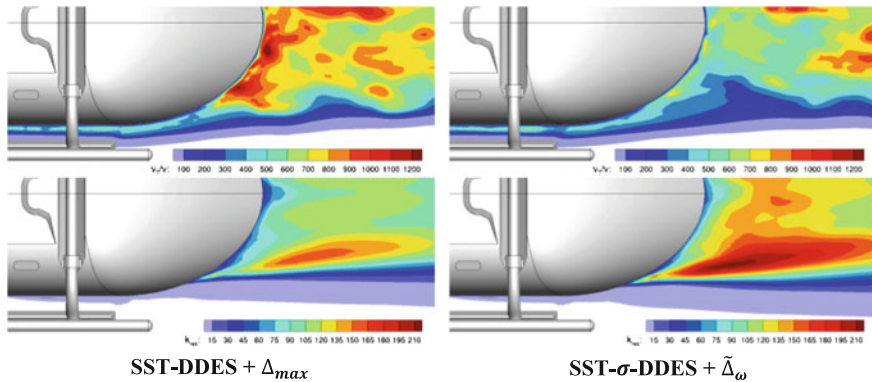


**Fig. 11** Contours of instantaneous viscosity ratio (*top*) and resolved kinetic energy (*bottom*). Cabin backdoor separation region is shown

is mildly increased for  $\sigma$ -DDES. A marked difference is seen for the surface pressure fluctuations, where the  $\sigma$ -DDES approach shows consistently higher fluctuations in the separation region on the backdoor, indicating increased activity of resolved scales in the early separated shear layer.

Although integral force coefficients and surface pressure distribution between the two DES variants are comparable, some local differences in model behaviour can be identified. In Fig. 11, contours of different flow variables and statistical quantities are shown for a horizontal slice and a magnified view of the wake region behind the backdoor (view is from below). In line with the  $\sigma$ -DES behaviour experienced for the delta wing (see Part IV, Results for Complex Test Cases, Delta Wing at High Angle of Attack) and isothermal jet (see Part IV, Results for Complex Test Cases, Single-stream Round Jet at  $M = 0.9$ ) test cases, the model attempts to mitigate the Grey Area following separation by reducing eddy viscosity when 2D flow is detected. This behaviour is also observed in the main separation region of the EC135, where eddy viscosity levels are lower than for standard DDES in the early shear layer region. Correspondingly, more turbulent content is resolved in the wake region using the same grid resolution.

The spectral solution content of both DES variants is assessed for two transducer locations situated downstream of the mast fairing and at the tail fin. As mentioned, these locations are not influenced by the skid/underbelly issues, so experimental comparison will likely be valid. For both locations, surface pressure spectra shown in Fig. 12 look very comparable and show acceptable agreement to the measurements.



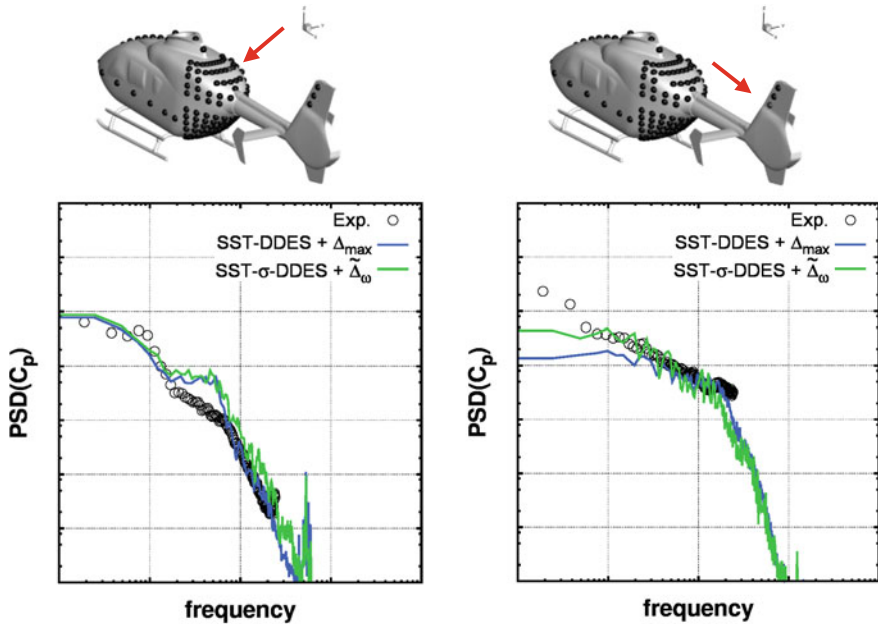


Fig. 12 Power spectral densities of surface pressure coefficient time signals at different locations

## 7 Conclusions

A realistic EC135 helicopter fuselage with skids and empennage has been computed using three different codes: OpenFOAM, STAR-CCM+ and PowerFLOW. Four different turbulence modelling approaches have been assessed: SA-DDES, SST-DDES, SST- $\sigma$ -DDES and LBM-VLES. For the mean quantities, there showed to be relatively little variation between the different codes and methods, which is encouraging for industrial users of hybrid RANS-LES methods. Where there were differences these were likely explained by the differing underlying RANS models and wall-functions utilized.

The newly developed Grey-Area Mitigation (GAM) model of CFDB proved to be robust and stable however the model itself did not show major differences over the standard DDES models. It was concluded that the grey-area issue does not strongly influence the global flow prediction for the EC135 helicopter. This test case however clearly demonstrates the need for future projects to address complex problems, ideally in combination with detailed complimentary experimental data, to assess new methods for industry.

**Part V**  
**The Common Assessment Platform**

# Rationale of Comparison in a Single CFD code

M. Fuchs, C. Mockett, A. Skillen and A. Revell

## 1 Introduction

An important component of any computational method research project must always be a comprehensive assessment of all new findings to ensure that meaningful and reliable conclusions can be obtained. This was also attempted in previous collaborative EU-funded turbulence modelling research projects such as Haase et al. (2009) and Schwamborn and Strelets (2012) in which a variety of novel ideas and models dedicated to solving specific issues of hybrid RANS-LES modelling were developed. While different partners were able to demonstrate considerable improvements with their developed method in their respective CFD codes, cross-code comparison and thus a more general assessment was often more difficult to achieve despite carefully selected validation test cases. Even when potential setup uncertainties such as boundary conditions, grid resolution and user input parameters were eliminated, differences of the numerical infrastructure still persisted and obscured clear conclusions.

Therefore, an activity was set up within Go4Hybrid referred to as the “Common Assessment Platform” (CAP) with the goal to implement and assess the most promising partner methods developed in the project using a common CFD code. In this way we aimed to eliminate many of the specific issues and complications previously encountered in similar benchmarking and model assessment exercises. The choice to use OpenFOAM for this activity was motivated as follows:

---

M. Fuchs (✉) · C. Mockett  
CFD Software Entwicklungs- und Forschungsgesellschaft mbH (CFDB),  
Bismarckstr. 10-12, 10625 Berlin, Germany  
e-mail: marian.fuchs@cfdb-berlin.com

A. Skillen · A. Revell  
School of Mechanical, Aerospace and Civil Engineering,  
University of Manchester, Manchester, UK

- The source code is open source and therefore accessible to all partners without cost or IP issues.
- Two Go4Hybrid partners, i.e. CFDB and UniMAN, have extensive experience with model development using this code.
- By implementing and assessing different partner methods in the unstructured OpenFOAM code, the suitability of these methods for general purpose CFD codes is further demonstrated, which adds additional value to the exercise.

Due to strategic and IP-related concerns of some partners, it was agreed that none of the Go4Hybrid methods implemented into OpenFOAM will be made publicly available as a consequence of the CAP activity. Within CAP, both non-zonal and zonal grey area mitigation (GAM) approaches were assessed for two fundamental test cases detailed in more depth in the following section. Despite eliminating numerical influences from the method comparison in CAP, the approach is not entirely without its drawbacks and limitations, which are detailed below:

- Due to time constraints, the scope of the activity was confined to assess the methods for two fundamental test cases on one mandatory grid each. No grid sensitivity study was conducted, neither were the models run for other test cases. However, by combining the findings of the CAP with those from the partner-wise simulations, we think that a more complete picture is obtained than has been possible in previous projects. This assumes that the CAP activity does not deliver contrary findings compared to the partner-wise studies.
- In some cases individual partner methods may have been developed with specific codes and applications in mind, and as such their comparison on a single mandatory case will not necessarily reflect their performance as originally intended in their native code base.
- It cannot be ruled out that the employed OpenFOAM numerics might be slightly biased towards a particular method. However, we expect this effect to be rather weak at most. In addition, OpenFOAM is numerically comparable to many other industrial CFD codes, so that there is a certain portability of the outcomes of the CAP.
- Some of the partner methods were developed in structured CFD codes and are based on certain assumptions requiring a structured code infrastructure. The implementation of these methods in the unstructured CAP hence necessitated some alteration relative to the original formulations.
- The CAP has compared the methods directly by eliminating numerical sensitivity. The degree of numerical sensitivity exhibited by a method is however valuable information in itself. An indication of this has been provided in previous partner-wise sections (partners have also implemented methods developed by others).
- Despite considerable care and thorough communication with the corresponding method authors, implementation bugs and / or misuse of any method tested within CAP cannot be ruled out completely.

## 2 Overview of the activity

As detailed in the previous section, the CAP activity aimed to assess the most promising GAM methods developed within Go4Hybrid by implementing the methods into a common CFD code, i.e. OpenFOAM, and to validate them for two fundamental test cases. The following two groups of GAM methods have been evaluated:

- **Non-zonal methods:** These are methods which provide an automatic switch between the RANS and LES regimes in the flow field. Methods from CFDB, NLR, NTS and ONERA have been selected for this activity (see Part II, Presentation of Approaches, Non-Zonal Approaches for Grey Area Mitigation). A detailed summary of this activity is given in Part V (The Common Assessment Platform, Direct Comparison of Non-Zonal Methods). This study was conducted by CFDB.
- **Embedded (zonal) methods:** These are all methods for which an explicit description of the RANS-LES interface/region is required by the user. For CAP, this concerns the different synthetic turbulence generator methods of DLR, NTS, ONERA and UniMAN (see Part II, Presentation of Approaches, Improved Embedded Approaches). All methods have been assessed for the zero-pressure gradient boundary layer flow over a flat plate (see Part III, Results for Fundamental Test Cases, The spatially developing flat plate turbulent boundary layer). A detailed summary of this activity is given in in Part V (The Common Assessment Platform, Direct Comparison of Embedded Approaches). This study was conducted by UniMAN.

Although both test cases are considered fundamental, they both feature physics which are of high relevance to the grey area issue seen in practical applications. Conclusions drawn from the test cases are very likely transferable to more complex applications such as jets or recirculating flows, as partner-wise results presented in Part IV demonstrate. The comparison to state-of-the-art hybrid RANS-LES methods within the CAP furthermore highlights that all tested methods essentially provide a considerable improvement over the current academic and industrial standards.

# Direct Comparison of Non-zonal Methods

M. Fuchs and C. Mockett

## 1 Introduction

Non-zonal hybrid RANS-LES models are generally considered a very promising approach to treat a wide range of practical applications at high Reynolds numbers, as no a priori knowledge about the flow field (e.g. potential separation zones) is required as user input. The model decides automatically when to apply RANS modelling and when to switch to scale-resolving LES mode in separated flow regions. When assessing potential remedies for the Grey Area problem frequently seen for such methods, naturally the extent to which a method is able to minimise this region should be a good measure for its suitability for practical applications. However, hybrid RANS-LES turbulence modelling poses additional requirements on method development, especially if the method is envisioned to be implemented in a general purpose CFD code and applied to complex practical applications. Some of these core requirements are:

- A potential remedy for the Grey Area problem must maintain the non-zonal nature of the original hybrid RANS-LES model. This means that a Grey-Area Mitigation (GAM) method requiring explicit user input about the distribution of RANS and LES regions inside the computational domain is considered non-practical in the context of non-zonal methods.
- Accelerating RANS-to-LES transition should not compromise other model features required for practical applications. For example, implementing an aggressive switch to LES-mode shortly after separation might have a beneficial effect on the Grey Area, but can at the same time weaken the shielding capa-

---

M. Fuchs (✉) · C. Mockett  
CFD Software Entwicklungs- Und Forschungsgesellschaft MbH (CFDB),  
Bismarckstr. 10-12, 10625 Berlin, Germany  
e-mail: marian.fuchs@cf-d-berlin.com

C. Mockett  
e-mail: charles.mockett@cf-d-berlin.com

bilities of the model in attached boundary layers. Likewise, a GAM method should improve behaviour in the early shear layer region, without impairing the sub-grid scale (SGS) behaviour of the LES-mode in fully resolved 3D turbulence regions downstream.

- A proposed GAM method should be general enough to be applicable to different hybrid RANS-LES models and ideally should show a consistent behaviour for mitigating the Grey Area for the different models. This is especially important since attached boundary layers are treated with RANS for hybrid models, so that the separation prediction is often sensitive to this modelling part. Being able to assess the separation prediction for different underlying RANS models and at the same time keep a consistent GAM mechanism is therefore considered very valuable.
- It is preferable that the proposed method involves only quantities which are readily available in unstructured CFD codes, as the majority of commercial CFD codes rely on an unstructured methodology.
- Although maintaining a purely local formulation is desirable for implementation into general purpose CFD codes, the addition of non-local features (e.g. spatial/temporal averaging, etc.) should not be discarded immediately, but has to prove an additional value with regard to mitigating the Grey Area when compared to purely local formulations.
- Ideally, the proposed method should not add a significant computational overhead to the underlying hybrid RANS-LES model.

Within the non-zonal CAP work package, the implemented GAM methods are both assessed with regard to their capabilities to mitigate the Grey Area issue as well as the degree to which they meet the above criteria.

## 2 Non-zonal Methods Implemented

For the non-zonal part of the CAP, GAM methods of four different partners have been selected, namely of CFDB, NLR, NTS and ONERA. An overview about all conducted simulations is given in Table 1. The GAM methods considered for the CAP have been selected based on the following criteria:

1. The proposed method has to be mature enough and sufficiently well documented to be implemented into the common assessment platform.
2. The participating partners had to demonstrate in their native CFD code that their proposed method is able to significantly reduce the Grey Area for at least one meaningful test case.
3. The formulation of the proposed GAM method had to be suitable for implementation into the unstructured OpenFOAM code. No further method development was conducted within the CAP activity, however some of the selected methods had to be slightly adapted for implementation relative to the formulations presented in Part II (Presentation of Approaches, Non-Zonal Approaches for Grey Area Mitigation). All conducted changes were discussed and agreed upon with the original authors of the method.

**Table 1** Overview of CAP simulations conducted in OpenFOAM for non-zonal hybrid RANS-LES methods

GAM method originator	Model + GAM method
Datum model	SA-DDES + $\Delta_{max}$
CFDB	SA- $\sigma$ -DDES + $\Delta_{max}$
	SA- $\sigma$ -DDES + $\tilde{\Delta}_{\omega}$
NLR	SA-DDES + $\Delta_{max}$ + HPF
	SA-DDES + $\Delta_{max}$ + HPF + stoch. backscatter (uncorrelated)
NTS	SA-DDES + $\tilde{\Delta}_{\omega}$
	SA-DDES + $\Delta_{SLA}$
ONERA	SA-DDES + $\Delta_{\omega}$

The methods finally selected for assessment in the non-zonal CAP work package adhere to all three of the stated criteria. From ONERA, their alternative definition for the LES filter width  $\Delta_{\omega}$  was selected, see Deck (2012). It is the most mature (in terms of publication date) of all tested GAM methods within CAP, and has proven to be very efficient for both the shear layer test case (see Part III, Results for Fundamental Test Cases, Free Shear Layer) and the three-element airfoil (see Part IV, Results for Complex Test Cases, The 3-Element Airfoil) in conjunction with ONERA’s ZDES model applied in mode 2 (i.e. the non-zonal mode of ZDES) within Go4Hybrid.

CFDB assessed the performance of their  $\sigma$ -DDES approach for four different test cases within the project, namely the spatial shear layer, the EC135 helicopter (see Part IV, Results for Fundamental Test Cases, EC135 Helicopter Fuselage), the delta wing (see Part IV, Results for Fundamental Test Cases, Delta Wing at High Angle of Attack) and the static round jet (see Part IV, Results for Complex Test Cases, Single-stream Round Jet at  $M = 0.9$ ). For all test cases for which the Grey Area issue was seen to be important (for the helicopter flow, we see only a minor influence of the Grey Area), the method clearly outperforms the industrial standard hybrid RANS-LES model SA-DDES.

NTS also evaluated their two LES filter width definitions  $\tilde{\Delta}_{\omega}$  and  $\Delta_{SLA}$  (see Shur et al. 2015) for a range of test cases, including the spatial shear layer, the 2D hump (see Part IV, Results for Complex Test Cases, 2D Wall-Mounted Hump) and the jet test case. The  $\Delta_{SLA}$  formulation proved to be very effective when applied in conjunction with the SA-DDES model (although it is not limited to a particular hybrid model). The  $\tilde{\Delta}_{\omega}$  formulation however was seen to be incapable of completely mitigating the Grey Area (an appreciable ameliorating effect is seen, though), as anticipated by the method’s authors, so that it is not seen by them as a GAM method when applied in isolation. It is nonetheless included in the CAP comparison, since CFDB is using the formulation in conjunction with their  $\sigma$ -DDES approach as an additional means to accelerate RANS-to-LES transition on strongly anisotropic grids.



Both considered NLR approaches, namely the high-pass filtering of modelled Reynolds stresses and application of stochastic forcing in LES-mode, have been successfully tested in their code for the shear layer, the delta wing, the round jet and the three-element airfoil test cases. Unfortunately, the very promising approach of NLR to apply spatially and temporally correlated stochastic forcing (see Part II, Presentation of Approaches, Non-Zonal Approaches for Grey Area Mitigation) could not be considered for the CAP, as the required reformulation of the spatial smoothing for unstructured grids was not possible with the available resources (the original method was implemented and tested in a structured code).

## 2.1 *Implementation and Assessment Strategy*

An accurate and fair assessment of different GAM techniques is challenging, even when the methods are implemented and compared in a single CFD code. The key difficulty is to be able to distinguish between the actual impact of the GAM technique and further influences of other modelling aspects. When dealing with the Grey Area issue for non-zonal hybrid RANS-LES methods, we usually face the situation that the flow separates from the surface (either geometrically-induced or pressure-induced) and undergoes a transitional process from a smooth RANS boundary layer into a free shear layer treated by LES. The velocity profile in the boundary layer shortly before separation, the RANS modelling applied inside the boundary layer and potential shielding functions used in the formulation all influence the spatial extend of the Grey Area. To separate these issues from the assessment of the proposed GAM techniques, all methods are implemented and tested in conjunction with the same datum hybrid RANS-LES model. In this study, the delayed DES model of Spalart et al. (2006) based on the Spalart-Allmaras RANS model is chosen. The choice is motivated as follows:

- Three out of four partners contributing to the non-zonal CAP activity have successfully tested their respective GAM methods in conjunction with the SA-DDES model within Go4Hybrid.
- SA-DDES is a well-established hybrid RANS-LES model both in academia and industry, and is implemented in many general purpose CFD codes. Assessing the performance of the proposed GAM methods in conjunction with this model hence adds practical relevance to the study.
- Using the SA-DDES model for the non-zonal CAP eliminates the potential influence of different shielding formulations on the Grey Area performance, as the shield function  $f_d$  of DDES is utilised in all simulations. In addition, tests were conducted to establish the performance of each GAM method in conjunction with this particular shield function (see Sect. 2.2, “Preliminary tests”).

To provide a comprehensive documentation of all models assessed within the non-zonal CAP, the exact formulation of SA-DDES as detailed in Spalart et al. (2006) and implemented in OpenFOAM is re-iterated here.

The hybrid RANS-LES model is based on a transport equation for the modified turbulent eddy viscosity:

$$\begin{aligned} \frac{\partial \tilde{v}}{\partial t} + u_j \frac{\partial \tilde{v}}{\partial x_j} = c_{b1}(1 - f_{t2})\tilde{S}\tilde{v} - \left[ c_{w1}f_w - \frac{c_{b1}}{\kappa^2}f_{t2} \right] \left( \frac{\tilde{v}}{L_{DDES}} \right)^2 \\ + \frac{1}{\sigma} \left[ \frac{\partial}{\partial x_j} \left( (v + \tilde{v}) \frac{\partial \tilde{v}}{\partial x_j} \right) + c_{b2} \frac{\partial \tilde{v}}{\partial x_i} \frac{\partial \tilde{v}}{\partial x_i} \right]. \end{aligned} \quad (1)$$

The modelled Reynolds stresses entering the Navier-Stokes equations are computed from the turbulent eddy viscosity, which is related to the modified eddy viscosity via the  $f_{v1}$ -function:

$$\tau_{ij} = 2\mu_t \left( S_{ij} - \frac{1}{3} \frac{\partial u_i}{\partial x_j} \delta_{ij} \right) - \frac{2}{3} \rho k \delta_{ij}, \quad \mu_t = \rho f_{v1} \tilde{v}, \quad (2)$$

where  $S_{ij} = 1/2(\partial u_i/\partial x_j + \partial u_j/\partial x_i)$  and  $\delta_{ij}$  is the Kronecker delta. The function  $f_{v1}$  reads:

$$f_{v1} = \frac{\chi^3}{\chi^3 + c_{v1}^3}, \quad \chi = \frac{\tilde{v}}{v}. \quad (3)$$

The modified strain rate invariant included in the production term of the  $\tilde{v}$ -equation is defined as:

$$\tilde{S} = \max \left( \Omega + \frac{\tilde{v}}{\kappa^2 L_{DDES}^2} f_{v2}, 0.3\Omega \right), \quad \Omega = \sqrt{2\Omega_{ij}\Omega_{ij}}, \quad \Omega_{ij} = \frac{1}{2} \left( \frac{\partial u_i}{\partial x_j} - \frac{\partial u_j}{\partial x_i} \right). \quad (4)$$

The additional model functions read:

$$\begin{aligned} f_{v2} = 1 - \frac{\chi}{1 + \chi f_{v1}}, \quad f_w = g \left[ \frac{1 + c_{w3}^6}{g^6 + c_{w3}^6} \right]^{\frac{1}{6}}, \quad g = r + c_{w2}(r^6 - r), \\ r = \min \left( \frac{\tilde{v}}{\tilde{S}\kappa^2 L_{DDES}^2}, 10 \right), \quad f_{t2} = c_{t3} \exp(-c_{t4}\chi^2). \end{aligned} \quad (5)$$

The constants of the Spalart-Allmaras model are defined as:

$$\begin{aligned} c_{b1} = 0.1355, \quad \sigma = 2/3, \quad c_{b2} = 0.622, \quad \kappa = 0.41, \quad c_{w2} = 0.3, \\ c_{w3} = 2, \quad c_{v1} = 7.1, \quad c_{t3} = 1.2, \quad c_{t4} = 0.5, \quad c_{w1} = \frac{c_{b1}}{\kappa^2} + \frac{1 + c_{b2}}{\sigma}. \end{aligned} \quad (6)$$

The hybrid length scale  $L_{DDES}$  utilised to switch between RANS and LES mode of the simulation is defined as:

$$L_{DDES} = L_{RANS} - f_d \max(0, L_{RANS} - L_{LES}), \quad (7)$$

where

$$L_{RANS} = d_w, \quad L_{LES} = C_{DES} \Psi \Delta. \quad (8)$$

In Eq. (8),  $d_w$  is the wall distance,  $C_{DES} = 0.65$  is a calibrated constant,  $\Psi$  a model-specific correction function and  $\Delta$  the LES grid filter width. In DES,  $\Delta$  is usually computed by evaluating the maximum of the cell length in each grid direction, i.e.  $\Delta = \Delta_{max} = \max(\Delta_x, \Delta_y, \Delta_z)$ . The function  $f_d$  of Eq. (7) is the shielding function of delayed DES which aims to prevent activation of LES mode inside of attached boundary layers. It is defined as:

$$r_d = \frac{v_t + \nu}{\kappa^2 L_{DDES}^2 \max\left(\sqrt{\frac{\partial u_i}{\partial x_j} \frac{\partial u_i}{\partial x_j}}, 10^{-10}\right)}, \quad f_d = 1 - \tanh\left[(C_{d1} r_d)^{C_{d2}}\right]. \quad (9)$$

The default values of the blending function constants for SA-DDES are  $C_{d1} = 8$  and  $C_{d2} = 3$ . Equations (1)–(9) describe the model used both as a benchmark and underlying hybrid RANS-LES model for all non-zonal CAP simulations. The changes made relative to this model for all assessed GAM techniques are detailed in the following paragraphs.

### 2.1.1 Implementation of CFDB Method

The  $\sigma$ -DDES approach of CFDB was developed and first tested in OpenFOAM, so it is applied in its native code in the CAP. The proposed method is based on the substitution of the vorticity strain invariant in Eq. (4) with a formulation incorporating the equivalent velocity gradient based scale of the  $\sigma$  LES model:

$$S_{\sigma-DDES}^* = \Omega - f_d \text{pos}(L_{RANS} - L_{LES})(\Omega - B_\sigma S_\sigma^*), \quad (10)$$

where

$$S_\sigma^* = \frac{\sigma_3(\sigma_1 - \sigma_2)(\sigma_2 - \sigma_3)}{\sigma_1^2}. \quad (11)$$

In Eq. (11),  $\sigma_1 \geq \sigma_2 \geq \sigma_3 \geq 0$  are the three singular values of the velocity gradient tensor  $\mathbf{g} = g_{ij}$ .  $B_\sigma = 67.8$  is a calibrated constant to restore correct SGS model behaviour. The pos operator used to detect DES97 RANS and LES mode is defined as:

$$\text{pos}(a) = \begin{cases} 0 & \text{if } a \leq 0 \\ 1 & \text{if } a > 0 \end{cases}. \quad (12)$$

To maintain equivalent shielding behaviour compared to standard SA-DDES, the constant  $C_{d1}$  of Eq. (9) had to be re-calibrated to  $C_{d1} = 10$  (see Part II, Presentation of Approaches, Non-Zonal Approaches for Grey Area Mitigation).

### 2.1.2 Implementation of NLR Method

Two concepts proposed by NLR and detailed in Part II (Presentation of Approaches, Non-Zonal Approaches for Grey Area Mitigation) are implemented and assessed for the non-zonal CAP task. The first GAM technique evaluated concerns the high-pass filtering (HPF) of the SGS stresses to reduce the influence of high mean velocity gradients. The SGS stresses are computed from the velocity fluctuations  $u'$  instead of from the instantaneous velocity  $u$  as in the standard model (see Eq. 2):

$$\tau_{ij} = \tau'_{ij} = 2\mu_t \left( S'_{ij} - \frac{1}{3} \frac{\partial u'_i}{\partial x_j} \delta_{ij} \right) - \frac{2}{3} \rho k \delta_{ij}, \quad (13)$$

with  $S'_{ij} = \frac{1}{2} (\partial_j u'_i + \partial_i u'_j)$ . The substitution was implemented to be active only in LES mode and is additionally shielded by the DDES function  $f_d$ . The velocity fluctuations  $u'$  are obtained by applying a temporal high-pass filter to the velocity field, which requires temporal averaging of the velocity field. Computing the running averages of the velocity field introduces a dependency on the initial transient as temporal filtering is active from the beginning of the simulation. However, in simulations conducted by NLR, no significant delay in statistical convergence or a lengthening of the initial transient was observed due to this issue, so that it was not investigated in the CAP. Another disadvantage of the approach is that it is not suitable for flows containing unsteadiness unrelated to the local shear layer eddies, e.g. shear layer “flapping”.

The second GAM technique proposed by NLR and considered for the CAP concerns the stochastic SGS model approach. Here, the diffusion term containing the modelled sub-grid stress tensor entering the Navier-Stokes equations is defined as:

$$\frac{\partial \tau_{ij}}{\partial x_j} = \frac{\partial}{\partial x_j} \left[ 2\mu_t \left( S_{ij} - \frac{1}{3} \partial_k u_k \delta_{ij} \right) - \frac{2}{3} \rho k \delta_{ij} \right] - \frac{\partial R_{ij}}{\partial x_j}, \quad (14)$$

with  $R_{ij}$  a random stress tensor providing the backscatter. Again, the supplementary tensor  $R_{ij}$  is only active in LES mode and is additionally shielded by the DDES function  $f_d$ . The tensor  $R_{ij}$  is not modelled directly, but its gradient is modelled as the rotation of a stochastic vector potential:

$$\frac{\partial R_{ij}}{\partial x_j} = \frac{\partial}{\partial x_j} \times (C_B \rho k \xi), \quad (15)$$

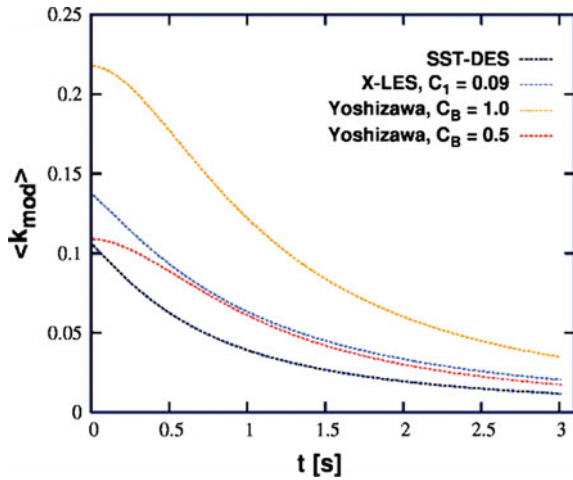
with  $C_B$  a model constant ( $C_B = 1$  by default) and  $\xi$  a vector of three independent stochastic variables  $\xi_i = N(0, 1)$ . For the CAP implementation, the components of the stochastic vector  $\xi$  were assumed to be uncorrelated in space and time. In Eq. (15), the turbulent kinetic energy  $k$  is used for scaling. Unfortunately, the Spalart-Allmaras model and its derivatives do not provide this quantity directly, so that an approximation had to be employed. It was decided to compute  $k$  from the relation given e.g. by the SGS one-equation model of Yoshizawa and Horiuti (1985):

$$k = \left( \frac{v_t}{C_k \Delta} \right)^2, \quad (16)$$

with  $C_k = 0.07$ . In Fig. 1, a comparison is shown between the relation of Eq. (16) when computed passively from SA-DES for decaying isotropic turbulence and when taken directly from the  $k$ - $\omega$ -based models SST-DES and X-LES (where the X-LES constant  $C_1$  was calibrated for the OpenFOAM numerics). To match  $k_{mod}$  values returned by the Yoshizawa & Horiuti formulation with values seen for the X-LES model, the scaling constant  $C_B$  of Eq. (15) was re-calibrated for the CAP simulations to  $C_B = 0.5$ .

The correct functionality of generating the stochastic vector components was also tested in OpenFOAM for decaying isotropic turbulence (see Fig. 2).

**Fig. 1** Spatially averaged values of modelled turbulent kinetic energy post-processed for different models for decaying isotropic turbulence (323 grid)



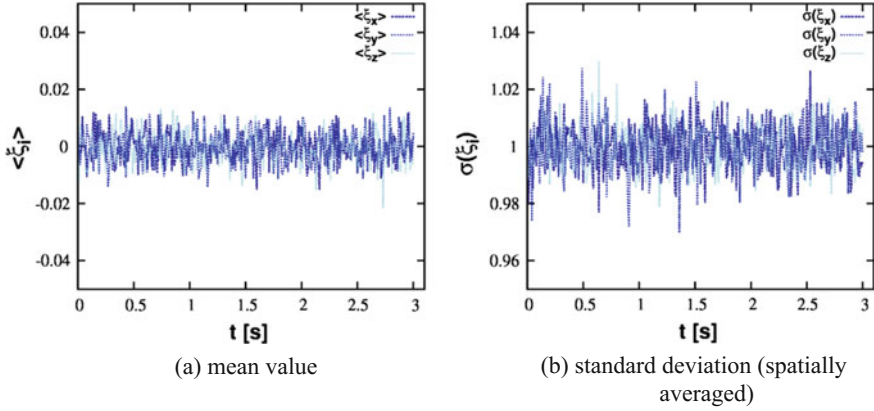


**Fig. 2** Test of basic functionality of routine to generate stochastic variable components in OpenFOAM

### 2.1.3 Implementation of NTS Method

For the NTS contribution, two alternative definitions of the LES filter width  $\Delta$  published in Shur et al. (2015) have been implemented and assessed. For convenience, we re-iterate the corresponding formulations from Part II (Presentation of Approaches, Non-Zonal Approaches for Grey Area Mitigation).

The first formulation denoted as  $\tilde{\Delta}_\omega$  represents a definition of the LES filter width which is sensitised to the direction of the vorticity vector. Considering a cell with its centre at  $\mathbf{r}$  and vertices at  $\mathbf{r}_n$  ( $n = 1, \dots, 8$  for hexahedra), the proposed definition reads:

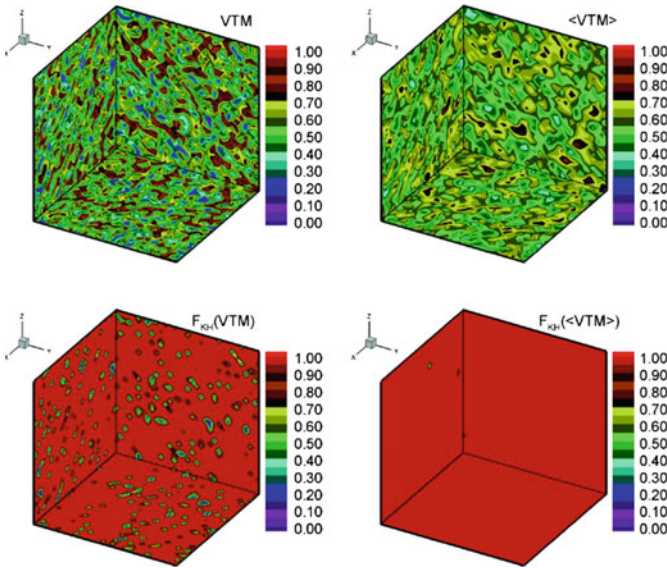
$$\Delta = \tilde{\Delta}_\omega = \alpha \frac{1}{\sqrt{3}} \max_{n,m=1,8} |(\mathbf{I}_n - \mathbf{I}_m)|, \quad (17)$$

where  $\mathbf{I}_n = \mathbf{n}_\omega \times (\mathbf{r}_n - \mathbf{r})$  and  $\mathbf{n}_\omega$  is the unit vector aligned with the vorticity vector. A value of  $\alpha = 1.025$  is used in the CAP to obtain equivalent behaviour compared with the standard  $\Delta_{max}$  formulation on isotropic cells.

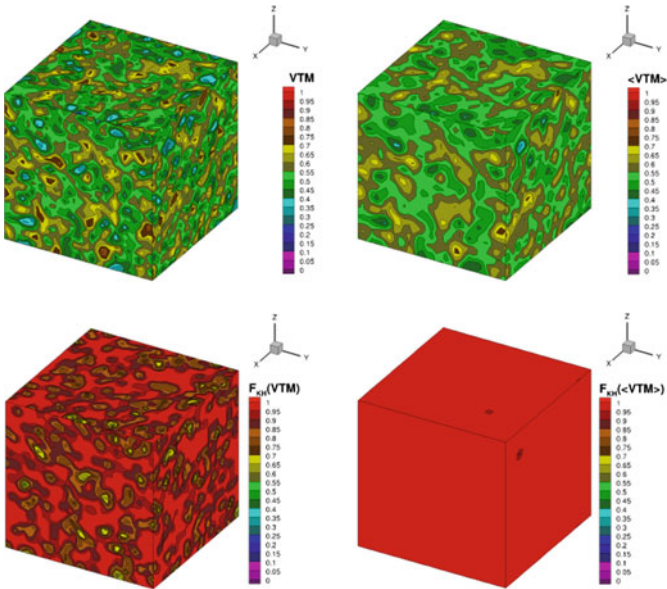
The second proposed  $\Delta$  formulation considered for the CAP represents an extension to the definition in Eq. (17) which additionally includes a kinematic measure of the flow field. The  $\Delta$  formulation added with the subscript SLA (for Shear Layer Adapted) is defined as:

$$\Delta = \Delta_{SLA} = \tilde{\Delta}_\omega F_{KH}^{lim}(\langle VTM \rangle). \quad (18)$$

The additional function  $F_{KH}^{lim}$  processes a quantity referred to as the Vortex Tilting Measure (VTM), where the brackets  $\langle \cdot \rangle$  indicating averaging over neighbouring cells:



(a) behaviour of different functions of  $\Delta_{SLA}$  in NTS code  
 (taken from Shur et al. (2015)),  $64^3$  grid



(b) behaviour of different functions of  $\Delta_{SLA}$  in OpenFOAM,  $32^3$  grid

**Fig. 3** Test of basic functionality of  $\Delta_{SLA}$  implementation in OpenFOAM for decaying isotropic turbulence test case

$$VTM = \frac{\sqrt{6} |(\widehat{S} \cdot \omega) \times \omega|}{\omega^2 \sqrt{3 \text{tr}(\widehat{S}^2) - [\text{tr}(\widehat{S})]^2}} \max\{1, (v^*/v_t)\}, \quad v^* = 0.2v. \quad (19)$$

In Eq. (19),  $\widehat{S}$  is the strain tensor,  $\omega$  is the vorticity vector and  $\text{tr}(\cdot)$  means trace. The definition of  $\Delta_{SLA}$  in Eq. (18) includes an additional shielding mechanism to prevent the activation of LES mode inside attached boundary layers. The complete formulation of the  $F_{KH}^{lim}$  function reads:

$$F_{KH}^{lim} = \begin{cases} 1.0 & , \text{if } f_d < (1 - \varepsilon) \\ F_{KH} & , \text{if } f_d \geq (1 - \varepsilon) \end{cases}, \quad (20)$$

$$F_{KH} = \max \left\{ F_{KH}^{min}, \min \left\{ F_{KH}^{max}, F_{KH}^{min} + \frac{F_{KH}^{max} - F_{KH}^{min}}{a_2 - a_1} (VTM - a_1) \right\} \right\}, \quad (21)$$

where  $\varepsilon = 0.01$  is set.

The additional constants read:

$$F_{KH}^{min} = 0.1, \quad F_{KH}^{max} = 1.0, \quad a_1 = 0.15, \quad a_2 = 0.30. \quad (22)$$

To check the corresponding implementation of  $\Delta_{SLA}$  in OpenFOAM, the functions detailed in Eqs. (19) and (21) were evaluated for decaying isotropic turbulence on a  $32^3$  grid. The comparison to the behaviour of the functions in their native CFD code shown in Fig. 3 indicates a correct behaviour of the method.

#### 2.1.4 Implementation of ONERA Method

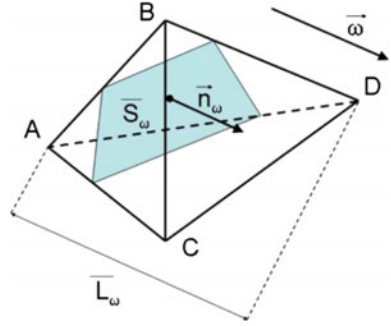
The ONERA formulation of their proposed alternative LES filter width definition  $\Delta_\omega$  (see Deck 2012) is adapted here for the non-zonal CAP. The formulation implemented into OpenFOAM reads:

$$\Delta = \Delta_\omega = \begin{cases} \Delta_{max}, & \text{if } f_d \leq f_{d0} \\ \alpha \Delta_\omega^*, & \text{if } f_d > f_{d0} \end{cases}, \quad (23)$$

where  $f_{d0} = 0.8$  and  $\alpha = 1.0$  (in the recommended ZDES practice) or  $\alpha = 1/0.82$  (as will be introduced and retained in the following). Here, the shield function  $f_d$  of DDES is essential to prevent the activation of  $\Delta_\omega^*$  inside attached boundary layers, where the standard definition of  $\Delta_{max}$  is used. This corresponds to the definition of  $\Delta$  in mode 2 of ZDES as employed by ONERA in their code. For the implementation into the unstructured OpenFOAM code, the structured formulation of  $\Delta_\omega^*$  as implemented in the ONERA code is impractical, so the unstructured formulation



**Fig. 4** Illustration of definition of  $\Delta_\omega^*$  for unstructured cells (Deck 2012) (e.g. tetrahedral cell)



presented in Deck (2012) (Appendix A) was applied. The general concept behind the formulation is illustrated in Fig. 4.

When considering the area of the cell cutting plane  $\bar{S}_\omega$  with its normal vector being the normalised vorticity vector  $\vec{n}_\omega = \vec{\omega}/|\vec{\omega}|$ , the length scale is defined as  $\Delta_\omega^* = \sqrt{\bar{S}_\omega}$ . For an unstructured cell, the square root of the cell cutting plane area is computed via  $\bar{S}_\omega = \bar{\Omega}/\bar{L}_\omega$ , where  $\bar{\Omega}$  is the cell volume and  $\bar{L}_\omega$  characterises the projection of  $\vec{n}_\omega$  on the edges of the cell. It is defined as:

$$\bar{L}_\omega = \max_{k=1\dots n, l=1\dots n} \left( \left| \vec{n}_\omega \cdot \overrightarrow{A_k A_l} \right| \right), \quad (24)$$

where  $n$  is the number of cell edges and  $\overrightarrow{A_k A_l}$  the vector defined by two vertices  $\bar{A}_k$  and  $\bar{A}_l$ . This means that for a cell with  $p$  vertices the number of scalar products to be effectively computed is equal to the number of cell edges, including diagonals, namely  $\frac{p(p-1)}{2}$ .

One particular property of the unstructured formulation is that it does not reduce to  $\Delta_{max}$  for isotropic cells, but returns lower values of  $\Delta_\omega^* \approx 0.82\Delta_{max}$ . In Fig. 5a, a time signal of the spatially averaged value of  $\Delta_\omega^*$  on a purely isotropic grid and resolved 3D turbulence is shown. The effect of using this definition of  $\Delta_\omega^*$  on predicting the energy cascade for decaying isotropic turbulence is demonstrated in Fig. 5b. The reduced LES filter width leads to a stronger pile-up of energy at small scales, as the SA-DES model was calibrated with the  $\Delta_{max}$  formulation. To restore the correct behaviour on isotropic cells, an additional scaling factor  $\alpha = 1/0.82$  was introduced. When using the rescaled  $\Delta_\omega^*$  definition, the SGS behaviour of the benchmark model is restored. For the CAP simulations, it was decided to apply the rescaled  $\Delta_\omega^*$  formulation, as we want to maintain correct SGS behaviour on isotropic cells without being forced to recalibrate the  $C_{DES}$  parameter of DES. It is noted that a smaller value of  $\Delta$  may be beneficial for reducing the Grey Area, and the recalibration of the  $\alpha$  coefficient might diminish the effectiveness of  $\Delta_\omega^*$  inside this region somewhat.

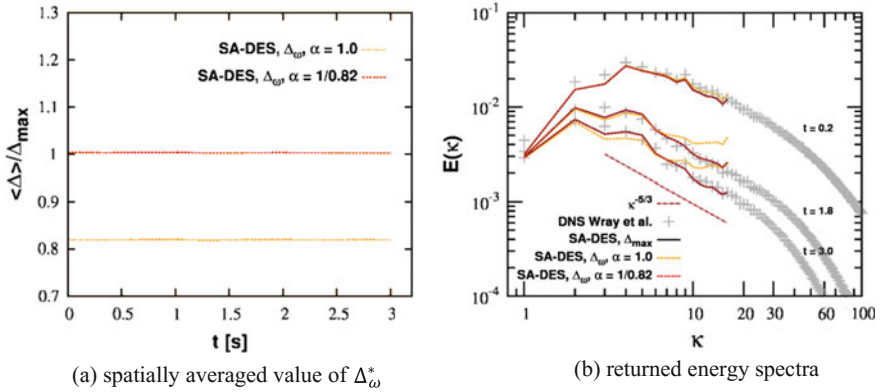


Fig. 5 Test of unstructured formulation of  $\Delta_\omega^*$  for decaying isotropic turbulence,  $32^3$  grid

However, the correct SGS behaviour in regions of resolved homogeneous isotropic turbulence is considered more important. Note that the authors of ZDES on the contrary put their emphasis on sheared flows rather than on isotropic flows because of their potential application relevance in aerospace.

## 2.2 Preliminary Tests

Selected fundamental test cases have been performed prior to the shear layer simulations in order to investigate two core functionalities of the proposed GAM methods, namely their SGS mode functionality and their effect on the DDES shielding capability. The test cases complement the general implementation checks presented in the previous section.

First, the SGS mode functionality of all methods is assessed for decaying isotropic turbulence (DIT) on a  $32^3$  box grid (simulations were also conducted on a  $64^3$  grid with equivalent results). In Fig. 6, energy spectra of all implemented partner methods are presented. Generally, all methods predict the energy cascade very well and exhibit only negligible deviations to the standard model (SA-DES). The CFDB approach of  $\sigma$ -DES has been calibrated to match returned energy spectra of SA-DES using the additional model parameter  $B_\sigma$  (see Eq. 10).

For the NLR approach, the high-pass filtering approach was implemented for DIT using spatial averaging instead of temporal averaging to compute the filtered Reynolds stresses of Eq. (13). In line with expectation, using HPF is effectively neutral for isotropic turbulence as the spatially averaged flow velocity is zero. The same is true for applying the uncorrelated backscatter approach to DIT, which also returns equivalent spectra to the standard model. For the NTS approaches, the two alternative definitions of the LES filter width  $\Delta$  have been tested, i.e.  $\tilde{\Delta}_\omega$  and  $\Delta_{SLA}$ . Both formulations prove to be neutral on isotropic cells and return identical energy

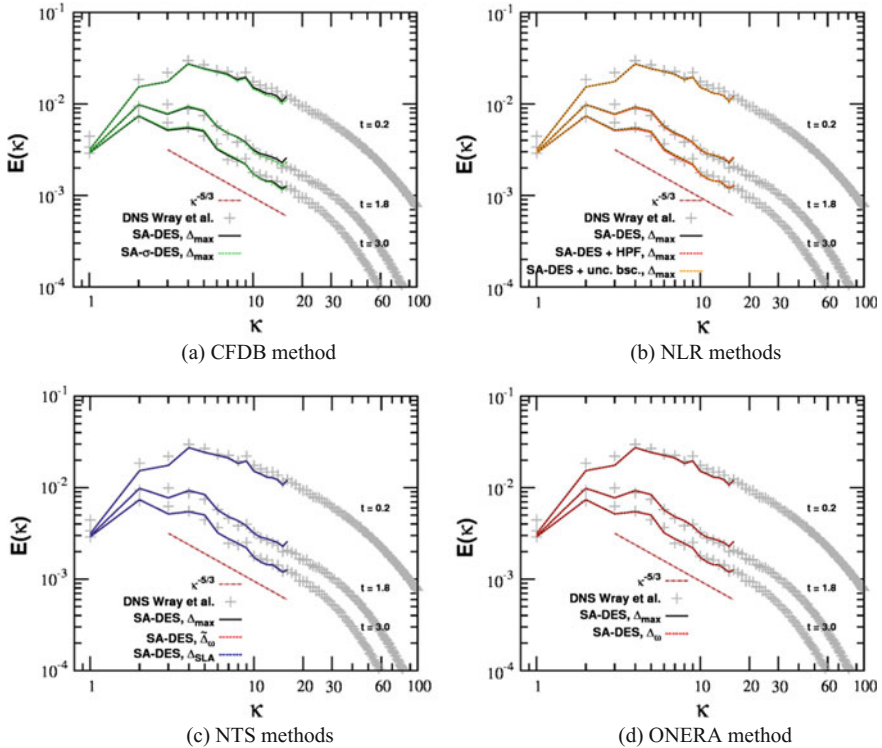


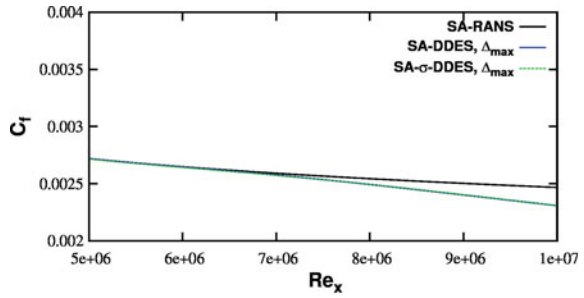
**Fig. 6** Assessment of SGS mode functionality of all partner methods for decaying isotropic turbulence test case,  $32^3$  grid

spectra compared to using  $\Delta_{max}$ . For the ONERA approach, the rescaled  $\Delta_{\omega}$  discussed above is applied, which guarantees correct SGS model behaviour on isotropic cells.

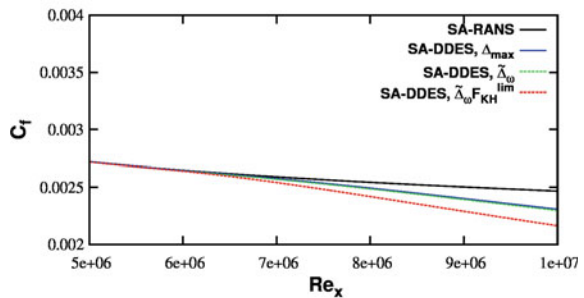
As a second fundamental test, the capabilities of all methods to effectively shield attached RANS boundary layers from switching into LES mode are assessed for zero-pressure gradient flow over a flat plate. The test case setup is similar as the one presented in Spalart et al. (2006). The applied 2D structured grid consists of an anisotropic region stretching from  $0 \leq Re_x \leq 5.0 \times 10^6$ , in which the resolution of  $\Delta_{max}/\delta > 1.5$  ( $\delta \dots$  boundary layer thickness) is sufficiently coarse to keep the simulation in RANS mode according to the DES97 length scale switch. From  $5.0 \times 10^6 \leq Re_x \leq 1.0 \times 10^7$ , an equidistant grid spacing is applied, meaning that the grid resolution relative to the boundary layer thickness is virtually refined downstream as the boundary layer thickens ( $0.175 > \Delta_{max}/\delta > 0.09$  in this region). This causes a depletion of modelled stresses at some point inside this grid resolution, as the shield function  $f_d$  of DDES starts to retreat at a ratio of  $\Delta_{max}/\delta \approx 0.1$ .

A shielding functionality is essential for any hybrid RANS-LES method for application to high Reynolds number wall-bounded flows in practice. Introducing a

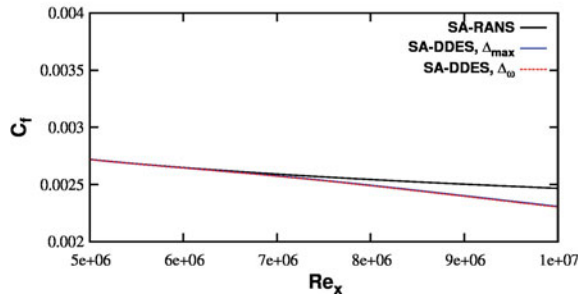
**Fig. 7** Assessment of shielding functionality of all partner methods for zero pressure gradient boundary layer over flat plate



(a) CFDB method



(b) NTS method



(c) ONERA method

new GAM method which aggressively switches to LES mode shortly after separation also bears the risk of weakening the shielding capability, so that this test is considered important to show a broader picture of the method. Although the flat plate test case can give a first indication about potential shielding problems of a particular method, it has to be emphasised that more rigorous testing would be required to prove general suitability of a particular method for complex problems (e.g. for flows subjected to strong pressure gradients), which is beyond the scope of this exercise.

Results from all conducted simulations are presented in Fig. 7. For the CFDB method of  $\sigma$ -DES, the DDES shield function  $f_d$  was re-calibrated to obtain a consistent level of shielding compared to standard DDES. The two proposed  $\Delta$

formulations of NTS also show good shielding behaviour. The  $\tilde{\Delta}_\omega$  formulation provides equivalent shielding compared to the standard  $\Delta_{max}$  formulation, as it reduces to  $\mathcal{O}(\max(\Delta_x, \Delta_y))$  in the boundary layer region. In this test, the influence of the spanwise  $\Delta_z$  is discarded. It is however acknowledged that in a 3D case featuring a 2D boundary layer aligned with the  $xy$ -plane rigorous grid refinement in the  $x$ - and  $y$ -directions would imply a different behaviour of  $\Delta_{max}$  and  $\tilde{\Delta}_\omega$ , as  $\Delta_{max} = \Delta_z$  in this case, whereas the influence of the  $\Delta_z$  spacing is discarded for the evaluation of  $\tilde{\Delta}_\omega$ . The  $\Delta_{SLA}$  formulation uses additional shielding based on the  $f_d$  function to revert to the  $\tilde{\Delta}_\omega$  formulation inside the boundary layer (see Eq. 20). For the flat plate test case, a tangible weakening of the shielding is seen. Also, modelled stress depletion starts to occur further upstream relative to standard SA-DDES. The ONERA formulation of  $\Delta_\omega$  also uses additional shielding for the LES filter width definition, which is set to be equivalent to  $\Delta_{max}$  inside the boundary layer (see Eq. 23). This is necessary as  $\Delta_\omega^*$  reduces to  $\mathcal{O}(\sqrt{\Delta_x^2 + \Delta_y^2})$ , so that  $\Delta$  would be decreased relative to  $\Delta_{max}$  if this definition is going to be used inside the boundary layer. Due to time constraints, no tests were performed for the two approaches of NLR. However, consideration of the formulations leads to no anticipated shielding issues.

### 2.3 Test Case Setup for Spatial Shear Layer in the CAP

The setup used for all non-zonal CAP simulations corresponds largely to the mandatory setup described in Part III (Results for Fundamental Test Cases, Free Shear Layer). An overview of the employed grid and computational domain is given in Fig. 8. The domain size is equivalent to the mandatory grid used by all partners. It extends to  $L_y = \pm 1m$  in the lateral direction as well as  $L_x = 2m$  downstream of the splitter plate. The domain extent in the spanwise direction is  $L_z = 0.15m$ . A resolution of 48 cells is applied in the  $z$ -direction, resulting in a grid spacing of  $\Delta_z = 0.003125m$ . The region downstream of the splitter plate consists of two regions, a focus region ( $x < 1.0m$ ) in which the streamwise grid spacing is kept constant at  $\Delta_x = \Delta_z = 0.003125m$ , and a departure region where  $\Delta_x$  is gradually coarsened. The employed grid hence corresponds to the mandatory grid presented in Part III (Results for Fundamental Test Cases, Free Shear Layer), but coarsened by a factor of 2 in each grid direction (resulting in a reduced cell count of 2M relative to 13M for the mandatory grid). Correspondingly, the time step size is doubled to  $\Delta t = 2.0 \times 10^{-5}$  s, but guarantees  $CFL < 1.0$  in the entire LES region including the early shear layer part. This coarsened grid was chosen because it was believed to lead to clearer differences in the performances of the approaches. A coarser initial shear layer is also more representative of most practical applications in which the separation location is not known in advance. This does however lead to a strengthened influence of the (common) underlying numerics.

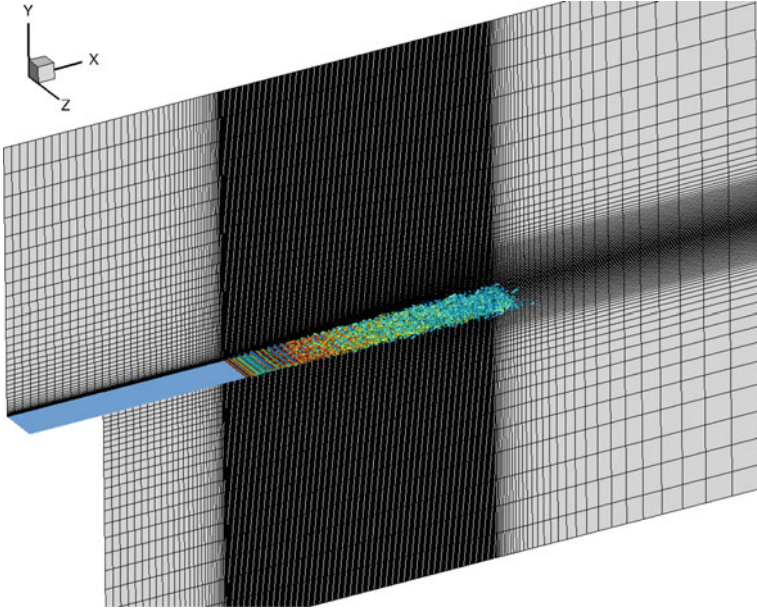


**Fig. 8** View of computational domain and grid for shear layer test case setup in non-zonal CAP

The OpenFOAM package version 2.3x was used for this study, where an incompressible pressure-based solver was applied. For time integration, a second order accurate implicit Euler scheme was selected. To discretise the convection term of the momentum equation, the hybrid blending scheme of Travin et al. (2000a) was employed, which guarantees second order accurate central differences in the turbulent shear layer region and switches to an upwind-biased scheme in the outer irrotational region.

To match velocity profiles at the edge of the splitter plate with existing experimental data, boundary layer tripping as proposed in Deck (2012) was used. As detailed in the previous section, each GAM method is assessed in conjunction with standard SA-DDES, meaning that the same SA-RANS model is active inside the attached boundary layers in each simulation. Correspondingly, velocity and eddy viscosity profiles at the tip of the splitter plate shown in Fig. 9 are virtually identical (except for a sharper drop of  $v_t$  at the edge of the boundary layer seen for  $\Delta_{SLA}$ ). Any undesired influence of the incoming boundary layer characteristics on the separated flow regime downstream of the plate is therefore not anticipated.

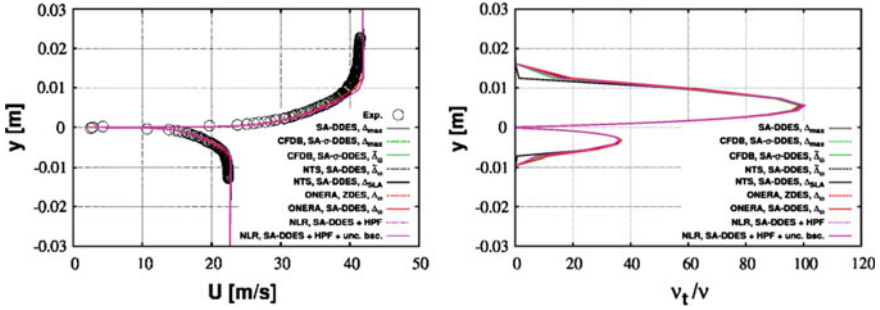


Fig. 9 Profiles of mean velocity and eddy viscosity ratio at tip of splitter plate

### 3 Performance of Non-zonal Methods

As listed in Table 1, 9 different simulations (including the benchmark model SA-DDES +  $\Delta_{max}$ ) have been conducted within the non-zonal work package of the CAP, including proposed GAM methods from 4 different partners.

In Fig. 10, instantaneous flow structures are shown for a selection of different methods, including the most effective method from each partner. For the relatively coarse grid used in this study, the benchmark shows a stationary behaviour downstream of separation in the entire focus region of the grid, as the separated shear layer is stabilised by high values of eddy viscosity. This is different for the best method combination of CFDB, where the new  $\sigma$ -DDES approach is combined with the  $\tilde{\Delta}_\omega$  length scale. In the early shear layer region, close to the splitter plate, correlated 2D structures are still visible, but transition to a fully 3D flow state can be observed further downstream. The alternative LES filter width  $\Delta_{SLA}$  proposed by NTS shows an even further accelerated RANS-to-LES transition.

This is different for the  $\Delta_\omega$  length scale definition of ONERA with  $\alpha = 1/0.82$  (which is not the ZDES recommended value), which shows comparable behaviour to the standard definition  $\Delta_{max}$ . This is potentially caused by the relatively coarse grid resolution. Unlike the  $\sigma$ -DDES and  $\Delta_{SLA}$  GAM methods, the reduction of  $\Delta$  (and hence  $v_t$ , as  $v_t \propto \Delta^2$ ) provided by the  $\Delta_\omega$  definition in the early shear layer region is bound by the geometrical dimensions of the cell, as  $\Delta_\omega$  reduces to  $\mathcal{O}\left(\sqrt{\Delta_x^2 + \Delta_y^2}\right)$  in 2D flow regions. The  $\sigma$ -DDES approach in contrast includes a kinematic measure of the flow state, and is able, to reduce  $v_t$  to near zero levels and thus acts as a quasi-implicit LES in a confined region. The same is true for the  $\Delta_{SLA}$  approach, which can reduce the LES filter width to levels of  $0.1\Delta_{max}$ , meaning that eddy viscosity levels are reduced by a factor of 100. Compared to these two approaches, the reduction of  $\Delta$  provided by  $\alpha\Delta_\omega^*$  (with  $\alpha = 1/0.82$  conversely to the ZDES practice where  $\alpha = 1$ ) hence seems to be insufficient on this grid. In addition, the filter width  $\Delta_\omega \sim \mathcal{O}\left(\sqrt{\Delta_x^2 + \Delta_y^2}\right)$  increases downstream of separation due to

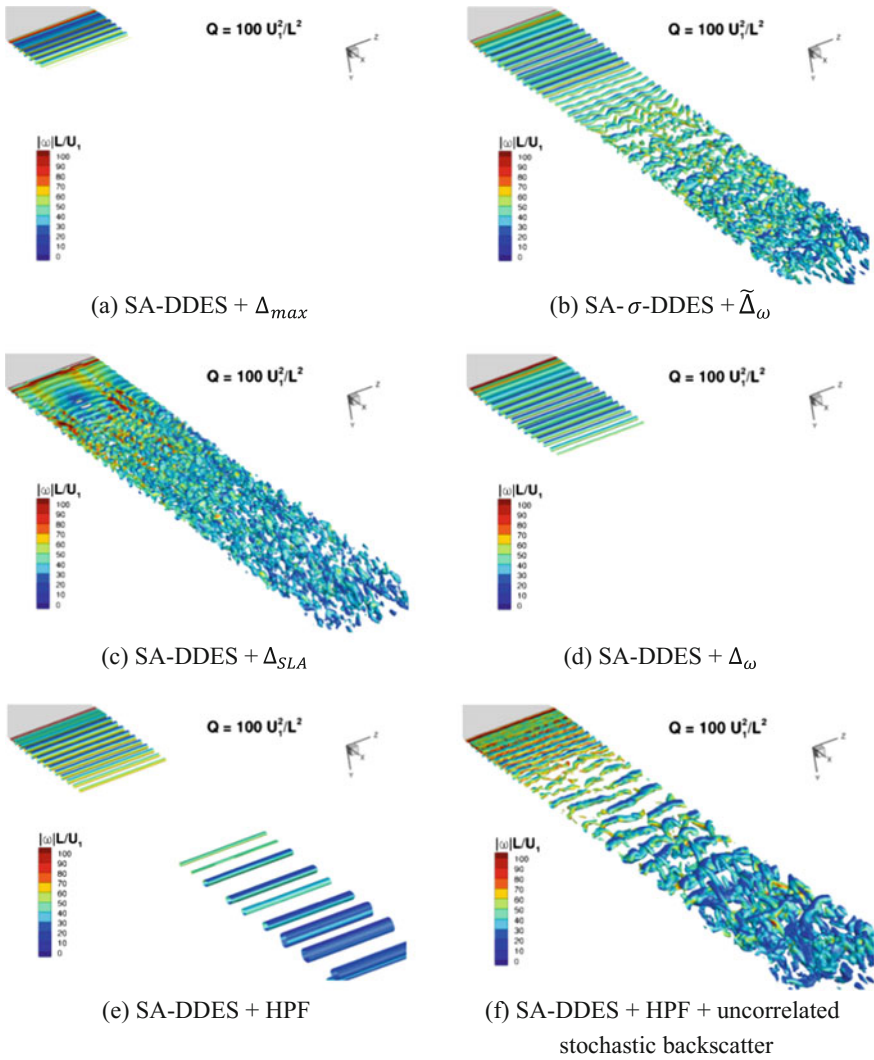


**Fig. 10** Turbulent flow structures visualised via Q criterion for different partner approaches

gradual coarsening of the grid, thus making it increasingly unlikely that the flow will eventually transition to resolved LES content in case instabilities are not triggered immediately after separation. The GAM methods of CFDB and NTS in contrast actively react on the flow state and maintain very low levels of  $v_t$  as long as a purely 2D flow state is detected. This enables a transition to LES further downstream even when the grid proved to be too coarse in the initial shear layer region to trigger instabilities, as can be seen e.g. for the CFDB simulation in Fig. 10b.



In Fig. 10e, the effect of using high-pass filtering in addition to the benchmark model is shown. For the chosen value of the  $Q$  criterion, a mild effect is seen compared to the benchmark model, where the simulation behaviour switches from a quasi-stationary flow to unsteady shedding of pronounced 2D structures. A more significant improvement is seen when additionally applying stochastic forcing, as shown in Fig. 10f. Similar to both the  $\sigma$ -DDES and  $\Delta_{SLA}$  methods, transition to 3D turbulent structures is seen after an initial stage of correlated 2D vortices in the vicinity of the edge of the splitter plate. In contrast to the two other approaches, the turbulent structures in the downstream region seem to be noticeably coarser for the forcing approach, and some small-scale perturbations can be noted in the early shear layer.

To study the method behaviour in the important early shear layer region, the computed eddy viscosity ratio as well as the effective modelled shear stress component  $\overline{u'v'}$  entering the momentum equation are shown in Fig. 11 on the symmetry plane. All proposed LES filter width formulations, i.e.  $\Delta_{\omega}$ ,  $\tilde{\Delta}_{\omega}$  and  $\Delta_{SLA}$ , as well as the  $\sigma$ -DDES aim at actively reducing the effective eddy viscosity entering the diffusion term to promote natural Kelvin-Helmholtz instabilities in the shear layer. Accordingly, much lower levels of  $\nu_t$  are seen compared to employing the standard  $\Delta_{max}$  formulation. The HPF approach of NLR is fundamentally different, as it reduces the velocity gradients entering the modelled stresses (see Eq. 13) in contrast to reducing  $\nu_t$ . Despite these different approaches, the resulting modelled stress component  $\overline{u'v'}$  is in all cases significantly reduced compared to the datum SA-DDES, albeit to differing extents.

To allow for a more quantitative comparison, the evaluated momentum thickness in the downstream direction is plotted in Fig. 12. Here, none of the methods are able to exactly reproduce the experimental growth rate on the applied computational grid, but clear differences in performance between the methods are nonetheless seen. The benchmark model SA-DDES significantly under-predicts the shear layer growth rate due to the severe impact of the Grey Area on the applied grid. The model switches to LES-mode downstream of the splitter plate, which results in a reduction of modelled stresses below RANS levels. Due to the lack of resolved structures, the total stress balance is significantly under-predicted. This problem seems even more severe when applying the SA-DDES model in conjunction with the LES filter definitions  $\Delta_{\omega}$  and  $\tilde{\Delta}_{\omega}$ . Both formulations fail to trigger the onset of resolved turbulence on this particularly coarse grid, but return lower values of  $\Delta$  compared to the standard formulation  $\Delta_{max}$  (and hence lower modelled stresses). In the region  $x/L < 0.5$ , an equivalent behaviour is seen for the  $\sigma$ -DDES +  $\tilde{\Delta}_{\omega}$  approach. However, unlike the two former GAM methods, transition to resolved turbulence is eventually triggered here, which means that the model correctly predicts the shear layer growth rate in the second part of the grid focus region (albeit the initial offset due to the Grey Area cannot be compensated). In comparison to the  $\sigma$ -DDES method, high-pass filtering proves to be less effective.

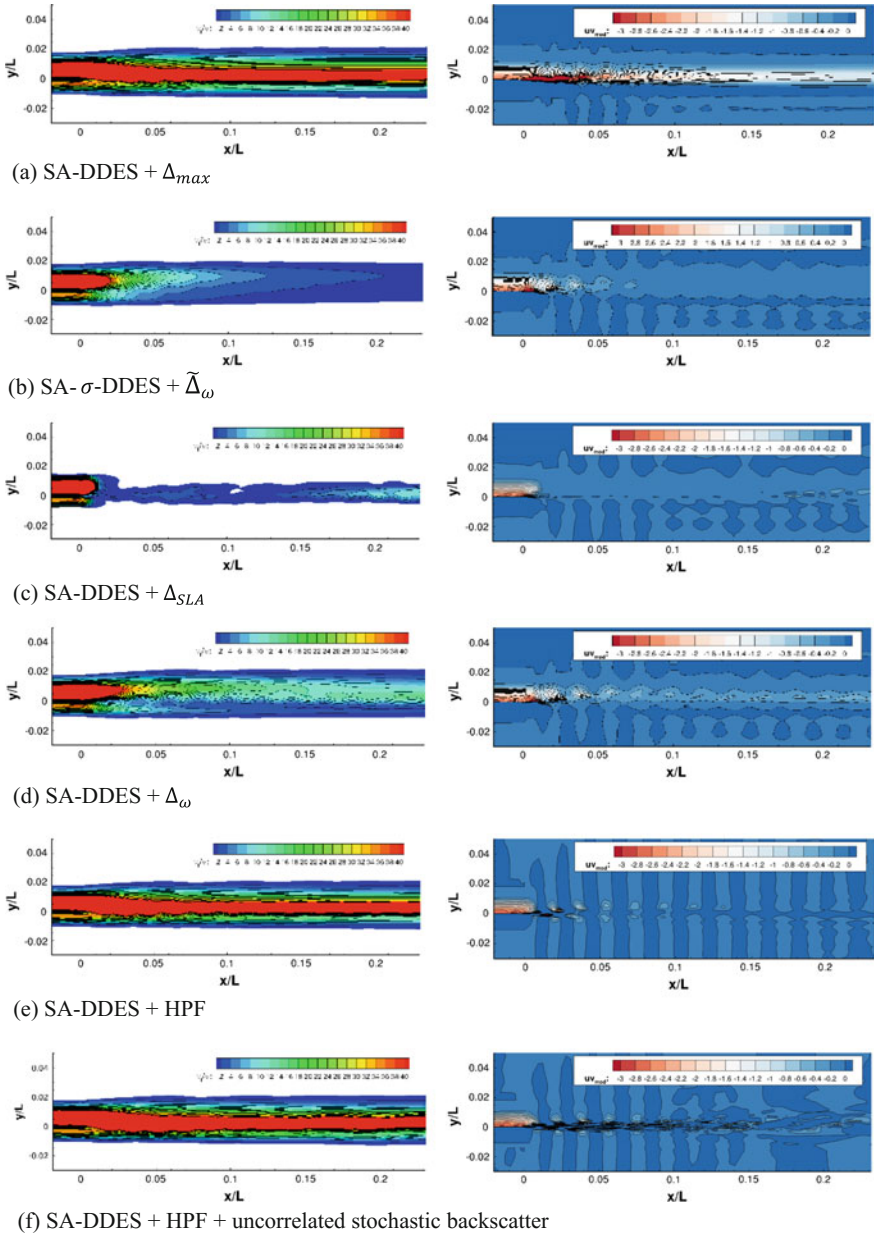
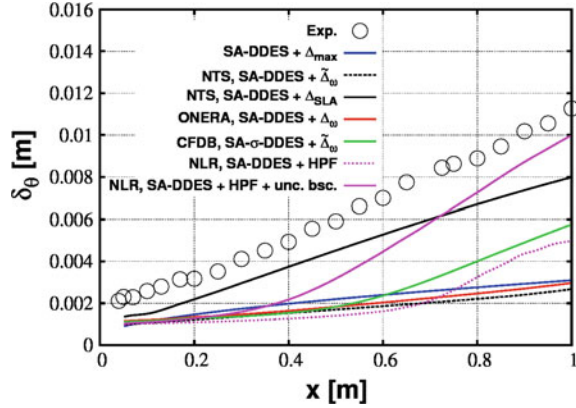


**Fig. 11** Contour plot of eddy viscosity ratio on centre plane (*left*), contour plot of modelled Reynolds stress component  $\overline{u'v'}$  on centre plane (*right*)

**Fig. 12** Comparison of development of shear layer momentum thickness downstream of splitter plate for different partner approaches



The LES filter width formulation  $\Delta_{SLA}$  proposed by NTS delivers the best performance of all assessed methods in promoting fast RANS-to-LES transition. The initial Grey Area region is significantly smaller than for every other GAM method, although the predicted shear layer growth rate seems to be slightly lower than in the experiment. The opposite trend is seen for the high-pass filtered SA-DDES model with additional stochastic forcing. After an initial delay in the early shear layer region  $x/L < 0.3$ , the shear layer growth rate is over-predicted. This is potentially related to the somewhat coarser 3D structures seen for the approach in this region.

Profiles of mean streamwise velocity and velocity fluctuations are visualised in Fig. 13 for two selected locations. For the location  $x = 0.2m$  relatively close to the edge of the splitter plate, expectedly a significant difference in resolved stresses is seen between the methods. In line with expectation derived from the instantaneous flow field, the  $\Delta_{SLA}$  approach gives the best agreement with the experimental data. Surprisingly,  $\sigma$ -DDES +  $\tilde{\Delta}_{\omega}$  and  $\Delta_{\omega}$  perform very similarly in this region, i.e. very comparable  $u'$ -profiles are seen, but both methods fail to immediately trigger instabilities after separation. This is different for the downstream position at  $x = 0.8m$ , where  $\Delta_{\omega}$  significantly under-predicts streamwise velocity fluctuations in contrast to the  $\sigma$ -DDES approach. This can be associated with the properties of the  $\sigma$ -DDES, which maintains near zero levels of  $v_t$  as long as the flow remains 2D, and hence enables the onset of flow instabilities even further downstream of the plate.

In Fig. 14, power spectral densities of the streamwise velocity component are shown for the same two positions. In the early shear layer region, each method fails to predict the broadband character of the solution content, where tonal components associated with the shear layer roll-up are noticed. The signal of the stochastic forcing approach of NLR shows an apparent high-frequency content which is not present for the other partner methods. This could indicate potential problems with the strength of the implemented forcing term, since a similar artefact was not observed by NLR for their native model implementation. This also indicates that the stochastic forcing approach of NLR cannot be effortlessly transferred to hybrid

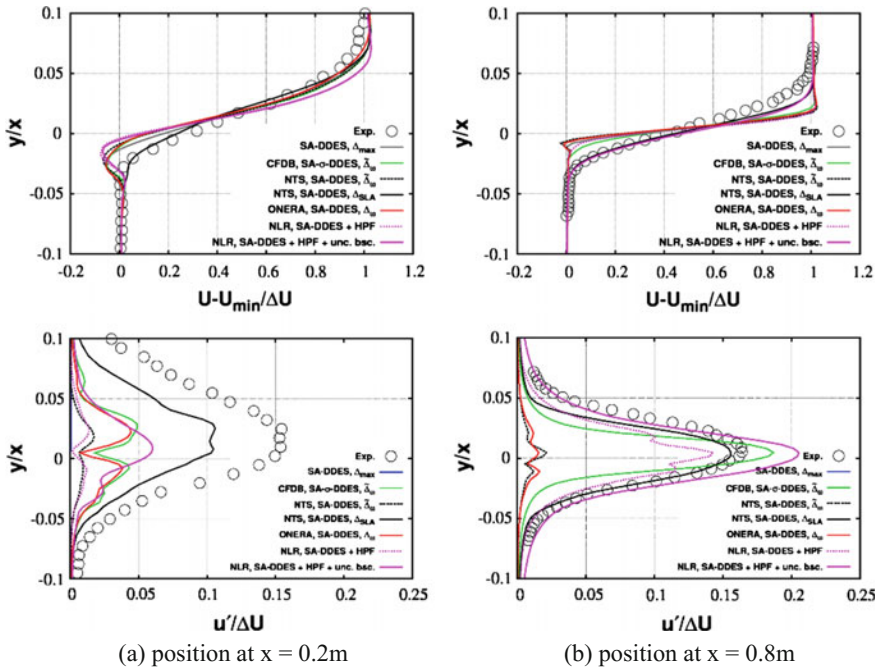


**Fig. 13** Time- and spanwise-averaged profiles of mean velocity and streamwise velocity fluctuations at two locations downstream of splitter plate

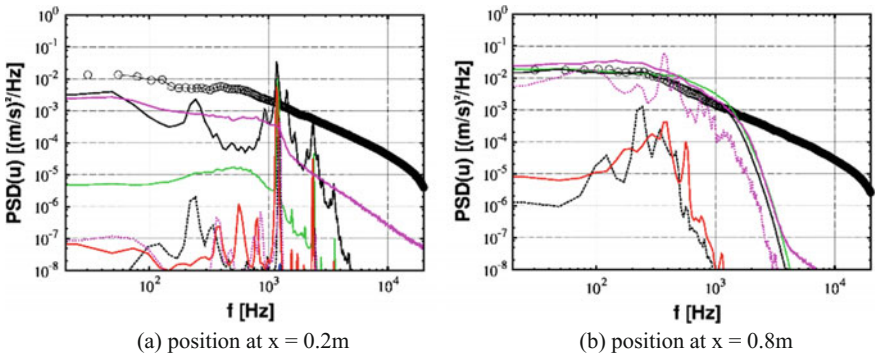


**Fig. 14** Power spectral densities of streamwise velocity component at two locations downstream of splitter plate (for legend, see Fig. 13)

RANS-LES models for which the turbulent kinetic energy is not readily available, but would require additional calibration (which could unfortunately not be pursued due to time constraints). At the downstream location  $x = 0.8m$ , the three approaches of CFDB, NTS and NLR, namely  $\sigma$ -DDES,  $\Delta_{SLA}$  and the stochastic forcing,

show good agreement with the experimental measurements. Additionally, a mild preference of the  $\Delta_\omega$  relative to the  $\tilde{\Delta}_\omega$  formulation is seen, but both LES filter width definitions significantly under-predict PSD levels.

## 4 Conclusions

The conducted assessment study for selected non-zonal GAM approaches of different Go4Hybrid partners revealed significant differences in performance for the selected test case, i.e. the spatially developing shear layer. The summarised findings of the study are:

- Although no non-zonal GAM method was able to completely mitigate the Grey Area problem for the employed test case setup, the  $\Delta_{SLA}$  formulation of NTS clearly showed the best performance. A clear advantage of the approach is that the proposed substitution of the LES filter width can be employed in conjunction with different hybrid RANS-LES and indeed pure LES models as well. A mildly weakened shielding capability was seen for the flat plate test case, which did not pose a problem for the shear layer test case. However, implications of this would have to be assessed for more practical cases to draw meaningful conclusions. The results achieved for  $\Delta_{SLA}$  in CAP generally confirm the behaviour of the method seen by NTS in their code, i.e.  $\Delta_{SLA}$  is a potent method to tackle the Grey Area problem.
- The  $\sigma$ -DDES approach of CFDB also shows a significant improvement compared to the benchmark model SA-DDES, but falls short of the performance of  $\Delta_{SLA}$ . Using either the standard  $\Delta_{max}$  or  $\tilde{\Delta}_\omega$  definition in conjunction with the model has a mild ameliorating effect on the prediction, but the main acceleration mechanism for RANS-to-LES transition comes from the  $\sigma$  substitution (note however, that this is grid dependent, as the  $\tilde{\Delta}_\omega$  scale is more efficient on strongly anisotropic grids). Additionally, the grid used in CAP might also be slightly too coarse with respect to the streamwise  $\Delta_x$  spacing to trigger the onset of 3D structures immediately downstream of the splitter plate for the  $\sigma$ -DDES approach, as a supplementary grid refinement study conducted by CFDB demonstrated.
- In contrast to the approaches of CFDB and NTS, the DDES approach with the  $\Delta_\omega$  formulation of ONERA (with  $\alpha = 1/0.82$  adopted here contrary to the ZDES common practice where  $\alpha = 1$ ) proved to be less effective in this study, which is a conflicting finding in light of studies conducted by ONERA using standard ZDES in their respective CFD code. A potential explanation may lie in the different values of  $\alpha$  as well as the relatively coarse grid employed in this study. ONERA have not conducted simulations on an equivalently coarse grid within Go4Hybrid, so that a direct comparison between codes and methods is unfortunately not possible. The results obtained within the non-zonal CAP indicate that a reduction of  $\Delta \sim \mathcal{O}\left(\sqrt{\Delta_x^2 + \Delta_y^2}\right)$  associated with an equivalent reduction in  $v_t$  might not be

sufficient to counter the Grey Area on coarser grids if  $\alpha < 1$  is chosen, as both CFDB and NTS methods apply a stronger reduction of  $v_t$  in the early 2D shear layer region. Additionally, the re-scaling of the unstructured  $\Delta_\omega$  formulation should be investigated in more depth when assessing the method for unstructured CFD codes. Another possible explanation for the observed difference in method performance between this study and the ONERA experience concerns the employed hybrid RANS-LES turbulence model, i.e. SA-DDES. ONERA generally apply their ZDES formulation in its non-zonal mode 2 for such applications. Apart from the  $\alpha$  value, the main difference between ZDES and SA-DDES is that ZDES does not use the correction function  $\Psi$  in the definition of the LES length scale  $L_{LES}$  (see Eq. 8). The function  $\Psi$  generally boosts eddy viscosity values in low Reynolds flow regions such as the early shear layer, so that ZDES is expected to return lower values of  $v_t$  here. This might have an enhancing effect on the RANS-to-LES transition relative to standard SA-DDES.

- High-pass filtering of the effective velocity gradients entering the modelled Reynolds stresses as proposed by NLR seems to have a limited effect on the prediction, at least for this test case setup using SA-DDES. In contrast, a significant, positive effect was found on the same coarse grid by NLR using its own code and the X-LES method (see Kok 2016). Given the additional implementation and generality limitations associated with HPF, the method seems to be less favourable compared to the approaches of CFDB and NTS for Grey Area mitigation.
- For the stochastic uncorrelated backscatter approach of NLR, a fair assessment seems to be rather difficult. The decision to base all CAP models on a common hybrid RANS-LES background model SA-DDES handicaps the approach relative to others, as the turbulent kinetic energy is not provided by the Spalart-Allmaras model. The required fine tuning of the adapted CAP formulation could not be carried out within the time frame of the work package, so that the formulation finally run in the CAP suffered from an excessive forcing strength. Additionally, the more promising NLR approach of correlating the stochastic variables employed for the forcing in time and space could not be tested in the CAP, as deriving an unstructured formulation of the method proved to be impossible within the given time. However, simulations conducted by NLR for the coarse grid applied in the CAP showed very convincing results for this approach (Kok 2016), so that a direct comparison with the partner methods in one CFD code remains an interesting task.

Despite the significant differences in performance seen between the different partner methods in the non-zonal CAP, drawing generally valid conclusions from this exercise remains challenging. The assessment platform seeks to evaluate the performance of a method for one particular test case setup, grid and CFD code, albeit the case was carefully selected to well represent the core issue to be investigated (i.e. the Grey Area problem). However, aspects such as grid resolution dependency, numerical sensitivity, sensitivity to underlying RANS-LES method, Reynolds number dependency and general suitability for different applications could not be studied.

# Direct Comparison of Embedded Approaches

A. Skillen, J. Holgate and A. Revell

## 1 Introduction

Enhanced computational resources and improvements in synthetic turbulence generation methods have motivated a higher level of activity in embedded (zonal) approaches for turbulence simulation in recent years. These new techniques have all been developed with the following objectives in mind:

- The development length, or downstream distance before physically accurate statistics are realizable, should be minimized;
- The turbulent inflow boundary conditions should have minimal adverse effect on the downstream flow;
- The computational cost of the inlet data generation must be a small fraction of overall computational expense;
- The method should ideally be generally applicable for all types of mesh and geometries with minimal effort required from the user.

It should also be noted that these methods are developed for use within industrial codes and thus should be expected to operate within the practical constraints therein imposed.

The following report shall document the performance of a number of different synthetic turbulence generation techniques, namely: Synthetic Eddy Method (SEM, both original and improved formulations), a modification of the SEM from Pamiès et al. (2009), and The Synthetic Turbulence Generator (STG). The aim is to investigate the suitability and effectiveness of each method to accurately re-generate the turbulent statistics from the corresponding set of mean inlet data.

---

A. Skillen (✉) · J. Holgate · A. Revell  
The University of Manchester, Manchester, UK  
e-mail: alex.skillen@manchester.ac.uk

## 2 Embedded Approaches Implemented

### 2.1 Introduction

The following models have been implemented in OpenFOAM Extend 3.1 for the purposes of cross comparison within a common platform. Full details of these schemes are provided in Part II (Presentation of Approaches, Improved Embedded Approaches), original SEM, improved SEM (iSEM), modified SEM (Pamiès) and the original STG.

Table 1 provides a summary of the approaches used in Part II (Presentation of Approaches, Improved Embedded Approaches) to achieve the ‘Partner Best’ results for the fundamental test case of the flat plate. As noted at the bottom of Table 1, a series of compromises have been necessary versus the ‘Partner Best Approaches’ in order to facilitate a single-code comparison.

Unfortunately, in the a priori testing of the methods (described in Sect. 2.2) strong evidence of an implementation error for the STG approach arose. Even though the erroneous implementation returned in some respects some of the best results for the flat plate case, it was decided not to include the STG predictions in the cross-plots of the CAP.

**Table 1** Simulation information for the different inlet methods

Partner	Solver	Model	Spatial scheme	Time step	Method details
<i>Partner best approach</i>					
DLR	TAU compressible	IDDES-SA	Central+Matrix dissipation	$8 \times 10^{-7}$ s	Original SEM
NTS	NTS compressible	IDDES-SST	Hybrid 4th center/3rd upwind	$3 \times 10^{-6}$ s	STG (Shur et al. 2014)
ONERA	FLU3M compressible	ZDES-SA mode 3	Modified AUSM+P	$3.2 \times 10^{-7}$ s	SEM of Pamiès +Forcing
UniMan	FOAM-EXTEND 3.1 incompressible	IDDES-SA	Central	$1 \times 10^{-6}$ s	Improved (i) SEM
<i>Common Configuration: CAP</i>					
	FOAM-EXTEND 3.1 incompressible	IDDES-SA	Central	$1 \times 10^{-6}$ s	Original SEM Unforced Pamiès SEM Improved (i) SEM



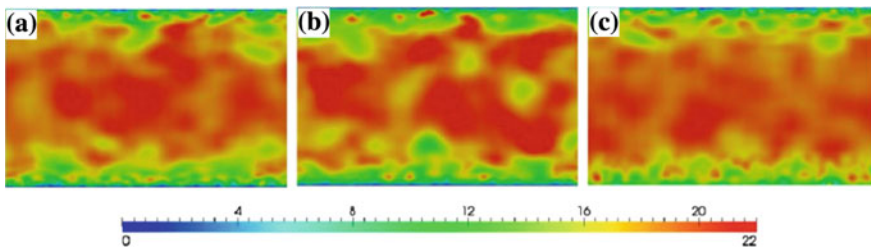
## 2.2 A Priori Testing of Inlet Methods

In order to assess the feasibility and robustness of each method it was first necessary to carry out a validation test. These tests focused upon the generation of fluctuations at the inlet plane itself i.e. at the point where the synthetic turbulence was being generated, and neglected the simulation of the downstream flow. The mean data considered here is taken from DNS of turbulent flow through a plane channel at a Reynolds number, based on the friction velocity and channel half height, of  $Re_\tau = 395$ . The main objective here is to investigate the extent to which each synthetic turbulence method is able to re-generate the correct turbulence statistics from a given input data. In addition, further studies have been performed that assess the sensitivity of the method to the source of the input statistics; either from DNS data or a RANS SST model.

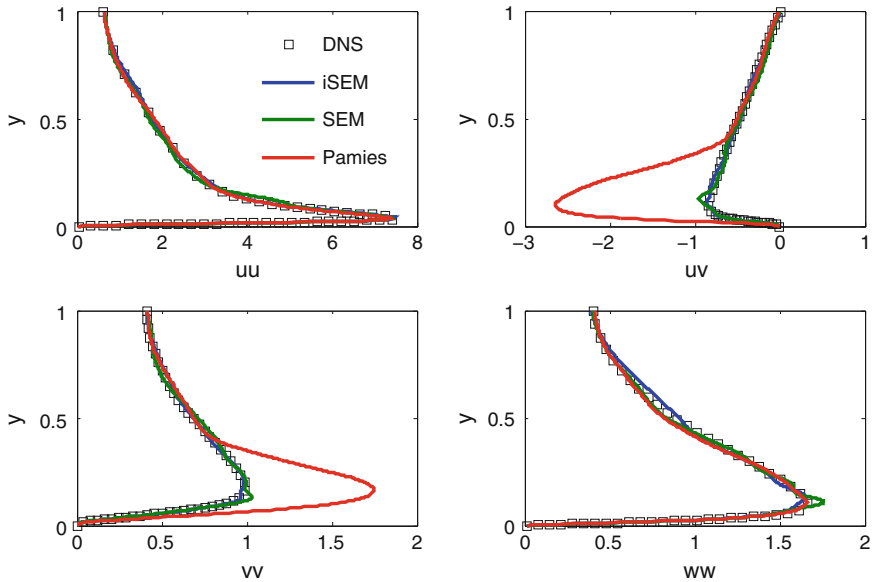
All simulations are carried out using the open source CFD software, OpenFOAM Extend 3.1. Moreover, all calculations close the filtered Navier-Stokes equations with the dynamic Smagorinsky sub-grid scale model. All simulations are computed using the same numerical mesh, with a total of approximately 15,000 cells. The grid resolution is:  $N_x = 1$ ,  $N_y = 125$  and  $N_z = 120$ ; where the non-dimensional wall normal distance,  $y_1^+$  is in the range 0.2–0.8.

Figure 1 provides a snapshot of the instantaneous velocity. It can be deduced from this that each method acts to provide a velocity field that appears turbulent in nature, and demonstrates a decrease in physical length scale towards the channel wall as expected.

Figure 2 illustrates the stress profiles for the various methods after averaging, along with the original DNS input statistics. Generally positive comparisons are drawn between the methods and their ability to produce the correct turbulent statistics. In particular, the iSEM appears to provide a good match with the DNS data. In general, all techniques appear to replicate the input data to a reasonable degree of accuracy, certainly for the  $uu$  and  $ww$  components. However strong deviations are apparent within  $vv$  and  $uv$  components, and it would appear, that Pamiès is the most extreme case with large over-predictions in the magnitude of shear stress.



**Fig. 1** Instantaneous velocity field at the inlet plane for **a** iSEM, **b** SEM, **c** Pamiès methods



**Fig. 2** Reynolds stress re-generation for channel flow at  $Re_\tau = 395$

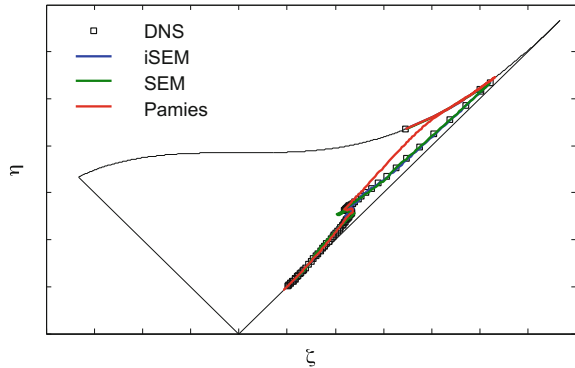
**Table 2** Root mean square error percentage between the DNS target data and the generated Reynolds stress profiles for each method with DNS inlet statistics

Method	RMS uu	RMS vv	RMS ww	RMS uv
iSEM	5.32	1.08	3.20	1.26
SEM	12.83	2.05	2.77	3.48
Pamiès	4.74	31.39	3.07	76.13

From considering the method formulation, it seems that this over-prediction is due to the correlation of the velocity components. Additionally, such effects are believed to be apparent due to the non-random spin allocation applied to the eddies by the shape functions within modes  $p = 1$  and  $p = 2$ . Although this does act to provide a more precise control of the eddy shapes it is believed the over-prediction in the peak shear stresses could produce implications in certain situations. The method originators (ONERA) agree that this explanation is plausible. However, the possibility of an implementation error cannot be ruled out, since a comparable study for channel flow has not been carried out in the original implementation.

The overall accuracy to which the re-generated stresses compare to the target DNS stresses is provided in Table 2 with the Root Mean Square error percentages being shown. This highlights the overall extent to which the stresses differ from the target DNS, and suggest all methods are adequate with iSEM demonstrating the lowest error. However, when tracking the computational expense of these methods, it is tentatively observed that the (erroneous) STG implementation is able to provide

**Fig. 3** Lumley diagram measuring stress anisotropy for the channel flow at  $Re_\tau = 395$



the fastest approximation, as indicated in Table 2. Indeed, the STG algorithm is 2 times faster than the SEM method and 1.67 times faster than the iSEM. It is not considered likely that the STG implementation error affects the computational overhead statistics.

A visual interpretation of the normalized Reynolds-stress anisotropy is provided via the second and third invariants of the anisotropy tensor,  $a_{ij}$ . These two values are commonly used to characterize the state of the anisotropy across the channel and help interpret the shape of turbulent structures. The trace for all three methods is provided in Fig. 3. From experimental and DNS data it is known that in the very near wall region of the channel ( $y^+ < 5$ ) the turbulence should largely be two component, such that  $\langle vv \rangle$  is much smaller than  $\langle uu \rangle$  and  $\langle ww \rangle$ . Furthermore, the level of anisotropy, which is measured by  $\eta$ , reaches a maximum value at approximately  $y^+ = 7$ . As one moves further from the near wall region the stress exhibits a close axisymmetric nature whilst becoming more isotropic with increasing distance from the wall. The Pamies method appears to be unable to capture the full extent of the axisymmetry of the turbulence in the buffer layer region, which again could be linked to the non-random spin allocation in modes  $p = 1$  and  $p = 2$ .

### 2.3 Sensitivity to Inlet Data Source

In the previous section the mean turbulent inlet data has been taken from the relevant DNS database, however it is arguably far more relevant to the current research to assess the capability of these methods when provided with data from a RANS simulation, as would be the direct scenario within an Embedded LES computation. Thus, the simulations have been run again with data provided from a periodic simulation utilizing the  $k-\omega$  SST eddy viscosity model (EVM), at the same Reynolds number. Likewise, the regenerated Reynolds Stresses have been plotted against those from DNS statistics.

Figures 4, 5, 6 provide an assessment of the sensitivity to the inlet statistics for each technique, with each showing the computed profiles of Reynolds stresses obtained from both DNS and SST mean data, along with the target DNS data. In general, it would appear that there is little sensitivity to these inlet statistics, with the SST initiated simulations providing predictions which are qualitatively very similar to those obtained using the DNS data. However, when one considers instead a quantitative assessment, as provided in Table 3, it there is a notable increase in error compared to the simulations that utilize the DNS statistics (Table 2). In addition, it would appear, that the greatest error increases are sourced from the  $w w$  component of stress, with the SST inlet statistics generating a significant overshoot in the maximum value within the log region. This is not unexpected considering the reduced capability of the standard EVM to predict this near wall turbulence anisotropy (Table 4).

### 3 Performance of Embedded Approaches

#### 3.1 Introduction

Two test cases have been used for model evaluation; namely a plane channel flow and a spatially developing boundary layer. The former test case has been selected in order to provide a clean comparison of model performance in a pure LES simulation, with high-quality input statistics. The latter case has been selected, to

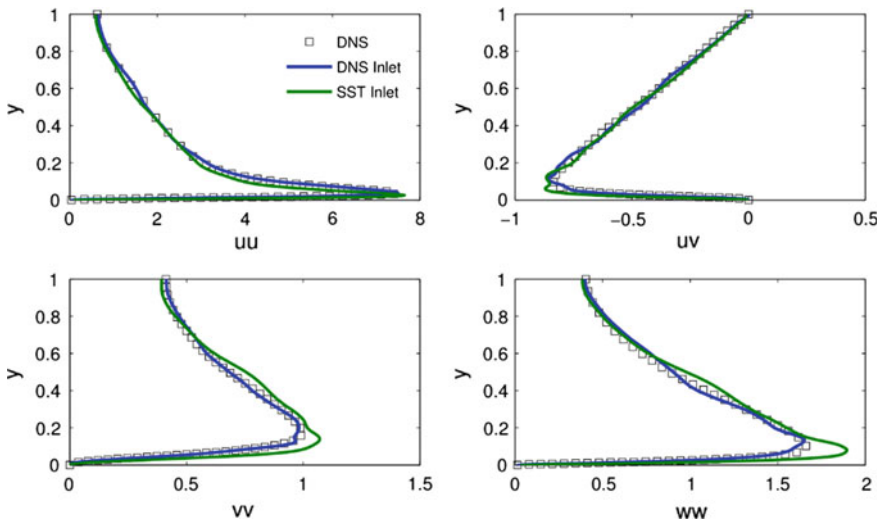


Fig. 4 iSEM stress plots with inlet data taken from DNS and  $k-\omega$  SST

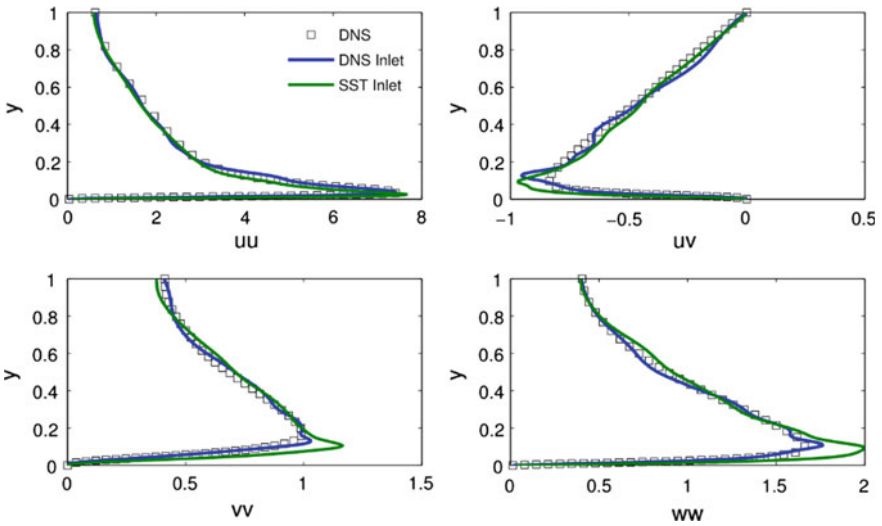


Fig. 5 SEM stress plots with inlet data taken from DNS and  $k-\omega$  SST

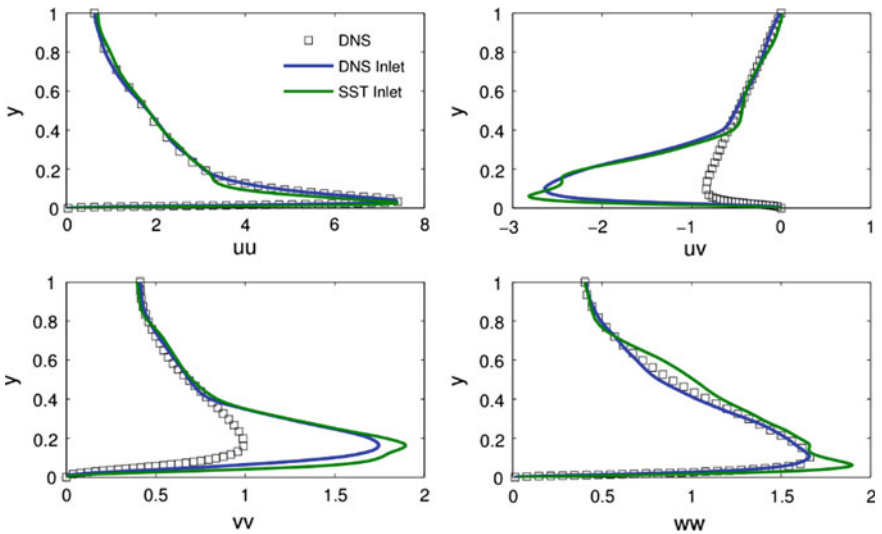


Fig. 6 Pamiès SEM stress with inlet data from DNS and  $k-\omega$  SST

**Table 3** Simulation information for the different inlet methods

Method	No. of Eddies	Calculation time per step (s)
iSEM	6342	5
SEM	10,000	6
Pamiès	6342	6
STG	N/A	3

Calculation time from the erroneous STG implementation is included tentatively for information

**Table 4** Root mean square error percentage between the DNS target data and the generated Reynolds stress profiles for each method with RANS inlet statistics

Method	RMS uu	RMS vv	RMS ww	RMS uv
iSEM	38.06	8.72	11.60	4.31
SEM	35.02	9.65	12.95	5.94
Pamiès	35.21	40.79	11.56	80.35

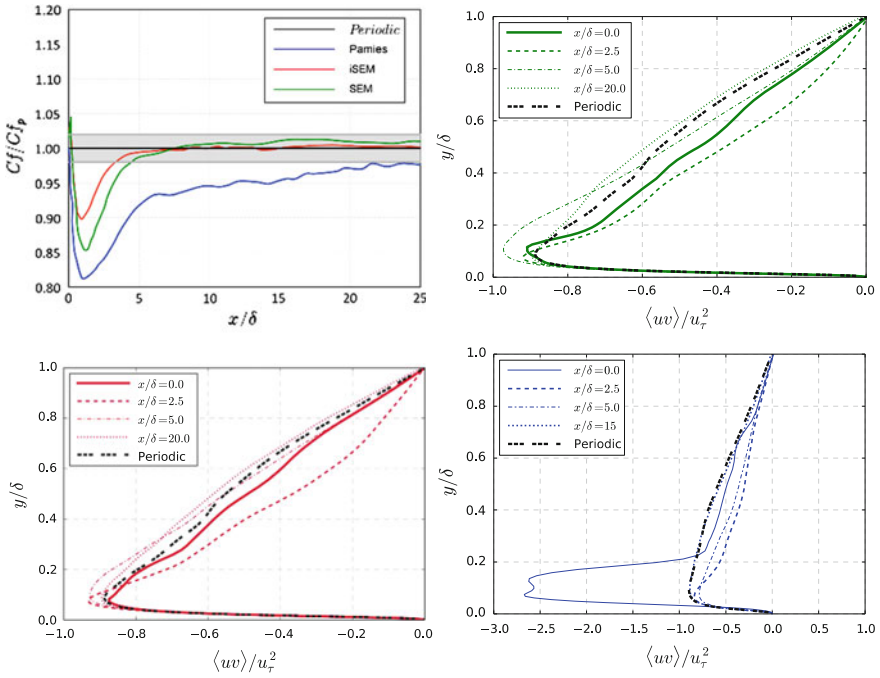
evaluate the models' performance under conditions typical to the aerospace industry, using a WMLES strategy of turbulence closure. In the first instance a series of a priori tests have been conducted in order to evaluate the implementation.

### 3.2 Channel Flow

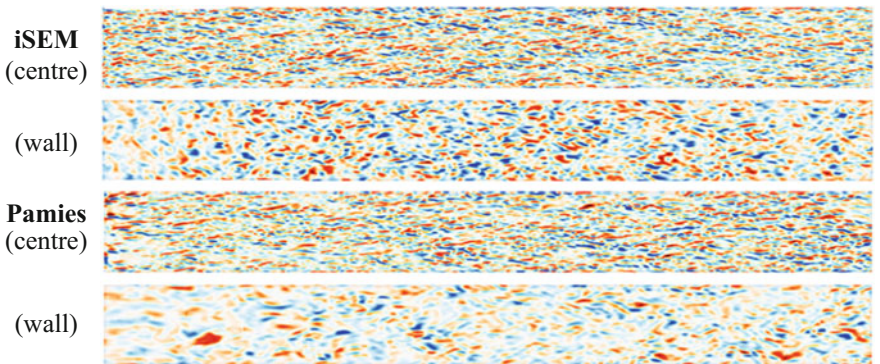
The first test-case we consider here is the flow through a plane channel at a Reynolds number, based on the friction velocity and half channel height, of  $Re\tau = 590$ . This case is attractive, as it allows for a definite quantification of the development length. The input statistical data for the various algorithms has been obtained from the DNS database of Moser et al. (1999). The filtered Navier-Stokes equations are closed through the use of the Smagorinsky model. A mesh comprising approximately 7M cells has been employed. The mesh has a resolution, in wall units, of  $\Delta x^+ \approx 25$ ,  $\Delta y^+ \approx 1.2 - 12$  and  $\Delta z^+ \approx 12$ .

Figure 7 presents a comparison of the skin friction recovery downstream of the inlet, as well as the shear stress development at various downstream locations.

Figure 8 displays contours of streamwise vorticity for both iSEM and Pamiès methods; in each case a plane is displayed at the channel centre,  $y/\delta = 1$ , and the near wall region  $y/\delta = 0$ . Contours for SEM and iSEM are visually very similar and so only the latter is displayed. Note the over-prediction of stresses at the inlet for the Pamiès model. This is thought to be due to the correlation of velocity components, as discussed previously. For modes  $p = 1$  and  $p = 2$ , the shape functions do not employ a separate random sign ( $\epsilon$ ) for each component. While this does allow for more precise control of the shape of the injected eddies, the initial spurious peak in shear stresses may have implications in some situations.



**Fig. 7** Channel flow results: (top left) comparison of skin friction coefficient; (top right) evolution of shear stress for original SEM; same for (bottom left) iSEM and (bottom right) Pamiès



**Fig. 8** Contours of vorticity for iSEM and Pamiès at both channel centre and wall locations

### 3.3 Flat Plate Boundary Layer

We now consider the mandatory case of a spatially developing zero-pressure gradient turbulent boundary layer over a smooth flat plate as introduced in Part III (Results for Fundamental Test Cases, The spatially developing flat plate turbulent boundary layer). The free-stream velocity is  $U_0 = 70 \text{ ms}^{-1}$ , the static pressure is set to  $P_0 = 99120 \text{ Pa}$ , the temperature equals  $287 \text{ K}$  leading to a Reynolds number per meter  $Re = 4.72 \times 10^6 \text{ m}^{-1}$ . The initial boundary layer thickness is  $\delta_0 = 5.8 \text{ mm}$  so that the Reynolds numbers based respectively on the momentum thickness  $\theta_0$  is  $Re_{\theta_0} = U_0\theta_0/\nu = 3040$ . The mandatory structured grid, of  $7.8 \times 10^6$  points, was used for the simulations in this section as previously described in Part III (Results for Fundamental Test Cases, The spatially developing flat plate turbulent boundary layer). The computational domain sizes in the streamwise, spanwise and wall-normal directions are respectively  $L_x = 113 \delta_0$ ,  $L_z = 5 \delta_0$  and  $L_y = 52 \delta_0$ , such that the range of Reynolds number covered by the simulation is  $3040 \leq Re_{\theta} \leq 6100$ . The grid employed a resolution of  $\Delta x^+ \approx 100 - 200$ ,  $\Delta y^+ \approx 2$  and  $\Delta z^+ \approx 50$ . Further details of the grid and an in-depth evaluation of this case are provided in Part III (Results for Fundamental Test Cases, The spatially developing flat plate turbulent boundary layer). In contrast to early partner-wise work, all models in the CAP were evaluated using an incompressible framework. A second-order central scheme was employed for spatial discretization, and the time-step size has been set to  $1 \times 10^{-6} \text{ s}$ . The SA based IDDES turbulence model has been employed.

This case represents a considerable step from the fully wall resolved LES results in the previous section, which has been deemed to be of practical relevance for the evaluation of turbulent inlet conditions in this project. It should be noted that in the following section our focus is on synthetic turbulence and not the underlying WMLES. During the course of this project we identified some deviations between the OpenFOAM Extend implementation of SA-IDDES and the published formulation, which explains deviations from the ‘partner best approaches’ presented in

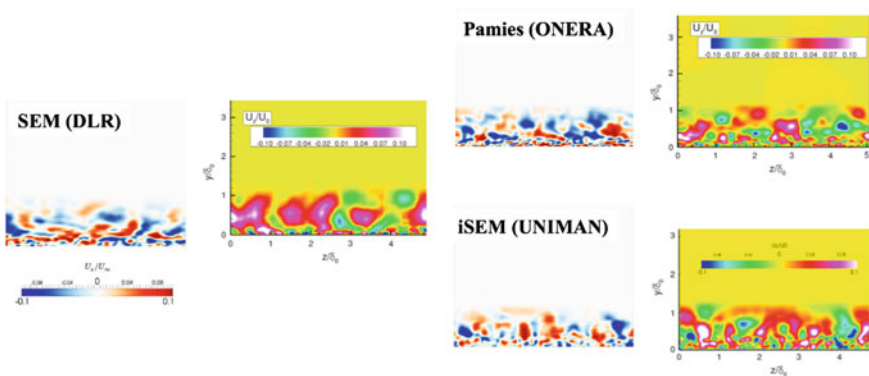


Fig. 9 Comparison of model implementation versus partner best scheme at inlet



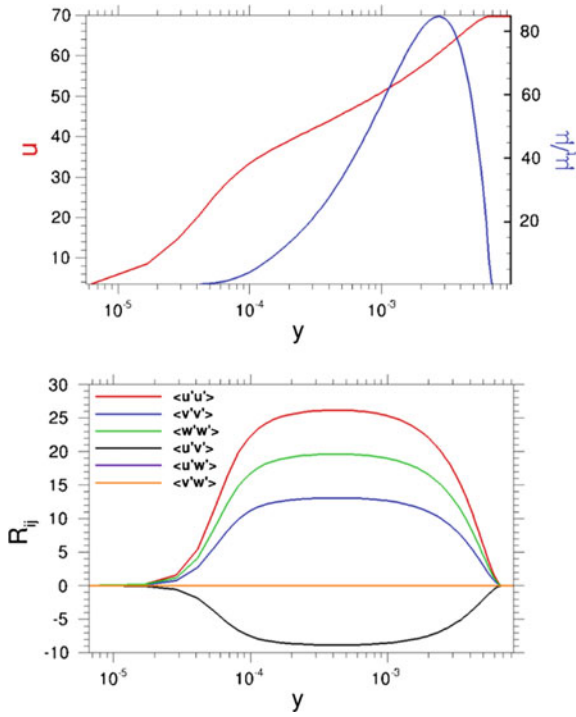


Fig. 10 RANS Inlet data provided (top), and reconstructed Reynolds Stress (bottom)

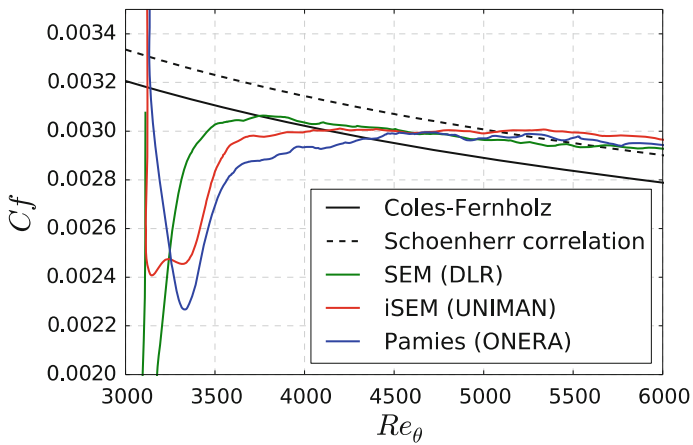


Fig. 11 Skin friction coefficient for spatially developing boundary later test case

Part III (Results for Fundamental Test Cases, The spatially developing flat plate turbulent boundary layer); unfortunately, the time constraints of the present project have precluded the undertaking of a rigorous cross-validation activity.

Figure 9 provides a comparison between partner best scheme and CAP implementation, at the inlet plane to the flat plate. Qualitative differences observed are expected due to a differing response to near-wall treatment specific to the underlying hybrid RANS-LES methodology, which usually act to transition from RANS to LES but may here interfere with synthetic turbulence generation. The RANS inlet data provided for these simulations are plotted in Fig. 10, and has been obtained from the SA 1-equation RANS model. As such, Reynolds stress quantities have had to be reconstructed from this data as plotted in the same figure. Details of this reconstruction have been provided in Part III (Results for Fundamental Test Cases, The spatially developing flat plate turbulent boundary layer).

Figure 11 shows the development of skin-friction along the flat plate from the inlet. From this figure, it is apparent that all models converge towards the Schoenherr correlation by the end of the functional computational domain (i.e. that excluding the stretched cells). All models appear to have a reasonable development length; in line with partner expectations for this case. The fact that the skin-friction is observed to increase long after the initial deficit, is a concern and is further evidence of an inconsistency in the implementation of IDDES in OpenFOAM. This is nonetheless experienced consistently by all the inlet models tested.

Velocity profiles and resolved stresses at  $Re_\theta = 4060$  are given in Figs. 12 and 13, respectively. Differences in the predicted velocity levels are small, and only minor variation is observed for the mean imposed velocity profile. However, outer scaling reveals differences in modeled content with each model, and this warrants further investigation since this could imply that the performance of a given synthetic turbulence approach depends on the downstream WMLES model employed. It should be noted that this test represents the first time that the SEM and iSEM

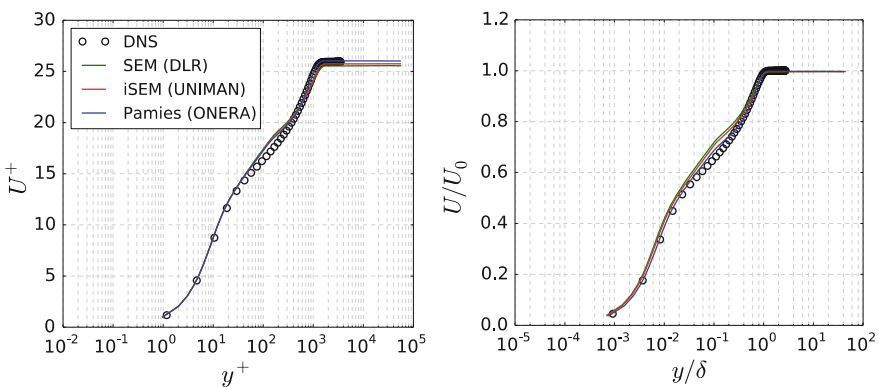
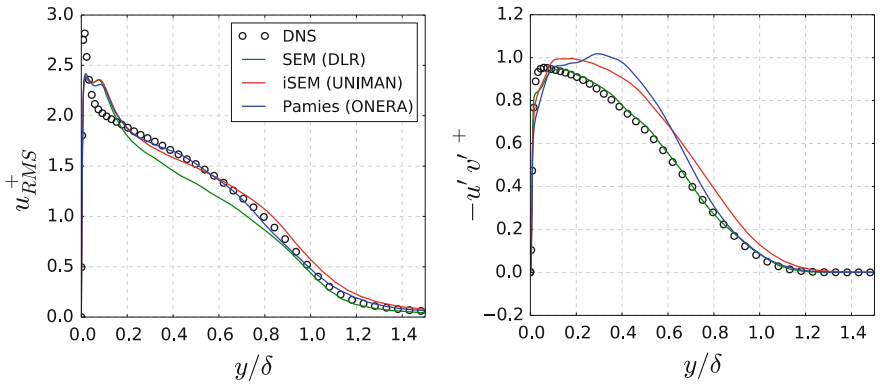
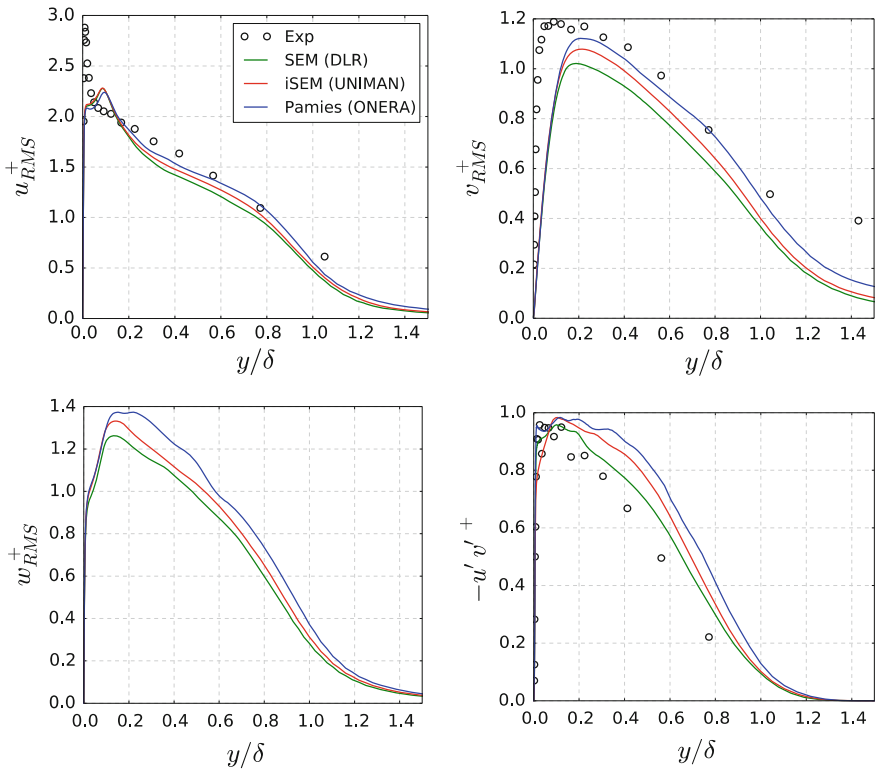


Fig. 12 Velocity at  $Re_\theta = 4060$ . Inner coordinates (left). Outer coordinates (right)



**Fig. 13** Resolved stresses at  $Re_\theta = 4060$



**Fig. 14** Resolved stresses at  $Re_\theta = 5200$ .  $u_+$  (top left),  $v_+$  (top right),  $w_+$  (bottom left),  $-uv_+$  (bottom right)

models have been used with a near-wall RANS model such as in IDDES-SA, while the SEM-Pamiès has been significantly tested for use with WMLES.

Pfiles of the resolved stresses at  $Re_\theta = 5200$ . are shown in Fig. 13. It can be seen, that differences are more pronounced in the  $uv$  plots. The SEM (DLR) appears to predict  $uv$  well but under-predicts  $u$ . away from the wall. Other models broadly do better at predicting  $u$  but over-predict  $uv$ .

Some differences are observed in the prediction of the split between resolved and modelled stresses for all approaches. Analysis of this split is particularly useful for establishing potential issues arising in the implementation of the near-wall modelling. When comparing these results to the IDDES-SA results obtained by partners from their own codes (see Fig. 6 in Part III Results for Fundamental Test Cases,

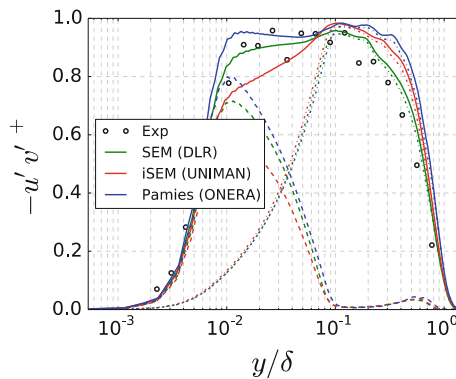


Fig. 15 Total shear stress (solid), modelled (dash), resolved (dash-dot)

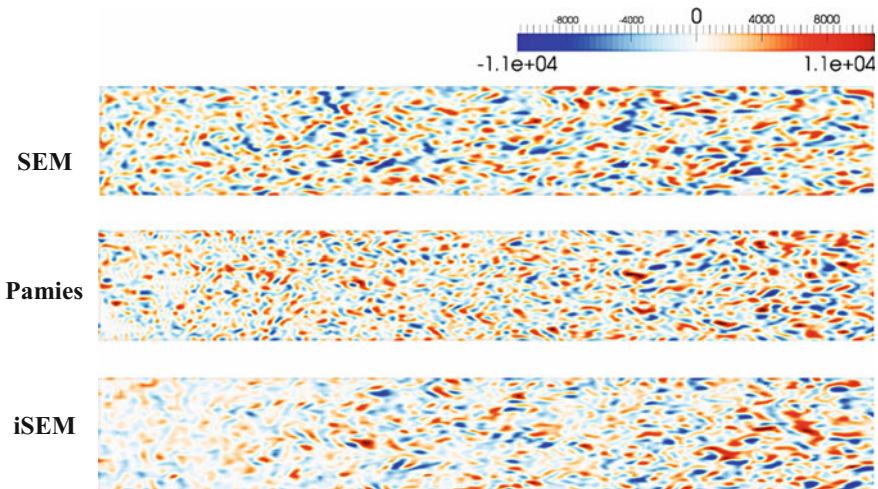
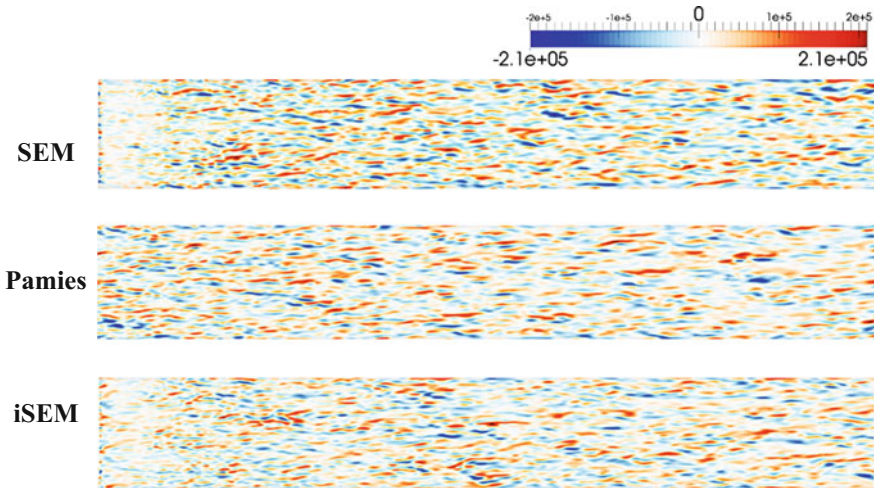


Fig. 16 Contours of vorticity at the top of the boundary layer,  $y/\delta_0 = 1$



**Fig. 17** Contours of vorticity at the wall,  $y/\delta_0 = 0$

The spatially developing flat plate turbulent boundary layer)—which for DLR and NTS have been extensively validated—the results in Fig. 17 indicate a higher level of resolved stress. In this work the OpenFOAM Extend implementation of IDDES-SA packaged with release 3.1 has been used as is, but underlying errors in the implementation of IDDES-SA may well be responsible for the consistent overproduction of resolved stresses here observed (Figs. 14 and 15).

Finally, Figs. 16 and 17 provide vorticity contours at the top of the boundary layer (at the inlet plane) and at the plate wall respectively. With reference to Fig. 11, we observe that the SEM and iSEM are apparently underestimating levels of turbulence in the immediate vicinity of the inlet plane. It can be seen, that the iSEM takes some time to develop fully the correct levels of turbulence near to the top of the boundary layer, whereas the SEM and SEM-Pamiès develop faster at this location.

## 4 Conclusions

In this chapter, we have reviewed the performance of several inlet turbulence generation approaches applied to both the LES flow through a turbulent channel and the WMLES flow over a flat plate. In the former case, a superior performance been demonstrated by methods developed for LES levels of refinement and sensitized to inlet data from turbulence models expected to perform well in RANS only mode. In the latter case, conclusions have been harder to reach in the light of

possible underlying errors in the form of the WMLES implemented in the baseline code. In what follows we provide a technical summary of these findings, which should be considered in the context of the difficulties and uncertainties previously reported.

In the channel flow with LES, the iSEM provided the shortest recovery towards reference periodic LES data, closely followed by the SEM and the method of Pamiès et al. For the flat plate with current WMLES approach and numerics, the SEM has shortest recovery region followed by iSEM and Pamiès et al. It is noted that while providing the shortest development length, the SEM exhibits a significantly pronounced dip in skin friction downstream of the interface; resulting in a considerably higher error magnitude than either the iSEM or the method of Pamiès et al.

Compared to results from other codes (reported for the flat plate case in Part III (Results for Fundamental Test Cases, The spatially developing flat plate turbulent boundary layer), the trend of skin friction with distance after the initial crisis is deficient. This may be due to the OpenFOAM Extend numerics or related to non-standard elements in the IDDES model implementation. Despite this however, all synthetic inlet methods are subject to the same conditions in the CAP test and comparisons remain relevant. Contrasting the flat plate results here with the partner-wise results in Part III (Results for Fundamental Test Cases, The spatially developing flat plate turbulent boundary layer) allows the conclusion to be drawn that there is a strong dependency on the underlying solver, numerics and/or WMLES model implementation.

The Common Assessment Platform has provided the framework for a number of direct comparisons across a single code that enable impact of different numerics to be eliminated for the first time. This was an ambitious project to assess and evaluate the different models developed in this project. While we have made some significant advances towards this objective this remains very much a work in progress. We have attempted to provide a short list of advantages and disadvantages and comments associated with the Common Assessment Platform, in order to try to summarize our experience in this work package.

## 5 Advantages

*A1: An 'ultimate' level of implementation detail to all partners.*

The common assessment platform has been motivated by previous observations that however careful one is to level the playing field for a comparison in terms of a common mesh, common numerics, common modeling etc., it is generally extremely difficult to draw absolute comparisons when completely different software tools are

used. As such the pinnacle of computational benchmarking of physical modeling would be the implementation of models in a single common code.

*A2: The process can be used to generate Best Practice Guidelines for industrial implementation in other codes*

Following from the previous point, if one were able to arrive at a well validated and verified common assessment platform, one would be able to use this to objectively and systematically assess the robustness and accuracy limitations of all approaches with respect to differing numerical grids and numerical options. This would provide extremely valuable knowledge to the industrial user so as to be able to accurately inform their decision regarding which modeling option to use according to their specific numerical requirements and computational resources.

*A3: Removes numerical sensitivity and hidden features from comparison*

When attempting to implement a numerical method, there will usually be some minor details that are either missing from the original reference or which arise due to differences between the codebase of the originator and the implementer, which require substantial effort to identify and rectify during the implementation procedure. As such it is generally quite difficult to entirely reproduce the intended performance of a model. While this source of error may not ever be entirely eliminated, the use of the common assessment platform provides a level playing field and can help identify common issues.

*A4: Enables future 'cross-pollination' of models*

One aspect that we can envisage to be advantageous for a common assessment platform would be the subsequent ability of the user to mix and match elements of different approaches to improve the overall predictive capability of a particular scheme. Indeed, it is often the case that small corrections and limiters present in the numerical scheme of any particular model, are the result of code-specific dependencies. The ability to combine models on a common platform is expected to yield enhanced performance beyond the best model as used individually.

## 6 Disadvantages

*D1: It is difficult to iron out all implementation bugs*

In the context of this project and with limited resources, it has proven to be a difficult and time-consuming exercise to implement and fully validate each of these schemes. A number of models were here implemented for the first time into an incompressible code and for the first time for use with inlet data from simple RANS models. Further work is ongoing to fully explore and eventually eliminate implementation bugs and the issues associated with combining models with the specific characteristics of a new CFD solver.

*D2: Assessment is limited in the present context*

The present work is limited in light of the above issues, and conclusions may not be expected to hold once the WMLES model is deemed to be correct. As such, the technical conclusions proposed above are formulated in an appropriately tentative manner. However, the value of the common assessment platform is clear and we fully anticipate its benefits once this work has been completed.

*D3: We have had to choose a single platform and our conclusions may be a function of this choice, due to a bias towards methods in the selected solver?*

Unambiguous conclusions regarding the relative performance of these models would require multiple codes, numerical options and cases to be tested. This has been beyond the scope of the current project. There have been significant challenges associated with the implementation and testing of methods designed for the specifics of one software, in an entirely new computational code. Perhaps the most significant issue is the adaptation of inlet methods which have previously been used for wall resolved LES to Hybrid RANS LES methods where the wall turbulence is modeled using RANS, as in the case for IDDES-SA. In addition, the use of SA entails significant approximation of the Reynolds Stress anisotropy, which is expected to have a considerable impact on the results for inlet methods which have been developed to be sensitive to this anisotropy.



# **Part VI**

## **Conclusions**

# The Go4Hybrid Project Achievements

C. Mockett and S. Wallin

## 1 Introduction

The Go4Hybrid project has served as a pioneering R&D project to explore various possibilities to mitigate the grey area problem facing hybrid RANS-LES methods. Despite the comparatively small consortium of seven partners and the short, two-year duration, highly-innovative work has been carried out in which very promising results have been achieved.

In this closing chapter, a summary of the technical work conducted will be given (Sect. 2), before the project findings are collated in a review of the novel methods (Sect. 3). Alongside this, a key outcome of any such project, and one that is of particular value to industrial end-users, is a set of Best Practice Guidelines. Due to the exploratory and innovative nature of the project, this aspect proves particularly challenging, a fact which is not helped by the short duration and the inherent complexity of the problem. Note that the pioneering nature of Go4Hybrid is in contrast to “consolidation” projects concerned with more mature methods, such as the precursor project ATAAC (which was the third in a sequence of projects addressing hybrid RANS-LES methods). Despite these inherent limitations, a collection of lessons learned and preliminary BPG are presented in Sect. 4. Importantly, the change in hybrid RANS-LES BPG achieved in Go4Hybrid over the ATAAC status is highlighted.

---

C. Mockett (✉)  
CFD Software Entwicklungs- und Forschungsgesellschaft mbH (CFDB),  
Bismarckstr. 10-12, 10625 Berlin, Germany  
e-mail: charles.mockett@cfdb-berlin.com

S. Wallin  
Swedish Defence Research Agency (FOI), 16490 Stockholm, Sweden

Finally, the document concludes with an assessment of the direction of future research on this topic required in order to further satisfy industrial needs for productive hybrid RANS-LES methods (Sect. 5).

## 2 Summary of Work Conducted

Before assessing the strengths and weaknesses of the studied methods and the drawing of conclusions, an overview of the technical work carried out is given here. Summaries of the methods applied by each partner to the various test cases are given in tabular form, for the non-zonal methods in Sect. 2.1 and for the embedded approaches in Sect. 2.2. Acronyms are used and the reader is referred to Sect. 2 for detailed descriptions of the non-zonal formulations and to Sect. 3 for the embedded approaches.

### 2.1 *Non-zonal Methods*

Unified approaches without explicit user-defined interfaces between the RANS and LES regions are in this study being denoted as “non-zonal” methods, although many other classifications can be made. Typically, these methods are less complex to implement and less dependent on code-specific solutions implying that cross-comparisons are more easily made. Hence, the rather extensive amount of comparisons shown here.

The application of different non-zonal GAM approaches to the Go4Hybrid test cases are summarised in Table 1.

The following remarks can be made:

- All GAM methods have been tested on the mandatory shear layer case (F2)
- The most simulated complex case is the round jet (I5), with 8 simulations using GAM techniques and 2 reference simulations
- The delta wing (I2), 3-element airfoil (I3) and 2D hump (I4) have also been extensively tested, however the only one simulation with GAM approaches has been carried out on the helicopter fuselage case (II)
- The most widely-tested GAM strategies are  $\Delta_{SLA}$  and  $\sigma + \tilde{\Delta}_\omega$  (4 cases each), followed by HPF + stoch. BS and WALE +  $\tilde{\Delta}_\omega$  (3 cases each)
- Excluding the common assessment platform, four approaches have been implemented in two different codes, indicating strong collaboration between the partners. The approaches in question are WALE +  $\tilde{\Delta}_\omega$  (CFDB and NTS) and  $\sigma$  (CFDB and NLR) as well as the two vorticity-adaptive filter widths  $\tilde{\Delta}_\omega$  (CFDB and NTS) and  $\Delta_\omega$  (ONERA, also tested by DLR).

**Table 1** Application of non-zonal methods to test cases in Go4Hybrid

Partner	Underlying HRLM	Code	Non-zonal GAM approach	F1 Flat plate	F2 Shear layer	I1 Helicopter	I2 Delta wing	I3 3-el. airfoil	I4 2D hump	I5 Round jet
FOI	HYB0	Edge	-		•			•	•	
Exa	RKE-proprietary	PowerFLOW	-		•	•				
CFDB	SA-DDES	OpenFOAM	-		•		•			•
NTS	SA-DDES	NTS	-					•	•	•
ONERA	SA-DDES	FLU3M	-		•					
UniMan	SA-DDES	Star-CCM+	-			•				
NTS	SA-IDDES	NTS	-					•	•	
CFDB	SST-DDES	OpenFOAM	-			•				
NLR	SST-DDES	ENSOLV	-				•			
DLR	SST-IDDES	TAU	-					•		
NTS	SST-IDDES	NTS	-					•		
UniMan	SST-IDDES	Star-CCM+	-					•		
NLR	DX-LES	ENSOLV	HPF		•					
NLR	DX-LES	ENSOLV	HPF + Stoch. BS		•			•		•
FOI	HYB0	Edge	Leonard BS		•					
CFDB	SA-DDES	OpenFOAM	WALE		•					•
CFDB	SA-DDES	OpenFOAM	WALE + $\tilde{\Delta}_o$		•		•			•
NTS	SA-DDES	NTS	WALE + $\tilde{\Delta}_o$							•
FOI	HYB0	Edge	ETC ( $\Delta$ -tr)		•				•	
FOI	HYB0	Edge	$\Delta_{min}$		•			•		
FOI	HYB0	Edge			•			•		

(continued)

Table 1 (continued)

Partner	Underlying HRLM	Code	Non-zonal GAM approach	F1 Flat plate	F2 Shear layer	I1 Helicopter	I2 Delta wing	I3 3-el. airfoil	I4 2D hump	I5 Round jet
			$\Delta_{\min}$ + Leonard BS							
NTS	SA-DDES	NTS	$\Delta_{SLA}$		•			•	•	•
NTS	SA-IDDES	NTS	$\Delta_{SLA}$					•		
DLR	SST-IDDES	TAU	$\Delta_{\sigma}$						•	
ONERA	ZDES-M2	FLU3D	$\Delta_{\sigma}$		•					
FOI	HYB0	Edge	$\Delta_{\sigma}$		•			•		
CFDB	SA-DDES	OpenFOAM	$\tilde{\Delta}_{\sigma}$		•					•
NLR	DX-LES	ENSOLV	$\sigma$		•					
CFDB	SA-DDES	OpenFOAM	$\sigma$		•					•
CFDB	SA-DDES	OpenFOAM	$\sigma + \tilde{\Delta}_{\sigma}$		•		•			•
CFDB	SST-DDES	OpenFOAM	$\sigma + \tilde{\Delta}_{\sigma}$			•				
Sum				0	19	4	6	11	6	10

## 2.2 *Embedded Approaches*

In Go4Hybrid, predominantly RANS-to-LES interface conditions have been studied in the framework of embedded approaches. The embedded approaches are hence chiefly characterised by the choice of method applied to impose resolved turbulent fluctuations at the inlet to the scale-resolving region. The application of embedded approaches to the Go4Hybrid test cases is summarised in Table 2 (on the following page).

The following remarks can be made:

- All partners chose methods that can be categorised as synthetic turbulence approaches (as opposed to e.g. recycling/rescaling or database approaches)
- All synthetic turbulence generating methods were tested on the mandatory flat plate test case (F1)
- The test cases most studied with embedded approaches are the 3-element airfoil (I3) and the 2D hump (I4)
- Variants of the SEM are the most widespread approach, having been tested by 3 different partners (DLR, ONERA and UniMan)
- Imposition of fluctuations over a volume rather than a plane has been a widely pursued approach, tested by DLR, ONERA and NTS. Although DLR uses a “volume-source term” to impose fluctuations, the forcing region is restricted to points lying in a plane.

## 3 **Review of Methods**

### 3.1 *Non-zonal Methods*

#### 3.1.1 **Short Description of the Different Methods**

For convenience, the key features of the different explored approaches for GAM in non-zonal methods are summarised with reference to Sect. 2.2 for full descriptions.

The methods all seek to reduce the modelled SGS stresses in the early shear layer. Some take a further step to excite the development of fine turbulent scales:

- $\Delta_\omega$ : ONERA, relax grid dependency in the direction of vorticity. Reduces to  $\sqrt{\Delta_x \Delta_y}$  with vorticity vector in  $z$ -direction.
- $\tilde{\Delta}_\omega$ : NTS, modification of  $\Delta_\omega$  to reduce influence of smallest grid size. Returns approximately  $\max(\Delta_x, \Delta_y)$  with vorticity vector along  $z$ -direction.
- $\Delta_{SLA}$ : NTS, further reduction of  $\tilde{\Delta}_\omega$  based on a “Kelvin-Helmholtz sensor” for detection of quasi 2D regions. Active also on uniform grids.

**Table 2** Application of embedded approaches to test cases in Go4Hybrid

Partner	Underlying HRLM	Code	Turbulent fluctuations	F1 Flat plate	F2 Shear layer	I1 Helicopter	I2 Delta wing	I3 3-el. airfoil	I4 2D hump	I5 Round jet
DLR	SST-IDDES	TAU	-					•		
ONERA	ZDES-M0	FLU3M	-					•		
ONERA	ZDES-M3	FLU3M	DF					•		
ONERA	ZDES-M3	FLU3M	DF + WN					•		
DLR	SA-IDDES	TAU	SEM	•						
DLR	SST-IDDES	TAU	SEM	•				•		
DLR	SA-IDDES	TAU	DFSEM	•						
DLR	SST-IDDES	TAU	DFSEM	•						
UniMan	SA-IDDES	Star-CCM +	DFSEM	•						
ONERA	ZDES-M3	FLU3D	DF + SEM (Parniès)	•						
NTS	SA-IDDES	NTS	STG	•	•				•	
NTS	SST-IDDES	NTS	STG	•				•	•	
NTS	SST-IDDES	NTS	VSTG	•						
Sum				9	1	0	0	6	3	0

- $\Delta_{\min}$ : FOI, length scale based on minimum grid size  $\min(\Delta_x, \Delta_y, \Delta_z)$  in combination with the conventional LES length scale based on the control volume,  $(\delta v)^{1/3}$ .
- WALE: CFDB, reduces  $\nu_{\text{SGS}}$  in 2D plane shear based on a non-linear operator in terms of the resolved velocity gradient tensor.
- $\sigma$ : CFDB, reduces  $\nu_{\text{SGS}}$  in all 2D and two-component local flow states based on the eigenvalues of the resolved velocity gradient tensor.
- HPF: NLR, high-pass filtered SGS model
- HPF + Stoch. BS: NLR, added stochastic backscatter to HPF
- Leonard BS: FOI, backscatter based on the Leonard term
- ETC: FOI, Energy Transfer Correction to account for energy transfer between resolved and modelled scales by a transport eq. for the length-scale.

### 3.1.2 Performance of Non-zonal Methods for the Mandatory Case (Shear Layer)

The shear layer is a well-defined case that is extremely sensitive to the grey area problem and is, hence, of large value in assessing the effectiveness of the different GAM methods studied. As such, it is also the general finding that this case is sensitive to fine details about the grid and numerical methods. Therefore, the results here and conclusions made can be seen as exaggerated compared with what one can expect on more complex industrial cases. The CAP activity, in which selected methods are compared directly using the same CFD code, is thus of particular importance in this case because the influence of grid and numerical methods can be eliminated. Note that a coarse grid was chosen for the CAP study to further exaggerate the differences between methods.

Based on partners' results and the CAP activity, the following statements can be made:

- All studied GAM strategies have achieved significant acceleration of RANS to LES transition compared to the baseline hybrid models.
- The approaches that seek to strongly reduce eddy viscosity in the early shear layer all prove effective. Under the specific conditions (code and grid) studied in the CAP, the  $\Delta_{\text{SLA}}$  approach exhibited the strongest GAM effect, followed by the HPF plus (uncorrelated) stochastic backscatter, then the  $\sigma + \tilde{\Delta}_{\omega}$  method, which showed a stronger effect than the HPF method without stochastic backscatter. These results are shown in Fig. 1. Both vorticity-adaptive grid filter methods on their own gave very poor results on the coarse CAP grid, however ONERA achieved good results with the  $\Delta_{\omega}$  approach in their own code on a finer mesh.
- The individual partner simulations showed that all non-zonal GAM methods are effective in their native codes and on specialised/refined meshes. This highlights the importance of not drawing conclusions exclusively from the findings of the CAP.



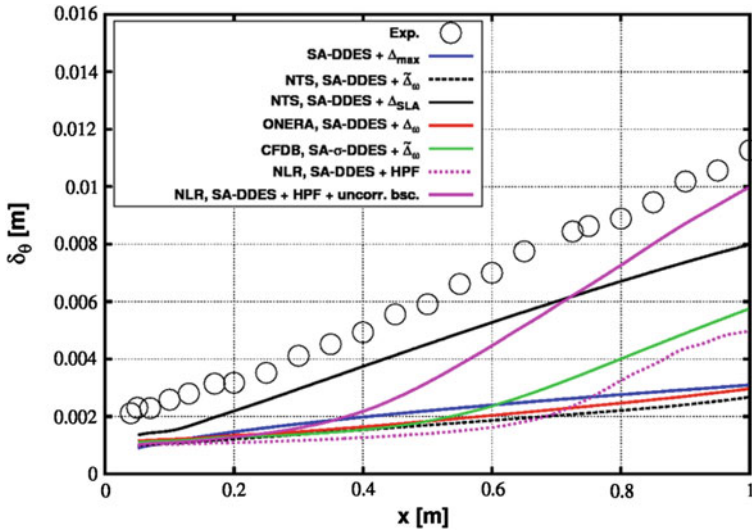


**Fig. 1** Shear layer thickness development downstream of a splitter plate (trailing edge at  $x = 0$ ) compared directly (on a coarse mesh) for different non-zonal GAM approaches in the Common Assessment Platform

- From NLR's simulations it appears as if the additional excitement of small scales via stochastic backscatter achieves a further degree of Grey Area Mitigation compared to reduction of the modelled Reynolds stresses via the HPF approach alone. This additional performance increase due to backscatter was strong on a coarse grid but less so on a finer grid where HPF alone gave reasonable results. A corresponding assessment of the Leonard backscatter and the energy transfer correction (ETC) approaches cannot be made due to the suspected contamination of results by strong numerical dissipation.

### 3.1.3 Overall Evaluation of Strengths and Weaknesses of Non-zonal Methods

Alongside the performance of the improved methods for accelerating RANS-LES transition in a pure planar shear case, it is essential to conduct an overall evaluation from the information available from the broader selection of test cases and from a critical analysis of the model formulations.

#### *Implementation and usability issues*

The most straightforward implementations are the vorticity-adaptive grid scales  $\Delta_\omega$  and  $\tilde{\Delta}_\omega$  and the eddy-viscosity reducing formulations  $\Delta_{SLA}$ , WALE and  $\sigma$ , since these are explicit and local formulations. These furthermore introduce no additional

user parameters. The HPF approach requires some kind of temporal filter to be implemented—the option of a running time-average leads to a non-local formulation in time and in all cases the specification of the temporal filter width introduces an additional user parameter. The energy transfer correction (ETC) approach requires the implementation of an additional transport equation for the length scale, which represents a slight increase in implementation inconvenience and computational overhead. For the stochastic backscatter approach to be effective it was shown that spatial and temporal correlations need to be imposed involving the solution of three additional transport equations. The Leonard backscatter term is local and explicit but the dissipative part should be limited to keep total  $\nu_{SGS} > 0$  for numerical stability reasons.

### *Generality*

It is conceivable that some approaches may give very good performance in terms of RANS to LES acceleration in the particular case of the planar shear layer, but introduce disadvantages in more general situations. Any such known limitations to generality are discussed here.

Beginning with the grid scale definitions, a regular topic for heated discussions in the Go4Hybrid consortium is the validity of measures involving the minimum grid cell edge length (and it should be stated that no unanimous agreement on this topic has been reached). There are well-founded concerns that such formulations (i.e.  $\Delta_{min}$  and  $\Delta_\omega$ ) will strongly under-predict eddy viscosity in situations such as isotropic turbulence on an anisotropic grid. Moreover,  $\Delta_{min}$  based formulations obviously are not applicable in the flows including regions with attached boundary layers. The  $\tilde{\Delta}_\omega$  approach in contrast was formulated specifically to avoid reliance on the minimum grid dimension and is hence considered by its proponents as more general.

All GAM approaches seeking to exploit anisotropy of the grid (i.e.  $\Delta_{min}$ ,  $\Delta_\omega$  and  $\tilde{\Delta}_\omega$ ) will of course be ineffectual on isotropic grids. They are hence useful in situations such as jets or airfoil wakes, where prior knowledge of the shear layer location is combined with carefully designed structured grids. Unstructured grids by contrast tend to be more isotropic except for the near-wall prism layers.

It appears as if all non-zonal GAM approaches pursued in Go4Hybrid are in principle applicable to unstructured meshes, however only the  $\sigma + \tilde{\Delta}_\omega$  method has actually been tested on an unstructured grid (successfully, for the helicopter fuselage test case—see Sect. 10).

In principle, the NLR stochastic backscatter approach with spatial and temporal correlations can be applied to unstructured grids. For the temporal correlations, transport equations are solved which can be done on unstructured grids. The spatial correlations are created on structured grids by 1D implicit smoothing per computational direction. To generalize this method to unstructured grids, this could be replaced by full 3D smoothing (essentially solving a Laplace-type equation) at the price of increased computational costs.

Another generality issue has been seen to arise in the form of sensitivity to the flow topology. CFDB showed that the WALE approach was effective in situations of approximately planar shear (shear layer and round jet test cases), however performed very poorly for the vorticity-dominated delta wing case. Similar findings were reported by NLR for an analogous approach based on the Vreman sub-grid scale model. In contrast, the  $\sigma$  approach was found to perform well in all cases owing to increased generality of the underlying formulation. CFDB conducted an equivalent test of the  $\Delta_{SLA}$  formulation on the delta wing case and found that it too gave strong GAM performance.

Exclusively single-phase flows pertaining to aerodynamic and aeroacoustic applications were studied in Go4Hybrid. Regarding generality issues, it is however important to consider applicability to more complex scenarios. For cases involving e.g. reacting flows or combustion, the eddy viscosity has an important secondary function in the fine-scaled reaction modelling. It could hence arise that reducing the Reynolds stress rather than the eddy viscosity (as e.g. carried out in the HPF approach) is preferable, however such expectations must naturally be assessed using numerical experiments.

### *Robustness*

Reducing eddy viscosity to promote the development of resolved turbulence can be expected to bring an overall trend to reduced numerical stability, particularly when the early shear layer is coarsely resolved. Strongly related is the amount of dissipation introduced by the numerics. This should be as low as possible to avoid damping the insipid resolved turbulence, which may make the solution less robust. It has generally been observed that the development of the early shear layer region, particularly on a coarse grid, is extremely sensitive to fine differences in the turbulence modelling and numerics.

Anecdotal evidence indeed indicated that the GAM approaches that produce the most sudden drop in eddy viscosity exhibited lower numerical robustness. Although all simulations could be successfully run without serious difficulties, the strong interplay between numerics, turbulence modelling and mesh resolution should be studied more closely in the future. Optimal approaches are very likely to be code-specific.

Another key robustness issue relates to proper shielding of attached boundary layers (e.g. as addressed by the DDES approach), or any other measure taken to ensure proper prediction of attached boundary layers. CFDB reported a degradation of the DDES shielding performance when combined with the  $\sigma$  and WALE GAM approaches. A similar effect should be expected with other GAM approaches. A recalibration of the DDES shield function was needed to restore the shield functionality. Special measures preventing a premature switching from RANS to LES mode of DDES were required also in the  $\Delta_{SLA}$ -based DDES formulation. Also the HYB0-ETC approach had problems in shielding the BL, essentially because of the underlying HYB0 model. Not taking into account such secondary modelling

effects would lead to an increased likelihood of spurious “grid-induced separation” in practical simulations.

## 3.2 *Embedded Approaches*

### 3.2.1 Short Description of the Different Approaches

As for the non-zonal approaches, the key features of the different explored embedded approaches are summarised with reference to Sect. 3 for full descriptions.

- SEM (Pamiés): ONERA Synthetic-Eddy Method. Injection of random coherent structures at the interface. The structures are based on real boundary layer turbulence.
- DF: ONERA Dynamic Forcing downstream of the SEM plane to match target Reynolds normal stress. Can be combined with SEM.
- DF + WN: ONERA as above, with additional White Noise to speed up turbulence development.
- DFSEM: UniMan Divergence-Free Synthetic-Eddy Method. Injection of random vortices in a local volume around the interface. Global (correlations) in space and time including running averages.
- SEM: DLR Synthetic-Eddy Method. Injection of random vortices at the interface via volume-source terms. Global (correlations) in space and time. Optional automatic determination of the RANS-LES interface requires local BL properties (wall-normal integration).
- DFSEM (2011): DLR Divergence-Free Synthetic-Eddy Method in a formulation of Poletto et al. (2011).
- STG: NTS Synthetic Turbulence Generator. Injection of random Fourier modes at the interface plane. Global (correlations) in space and time.
- VSTG: NTS Volume distributed STG. Distributed source term in the momentum equation with a related sink term in the  $k$ -equation. Non-forced RANS solution needed, requires a two-stage procedure or overset grids in the interface zone.

### 3.2.2 Performance of Embedded Approaches for the Mandatory Case (Flat Plate Boundary Layer)

Selected methods have been compared directly using the same CFD code within the Common Assessment Platform (CAP). For high-Re boundary layers, there are two difficulties associated with embedded approaches in general and the mandatory flat plate case in particular. These are (i) the under resolved LES region that requires a reliable WMLES method and (ii) the RANS-LES interface that requires injection of

turbulent structures. The WMLES method within the LES region is assumed to be sufficiently well known and has been studied elsewhere. This is not of primary concern in this project, although some sensitivity of different approaches has been studied.

The comparison is, hence, specifically dedicated the inflow interface to the embedded LES region and the following statements can be made.

- Different methods of injecting turbulent structures are tested. The transition phase for the turbulence to rebuild is found to be 5–10  $\delta$ , which can be seen as acceptable and a rather unavoidable consequence of the turbulence cascade.
- The error level in the transition region is dependent on the quality and physicality of the injected turbulence. Overall, it should be emphasised that all methods show good behaviour with significant improvements over results considered good only a few years previously. From the CAP, the selected methods can be ranked in terms of the length and strength of the transition phase, visualised via the skin friction coefficient (Fig. 2). The shortest recovery length is returned by the NTS STG approach, followed by the DLR implementation of the SEM (although the depth of the “skin friction crisis” is much stronger for this method), then the DFSEM of UniMan followed by the Pamiès et al. method of ONERA.
- From visualisations of the synthetic 3D turbulence fields, the ONERA SEM and NTS STG are seen to produce qualitatively similar resolved turbulence.

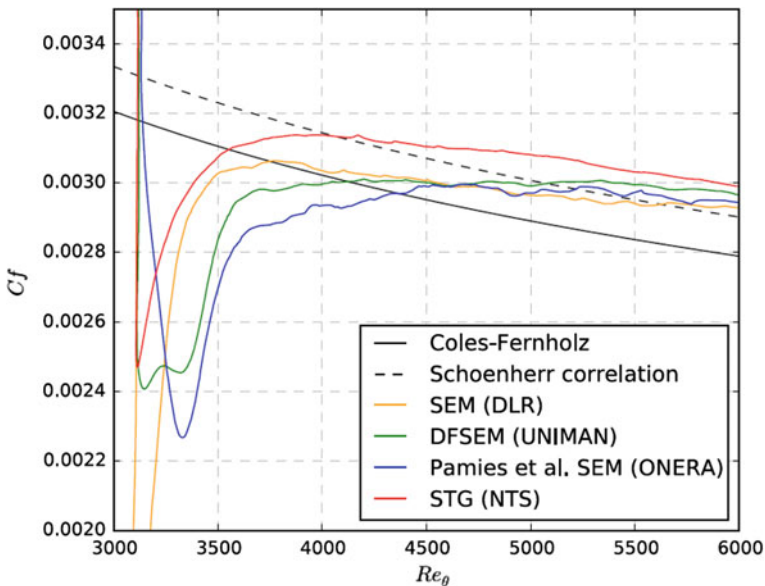


**Fig. 2** Comparison of recovery length downstream of different synthetic turbulence inlet methods from the Common Assessment Platform simulations (see Sect. 13 for details)

DLR SEM produces some quite large structures in comparison which, however, have no large impact on the down-stream turbulence.

- The NTS VSTG with distributed forcing in the interface region is consistent with the local STG approach but enables some additional generality and possibilities (mentioned later).
- As an addition to the planned CAP activities focusing on the flat plate boundary layer, a direct comparison was also carried out for fully-developed turbulent channel flow. Here the ranking of method performance was different to that established for the flat plate, with DFSEM performing best, followed by either the Pamiès et al. method or the STG depending on the assessment criteria (the former approaches the benchmark  $C_f$  value more rapidly downstream of the transition region, the latter has a much lower level of error in the transition region). This gives a strong indication that different methods will perform best for different applications and warns against drawing firm conclusions from a limited test case repertoire.
- The sudden introduction of turbulence structures at the interface will generate spurious noise emanating from the interface contaminating aero-acoustic predictions. A distributed volume forcing will mitigate the spurious noise and was adopted by NTS VSTG. Also, NTS Internal Damping Layer (IDL) STG is particularly developed for eliminating spurious noise by blending RANS and LES pressure in an overlap region (the NTS implementation strategy uses overset grids). Moreover, DLR tested acoustic sponge terms near the interface to damp spurious pressure oscillations.

### 3.2.3 Overall Evaluation of Strengths and Weaknesses of Embedded Approaches

Let us first briefly discuss the underlying WMLES approaches and their relevance for comparison of the different turbulence generators. The length of the flat plate was chosen to be sufficient for obtaining a reasonable fully developed boundary layer without major effects from the inlet procedure, in particular when plotted vs.  $Re_\theta$ . The primary observation from the different computations is that downstream of the end of the relaxation region the different WMLES approaches used (IDDES S-A, IDDES SST and ZDES) are accurate to within 5% for mean quantities like skin friction and mean velocity. The requirements and best practice for WMLES has been covered elsewhere and will not be further considered herein. The following discussion will be focused on the different methods of generating turbulence at the LES zone inflow.

#### *Implementation and usability issues*

Embedded approaches are inherently more complex to implement compared with the non-zonal approaches. Also the user input concerning the setup of the case and choices of parameters require significantly more effort. All methods require the

setup and meshing of an explicitly user defined LES region or zone embedded in a RANS environment. Inflow and outflow interfaces or zones must be defined by the user. The only exception here is the automatic approach being developed by DLR, which will be discussed later.

For most methods (ONERA and UniMan SEM and NTS STG) a RANS-LES interface must be defined which will act as a RANS outflow BC and an LES inflow BC where fluctuations are added to the RANS mean velocity profile. The procedure for generating the fluctuations is non-local (giving rise to surmountable parallelisation issues) or might need running averaging (UniMan DFSEM). However, all methods are applicable on structured as well as unstructured meshes. Moreover, the RANS solution is used for defining the fluctuating velocity amplitudes and scales.

For the NTS VSTG and DLR SEM the interface is replaced by a zone extended in the stream-wise direction where volume forcing is utilised for building up the turbulence structures. Note, however, that DLR restricted the zone in its Go4Hybrid computations to the actual hybrid RANS-LES interface plane in order to comply with the mandatory test-case setup. Volume forcing will relax the grid requirements compared with an interface plane leading to improved applicability on unstructured grids. Here, the RANS solution needed for deriving the fluctuations cannot just be sampled within the interface. DLR (SEM) samples the RANS solution “somewhat upstream of the interface”, which will require solutions only slowly varying in the stream-wise direction. NTS VSTG, on the other hand, utilises their possibility of overlapping grids and the RANS and LES regions then overlap in the interface zone.

An interesting method to define the LES zone has been investigated by DLR. Here, the LES zone is automatically defined within the running computation as the region of the flow with separated boundary layer identified by the boundary layer shape factor. The boundary layer properties must then be integrated through the boundary layer along all grid lines emanating from the wall nodes and DLR has presented a methodology also for unstructured grids. However, this advanced method was not fully demonstrated for a Go4Hybrid test case during the course of the project.

### *Generality*

All methods need information about the length and velocity scales of the injected turbulence structures. The length scale is related to the wall distance and RANS integral length scale. The time scale requires a “convective velocity” to be specified by the user, or to be locally integrated from the (mean) velocity in the interface plane (DLR). Interfaces located in three-dimensional mean flows might have different length and time scales at different parts of the interface which cannot easily be accounted for.

The ONERA SEM introduces real boundary-layer turbulence structures which might need to be adapted when used for an interface within a free shear flow like jets, wakes or mixing layers. The NTS STG method and the SEM variants used (by DLR and UniMan) on the other hand use only information from the RANS

anisotropy when generating the structures. This approach is more general which was proven for the mixing layer case using the NTS STG method with the interface at different down-stream positions.

All methods can be transformed to work with an arbitrary direction of the interface plane. More general geometries with curved interface surfaces or oblique flow relative the interface cannot easily be considered within the present formulations, except for VSTG where the interface is distributed over a volume. Moreover, a mixed in and outflow interface, such as locating the interface within a region of recirculating flow, is out of scope and not recommended for the existing embedded approaches.

### *Robustness*

The turbulence structures are injected either as a boundary condition at the internal interface or as a volume forcing in a local volume in the interface region. Both boundary conditions and volume forcing can be made preserving numerical stability with well-known considerations. Some of available methods are not divergence free, meaning that the generated structures do not fulfil the divergence or incompressibility criteria. For some incompressible solvers this could lead to numerical problems since no mechanism is present for damping strong divergence. For compressible solvers, unphysically high levels of divergence will lead to local compression and related pressure waves which might cause numerical issues and contribute to spurious generation of noise.

## **4 Lessons Learned and Best-Practice Findings**

Before adopting and assessing the different improvements for GAM proposed in this project, the baseline hybrid RANS-LES method must be well tested, understood and tuned. The particular GAM methods cannot overcome problems such as excessive numerical dissipation or poor resolution in time and space. This is valid for both non-zonal and embedded methods.

The implementation and use of non-zonal GAM methods is, in general, not much different from the base-line hybrid RANS-LES methods with formulations local in time and space. The amount of complexity and computational overhead are very limited. However, the non-zonal methods are limited when it comes to the ability to quickly switch from RANS to LES. Although the most promising of the non-zonal methods presented show great improvements, they are still in principle incapable of completely eliminating the grey area. Embedded methods require much more from the user in terms of setting up the case and providing parameter input. Also the implementation issues are non-trivial involving new data structures and treatment of non-local relations. However, with a well working generation of turbulence structures at the RANS-LES interface the transition region can be kept to a minimum of a few large-eddy turn over times (or distances).



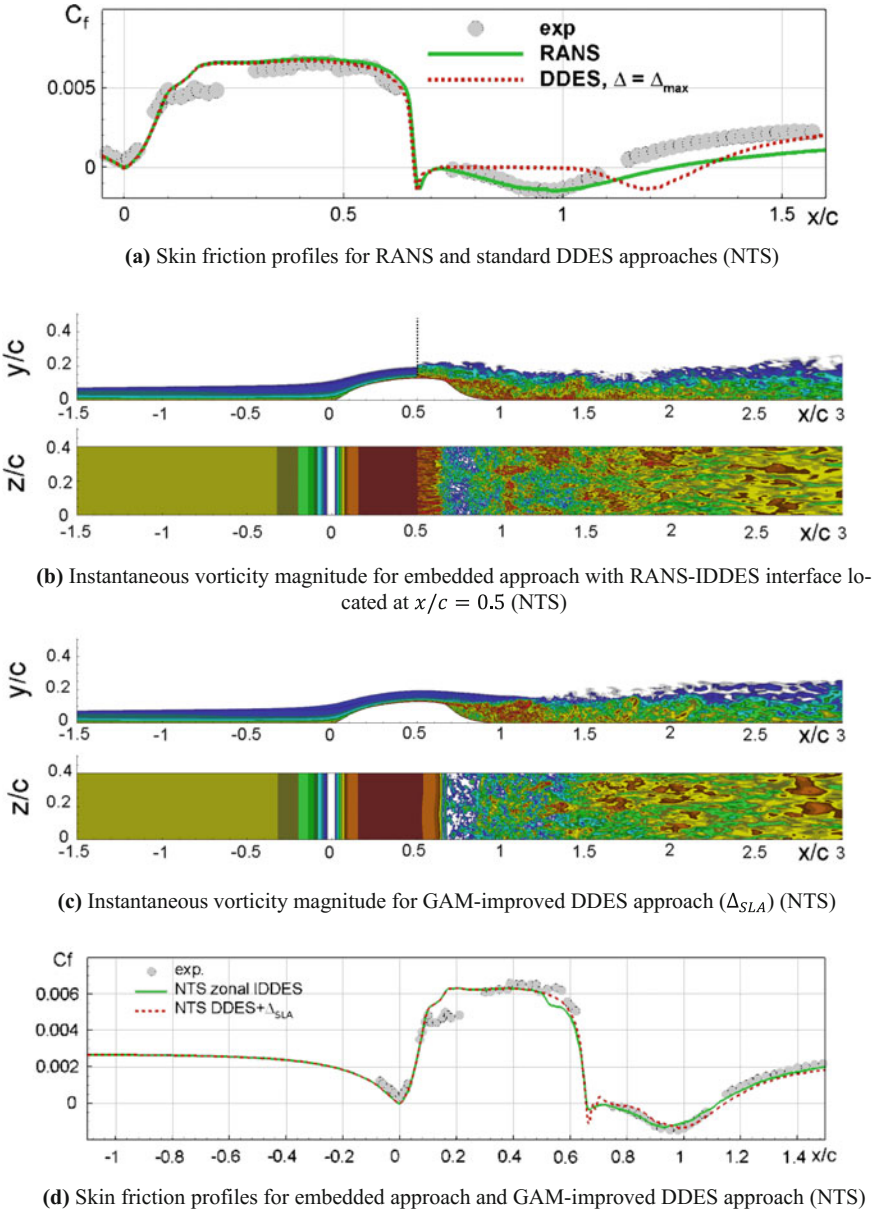


**Fig. 3** Results by NTS for the 2D wall-mounted hump test case highlighting the improvements achieved by both an embedded approach and a GAM-enhanced DDES approach compared to both RANS and standard DDES

Embedded approaches might lead to spurious noise which could contaminate aero-acoustic analyses. Some of the methods presented were shown to overcome this problem.

As was written in the introduction, the field of GAM with non-zonal as well as embedded methods is still progressing. Nonetheless, with the aid of the contributing project partners and observers, tentative conclusions are given in terms of overall findings, lessons learned and initial best practice.

A particularly illustrative result is collated in Fig. 3. The 2D hump test case was found in previous projects to be particularly challenging both for RANS as well as for standard non-zonal hybrid RANS-LES approaches. For the latter, the grey area was suspected to be the cause of the problem. Results by NTS for both an embedded approach as well as a GAM-enhanced non-zonal method in contrast both produce very good agreement with the measurements, thereby confirming the grey area to be the culprit. It is particularly encouraging that the two fundamentally different approaches are both successful for this flow. The embedded approach gives an incremental improvement over the non-zonal approach in the very early separated region due to the inclusion of resolved boundary layer turbulence upstream.

At the conclusion of the ATAAC project, Best Practice Guidelines were drawn up concerning the applicability of different types of model to different classes of flows (the corresponding diagram was discussed in Chap. 1). The flow classification followed the suggestion of Menter et al. (2012) based on consideration of the level of inherent stability in the flow due to which LES content is generated. It was concluded that “locally-stable” flows, such as shallow separating/reattaching flows were particularly poorly-served by hybrid RANS-LES methods: non-zonal approaches suffering from the grey area issue and embedded approaches were considered insufficiently mature. Following the Go4Hybrid project these guidelines can be updated as summarised in Fig. 4.

We propose somewhat tentatively that based on the developments and findings of the Go4Hybrid project, “locally unstable” flows can be considered manageable using both the grey-area improved non-zonal methods as well as improved embedded approaches. The caution here is due to the limited experience and need for significantly more testing with these novel methods.

## 5 Concluding Remarks and Outlook

### 5.1 Concluding Remarks

The Go4Hybrid project has gathered some of the groups that are active in the further development of hybrid RANS-LES methods resulting in novel developments and increased experience related to the grey area problem. The lessons learned and initial best practice has been collected in this chapter.

"Globally unstable" flows	"Locally unstable" flows	"Stable" flows
<b>Status before Go4Hybrid:</b>		
Applicability of DES-like methods		
Applicability of SAS	(SAS requires forcing to enter scale-resolving mode)	
Embedded approaches necessary		
Applicability/suitability of WMLES		
<b>Status after Go4Hybrid:</b>		
Applicability of DES-like methods with grey-area enhancement		
Applicability of embedded approaches		

**Fig. 4** Best practice guidelines regarding method applicability before the Go4Hybrid project and afterwards

Obviously, there are additional activities outside of this group that have not been considered which makes the best practice incomplete. Moreover, there are other urgent problems related to hybrid RANS-LES which have not been addressed in this study.

Every indication from the Go4Hybrid work is that the particularly difficult yet important class of "locally-unstable" flows (e.g. shallow separation and reattachment), which were previously poorly served both by hybrid RANS-LES as well as RANS, can now be reliably predicted using both non-zonal methods with grey area improvements and improved embedded approaches. Although caution must be observed due to the limited testing carried out so far, this can be considered a significant success.

Non-zonal and embedded methods are conceptually very different but an interesting attempt undertaken by DLR to adopt the embedded method by an automatic procedure of identifying the embedded LES region demonstrates that in terms of the user interaction, the embedded methods may become not more user demanding than the non-zonal ones.

## 5.2 *Future Trends and Needs*

The most promising of the newly developed methods and model extensions must now be carefully assessed and tested on a wider variety of flow cases and application scenarios in order to gain experience and, most importantly, to capture any inconsistencies and degenerate behaviour in more general conditions. These are e.g. the boundary layer shielding capabilities and baseline LES capabilities. It is essential to ensure that we don't improve grey area aspects at the expense of other important properties.

Such investigations together with careful improvements and further calibrations would then offer the basis for a more complete and rigorous best practice guide.

Based on this experience and on the needs of engineers and researchers without in-depth, "developer" knowledge, the need for *generalisation* and automation is obvious. Here, the Go4Hybrid project findings can be an important support for software vendors and engineering development departments.

Looking forward then, a clear need is for improved *industrialisation* of the new methods generating within this pioneering project. Topics that need to be studied further include:

- Assessment of performance for more complex cases and mixed flow types (as mentioned above).
- Testing for inter-disciplinary applications (e.g. multi-phase and reacting flows, flows with combustion).
- Resolution of numerical issues, relating to the high sensitivity of the typically poorly-resolved early shear layer. The balance between low-dissipation and robustness is key here.
- A more detailed study of the influence of grid resolution, targeting more concrete best practice guidelines and potentially informing automatic grid adaptation algorithms.
- An assessment of the impact of grey-area improved hybrid methods on grid resolution requirements: For example, do the improved methods exhibit relaxed grid requirements relative to standard methods?
- Further improvement to the flexibility of embedded approaches, including LES-to-RANS conditions, mixed inlet-outlet conditions to the LES region, automatic detection of resolved and modelled zones.

# References

- Adamian, D., Travin, A.: An Efficient Generator of Synthetic Turbulence at RANS–LES Interface in Embedded LES of Wall-Bounded and Free Shear Flows. *Comput. Fluid Dyn.* **2010**, 739–744 (2011)
- Adamian, D.Y., Strelets, M.Kh, Travin, A.K.: An efficient method of synthetic turbulence generation at LES inflow in zonal RANS-LES approaches to computation of turbulent flows. *Math. Model.* **23**(7), 3–19 (2011). In Russian
- AGARD.: A selection of test cases for the validation of large-eddy simulations of turbulent flows, AGARDograph 345 (1998)
- Arakeri, V., Krothapalli, A., Siddavaram, V., Alkisar, M., Lourenco, L.: On the use of microjets to suppress turbulence in a Mach 0.9 axisymmetric jet. *J. Fluid Mech.* **490**, 75–98 (2003)
- Bridges, J., Wernet, M.: Establishing consensus turbulence statistics for hot subsonic jets, AIAA Paper, AIAA 2010-3751 (2010)
- Castillo, L., Wang, X., George, W.K.: Separation criterion for turbulent boundary layers Via Similarity Analysis. *J. Fluids Eng.* **126**(3), 297–304 (2004). doi:[10.1115/1.1758262](https://doi.org/10.1115/1.1758262)
- Chauvet, N., Deck, S., Jacquin, L.: Zonal-detached-eddy simulation of a controlled propulsive jet. *AIAA J.* **45**(10), 2458–2473 (2007)
- Chen, S., Doolen, G.: Lattice Boltzmann method for fluid flows, *Ann. Rev. Fluid Mech.* **30**:329–364 (1998)
- Chen, H., Kandasamy, S., Orszag, S., Shock, R., Succi, S., Yakhot, V.: Extended Boltzmann kinetic equation for turbulent flows. *Science* **301**(5633), 633–636 (2003)
- Chu, J., Luckring, J.M.: Experimental surface pressure data obtained on 65° delta wing across Reynolds number and Mach number ranges. NASA TM 4645 (1996)
- Cummings, R.M., Morton, S.A., McDaniel, D.R.: Experiences in accurately predicting time-dependent flows. *Prog. Aerosp. Sci.* **44**, 241–257 (2008)
- Deardorff, J.: A numerical study of three-dimensional turbulent channel flow at large Reynolds numbers”. *J. Fluid Mech.* **41**(2), 453–480 (1970)
- Deck, S.: Numerical simulation of transonic buffet over a supercritical airfoil. *AIAA J.* **43**(7), 1556–1566 (2005)
- Deck, S.: Zonal-detached-eddy simulation of the flow around a high-lift configuration. *AIAA J.* **43**(11), 2372–2384 (2005)
- Deck, S.: Recent improvement in the Zonal Detached Eddy Simulation (ZDES) formulation. *Theor. Comput. Fluid Dyn.* **26**, 523–550 (2012)
- Deck, S., Laraufie, R.: Numerical investigation of the flow dynamics past a three-element airfoil. *J. Fluid Mech.* **732**, 401–404 (2013). doi:[10.1017/jfm.2013.363](https://doi.org/10.1017/jfm.2013.363)
- Deck, S., Renard, N., Laraufie, R., Sagaut, P.: Zonal Detached Eddy Simulation (ZDES) of a spatially developing flat plate turbulent boundary layer over the Reynolds number range  $3 \leq Re_\theta \leq 14,000$ . *Phys. Fluids* **26**, 025116 (2014)

- Deck, S., Renard, N., Laraufie, R., Weiss, P.E.: Large-scale contribution to mean wall shear stress in high-Reynolds-number flat-plate boundary layers up to  $Re_q=13650$ . *J. Fluid Mech.* **743**, 202–248 (2014)
- Deck, S., Weiss, P.E., Pamiès, M., Garnier, E.: Zonal detached eddy simulation of a spatially developing flat plate. *Comput. Fluids* **48**, 1–15 (2011)
- DeGraaff, D.B., Eaton, J.K.: Reynolds number scaling of the flat-plate turbulent boundary layer. *J. Fluid Mech.* **422**, 319–346 (2000)
- Delville, J.: La décomposition orthogonal aux valeurs propres et l'analyse de l'organisation tridimensionnelle de écoulements turbulents cisailés libres. PhD thesis, Université de Poitiers (1995)
- Fuchs, M., Le Chuiton, F., Mockett, C., Sesterhenn, J., Thiele, F.: Detached-Eddy Simulation of separated wake flow around complex helicopter configuration, *Progress in Hybrid RANS-LES Modelling, Notes on Numerical Fluid Mechanics and Multidisciplinary Design*, vol. 130, pp. 131–140. Springer, Heidelberg (2015)
- Fuchs, M., Mockett, C., Steger, M., Thiele, F.: A novel DES-based approach to improve transition from RANS to LES in free shear layers. *Proceedings of the 10th International ERCOFTAC Symposium on Engineering Turbulence Modelling and Measurements*, Marbella, Spain (2014)
- Fuchs, M., Sesterhenn, J., Thiele, F., Mockett, C.: Assessment of novel DES approach with enhanced SGS modelling for prediction of separated flow over a delta wing. *22nd AIAA Computational Fluid Dynamics Conference, AIAA Aviation, AIAA 2015-3433*, Dallas, Texas (2015)
- Furman, A., Breitsamter, C.: Turbulent and unsteady flow characteristics of delta wing vortex systems. *46th AIAA Aerospace Sciences Meeting and Exhibit, AIAA Paper 2008-0381* (2008)
- Furman, A., Breitsamter, C.: Experimental investigations on the VFE-2 configuration at TU Munich, Germany. Chapter 21 In: Lamar, J.E., et al (2009)
- Girimaji, S.S.: Partially-Averaged Navier-Stokes Model for Turbulence: A Reynolds-Averaged Navier-Stokes to direct numerical simulation bridging method. *ASME J. Appl. Mech.* **73**, 413–421 (2006)
- Girimaji, S.S., Wallin, S.: Closure modeling in bridging regions of variable-resolution (VR) turbulence computations. *J. Turbul.* **14**(1), 72–98 (2013)
- Grawunder, M., Reiß, R., Breitsamter, C., Adams, N.A.: Flow characteristics of a helicopter fuselage configuration including a rotating rotor head. In: *Proceedings of the 28th Congress of the International Council of the Aeronautical Sciences*, Brisbane, Australia, 23–28 Sept 2012
- Greenblatt, D., Paschal, K.B., Yao, C.-S., Harris, J., Schaeffler, N.W., Washburn, A.E.: Experimental investigation of separation control Part 1: baseline and steady suction. *AIAA J.* **44**(12), 2820–2830 (2006)
- Greenblatt, D., Paschal, K.B., Yao, C.-S., Harris, J.: Experimental investigation of separation control Part 2: zero mass-efflux oscillatory blowing. *AIAA J.* **44**(12), 2831–2845 (2006)
- Gritskevich, M.S., Garbaruk, A.V., Schütze, J., Menter, F.R.: Development of DDES and IDDES formulations for the  $k-\omega$  shear stress transport model. *J. Flow Turbul. Combust.* **88**(3), 431–449 (2012)
- Haase, W., Braza, M., Revell, A.: *DESider—A European effort on Hybrid RANS-LES modelling*. vol. 103 of *Notes on Numerical Fluid Mechanics and Multidisciplinary Design*, Springer, Berlin (2009)
- Jakirlic, S., Hanjalic, K.: A new approach to modelling near-wall turbulence energy and stress dissipation. *J. Fluid Mech.* **439**:139–166 (2002)
- Jarrin, N., Benhamadouche, S., Laurence, D., Prosser, R.: A Synthetic-Eddy Method for Generating Inflow Conditions for LES. *Int. J. Heat Fluid Flow* **27**, 585–593 (2006)
- Jarrin, N., Benhamadouche, S., Laurence, D., Prosser, R.: Divergence free synthetic eddy method for embedded LES inflow conditions. *Int. J. Heat Fluid Flow* **27**, 585–593 (2009)
- Jarrin, N., Prosser, R., Uribe, J., Benhamadouche, S., Laurence, D.: Reconstruction of turbulent fluctuations for hybrid RANS/LES simulations using a synthetic-eddy method. *Int. J. Heat Fluid Flow* **30**, 435–442 (2009)

- Khalighi, Y., Nichols, J., Lele, S., Ham, F., Moin, P.: Unstructured Large Eddy Simulation for Prediction of Noise Issued from Turbulent Jets in Various Configurations, AIAA-2011-2886, 17th AIAA/CEAS Aeroacoustics Conference. Portland, Oregon, USA (2011)
- Kok, J.C.: A high-order low-dispersion symmetry-preserving finite-volume method for compressible flow on curvilinear grids. *J. Comput. Phys.* **228**, 6811–6832 (2009)
- Kok, J.C.: A stochastic backscatter model for grey-area mitigation in detached eddy simulations. NLR-TP-2016-233. (To be submitted to *Flow, Turbulence and Combustion*) (2016)
- Kok, J.C., van der Ven, H.: Destabilizing free shear layers in X-LES using a stochastic subgrid-scale model. In: Peng, S.H., Doerffer, P., Haase, W. (eds.), *Progress in Hybrid RANS-LES Modelling*, Volume 111 of *Notes on Numerical Fluid Mechanics and Multidisciplinary Design*, pp. 179–189. Springer, Berlin. NLR-TP-2009-327 (2009). (<http://hdl.handle.net/10921/238>)
- Kok, J.C., van der Ven, H.: Capturing free shear layers in hybrid RANS-LES simulations of separated flow. Third Symposium ‘Simulation of Wing and Nacelle Stall’, Braunschweig, Germany, 21–22 June. NLR-TP-2012-333 (2012)
- Kok, J.C., Dol, H.S., Oskam, B., van der Ven, H.: Extra-large eddy simulation of massively separated flows. In: 42nd AIAA Aerospace Sciences Meeting, Reno, NV, 5–8 January 2004. AIAA paper 2004-264 (2004)
- Kok, J.C., van der Ven, H., Tangermann, E., Sanchi, S., Probst, A., Weinman, K.A., Temmerman, L.: Vortex breakdown above a delta wing with sharp leading edge, ERCOFTAC QNET-CFD Wiki, (2015). (<http://qnet-ercoftac.cfms.org.uk/w/index.php/AC1-09>)
- Kraichnan, R.: Diffusion by a random velocity field. *Phys. Fluids* **13**, 22–31 (1970)
- Lamar, J.E., et al.: *Understanding and Modeling Vortical Flows to Improve the Technology* (2009) Readiness Level for Military Aircraft, Summary Report of Task Group AVT-113, RTO-TR-AVT-113, RTO/NATO, Oct 2009
- Laraufie, R., Deck, S.: Assessment of Reynolds stresses tensor reconstruction methods for synthetic turbulent inflow conditions. Application to hybrid RANS/LES methods. *Int. J. Heat Fluid Flow* **42**, 68–78 (2013)
- Laraufie, R., Deck, S., Sagaut, P.: A dynamic forcing method for unsteady turbulent inflow conditions. *J. Comput. Phys.* **230**, 8647–8663 (2011)
- Lau, J.: Effects of Exit Mach number and temperature on mean-flow and turbulence characteristics in round jets. *J. Fluid Mech.* **105**, 193–218 (1981)
- Leith, C.E.: Stochastic backscatter in a subgrid-scale model: Plane shear mixing layer. *Phys. Fluids A* **2**(3), 297–299 (1990)
- Lüdeke, H.: Detached Eddy Simulation of a Delta Wing With Rounded Leading Edge. In: *Proceedings of the 7th ONERA DLR Aerospace Symposium ODAS* (2006)
- Manoha, E., Caruelle, B.: Summary of the LAGOON Solutions from the Benchmark problems for Airframe Noise Computations-III Workshop. 21st AIAA/CEAS Aeroacoustics Conference, AIAA AVIATION Forum, (AIAA 2015-2846) (2015). doi:[10.2514/6.2015-2846](https://doi.org/10.2514/6.2015-2846)
- Menter, F.R.: Zonal two-equation  $k$ - $\omega$  turbulence models for aerodynamic flows. AIAA Paper, AIAA 1993-2906 (1993)
- Menter, F.R., Kuntz, M.: *Adaptation of Eddy-Viscosity Turbulence Models to Unsteady Separated Flow Behind Vehicles*. Proc. Conf. The Aerodynamics of Heavy Vehicles: Trucks, Busses and Trains, Asilomar, Ca. Berlin, Springer (2003)
- Menter, F., Schütze, J. and Gritskevitch, M.: Global vs. zonal approaches in hybrid RANS-LES turbulence modelling. In: *Proceedings of 4th Symposium on Hybrid RANS-LES Methods*, Beijing, China (2012)
- Michel, R., Quémard, R., Durant, R.: Application d’un schéma de longueur de mélange à l’étude des couches limites turbulentes d’équilibre. ONERA, Note Technique No. 154 (1969)
- Mockett, C., Le Chuiton, F., Fuchs, M., Thiele, F.: Helicopter fuselage wake prediction using Detached-Eddy Simulation. *Progress in Hybrid RANS-LES Modelling*, Notes on Numerical Fluid Mechanics and Multidisciplinary Design, vol. 117, pp. 413–425, Springer, Berlin (2012)

- Mockett, C., Fuchs, M., Garbaruk, A., Shur, M., Spalart, P., Strelets, M., Thiele, F., Travin, A.: Two Non-Zonal Approaches to Accelerate RANS to LES Transition of Free Shear Layers in DES. In: Progress in Hybrid RANS-LES Modelling, Notes on Numerical Fluid Mechanics and Multidisciplinary Design, vol. 130, pp. 187–201 (2015)
- Morton, S.: Detached-Eddy Simulations of Vortex Breakdown over a 70-Degree Delta Wing. *J. Aircr.* **46**, 746–755 (2009)
- Nagib, H.M., Chauhan, K.A., Monkewitz, P.A.: Approach to an asymptotic state for zero pressure gradient turbulent boundary layers. *Philos. Trans. R. Soc. A* **365**, 755–770 (2007)
- Naughton, J.W., Viken, S., Greenblatt, D.: Skin-Friction Measurements on the NASA Hump Model. *AIAA J.* **44**(6), 1255–1265 (2006)
- Nicoud, F., Ducros, F.: Subgrid-scale stress modelling based on the square of the velocity gradient tensor. *Flow Turbul. Combust.* **62**(3), 183–200 (1999)
- Nicoud, F., Baya Toda, H., Cabrid, O., Bose, S., Lee, J.: Using singular values to build a subgrid-scale model for large eddy simulations. *Phys. Fluids* **23**(085106) (2011)
- Österlund, J.M., Johansson, A.V., Nagib, A.V., Hites, M.: A note on the overlap region in turbulent boundary layers. *Phys. Fluids* **12**, 1–4 (2000)
- Pamiès, M., Weiss, P.E., Garnier, E., Deck, S., Sagaut, P.: Generation of synthetic turbulent inflow data for large eddy simulation of spatially evolving wall-bounded flows. *Phys. Fluids* **21**, 045103 (2009)
- Peng, S.-H.: Hybrid RANS-LES modeling based on zero- and one-equation models for turbulent flow simulation. In: Proceedings of 4th International Symposium on Turbulence and Shear Flow Phenomena, vol. 3, pp. 1159–1164. 27–29 June 2005, Williamsburg, Virginia, USA (2005)
- Peng, S.-H.: Algebraic Hybrid RANS-LES Modelling Applied to Incompressible and Compressible Turbulent Flows. AIAA Paper-3910, San Francisco (2006)
- Peng, S.-H.: Hybrid RANS-LES modelling with an energy-backscatter function incorporated in the LES mode. In: Proceedings THMT-2012, Begell House, Inc (2012)
- Peng, S.-H., Davidson, L.: Some remarks on approximation for subgrid scale modelling in large eddy simulation, Scientific Report FOI-R-0381-SE, ISSN 1650-1942, Swedish Defence Research Agency, Stockholm (2002)
- Peng, S.-H., Davidson, L.: Approximation of subgrid-scale stresses based on the Leonard expansion. In: Hanjalic, K., Nagano, Y., Jakirlic, S. (eds.) *Turbulence, Heat and Mass Transfer*, vol. 6, Begell House, Inc (2009)
- Peng, S.-H., Deck, S., van der Ven, H., Knopp, T., Catalano, P., Rodriguez, C.L., Zwerger, C., Kok, J.C., Jirasek, A., Capizzano, F., Breitsamer, C.: Scrutinizing Hybrid RANS-LES Methods for Aerodynamic Applications. GARTEUR Technical Report TP-182 and FOI-S-4866-SE (2014)
- Peng, S.-H., Nebenfuhr, B., Davidson, L.: Lessons learned from hybrid RANS-LES computations of a three-element airfoil flow. AIAA Paper 2013-2841, 21st AIAA Computational Fluid Dynamics Conference (2013)
- Poletto, R., Craft, T., Revell, A.: A new divergence free synthetic eddy method for the reproduction of inlet flow conditions for LES. *Flow Turbul. Combust.* **91**(3), 519–539 (2013)
- Poletto, R., Revell, A., Craft, T., Jarrin, N.: Divergence free synthetic eddy method for embedded LES inflow conditions. In: 7th International Symposium on Turbulence and Shear Flow Phenomena, Ottawa (2011)
- Probst, A., Garbaruk, A., Schwamborn, D., Shur, M., Strelets, M.: Hybrid RANS/LES Simulations of Multi-Element Airfoil Stall Using Different Flow Solvers. 6th European Conference on Computational Fluid Dynamics, Barcelona, 20–25 July (2014)
- Probst, A., Löwe, J., Reuß, S., Knopp, T., Kessler, R.: Scale-Resolving Simulations with a Low-Dissipation Low-Dispersion Second-Order Scheme for Unstructured Finite-Volume Flow Solvers. In: AIAA 2015-0816 (2015)



- Probst, A., Radespiel, R.: Implementation and Extension of a Near-Wall Reynolds-Stress Model for Application to Aerodynamic Flows on Unstructured Meshes. AIAA Paper 2008-0770 (2008)
- Probst, A., Radespiel, R., Knopp, T.: Detached-Eddy Simulation of Aerodynamic Flows Using a Reynolds-Stress Background Model and Algebraic RANS / LES Sensors. In: AIAA Paper 2011-3206 (2011)
- Renard, N., Deck, S.: Improvements in the formulation of Zonal Detached Eddy Simulation for Wall-Modeled Large-Eddy Simulation. AIAA J. **53**(11), 3499–3504 (2015)
- Rogers, S.E., Kwak, D.: An Upwind Differencing Scheme for the Time Accurate Incompressible Navier-Stokes Equations. AIAA Paper, AIAA 88–2583 (1988)
- Sagaut, P., Deck, S., Terracol, M.: Multiscale and multiresolution approaches in turbulence—LES, DES and Hybrid RANS/LES Methods: Applications and Guidelines (2nd edn.). Imperial College Press, 448p. (2013)
- Schiavetta, L.A., Badcock, K.J., Cummings, R.M.: Comparison of DES and URANS for unsteady vortical flows over delta wings, AIAA Paper 2007-1085, 45th AIAA Aerospace and Sciences Meeting and Exhibit, 8–11 January 2007. Reno, Nevada (2007)
- Schiestel, R., Dejoan, A.: Towards a new partially integrated transport model for coarse grid and unsteady turbulent flow simulations. Theor. Comp. Fluid Dyn. **18**, 443–468 (2005)
- Schlatter, P., Örlü, R.: Assessment of direct simulation data of turbulent boundary layers. J. Fluid Mech. **659**, 116–126 (2010)
- Schumann, U.: Stochastic backscatter of turbulence energy and scalar variance by random subgrid-scale fluxes. Proc. R. Soc. Lond. A **451**, 293–318 (1995)
- Schwaborn, D., Gerhold, T., Heinrich, R.: The DLR TAU-Code: recent applications in research and industry. In: Wesseling, P., Oñate, E., Périaux, J. (eds.) ECCOMAS CFD. TU Delft, The Netherlands (2006)
- Schwaborn, D., Strelets, M.: ATAAC—An EU-Project Dedicated to Hybrid RANS/LES Methods. Progress in Hybrid RANS-LES Modelling, Notes on Numerical Fluid Mechanics and Multidisciplinary Design, vol. 117, pp. 59–75, Springer, Berlin. ISBN:978-3-642-31817-7 (2012)
- Seifert, A., Pack, L.G.: Active flow separation control on wall-mounted hump at high Reynolds numbers. AIAA J. **40**(7), 1363–1372 (2002)
- Shields, F., Bass, H.: Atmospheric absorption of high frequency noise and application to fractional-octave bands, NASA report, NASA CS-2760 (1977)
- Shur, M., Spalart, P., Strelets, M.: Noise prediction for increasingly complex jets. Part I, Methods and tests; Part II, Applications, International Journal of Aeroacoustics, vol. 4, pp. 213–266 (2005)
- Shur, M., Spalart, P., Strelets, M.: LES-Based Evaluation of a Microjet Noise Reduction Concept in Static and Flight Conditions. J. Sound Vib. **330**(17):4083–4097 (2011)
- Shur, M.L., Spalart, P.R., Strelets, M.Kh, Travin, A.K.: A Hybrid RANS-LES approach with delayed-DES and wall-modelled LES capabilities. Int. J. Heat Fluid Flow **29**(6), 406–417 (2008)
- Shur, M.L., Spalart, P.R., Strelets, M.Kh, Travin, A.K.: Synthetic turbulence generators for RANS-LES interfaces in zonal simulations of aerodynamic and aeroacoustic problems. Flow Turbul. Combust. **93**, 63–92 (2014)
- Shur, M.L., Spalart, P.R., Strelets, M.Kh, Travin, A.K.: An enhanced version of DES with rapid transition from RANS to LES in separated flows. Flow Turbul. Combust. **95**, 709–737 (2015)
- Shur, M.L., Strelets, M.Kh.: Detailed (Sufficient for Implementation) Formulation of Different Techniques (Embedded Methods). Go4Hybrid, Technical Report D3.1-06 (2014)
- Shur, M.L., Strelets, M., Travin, A.: High-order implicit multi-block Navier-Stokes code: Ten-years experience of application to RANS/DES/LES/DNS of turbulent flows. In: 7th Symposium on Overset Composite Grids & Solution Technology, Huntington Beach, California (2004). [http://cfd.spbstu.ru/agarbaruk/c/document\\_library/DLFE-42505.pdf](http://cfd.spbstu.ru/agarbaruk/c/document_library/DLFE-42505.pdf)

- Simonich, J., Narayanan, S., Barber, T., Nishimura, M.: Aeroacoustic characterization, noise reduction and dimensional scaling effects of high subsonic jets, AIAA paper, AIAA 2062-2069 (2001)
- Spalart, P.R.: Detached Eddy simulation. *Annu. Rev. Fluid Mech.* **41**, 181–202 (2009)
- Spalart, P.R., Allmaras, S.R.: A one-equation turbulence model for aerodynamic flows. AIAA Paper, AIAA 1992-0439 (1992)
- Spalart, P., Allmaras, S.: A one-equation turbulence model for aerodynamic flows. *La recherche aérospatiale* **1**(1), 5–21 (1994)
- Spalart, P.R., Deck, S., Shur, M.L., Squires, K.D., Strelets, M.K., Travin, A.: A new version of detached-eddy simulation, resistant to ambiguous grid densities. *Theor. Comput. Fluid Dyn.* **20**(3), 181–195 (2006)
- Strelets, M.: Detached eddy simulation of massively separated flows. AIAA Paper, AIAA 2001-0879 (2001)
- Travin, A., Shur, M.: Physical and numerical upgrades in the detached-eddy simulation of complex turbulent flows. *Adv. LES Complex Flows* **65**(5), 239–254 (2004)
- Travin, A., Shur, M., Strelets, M., Spalart, P.: Detached-eddy simulations past a circular cylinder. *Flow Turbul. Combust.* **63**(1), 293–313 (2000)
- Travin, A., Shur, M., Strelets, M., Spalart, P.: Physical and numerical upgrades in the detached-eddy simulation of complex turbulent flows, In: Proceedings of the 412th Euromech Colloquium on LES and Complex Transitional and Turbulent Flows, Munich, Germany (2000)
- Viswanathan, K.: Aeroacoustics of hot jets. *J. Fluid Mech.* **516**, 39–82 (2004). doi:[10.1017/S0022112004000151](https://doi.org/10.1017/S0022112004000151)
- Vogel, J., Eaton, J.: Combined heat transfer and fluid dynamic measurements downstream of a backward-facing step. *J. Heat Transf.* **107**(4), 922–929 (1985)
- Wallin, S., Girimaji, S.S.: Commutation error mitigation in variable-resolution PANS closure: Proof of concept in decaying isotropic turbulence. 6th AIAA Theoretical Fluid Mechanics Conference 27–30 June 2011, Honolulu, Ha-waii, AIAA paper 2011-3105 (2011)
- Wallin, S., Girimaji, S.S.: Modelling energy scale transfer in variable resolution simulation of turbulence. Presented at Fifth HRLM Symposium, 19–21 Mar 2014, A&M University, College Station, USA (2014)
- Wallin, S., Reyes, D.A., Girimaji, S.S.: Bridging between coarse and fine resolution in variable resolution turbulence computations. Proceedings of the Seventh International Symposium On Turbulence, Heat and Mass Transfer (THMT-12) Palermo, Italy, 24–27 Sept 2012
- Wild, J., Pott-Pollenske, M., Nagel, B.: An integrated design approach for low noise exposing high-lift devices. AIAA-2006-2843, 3rd AIAA Flow Control Conference (2006)